2023

Towards the Development of Smoothed Particle Hydrodynamics Model for Oscillating Water Column Devices

Zhu, Guixun
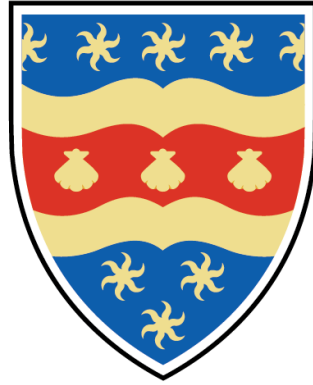
https://pearl.plymouth.ac.uk/handle/10026.1/20661

Copyright Statement

This copy of the thesis has been supplied on condition that anyone who consults it is understood to recognise that its copyright rests with its author and that no quotation from the thesis and no information derived from it may be published without the author's prior consent.

University of
Plymouth

Towards the Development of Smoothed Particle Hydrodynamics Model for Oscillating Water Column Devices

Guixun Zhu

School of Engineering, Computing and Mathematics

A thesis submitted to the University of Plymouth
in partial fulfilment for the degree of
Doctor of Philosophy

April 2023

'Hear wind sing, wait for blossom'

Acknowledgements

This PhD thesis presents the work I have been doing for the past four years. I also need to thank a lot of people for their help, encouragement and kindness. Without that, it would have been difficult for me to complete this thesis.

Finally, and most importantly, I would like to thank my parents, sisters, family and Ms. Zhuoying Li. The time and effort necessary to complete this research would not have been possible without their encouragement, dedication and love.

Declaration

At no time during the registration for the degree of Doctor of Philosophy has the author been registered for any other University award without prior agreement of the Doctoral College Quality Sub-Committee. This thesis has been proofread by a third party; no factual changes or additions or amendments to the argument were made as a result of this process. A copy of the thesis prior to proofreading will be made available to the examiners upon request. Work submitted for this research degree at the University of Plymouth has not formed part of any other degree either at the University of Plymouth or at another establishment. Word count of main body of thesis: 34970.

Guixun Zhu

April 2023

Towards the Development of Smoothed Particle Hydrodynamics Model

for Oscillating Water Column Devices

Abstract

The Oscillating water column (OWC) device is a type of wave energy converter (WEC) that has received wide investigation. Integrating OWC with breakwaters can reduce construction and maintenance costs. However, there is a risk of damage to these OWC devices under extreme sea conditions. This thesis focuses on the study of OWC devices based on the Smoothed Particle Hydrodynamics (SPH) model. The SPH method, a fully Lagrangian approach that simulates fluid problems using a set of moving particles carrying physical properties, is particularly well-suited to simulating flows with large deformation. The SPH model can therefore handle the strong non-linear situations resulting from wave slamming against OWC devices. Nevertheless, high computational cost of SPH model limits the large-scale investigation of SPH applications for OWC installations. The main work of this thesis can be therefore divided into two main parts: improving efficiency of SPH model and applying SPH model to the design of OWC devices.

First, to simulate OWC devices with power take-off (PTO) systems, a single-phase SPH model with a pneumatic model was developed. Based on the correlation between air pressure and airflow rate over the orifice, the air pressure inside the chamber is determined. In this way, only the water phase, which takes into account the effect of air inside the chamber, is simulated. To model the thin front wall of OWC devices, a regional ghost particle approach is introduced. As a result, particle resolution for the thin wall can be independent of wall thickness. Then a new massively parallel SPH framework with a dynamic load balance strategy is presented for free-surface flow. The development of the parallel SPH model has improved computational speed and allows the model to run on High Performance Computing (HPC) systems. A two-way coupled model to hybridize the SPH model with OceanWave3D is proposed. The nonlinear region is simulated using the SPH model, while the other regions are modelled using OceanWave3D, which is based on fully lessnonlinear potential flow

theory and has less computational expense. Finally, the present model is applied to study wave loads of a U-shaped OWC device for the purpose of reliable design. It is found that the maximum wave force can be decreased by more than 20% by carefully optimising the width and height of the U-OWC vertical duct.

Guixun Zhu

Publication List

0.1 Journal papers

Zhu, G., Samuel, J., Zheng, S., Hughes, J., David S., & Greaves, D. (2023). Numerical investigation on the hydrodynamic performance of a 2D U-shaped Oscillating Water Column wave energy converter. Energy, 127357.

Zhu, G., Hughes, J., Zheng, S., & Greaves, D. (2023). A Novel MPI-based Parallel Smoothed Particle Hydrodynamics Framework with Dynamics Load Balancing for Free Surface Flow. Computer Physics Communications, 284, 108608.

Zhu, G., Graham, D., Zheng, S., Hughes, J., & Greaves, D. (2020). Hydrodynamics of onshore oscillating water column devices: A numerical study using smoothed particle hydrodynamics. Ocean Engineering, 218, 108226.

Zheng, S., **Zhu, G.**, Simmonds, D., Greaves, D., & Iglesias, G. (2020). Wave power extraction from a tubular structure integrated oscillating water column. Renewable Energy, 150, 342-355.

Zheng, S., Antonini, A., Zhang, Y., Miles, J., Greaves, D., **Zhu, G.**, & Iglesias, G. (2020). Hydrodynamic performance of a multi-Oscillating Water Column (OWC) platform. Applied Ocean Research, 99, 102168.

Zheng, S., Meylan, M. H., **Zhu, G.**, Greaves, D., & Iglesias, G. (2020). Hydroelastic interaction between water waves and an array of circular floating porous elastic plates. Journal of Fluid Mechanics, 900.

Zhu, G., Hughes, J., Zheng, S., & Greaves, D. Development of a coupled Smoothed Particle Hydrodynamics Model and Its Application to Nonlinear Wave Simulations. (Submitted)

0.2 Conference papers

Zhu, G., Hughes, J., Zheng, S., & Greaves, D. (2021, June). A SPH Model with Open Relaxation Boundary for Wave Generation and Absorption. In The 31st International Ocean and Polar Engineering Conference. OnePetro.

Zhu, G., Hughes, J., Zheng, S., & Greaves, D. (2021, September). Investigation of the hydrodynamic performance of an oscillating water column wave energy device using a smoothed particle hydrodynamics model. Proceedings of the European Wave and Tidal Energy Conference, 2394, 1-5.

Zheng, S., Meylan, M., **Zhu, G.**, Greaves, D., & Iglesiasc, G. (2020, April). Wave scattering from multiple circular floating porous elastic plates. In The 35th International Workshop on Water Waves and Floating Bodies, 26-29.

Table of contents

List of figures

List of tables

Nomenclature

Symbols

α Parameters in artificial viscosity model

α_r Relaxation function

C Concentration

D Diffusion coefficient

g Gravitational acceleration

J Diffusion flux

u Velocity vector

δr_s^i Particle displacement in particle shifting algorithm

Δx_s area of segment

Δ Time step

δ Parameters in density diffusion model

Δ_V Volumn change

δ_η Dirac delta function

η Surface elevation

γ Polytropic constant

λ Wave length

$\mathbf{C}$ Interactive meshes

$\mathbf{C}(\mathbf{k}, \mathbf{m})$ Neighbouring search grid index list

$\mathscr{A}$ Container A

$\mathscr{B}$ Container B

$\mathscr{F}\!\int$ Free surface particles

ν Kinematic viscosity

Ω Solution space/region

ω Wave frequency

Φ Velocity potential at σ coordinate

Φ_a Particle physical properties

Φ_B Bissell transfer function

Π Viscous term in SPH discrete form of Navier-Stokes momentum equation

Ψ Density diffusion in SPH discrete form of Navier-Stokes continuity equation

ρ Density

ρ_0 Initial density

ρ_{ip} Density of interpolation nodes

σ σ coordinate transformation

$\tilde{\Phi}$ Free surface velocity potential

$\tilde{w}$ Free surface vertical velocity

ξ Capture efficiency

A^l Cross-sectional area of the duct

A_i Wave amplitude

A_s Shifting coefficient

a_w Acceleration of wall boundary

B_* Dimensionless damping coefficient

c Numerical velocity

$C(k,m)$ Grid index list

d Still water depth

dim Dimension

e_d Defined error tolerance

$E_{i,max}$ Global imbalance monitoring tag

E_i Local imbalance monitoring tag

e_s Strong scaling efficiency

e_w Weak scaling efficiency

$f(x,\mathrm{d}t)$ Reduction function in sponge layer

F_{1i} Horizontal wave force from inside part of lip wall

F_{1o} Horizontal wave force from outside part of lip wall

F_1 Horizontal wave force of lip wall

F_1^{max} Maximum horizontal wave force of lip wall

$FP1$ Local wave force peak 1

$FP2$ Local wave force peak 2

$FP3$ Local wave force peak 3

h Smoothing length

H_w Wave height

k_w Wave number

K_{dm} Pneumatic damping coefficient

L Computational load

m Mass

M_{1i} Wave moment from inside part of lip wall

M_{1o} Wave moment from outside part of lip wall

M_1 Wave moment of lip wall

$m_{d/a}$ change of mass due to particle generation/deletion

MAE_a Mean average errors of amplitude

MAE_p Mean average errors of phase

$MP1$ Local wave moment peak 1

$MP2$ Local wave moment peak 2

N_c Total core numbers

O_r Open rate

p Pressure

p_a Air pressure

p_{go} Pressure of ghost particles

P_{inc} Incident wave power

p_{ip} Pressure of interpolation nodes

P_{owc} Power of OWC devices

Q Weighted Residual

$q(r)$ Basic function

q_d Air velocity within the duct

Q_t Airflow rate

S_0 piston Stroke number

S_s Speedup

t Time

T_w Wave period

$U(t)$ Piston velocity

u_c Corrected particle velocity

u_{sg} velocity at the centre of segment

u_s Particle displacement velocity in particle shifting algorithm

V Volumn

W Kernel Function

w^u Vertical velocity at the free surface

W_G Gaussian Kernel Function

$X(t)$ Piston position

Operators

$\cdot$ Vector dot product

$\forall$ For all

$\frac{\partial a}{\partial b}$ Partial derivative of a with respect to b

$\frac{\mathrm{d}a}{\mathrm{d}b}$ Total derivative of a with respect to b

$\in$ Belong to

max   Maximum value of

$\nabla\cdot$ Divergence

∇ Gradient

$\otimes$ Vector tensor product

Acronyms / Abbreviations

2D   Two Dimension

3D   Three Dimension

BEM   Boundary Element Method

CFD   Computational Fluid Dynamics

CFL   Courant–Friedrichs–Lew

CSPH Corrected Smoothed Particle Hydrodynamics

CVP   Centroidal Voronoi Particle

EOS   Equation of State

FEM   Finite Element Method

FPM   Finite Particle Method

FVM   Finite Volume Method

GPU   Graphics Processing Unit

HPC   High Performance Computer

ISPH Incompressible Smoothed Particle Hydrodynamics

MLS   Moving Least Square

MPI   Message Passing Interface

HOBEM High Order Boundary Element Method

NSE   Navier-Stokes Equations

NWT   Numerical Wave Tank

OBC   Open Boundary Condition

OWC Oscillating Water Column

OWSE Oscillating Wave Surge Converter

PDEs Partial Differential Equations

PSA   Particle Shifting Algorithm

PTO   Power Take-off

QALE-FEM Quasi Arbitrary Langangian-Eulerian Finite Element Metho

SPH   Smoothed Particle Hydrodynamics

SWASH Simulating WAve till SHore

SWE   Sallow Water Equation

U-OWC U-shaped Oscillating Water Column

WAMIT Wave Analysis at Massachusetts Institute of Technology

WCSPH Weakly Compressible Smoothed Particle Hydrodynamics

WEC Wave Energy Converter

Chapter 1

Introduction

1.1 Motivation and Problem Statement

The European Union has set high goals for energy efficiency and climate change for the next few decades. The 2030 Framework for Climate and Energy sets a 40% decrease in greenhouse gas emissions relative to 1990 levels and at least a 27% rise in the use of renewable energy as EU-wide goals for 2030 (METIS Studies: Study S8). In order to formalise the 2050 climate-neutrality aim (an economy with net-zero greenhouse gas emissions), the European Union presented the first European Climate Law on March 4, 2020. For the power grid, this entails generating abundant energy consumption from renewable sources. A considerable portion of this additional renewable energy will be generated by intermittent renewable sources such as wind and solar technology. Meanwhile, alternative kinds of sustainable renewable energy with a high potential for power production should also be developed to reach a broad energy mix. In research released by the International Energy Agency in 2017 (Agency, 2017), it was determined that wave power has a theoretical capacity of 29,500 TWh/year globally. Wave energy is a high potential renewable energy source. Devices that convert wave energy into electricity are known as wave energy converters (WECs). The wave power between 15 and 75 KW/m in Fig. 1.1 is the expected operating range of wave energy converters (Gunn and Stock-Williams, 2012). Over a thousand designs have been patented, and a wide range of WECs have been examined. Although the prospect of converting wave energy into useable electricity has inspired a huge number of WEC technologies, none have reached the level of widespread commercial application due to a lack of economically viable technical solutions. The major obstacles to commercialising WECs are their high cost of development, installation, and maintenance, low power extraction efficiency, and low dependability. As a result, in-depth study on the design of WECs and reduction of costs remain the primary emphasis at the moment.

Chapter1/Figs/fig_101.png

Fig. 1.1 World distribution map of wave power (Gunn and Stock-Williams, 2012).(Figure has been removed due to Copyright restrictions.)

Among the vast variety of WECs, the Oscillating Water Column (OWC) device is one of the most classical WECs and has been widely studied (Falcão and Henriques, 2016). As illustrated in Fig. 1.2, a classic OWC is composed of a water column and an above air chamber with thin walls, with the bottom and sidewalls partly submerged and exposed to the sea. The water column is able to rise and fall in response to the incident waves. The trapped air is forced through a turbine. Finally, a generator connected to the turbine produces electricity. OWC devices can be installed onshore, nearshore and offshore deployments. OWC devices on shore can be integrated into breakwaters. This combination reduces the construction and maintenance costs. At the same time, OWC devices can reduce wave reflection, enhancing the hydraulic performance of the breakwater.

Chapter1/Figs/fig_102.png
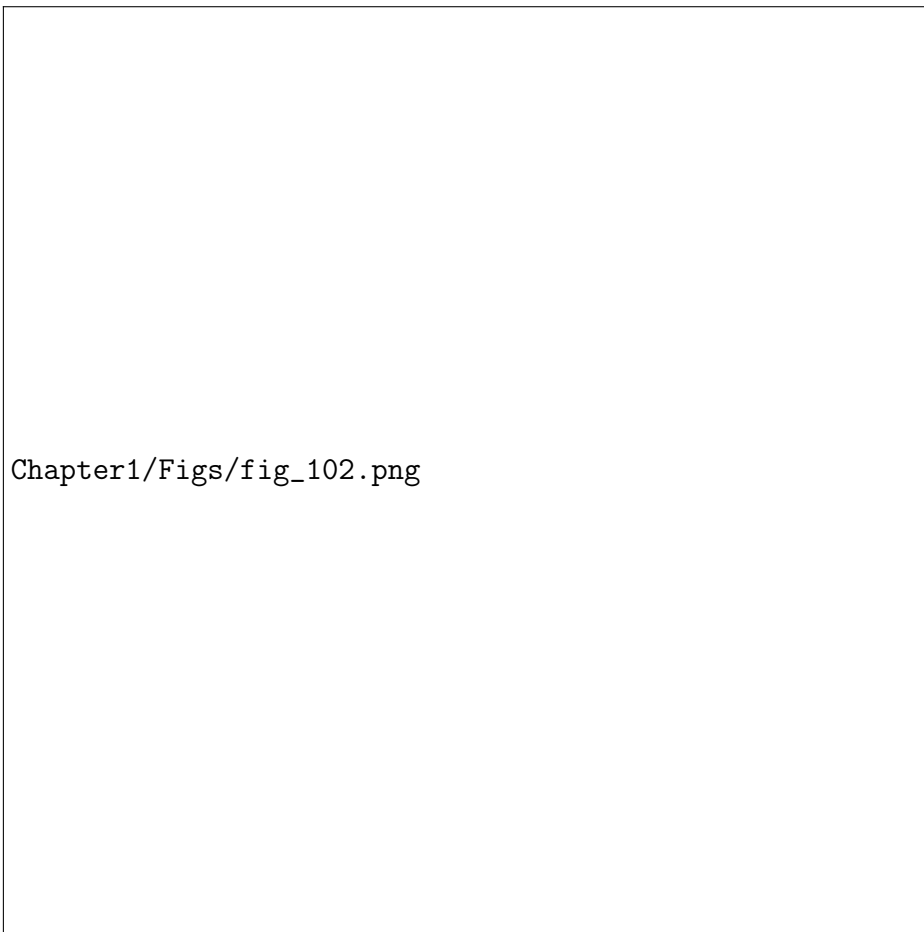
Fig. 1.2 Schematic layout of oscillating water column (OWC) (Muljadi and Yu, 2015).(Figure has been removed due to Copyright restrictions.)

Over the last several decades, there has been much research on OWC devices. Most of this has been focused on optimising geometrical characteristics and power take-off (PTO) systems to improve hydrodynamic performance. Improvements in optimising wave extraction

are one of the key milestones in consolidating the technology's progress towards the commercial stage. Investigations of hydrodynamic forces on OWC devices has been given more attention recently. In order to prevent the structure from slipping or overturning, an OWC caisson designer should anticipate excessive loads. Load evaluation is essential for design of operability and reliability. In 1985, a 500 kW demonstration plant based on a multi-resonant OWC system was built at Toftestallen, Norway (Fig. 1.3). A severe winter storm partially destroyed the plant after four years of operation. Bolts connecting the steel structure to the concrete structure were vulnerable to fatigue fracture (Bhattacharyya and McCormick, 2003). A 16-chamber OWC breakwater at Mutriku is another example, as seen in Fig. 1.4. Storms in 2007 and 2008, as well as 2009, caused significant damage. These incidents highlight the need for more investigation into overall structure loads (Vicinanza et al., 2019). The design of the OWC should thus improve not just its hydrodynamic efficiency but also take into account the hydrodynamic loads. The interaction between rough waves and the OWC structure can lead to nonlinear free-surface conditions. As demonstrated in Fig.1.5, incident waves hitting the front wall can cause wave breaking and large slam loads. In the event of extreme sea conditions, the chamber may experience free surface sloshing. These nonlinearities show that it is not easy to study OWC installations under rough sea conditions.

Investigations of OWC devices can be evaluated by laboratory tests. However, laboratory testing is time-consuming, expensive, and often only applies to a small selection of straightforward OWC geometries. Furthermore, the scale effect reduces the accuracy of physical models. Mechanical similarity should include geometry, time, velocity, gravity, viscosity, tension, pressure and many other aspects. When considering the ratio of all forces to inertial forces, this leads to some differences of the coefficients, the Froude number [1], the Reynolds number [2] and so on. A perfect similarity principle requires that these coefficients are the same between the model and the prototype. However, it is not possible to achieve. Moreover, there are just a few OWC factors that may be researched in laboratory experiments due to the expensive experimental models. The more effective studies greatly benefit from the use of numerical modelling tools. Numerical investigations are substantially less costly than physical model experiments. Additionally, scale effects and data extraction are two of the main limitions in physical modelling that may be mitigated by numerical models. Numerical simulations can provide an exhaustive flow field, an exhaustive description of the OWC hydrodynamics, and the capability to test a sizable number of various configurations without the need for extra resources.

---

[1]The Froude number is a dimensionless number defined as the ratio of the flow inertia to the external field.
[2]The Reynolds number is the ratio of inertial forces to viscous forces.

Chapter1/Figs/fig_103.png
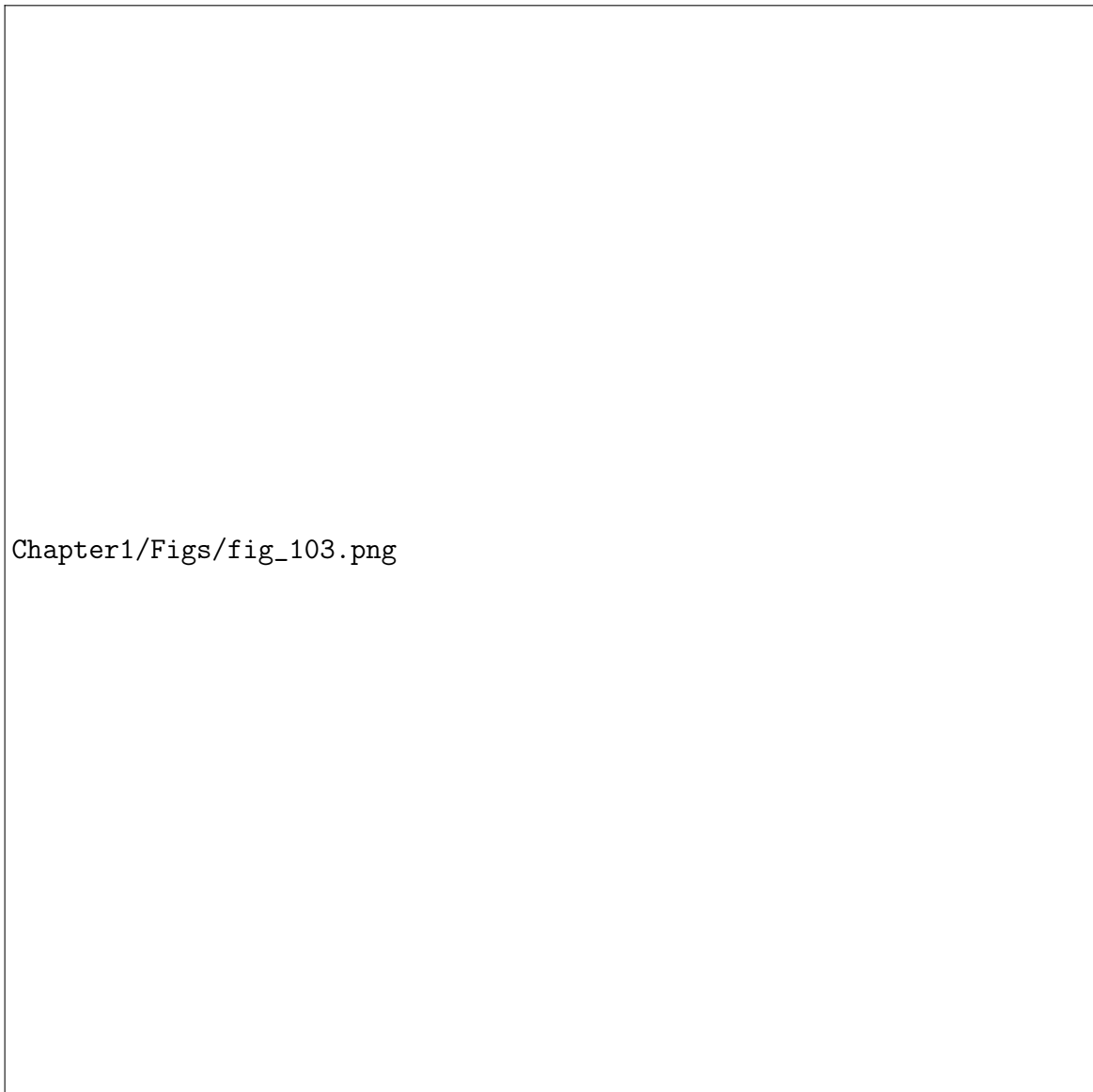
Fig. 1.3 Sectional drawing (left) and view (right) of the Kvaerner multi-resonant OWC (Bhattacharyya and McCormick, 2003).(Figure has been removed due to Copyright restrictions.)
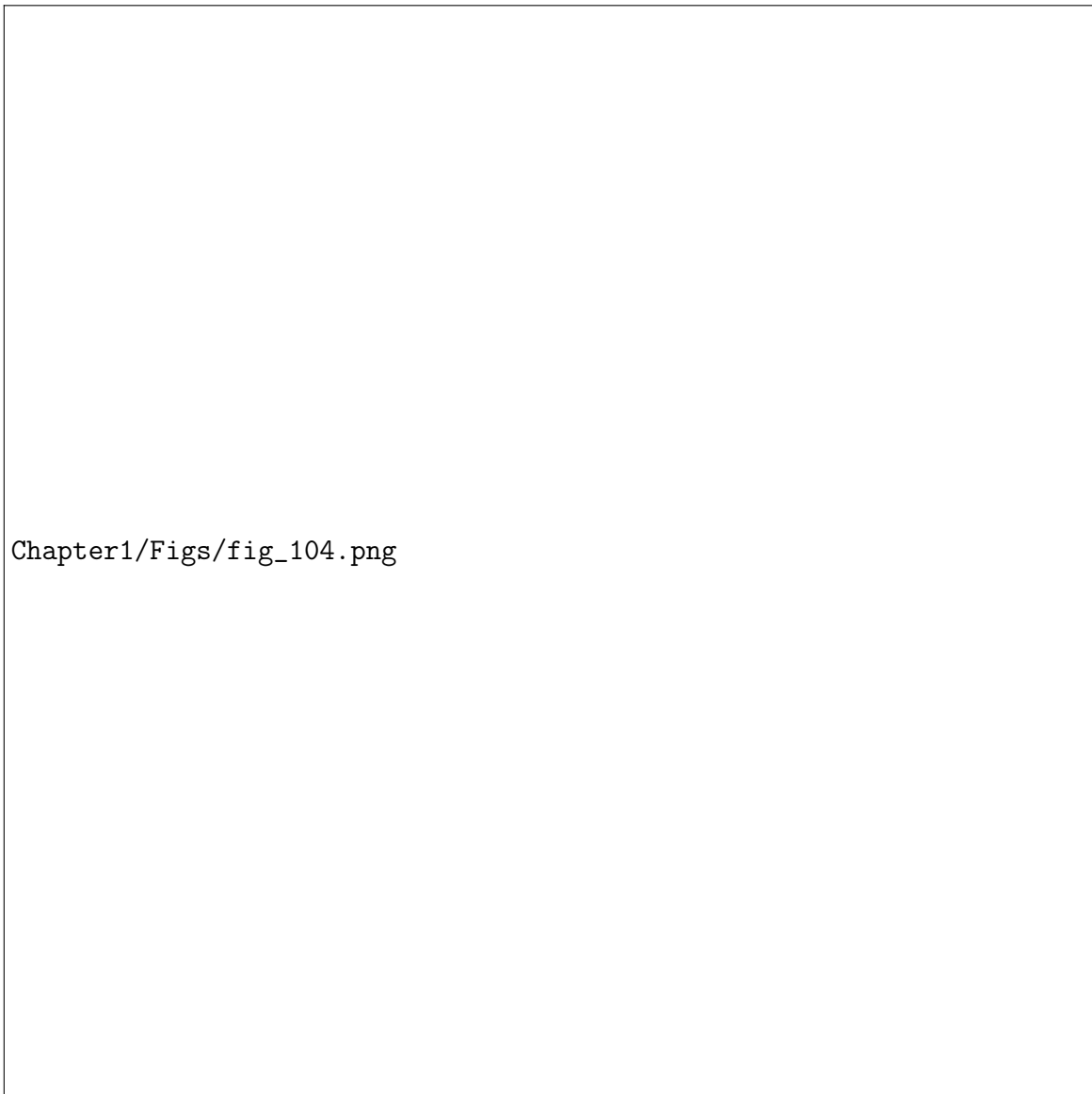
Fig. 1.4 The damage of OWC installed breakwater in Mutriku (Baez Rivero, 2018).(Figure has been removed due to Copyright restrictions.)

Chapter1/Figs/fig_105.png

Fig. 1.5 Wave slamming on the OWC installed breakwater in Mutriku (Torre-Enciso et al., 2009).(Figure has been removed due to Copyright restrictions.)

Numerous theoretical and numerical models based on potential flow theory have been proposed to study the hydrodynamic performance of OWC devices, with the fluid assumed to be inviscid, irrotational, and incompressible. Potential flow approaches have the drawback of only being applicable to waves with minor amplitude motion and being restricted to linear or weakly nonlinear systems. Another approach is Computational Fluid Dynamics (CFD), which has a high computing cost but achieves good accuracy when investigating completely nonlinear issues with severe nonlinear, viscous fluids, wave impact, and wave breaking. To solve the Navier-Stokes equations, these numerical CFD models discretize the flow fields in space and time. These numerical approaches may be classified into two major groups based on the partitioning approach: grid-based and mesh-free methods. Classical grid-based methods include, finite difference method (FDM), finite volume method (FVM), and finite element method (FEM). The FDM are numerical approaches for solving differential equations utilising difference equations (Smith et al., 1985). The derivatives in differential equations can be estimated using Taylor series expansion or polynomial fitting. The FDM is theoretically basic, easy to program. However, the FDM works well for simple regular grids. However, the FDM cannot guarantee variable conservation and is often limited to basic geometries. The FVM is a method for solving partial differential equations using the form of algebraic equations (LeVeque et al., 2002). Volume integrals in a partial differential equation can be transformed to surface integrals using divergence theory. According to the conservation theorem, the flux at each finite volume should be such that the flux entering a given volume is the same as the flux leaving the neighbouring volume. It is simple to formulate in order to support unstructured meshes. Therefore, the FVM is appropriate for complicated geometry issues and allows for local grid modification without disrupting the overall mesh. Indeed, many commercial CFD softwares such as FLUENT and STAR-CCM+, or some open souce code (OpenFOAM), make extensive use of this formulation. The FEM splits a computing field into finite element meshes. The simple equations that represent these finite elements are utilised to estimate the partial differential equations (PDEs) (Hughes, 2012). The procedure consists of creating an integral from the inner product of the weight function and residual function, then setting the integral to zero. It is a process that reduces approximation errors by fitting trial functions into the PDEs. Despite the fact that this approach can handle various geometries and grid refinement, it needs to determine the appropriate shape function to duplicate the data structure.

The preceding discussion demonstrates that all these grid-based approaches show a similar aspect of the requirements of high-quality grids. Under harsh wave conditions, the simulation of an OWC with a complex free surface necessitates the use of a high resolution grid, an unstructured grid, an adaptive grid, or other advanced grid generation approaches.

As shown in Fig. 1.5, wave slamming in an OWC unit tends to result in splashing and a nonlinear free surface conditions. Mesh-free approaches, as opposed to mesh-based methods, can simulate complicated free surfaces without the necessity for high-quality meshes. The primary principle behind the meshless approach is that by solving PDEs with arbitrarily dispersed particles, stable and accurate numerical solutions may be achieved. Smoothed Particle Hydrodynamics (SPH) is one of the most known mesh-free techniques and is often used in the research of complicated free-surface flows. The fluid domain is discretized into a set of particles based on kernel interpolation in the SPH framework. As a Lagrangian method, SPH works with discrete particles and determines each particle's motion independently. The SPH approach captures the free surfaces without the need of an algorithm to identify and follow the free-surface. SPH is regarded as a flexible approach that can easily handle severe deformations, unstable and nonlinear flows, and complicated topological evolution. However, the SPH model is known to be an expensive model with high computational costs. Each particle should be interpolated with tens or even hundreds of neighboring particles. The number of neighbouring particles in SPH is far greater than the number of neighbouring cells for mesh methods. Secondly, modelling incompressible fluids requires a small time step (weakly compressible SPH model) or solving the pressure Poisson equation (Incompressible SPH model). For the scale of engineering problems, SPH models often require the simulation of millions or even tens of millions of particles, which leads to significant time consumption. Therefore, the computational efficiency of the SPH model needs to be improved when using the SPH model to study OWC devices.

1.2   Description of the Project

The overall aim of the present study is to predict the survivability of OWCs. The project focuses on the hydrodynamic loads and efficiency response of OWC devices in rough wave conditions. In order to assess the performance of OWCs survivability, responses (i.e., hydrodynamic loading) and strongly nonlinear phenomena (i.e., wave slamming, splash, sloshing) need to be modelled accurately. SPH has shown its capability in the simulation of full strongly nonlinear free-surface flows. However, the high computational cost has limited the investigation of the SPH model on a large-scale for OWC installations. Thus, the aims of this thesis are:

  1. Development of an efficient SPH model for large-scale simulation of OWC installations

  2. Application of the SPH model to simulate OWC devices to investigate the structural reliability.

1.3   Outline

The flowchart of this thesis is schematically shown in Fig. 1.6 and is described as follows.
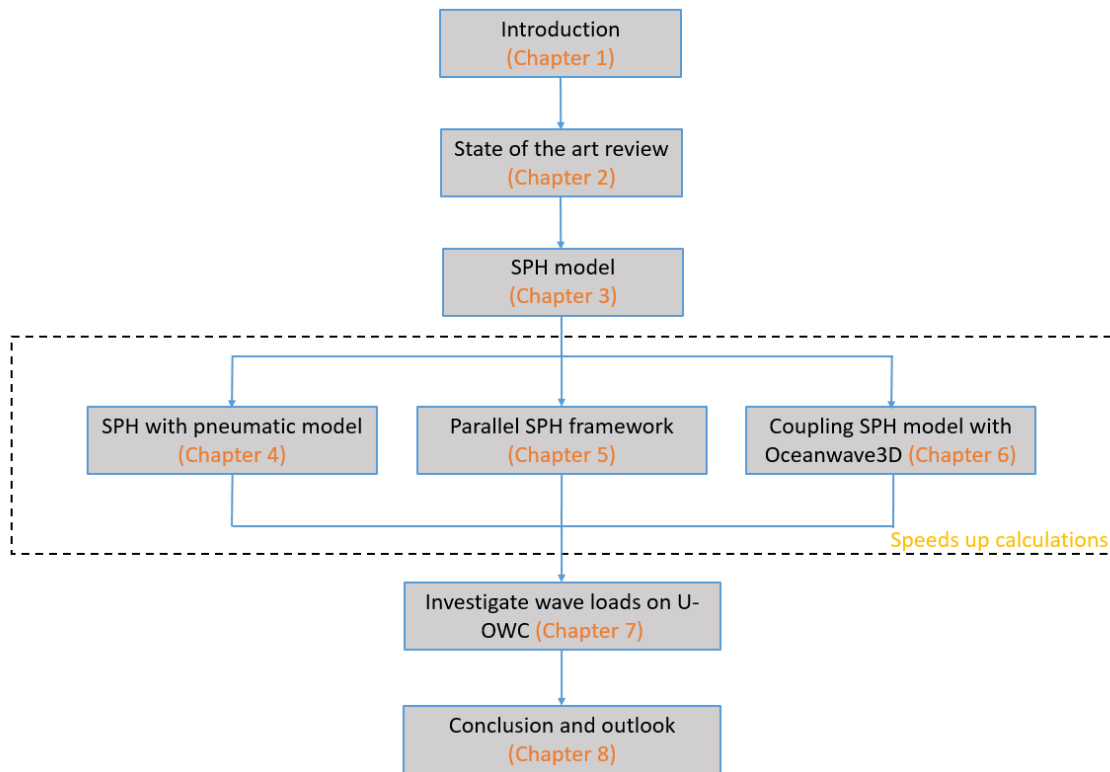
Fig. 1.6 Structural framework of the PhD thesis.

Chapter 1 provides an overview of the research work. The objectives are defined and the methodology followed to complete this research is enunciated. Chapter 2 presents a state-of-the-art review of the topics relevant to the study of SPH methods and OWC devices. Chapter 3 describes the detailed theory and numerical methods of the SPH model. Chapter 4 develops a single-phase SPH model with a pneumatic model for OWC devices and regional ghost particle approach for the front thin wall. Chapter 5 implements a parallel SPH framework using the message passing interface (MPI) for large-scale free-surface flows. Chapter 6 proposes the two-way coupled model between SPH and OceanWave 3D, which is an efficient solver based on fully nonlinear potential flow theory. Chapter 7 describes the coupled parallel SPH model proposed in this thesis to simulate a U-shaped OWC device. The OWC wave loads for different wave conditions and different OWC geometries are investigated. Chapter 8 presents the primary outcomes of this research project. The major finding of this study and a synopsis of the produced work are emphasised first. Finally, suggestions and points of view are offered for future work.

The code of this thesis is based on the author's previous MSc work. Chapters 4, 5, 6, and 7 describe the doctoral work, including code development, and numerical simulation.

Chapter 2

Review of Literature

2.1 Introduction

This chapter provides a review and analysis of the current research on Oscillating Water Column (OWC) devices and Smoothed Particle Hydrodynamics (SPH). The use of the SPH model for OWC devices are described. Numerical methods for improving the computational efficiency of the SPH model are also presented, including related work on parallel models and SPH coupling.

2.2 Oscillating Water Column

The working principle of OWC devices is based on the movement of the water column caused by the incident wave, resulting in the change of the air volume. The air pressure difference caused by the change in air volume causes the air to flow through the turbine and generate electricity. In 1910, Bochaux-Praceique, a Frenchman, created a 1 kW wave energy generator at his house, employing the theory of wave undulation to drive an air turbine, the sketch of which is shown in Fig. 2.1. This looks to be Europe's first device based on the OWC theory (Ricci, 2012). However, OWC seems to have appeared in print for the first time in 1978 (Evans, 1978). The simplicity of the OWC gives them a basic advantage over the majority of other wave energy converters (WECs) (Falcão and Henriques, 2016). Nevertheless, the commercial viability of OWC devices is still constrained by poor conversion efficiency and high installation costs. OWC devices have been the subject of several research projects, and many prototypes have already been built.

The OWC devices can also be divided into fixed OWC devices (Falcão, 2000) and floating OWC units (Rea et al., 2011; Washio et al., 2000; Falcão et al., 2012), depending on their

Chapter2/Figs/fig_201.png
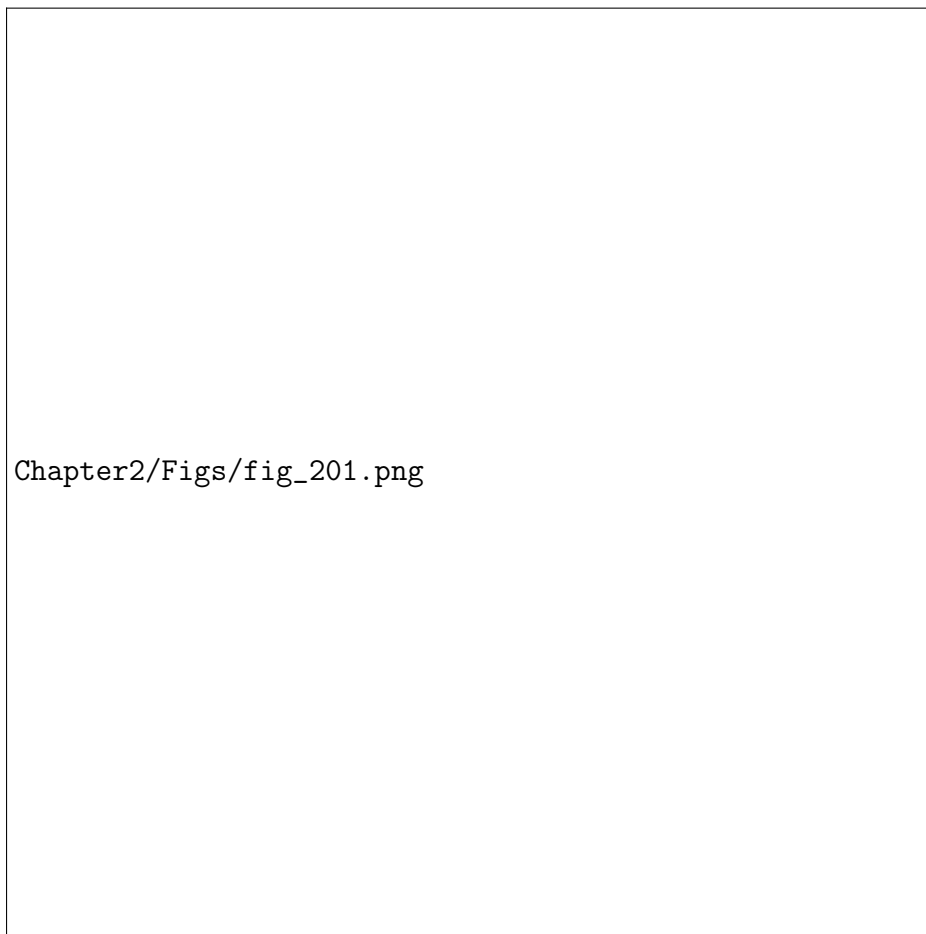
Fig. 2.1 Illustration of Praceique-Bochaux OWC device, 1920 (Ricci, 2012).(Figure has been removed due to Copyright restrictions.)

construction. The Kaimei (Fig. 2.2) was the first large-scale OWC device (Hotta et al., 1988; Masuda and McCormick, 1986). The hull of the huge barge Kaimei (80 m × 12 m) contained 13 OWC open-bottom chambers. In the following years, until the early 1990s, the activity in Europe remained mainly at the academic level, the most visible achievement being a small (75 kW) OWC shoreline prototype, equipped with a Wells turbine, deployed at the island of Islay, Scotland (Fig. 2.3) (Whittaker et al., 1993). Mighty Whale (Ogata et al., 2002; Washio et al., 2000) was an offshore floating OWC device consisting of a floating structure (50 m long, 30 m wide, 12 m draft, displacement 4400 t). Three side by side air chambers were used by Mighty Whale to capture wave energy. A shoreline OWC plant was built in Guangdong Province, China (Zhang et al., 2009). A floating OWC device with several separate chambers was deployed in Port Kembla, Australia (Falcão and Henriques, 2016).

The simplicity of the OWC principle makes it easy to be integrated/combined with marine structures, e.g., breakwater and other types of WECs. There are several benefits to integrating an OWC device into a breakwater, including shared construction costs and enhanced access to the wave energy plant. This was first done successfully at Sakata (Fig. 2.4), Japan, in 1990 (Ohneda et al., 1991), where one of the breakwater caissons was equipped with an OWC device. Later, a multi-chamber OWC device, which is composed of 16 air chambers, was integrated along a breakwater at the port of Mutriku in northern Spain. Additionally, OWC devices can be combined with other WECs as a small part of a whole system of WECs (Kim et al., 2015; Kurniawan et al., 2014).

Not only that, but improvements to the geometric design of the OWC device also result in new OWC models. Boccotti (2007) proposed a novel OWC breakwater device, which has a U-shaped cross-section, with the outer aperture facing up (Fig. 2.6). This strategy has the advantage of lengthening the water column as a whole without lowering the aperture below the free surface. This kind of breakwater-OWC devices (Fig. 2.6), known as U-OWC, is being constructed at Civitavecchia with 17 caissons, and it is utilised for breakwaters in Italy (Arena et al., 2013a).

Some of the OWC devices that have been deployed so far are listed in Table 2.1. These OWC devices may be considered to be demonstration prototypes. Despite the fact that it has been more than 40 years since the original large-scale OWC units were built, they have not been commercialised on a large scale. To improve the competitiveness of wave energy, it is hoped to reduce costs and improve capture efficiencies. This will therefore require a great deal of research into different aspects of OWC devices, e.g., hydrodynamic performance, control strategy, and survivability, to drive the industry towards true commercialisation.

Fig. 2.2 The Kaimei (Masuda and McCormick, 1986).(Figure has been removed due to Copyright restrictions.)

Table 2.1 Summary of the main OWC devices.

Name	Year	Device	Power	Country	Status	Ref.
KAIMEI	1978	Floating	-	Japan	Decommissioned	(Masuda and McCormick, 1986)
Kværner Brug	1985	Fixed	500 KW	Norway	Decommissioned	(Antonio, 2010; Bhattacharyya and McCormick, 2003)
Limpet	1985	Fixed	500 KW	Norway	Decommissioned	(Whittaker et al., 2004)
Vizhinjam	1990	Fixed	500 KW	India	Decommissioned	(Ravindran and Koola, 1991)
OWC ON THE ISLAND OF ISLAY	1991	Fixed	75 KW	Scotland	Decommissioned	(Whittaker et al., 1993)
OSPREY	1995	Fixed	100 KW	Scotland	Decommissioned	(Falcão and Henriques, 2016)
Mighty Whale	1998	Floating	120 KW	Japan	Decommissioned	(Ogata et al., 2002; Washio et al., 2000)
Pico OWC	1999	Fixed	400 KW	Portugal	Decommissioned	(Monk et al., 2018)
SHORELINE OWC PLANT	2001	Fixed	100 KW	China	Decommissioned	(Zhang et al., 2009)
OCEANLINX OWC	2005	Fixed	20 KW	Australia	Decommissioned	(Falcão and Henriques, 2016)
MUTRIKU	2008	Fixed	296 KW	Spain	Operating	(Torre-Enciso et al., 2009)
Oceanlinx Mk3	2010	Floating	2.5 MW	Australia	Decommissioned	(Falcão and Henriques, 2016)
OCEANLINX GREENWAVE	2014	Fixed	1 MW	Australia	Operating	(Falcão and Henriques, 2016)
YONGSOO PLANT	2016	Fixed	500 KW	South Korea	Operating	(Cascajo et al., 2019)
REWEC3	2016	Fixed	2.5 MW	Italy	Operating	(Arena et al., 2013b)
Wave Swell	2019	Fixed	200 KW	Australia	Operating	(Cossu et al., 2020)

```
Chapter2/Figs/fig_203.png
```

Fig. 2.3 Scottish island of Islay's shoreline OWC (Whittaker et al., 1993).(Figure has been removed due to Copyright restrictions.)

Chapter2/Figs/fig_204.png

Fig. 2.4 OWC plant built within a breakwater at Japan's Sakata harbour (Ohneda et al., 1991).(Figure has been removed due to Copyright restrictions.)

Chapter2/Figs/fig_206.png

Fig. 2.5 Multi-chamber OWC plant at Mutriku harbour (Torre-Enciso et al., 2009).(Figure has been removed due to Copyright restrictions.)

Chapter2/Figs/fig_207.png

Fig. 2.6 Partly constructed breakwater at Civitavecchia harbour, 2014 (left); Cross section of U-OWC (right) (Arena et al., 2013b). (Figure has been removed due to Copyright restrictions.)

Potential Flow Models

It should be emphasised that most of the early simulations rely on potential theory, with the assumption of inviscid, irrotational, and linear flows. Evans (1978) developed a theoretical model for OWC devices, in which the internal water surface was modeled as an imaginary stiff weightless rigid piston. The stiff piston model, as illustrated in Fig. 2.7 (a), imposed force on the piston due to the pressure drop resulting from the power take-off (PTO) system. The stiff piston model may give good approximate results when the wavelength of incident waves is very long compared with the horizontal length of the air chamber. Sarmento and Falcão (1985) found that the maximum efficiency of the OWC under the nonlinear PTO system was slightly lower than the maximum efficiency under linear systems. By assuming incompressible air, Evans (1982) created a relationship between the diffraction characteristics and air pressure, and provided formulae for power measurement. To address air pressure, the uniform pressure distribution model, initially developed by Falcão et al. (1980), was employed on the free surface. The pressure distribution model applies air pressure uniformly to the uneven free surface as shown in Fig. 2.7 (b). The compressibility of the air phase inside the chamber is not considered in any of the above potential flow models. Sarmento and Falcão (1985) first considered the compressibility of air in their model. The results show that air compressibility can be important in practice, and OWC devices can still have high power for smaller chamber lengths and turbine sizes. The Piston type and distributed pressure methods are two methods for exerting the influence of air pressure in potential flow theory, where the air phase is not simulated.

Later, the potential flow theory was widely used to simulate OWC devices and improve their efficiency. Evans and Porter (1995) developed a potential flow theory model of an OWC, which is composed of a thin vertical surface-piercing barrier next to a vertical wall. They found that the changes in the draught of the vertical barrier led to changes in the frequencies where the maximum capture efficiency occurs. Ning et al. (2015) developed a two-dimensional (2D) completely nonlinear wave tank using the higher-order boundary element method (HOBEM) to study on-shore OWC devices. The hydrodynamic efficiency of the device was found to be highly influenced by the incident wave amplitude for the given OWC geometrical parameters. Their model was later extended by Wang et al. (2018) to explore the nonlinear impacts and the viscosity influence on capture efficiency of a fixed OWC device. Three-dimensional (3D) models for OWC devices have been developed. Wang et al. (2002) used a boundary element method (BEM) model to evaluate the performance of a shoreline-mounted OWC device. The topographical influences such as bottom slope and water depth on the hydrodynamic performance of the device were incorporated in their studies. Delauré and Lewis (2003) used WAMIT (wave analysis at Massachusetts Institute of
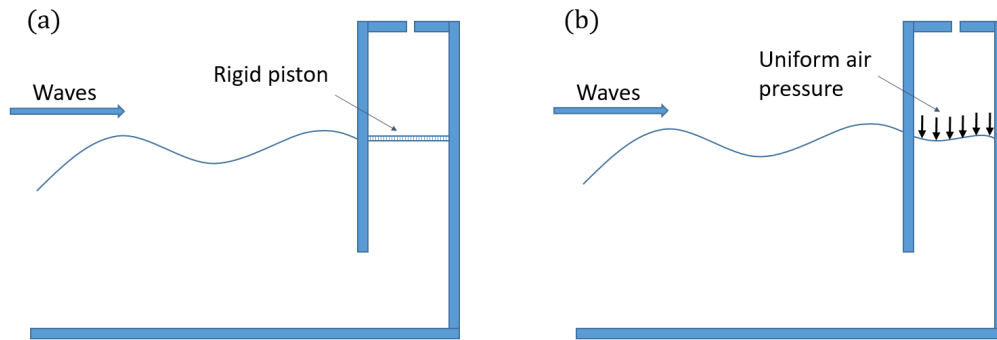
Fig. 2.7 The OWC models with stiff piston model (left) and uniform pressure distribution model (right).

Technology) to simulate a stationary OWC device. Martins-rivas and Mei (2009a,b) proposed a couple of linear potential flow theory-based to 3D theoretical models to study a thin-walled OWC installed along a straight coast and at the tip of a breakwater, respectively.

Potential flow theory has also been used to investigate several non-conventional OWC devices. Deng et al. (2013) developed an analytical model to study the hydrodynamic performance of an OWC device with a coaxial tube-sector-shaped supporting structure. Optimization of the PTO and the effects of the structural geometry and incident wave direction on energy conversion efficiency of the device were discussed. Rezanejad et al. (2015) assessed a dual chamber OWC device with a bottom step and found the efficiency to be significantly improved compared to that of the OWC devices with only one chamber. He et al. (2019a) studied the hydrodynamics of a pile-supported OWC breakwater based on linear wave theory. Zheng et al. (2019b) studied an OWC breakwater without being constrained by the thin-wall assumption. It was reported that the thinner the chamber wall, the greater the wave power capture efficiency. The model was further extended to study the performance of an array of multiple OWC devices deployed along a straight coast/breakwater (Zheng et al., 2019a). Deng et al. (2020) developed a new OWC device with a freely surging front wall. It was found that the power absorption throughout a wide frequency band might be improved thanks to the existence of the freely surging front walls. Wang et al. (2021) raised a concept of a dual-chamber OWC device consisting of a pitching mid-wall, and developed a theoretical model to examine the effect of the pitching mid-wall on wave power absorption of the device. Khan and Behera (2021) evaluated and discussed the effect of a sloping porous bottom on the efficiency of an OWC device against oblique waves. Their study was carried out by using a multi-domain BEM assuming the linear potential flow theory. It was revealed

that the efficiency of the device was sensitive to the slope of the porous seabed, and the seabed porosity could stabilize the resonant frequency against changes in water levels.

As indicated above, the study of OWC devices has been widey carried out with the employment of the potential flow techniques that have a high computing efficiency. It should be noted that the studies based on potential flow theory are generally restricted to small amplitude oscillations, hence they are most suited for evaluating the performance and optimising the OWC devices under operation conditions. Extreme/rough wave conditions will lead to violent slamming, vortex shedding, and other nonlinear hydrodynamic effects. Due to these problems, using potential flow theory to investigate OWC devices under rough sea conditions is inappropriate.

Computational Fluid Dynamics

Computational fluid dynamics (CFD) models are developed to solve the Navier-Stokes equations (NSE). Meshes or particles are used to accomplish spatial discretization of computation domains. CFD approaches offer the benefit of capturing all relevant hydrodynamic nonlinearities, in comparison to potential flow theory with lesser fidelity. The analysis of OWC devices under rough sea conditions is made possible by the high-resolution data that more computationally expensive CFD simulations provide.

CFD models have been widely used to study OWC devices. El Marjani et al. (2008) developed a numerical model for OWC devices using the commercial Fluent software. Energy losses encountered in the chamber are well predicted, and it was shown that their evolution follows a parabolic law with the frequency variation. Zhang et al. (2012) used a two-phase level-set immersed boundary approach to investigate the effect of incident wave conditions and geometry of a fixed OWC device. It was found that increasing the dimension of the orifice at the bottom of the chamber leads to lower hydrodynamic efficiency of the OWC due to reduced pressure in the chamber. López et al. (2014) investigated the effect of the damping factor on a fixed OWC under regular and irregular waves using a 2D RANS-VOF model. The results show that the maximum capture efficiency is achieved by the presence of damping values for different incident wave frequencies. Therefore, the choice of the turbine may need to meet the requirements of the sea state. Luo et al. (2014) studied a heave-only floating OWC device using the Fluent commercial software. Various wave conditions, damping factors and spring systems were simulated to optimize efficiency. The frequency bandwidth of high efficiency can be adjusted by the turbine damping coefficient and elasticity coefficient of the mooring spring, to harness more energy from the marine environment with varied wave frequencies. Kamath et al. (2015) investigated a 2D OWC under operational wave conditions using REEF3D, an open-source CFD package. In addition to the wavelength of

the incident waves, the wave steepness also has a significant impact on the hydrodynamic efficiency of an OWC device. Iturrioz et al. (2015) used an OpenFOAM solver for wave and structural interaction to simulate an OWC in three dimensions. Small-scale laboratory tests are carried out to verify the numerical findings. It was found that air compressibility is not relevant at the laboratory scale and was not taken into account in the numerical model validation process. However, air compressibility must be considered for realistic power production at the prototype scale. Vyzikas et al. (2017) used an air-water two-phase solver to explore the behaviour of a fixed OWC, and the numerical results were found to have an error of less than seven percent from the experiment. Furthermore, a decay analysis based on mechanical vibrations was presented to estimate the OWC resonance frequency. Wang and Zhang (2021b) investigated an offshore dual-chamber OWC system, which is made up of two closely linked 3D circular sub-units that are aligned in the wave propagation direction, under the framework of CFD toolbox OpenFOAM. When resonant motion occurs in one chamber, in addition to the positive influences on itself, a contribution to the improvement of the capture width ratio in another chamber can also be identified.

Notice that the air phase is considered to be incompressible in the above CFD models. With the use of the OpenFOAM, Simonetti et al. (2017, 2018) studied the effect of damping factor with the consideration of air compressibility, wall draught, and chamber length on power efficiency of an offshore stationary asymmetric OWC device within compressible/incompressible air phase. Elhanafi et al. (2017b) and Elhanafi and Kim (2018) used StarCCM+ to simulate a 3D OWC device. It was found that the optimal damping during the resonant period could be reduced due to air compressibility. Deng et al. (2019) used OpenFOAM to study the hydrodynamic performance of an offshore-stationary OWC device with a horizontal bottom plate. The results indicated that, particularly for long waves, a bottom plate with a small opening ratio and a moderately long bottom plate is beneficial for wave power extraction. López et al. (2020) evaluated the influence of air compressibility on the performance of an OWC device through physical modelling. The open-source CFD code OpenFOAM was used as a complementary tool to calibrate the pressure-vs-flowrate curves, enabling the flow rate to be determined based on the pressure drop measurements from the physical model. It was found that significant errors would be introduced in the assessment of wave power absorption should the air compressibility in the chamber be disregarded, and the errors were strongly influenced by the wave conditions and turbine-induced damping. Numerous research on OWC devices has also been conducted using industry-standard CFD software and other numerical techniques (Mahnamfar and Altunkaynak, 2017; Liu et al., 2019; Wang and Zhang, 2021a; Chen et al., 2021; Abbasi and Ketabdari, 2022; Gubesch et al., 2022). The above study demonstrates that CFD models have been used extensively

in the study of OWC installations. CFD models have more fidelity than the potential flow theory in simulating air compressibility, capturing vortex shedding near walls and so on. However, the above studies on OWC installations are still at operation conditions. It is still a big challenge for most of the CFD models to simulate the strong nonlinear splash generated by the strong wave-structure interaction in rough sea conditions.

Wave Loads on OWC

As shown above, there has been a lot of research based on potential flow theory or CFD models, with the majority of the focus on optimising the hydrodynamic performance of OWC devices. In reality, many offshore and coastal devices, including OWC devices, have to face harsh sea conditions. For onshore OWC breakwater devices, in addition to their function as wave energy devices to generate electricity, another major function is coastal protection. The design and construction of these devices take into account wave loads in both operating and survival sea conditions. The cumulative fatigue degradation may reduce their structural lifetime. Therefore, a precise estimation of wave loads on OWC devices is crucial.

Patterson et al. (2010) proposed an early effort at the estimation of the force acting on an in-chamber back wall, but no supporting experiment was conducted. Boccotti (2012) evaluated the wave forces on U-shaped OWC devices installed on caisson breakwaters. It was discovered that when the greatest force acted on the breakwater for a wave group, the air pressure inside the chamber was practically at its maximum. Small-scale experiments of 1:40 and 1:60 scales were used to assess the pressure on the OWC caisson (Kuo et al., 2015). The results show that the wave pressure at OWC caisson breakwaters is smaller than that at a vertical wall. Thus, OWC breakwaters can reduce the wave load on the front wall. Ashlin et al. (2015) performed experiments to study the overall wave force on a OWC device. It was found that the total horizontal wave forces on the OWC device are greater than the vertical forces. Therefore, it may be more important to consider the effect of horizontal wave force on OWC devices. The effects of the geometry on wave force of fixed OWC devices were studied experimentally and numerically by Ning et al. (2016). They found that the horizontal wave force became larger when the length of the wave decreased. On an offshore OWC device, Elhanafi (2016) used Star-CCM+ to forecast the wave loads acting on an offshore OWC device. It was found that the hydrodynamic horizontal wave load is independent of the applied PTO damping even with increasing the incoming wave height. Elhanafi et al. (2017a) also used experiments and a numerical model to study the impact of sidewalls on the OWC device's wave loads. It was found that the horizontal and vertical wave forces have almost an opposite trend throughout the entire frequency range. Viviano et al. (2018) further investigated the wave force with different scales. The comparison of

dimensionless maximum forces at the outer front wall between large and small scale models is quite different, due to the presence of viscous stresses in the small scale models. Under regular waves, Viviano et al. (2019) studied the wave forces on both sides of the front wall. The air and water pressures at the OWC are related to the response of the device, which is shown to be strongly affected by the air compressibility. Pawitan et al. (2019) developed a model based on large-scale experiments to predict the wave forces. The vertical force was discovered to have a considerable impact on the overturning and sliding of OWC devices. Huang et al. (2019) ran a 3D numerical simulation and found that the wave forces and bending moment rose with wave height. Under regular waves, Wang and Ning (2020) then conducted a comprehensive analysis of the viscosity effects on the wave force. The results show that the viscosity effect on the total horizontal wave force increases with the increase of front wall draft due to the increasing flow separation and vortex shedding. Moreover, Viviano et al. (2016) studied the wave forces of OWC devices under random waves. The OWC turbine was suggested to be closed when near breaking wave conditions appear, both for the safety of the chamber structure and of the turbine. In addition, the wave loads of some new OWC devices are also investigated. Konispoliatis et al. (2016) studied wave forces on a three OWC array. Under regular waves, Wang et al. (2020) examined wave forces on a dual-chamber OWC apparatus that was attached to the ground. Zhou et al. (2021) developed a second-order HOBEM approach to predict wave forces on a stationary cylindrical-type OWC device. As shown above, there has been an increasing amount of research into wave forces on various OWC devices in recent years.

The geometric optimization of the OWC unit would also affect the hydrodynamic condition of the OWC unit. Most of the previous studies (López et al., 2014; Elhanafi and Kim, 2018; Zhu et al., 2020; Wang and Zhang, 2021a) have focused on improving the conversion efficiency of OWC devices through geometrical optimisation. However, the geometrical design for optimum efficiency also affects the wave loading of the OWC, and the reliability requirements of the OWC device, especially when integrated with a breakwater, are also very important. Although many studies on wave loads have been presented above, not many have been carried out on the effect of geometrical optimisation on the wave loads of OWCs. Therefore, the effect of geometry on OWC breakwater will be investigated in this thesis.

U-shaped OWC

Boccotti (2003) proposed a U-shaped OWC device, which adds a bottom-mounted vertical barrier in front of a conventional OWC device (see Fig. 2.6). In comparison with a typical OWC device, the vertical duct dramatically alters the excitation shape of the U-OWC device. The incident wave beam does not come into direct contact with the fluid in the chamber.

While, as the incident wave affects the fluid motion within the U-pipe, the incident wave ultimately affects the motion of the air inside the cavity. Adjusting the geometry of the U-pipe allows the natural frequency of the U-OWC to be adjusted (Boccotti, 2007). U-OWC devices can achieve high capture efficiency over a wide range of periods. In addition, it is possible to prevent sand and stones from entering the interior of the chamber due to the external submerged wall (Ning et al., 2020).

Boccotti (2007) proposed a theoretical framework for U-OWC devices based on the unstable Bernoulli theorem and conducted experiments to verify the theoretical model (Boccotti et al., 2007). Boccotti (2012) tested various engineering requirements for a full-size U-OWC devices. Arena et al. (2013b) outlines the key difficulties surrounding the design and fabrication of the U-OWC devices. Malara and Arena (2013) proposed a numerical model with linear potential theory for the flow field outside the chamber of U-OWC devices and enhanced the model with the consideration of head losses. Malara and Arena (2019) studied the efficiency of a multi-U-OWC system. Multi-U-OWC systems were less efficient than single U-OWC systems. However, this problem could be effectively solved by adjusting the distance between U-OWCs. Vyzikas et al. (2017) conducted experiments of various OWC devices. U-OWC devices with a sloping bottom in the front of the submerged wall could achieve the higher efficiency at the natural frequency than other forms of OWCs. Scialò et al. (2021) investigated the choice of the PTO system of U-OWC systems with multi-connecting chambers. A nonlinear model was developed by Scandura et al. (2021) to simulate U-OWC devices, and the numerical results showed good agreement with experimental data with/without the top cover. This is in addition to a number of U-OWC related studies (Spanos et al., 2018; Strati et al., 2015; Arena et al., 2018).

The U-OWC device can achieve high capture efficiencies over a wide range of cycles. By optimising the design of the U-tube it is possible to lead to even greater capture efficiencies. However, this design to maximise efficiency can also lead to the impact of wave loading on the U-OWC device. Wave loads are important for the reliable design of U-OWC structures. In this thesis, the effect of variations in U-shape geometry on the U-OWC front wall loading will be discussed.

2.3   Smoothed Particle Hydrodynamics

Gingold and Monaghan (1977); Lucy (1977) first introduced Smoothed Particle Hydrodynamics (SPH) method, a Lagrangian mesh-free method for studying issues in astrophysical dynamics, around forty-five years ago. SPH has been used to explain different free-surface flow issues since Monaghan initially employed it to study them (Monaghan, 1994). The

ability of SPH to represent very complex processes using particles rather than computational meshes or grids is one of its most attractive aspects. Particle interactions are created using the kernel function, which discretizes the governing equation of continuous fields. The arbitrary distribution of particles makes it well suited to complex interfaces and large deformation problems which are difficult to discretize regularly/perfectly using meshes. In ocean engineering, the study of wave and wave structure interaction is often confronted with a splash, wave breaking, and other large free-surface deformation situations. SPH can simulate the hydrodynamic performance of OWC under extreme sea conditions due to its ability to handle large deformation free surface conditions. Extreme wave statistics, like the 50-year significant wave height,, or 50-year sea states,, are key metrics used to characterize extreme wave conditions for a host of ocean (offshore) and coastal engineering applications (Goda, 1924), including offshore wind and marine energy. The existence of extreme waves, as observed by seafarers, has been confirmed by data recording and modeling to be more common than previously assumed (Hansom et al., 2015). Extreme waves mainly occur during major storms at sea by means of constructive interference of wave trains or by nonlinear wave interaction, but extreme waves may also be associated with tsunami or meteotsunami events. If they arrive at the coast, most extreme waves have the potential to cause extensive remodeling and repositioning of the shoreline environment and landforms as well as causing significant damage to human infrastructure and threat to life.

There are two primary SPH frameworks for fluid flows, i.e., the weakly compressible SPH (WCSPH) and the incompressible SPH (ISPH), depending on whether an assumption of fluid compressibility is adopted. WCSPH is based on the compressible version of the NSE, in which density and pressure are connected by an equation of state (EOS). Monaghan (1994) employed this method for fluid simulations in the beginning. To model incompressible flows without imposing an incompressibility restriction in WCSPH, the Mach number needs to be selected in such a manner that compressibility is limited to a low value, typically under 1%. The second framework, ISPH (Cummins and Rudman, 1999), is a fully incompressible formulation that accounts for incompressibility by solving the pressure Poisson equation (PPE). A typical approach used in ISPH is to take the divergence of the momentum equation and use the continuity equation to get a PPE. Considering the number of neighbouring particles, the solution of the PPE requires solving a matrix of tens of elements ($n_p x n_p$ where n_p is the number of particles). This can lead to significant time computational expense. Therefore, the WCSPH model is used in this thesis.

The noisy/inaccurate pressure field (as shown in Fig. 2.8) is the most typical issue with WCSPH (Colagrossi and Landrini, 2003; Souto-Iglesias et al., 2006; López et al., 2010; Husain et al., 2014). The EOS in the WCSPH model is used to solve the pressure problem.
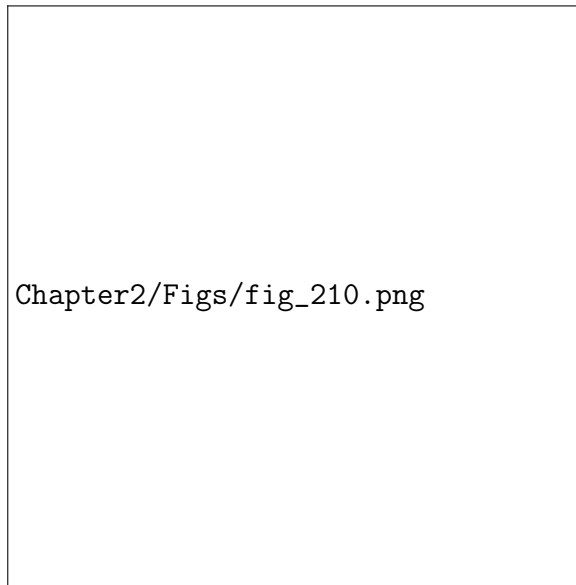
Fig. 2.8 The pressure field of Jet impinging on a flat plate as predicted by the standard SPH scheme (Antonio, 2010). (Figure has been removed due to Copyright restrictions.)

However, even little variations in density may result in significant pressure changes. Another drawback is that the tiny time step increases the computational expense. The lower time step is due to two factors: the Courant–Friedrichs–Lewy (CFL) condition deriving from the time integration methods, and the time step size constraint imposed by the high numerical speed of sound to minimise compressibility (Monaghan, 1994; Monaghan and Kos, 1999). Nevertheless, the WCSPH model has been much improved by the introduction of many numerical methods. The velocity field was re-normalized in Monaghan (1994), by adding a correction of velocity, called XSPH. Furthermore, pressure smoothness may be achieved by repeating re-normalization techniques in the pressure field every 10-20 time steps (Dalrymple and Rogers, 2006). Additional diffusive components, the best known of which is the δ-SPH model (Antuono et al., 2010; Marrone et al., 2011), were also applied to lessen density field oscillation. In addition to the numerical approaches mentioned above, the particle shifting technique is another way to reduce pressure noise (Xu et al., 2009; Lind et al., 2012; Sun et al., 2018a; Khayyer et al., 2017). It alters particle placements in the computational domain to guarantee a regular distribution of particles. In SPH, it is well-known that uneven particle distributions may cause loss of accuracy and stress instability. Particle shifting technique have been used to minimise pressure oscillations in a lot of recent computational work (Sun et al., 2018a; Zhu and Zou, 2020). Several enhanced SPH interpolation models, such as Corrected SPH (CSPH) (Bonet and Kulasegaram, 2001), Finite Particle Method (FPM) (Liu et al., 2005) and Moving Least Square SPH (MLSSPH) (Dilts, 1999), have also been created

to increase simulation accuracy. Stability and accuracy of the WCSPH model have been much improved.

As a result, the SPH model has been widely applied in marine/coastal engineering. Sub-grid scaling, Shephard filtering, and a novel temporal stepping method were used to enhance the JHU (Johns Hopkins University) SPH model (Dalrymple and Rogers, 2006). The improved model was successfully used to simulate waves breaking on the shore. To achieve better results, higher particle resolutions are required, which lead to a higher number of particles. However, smaller time steps entail a huge time consumption. Therefore, the SPH model is only suitable for smaller area simulations. The ripples formed by a narrow boat were simulated by Marrone et al. (2012) using a 3D SPH solver, with the bow breaking wave phenomena as the focus. Bouscasse et al. (2013) derived a fluid-solid interaction SPH model to simulate the motion of floating objects. Skillen et al. (2013) used the ISPH model to simulate water entry and the problem of wave structures. An improved particle displacement method was used to reduce numerical noise. A SPH-based wave tank under DualSPHysics framework was constructed to simulate a sea dike by Altomare et al. (2017). The use of active wave absorption allowed for the avoidance of error due to wavemaker reflection. Theoretical results and experimental findings were used to verify these implementations. SPHysics code was used to model wave-structure interactions with a vertical breakwater and a vertical cylinder (Wen et al., 2018). By using the DualSPHysics, Domínguez et al. (2019) simulated floating offshore constructions with mooring systems (using MoorDyn code). The results showed that DualSPHysics and MoorDyn work together to reproduce the experiments well. Dang et al. (2021) used DualSPHysics to study wave loads of seawall with different geometries in broken and unbroken wave conditions. The results indicated that overtopping water was reduced most significantly in case of steep-faced wall among the five examined cases.

Moreover, SPH methods have started to be used in OWC studies. Using SPHyCE, Didier et al. (2016) studied an onshore OWC device by comparing results with data from FLUENT. The numerical results demonstrated that the SPH model could simulate the interaction of wave OWC structures under severe sea conditions well. Crespo et al. (2017) used DualSPHysics to simulate an offshore OWC device with mooring system. The parallel computing power of GPUs was also exploited, with which real complex geometries and domains could be simulated with less computational time. Wen et al. (2018) considered turbulence effects in the SPH model to simulate an onshore OWC device. Sloshing conditions were found when the OWC device has a short front wall. Although the above studies shown that the SPH model could simulate the wave-structure interactions of OWC devices well, neither of them considered the air pressure inside the OWC chamber, not to say the assessment of wave power

absorption. To solve that, Zhu et al. (2020) proposed a single-phase SPH model with the consideration of the effect of a uniform air pressure distribution over the free surface inside the OWC chamber to assess the performance of OWC devices. Without needing to model the air phase, the air pressure is computed using a parabolic expression between pressure and airflow rate. An alternative way is to represent the PTO system of the OWC by a plate inside the chamber, e.g., see Quartier et al. (2021) who employed the project Chrono multi-physics package to impose forces on the plate to consider the effect of air pressure. The plate method is expected to give good approximate results for low wave frequencies. Both of these models implement the simulation of a PTO system in a single-phase model. Although air effects are considered, the air phase is not modelled, resulting in the inability to consider aerodynamics. It is a compromise due to the expensive computational cost of the SPH model. However, the development of a air-water two-phase SPH model is important for OWC installations to be considered in the future. The two-phase model simulates the movement of air. The inaccuracies associated with the simplification of the single-model (e.g. single-phase model ignoring air compressibility; influences on energy extraction because of aerodynamic) are avoided.

SPH models are used for many complex ocean engineering problems. However, given the scale of these problems, SPH models often require the simulation of tens or even hundreds of millions of particles. Therefore, computational acceleration techniques, such as parallel model, multi-resolution method, and coupled models are required such that complex problems with sufficient particles and higher resolution could be simulated with less computational time.

Hardware Acceleration and Parallel Framework

For effective calculation of enormous particle counts on the order of millions and more, parallel programming and hardware acceleration must be considered. Hardware acceleration is the specialised use of computer hardware to perform processes and tasks more effectively than a single central processing unit (CPU). Through the use of parallel programming, hardware acceleration allows for the simultaneous processing of repeated operations across large data sets. Hardware acceleration can be achieved through high performance computing (HPC) on multiple CPU cores (ranging into the thousands) or through specialist hardware architecture such as the graphics processing unit (GPU).

For large-scale parallel simulation of SPH techniques, many parallel frameworks exist. SWIFT is an open-source project, which is implemented SPH and Barnes-Hut tree-code for self-gravity in the cosmological hydrodynamics code (Schaller et al., 2018). By grouping nearby particles in cells, the calculation is broken up into very many short and inter-dependent

tasks, whereby a single task processes particles within a cell, or between pairs of cells. Thus, SWIFT uses a task-based parallel strategy. However, large numbers of particles in large-scale problems make each task computationally expensive. PySPH is an open-source framework for the SPH model programmed by Python (Ramachandran, 2016). PySPH can be run seamlessly in parallel using the Zoltan data management library. parallelSPHysics is an open-source code and has identical functionality as the serial SPHysics code but has been designed to perform simulations of millions of particles (Rogers et al., 2011). The open-source SPH codes based on single-GPU-acceleration have also been developed, including GPUSPH (Hérault et al., 2011), AquaGPUSPH (Cercos-Pita, 2015) and DualSPHysics (Crespo et al., 2015). Due to the parallel power processing of GPUs, the computations may be up to two orders of magnitude faster than the serial version.

In this thesis, an MPI-based parallel model is developed. MPI is a message-passing standard for parallel computing systems that is standardised and portable. MPI allows several processes to communicate with each other while running in parallel. MPI is powerful because it enables thousands of computing processors in a network to communicate across diverse architectures (distributed memory). For MPI frameworks, domain decomposition is the primary step. Ferrari et al. (2009) developed an MPI parallel SPH code by using the METIS library, a very powerful free software package for partitioning meshes and weighted graphs, proposed by Kirby et al. (1998). In their paper, each macro cell is regarded as input data to achieve decomposition. The combination of these macro cells is spanned by space-filling curves. Similar approaches are used by other parallel SPH frameworks with different space-filling curves, e.g., Z-curve (Ihmsen et al., 2011), Peano–Hilbert ordering (Yeylaghi, 2016), Hilbert ordering (Guo et al., 2018). In addition to METIS, a parallel version of ParMETIS is also used in particle-based methods (Murotani et al., 2014). Both METIS and ParMETIS use the same domain decomposition. Another approach divides the computational domain into parallel slices along the main (flow) direction (Marrone et al., 2012; Rogers et al., 2011; Cherfils et al., 2012). One obvious disadvantage is that this approach is only suitable for problems where the computing domain has one main direction. Orthogonal Recursive Bisection (ORB) (Fleissner and Eberhard, 2008; Maruzewski et al., 2010; Oger et al., 2016) recursively split the whole simulation domain into prismatic-shaped subdomains. Whether ORB or space-filling curve is employed, the updating of the subdomain requires consideration of the entire computational domain. This requires global communication to be accomplished. In addition, the partitioning method based on the Voronoi grid is used in SPH parallel strategies by Ji et al. (2019); Egorova et al. (2019). Due to the construction of the Voronoi grid, the partitioning results in convex, strictly-connected subdomains of a small aspect-ratio, which facilitate communication reduction.

The region partitioning method is important because it also directly affects the dynamic load balancing strategy. Based on the parallel scheme of the space-filling curve, dynamic load balancing can realize the partition of the molecular domain by calculating load along the space curve (Ferrari et al., 2009; Ihmsen et al., 2011; Yeylaghi, 2016; Guo et al., 2018). Therefore, the space-filling curve is only one arrangement of subdomains. The partitioning method based on ORB realizes load balancing in the process of partitioning molecular domains (Fleissner and Eberhard, 2008; Maruzewski et al., 2010; Oger et al., 2016), that is, subdomains are divided based on load distribution. However, the two strategies need to communicate globally in order to achieve load balance. Therefore, an updated subdomain is completely different from the previous one. Based on the Voronoi partitioning method, the computational load is projected onto Voronoi particles, and load balancing is realized according to the load distribution among Voronoi particles and the new grid (Ji et al., 2019; Egorova et al., 2019). This loading method is essentially the same as the load-balancing strategy of slice distribution in the computational domain (Fleissner and Eberhard, 2008; Maruzewski et al., 2010; Oger et al., 2016) The distribution of new subdomains is evaluated by the local subdomain load. However, the load balance of the slice distribution in the computational domain is only in one direction. In most dynamic loading strategies, the load is evaluated based on the number of particles. Because the number of particles seriously affects the calculated load. However, the run time is also used to evaluate the load (Domínguez et al., 2013). Moreover, the load strategy based on run time shows better parallel efficiency.

It is acknowledged that the computational efficiency of SPH has been actively addressed. For MPI parallel strategies, when these models are extended to the extreme scale (using a huge number of cores), the computational efficiency still shows a significant decline. How to reduce the communication cost to improve the scalability of the model is to be solved in the future. In addition, combining MPI with GPU acceleration model to realize a multi-GPU acceleration model to scale up to a larger scale is also a focus at present.

Coupled SPH Model

In addition to parallelisation of the SPH model, another way to improve efficiency is to couple the SPH model with other numerical methods. More specifically, the high computational cost of SPH simulates the region with complex interfaces, while other efficient numerical models simulate the remaining area. This approach preserves the advantages of the SPH model while improving computational efficiency. However, it needs to develop accurate coupled models to ensure the reliability of the results.

Many coupled SPH models have been presented in the previous decade to simulate various problems. Narayanaswamy et al. (2010) developed a two-way coupled model to

combine the SPH model with FUNWAVE, which is a finite difference model based on fully nonlinear Boussinesq equations, developed by Kirby et al. (1998). The overlap interface working as a moving boundary for the SPH model was located at the position far away from breaking regions. Altomare et al. (2014) used a one-way coupling strategy to combine Simulating WAve till SHore (SWASH) with DualSPHysics. The waves in DualSPHysics were created by a moving boundary whose displacement in time was reconstructed using the velocities from SWASH. The main weakness was its inability to adjust for wave reflection at the moving border, where a moving boundary hybridization technique was applied. To solve this issue, a relaxation zone approach coupling between SWASH and DualSPHysics was later developed by (Altomare et al., 2018). Napoli et al. (2016) presented an FVM–SPH approach for incompressible flows, in which the interface was solved using an iterative method. The numerical results showed that the proposed hybrid approach can predict viscous flows and wave processes correctly with a significant reduction in the computational efforts with respect to the standard SPH method. Marrone et al. (2016) proposed a unique coupled SPH–FV technique with a transition zone. The coupled model was shown to be both accurate and practical in terms of CPU time and memory needs. The approach was later improved by Chiron et al. (2018) to handle the net mass transfer and free surface transit over the coupling region. Zhang et al. (2020) presented a 3D hybrid model based on the SPH and the Quasi Arbitrary Lagrangian-Eulerian Finite Element Method (QALE-FEM) to study nonlinear wave-structure interaction. Verbrugghe et al. (2019) presented a two-way coupled model between the DualSPHysics solver and the fully nonlinear potential flow solver OceanWave3D. An open boundary condition (Verbrugghe et al., 2019) was used at the coupling contacts inside the SPH numerical domain. The buffer particles were imposed at the entrance with horizontal orbital velocities and surface elevations determined using OceanWave3D. The SPH surface elevation was sent back into OceanWave3D, which overwrites the previously computed free surface. To hybridise shallow water equations-based SPH model with an Navier Stokes equations-based SPH model, Ni et al. (2020) proposed a coupling scheme based on a non-reflective open boundary condition (Ni et al., 2018). Some properties of these coupled SPH models are listed and compared in Table 2.2. In addition, there are many other coupled models associated with the SPH method (Dalrymple and Rogers, 2006; Crespo et al., 2008; Fourtakas et al., 2018; Zhang et al., 2019; Lin et al., 2021).

The main purpose of the coupled models is to improve the computational efficiency of the SPH model. Note that different numerical models may not coincide with one another in terms of the control equations (e.g., potential flow theory vs. NSE model) and/or discrete methods (e.g., mesh vs. meshless). Both overlapping and non-overlapping regions are desirable in terms of coupled methods. However, due to the Lagrangian nature of SPH, the coupling

Table 2.2 Tabulated overview of the existing coupled models.

Authors	Models	Direction	Coupling information	coupling zone in SPH	Transfer type in SPH
Narayanaswamy et al. (2010)	FUNWAVE	Two-way	u	moving interface	wavemaker particles
Altomare et al. (2014)	SWASH	One-way	u	moving interface	moving particles
Napoli et al. (2016)	FVM	Two-way	all physical properties	overlap	mirror particles
Marrone et al. (2016), Chiron et al. (2018)	FVM	Two-way	all physical properties	overlap	open boundary
Zhang et al. (2020)	QALE-FEM	Two-way	u, p	overlap	boundary condition
Verbrugghe et al. (2019)	Oceanwave3D	Two-way	u_h, η	interface	open boundary
Ni et al. (2020)	SWE model	Two-way	u, η	interface	open boundary

interface in the SPH region may need to take into account particle generation and deletion if open boundaries are used. In addition, most coupling models use the two-way coupling method. The two-way coupling can take into account the interaction between two different models, for example, the transmission of reflected waves.

2.4   Summary of Literature Review

In this chapter, the development of OWC devices and SPH numerical models has been reviewed. Despite decades of research, OWC devices have not yet reached a large-scale commercial status, mainly due to low economic efficiency. One part of improving the economic feasibility is to improve the energy conversion efficiency of OWC devices, and based on potential flow theory and CFD methods, a great deal of research has been carried out on various OWC devices to address this. Among these, optimising the geometry to improve the wave energy conversion efficiency is widely studied. However, the damage under wave loading of some OWC projects has also shown the importance of structural reliability design. The design of structural reliability is influenced by the wave loading of OWC installations. Relatively little research has been carried out on the wave loading of OWC devices and optimising the geometry to improve efficiency may also have an impact on the wave loading. In this thesis, wave loading of U-OWC devices is considered and discussed, these are considered to have a better conversion efficiency than conventional OWC devices. Further improvements in efficiency are possible through the optimisation of U-shaped pipes, although this may lead to increased wave loads and this issue has been little studied. Studies of U-OWC wave loads will require consideration of some of the more severe sea conditions. In such cases, the wave contact with the U-OWC device is strongly nonlinear and some strongly nonlinear free-surface phenomena occur, such as wave breaking, sloshing inside the chamber and so on.

The SPH model is a Lagrangian particle method with good capability for the simulation of complex free surface conditions. In recent decades, the SPH model has been widely used to simulate problems related to marine and coastal engineering. Considering its powerful ability

to simulate highly nonlinear situations, the SPH model is suitable for wave energy devices under extreme sea conditions. The main reason is that the complex free surface phenomena, such as impacts, jets and splashes, can be easily reproduced by the SPH model. However, the high computational cost of SPH often makes it impractical for large-scale problems in marine engineering. Therefore, improving computational efficiency is one of the most important issues that need to be addressed to promote the application of SPH in engineering. In recent years, the computational efficiency of SPH models has been significantly improved based on computer acceleration methods. At the same time, the development of coupled models has further reduced the computational cost. The use of these techniques has made possible the application of SPH to marine engineering problems. Therefore, this thesis presents the development of parallel and coupled SPH models to improve computational efficiency.

Chapter 3

Smoothed Particle Hydrodynamics Model

3.1   Introduction

This chapter describes the formulation used to model flow problems of OWC devices. First, the SPH interpolation method is briefly described in this chapter. Then, it describes how the SPH interpolation method solves the governing equations. Finally, the numerical techniques in SPH used in this work are described, including equation of state (EOS), boundary conditions, time integration methods, and the SPH wave making approach.

3.2   SPH Approximation

When simulating the fluid problem near the OWC, it will be governed by Navier Stokes Equations (NSEs). The main concept of SPH is that the fluid is discretized into a series of particles with fluid properties. The control equations are solved discretely by using these particles and ultimately obtaining a solution over the entire computational domain. Here, the SPH theory is briefly introduced. The SPH approximation can be divided into two parts: the kernel approximation and the particle approximation. Kernel approximation means that a function can be written as the integral formulation by introducing a smoothing kernel function. Then the integral function can be solved by calculating the summation of a series of particles, called particle approximation.

Kernel Approximation

A function $\mathscr{F}$ can be described as a kernel approximation formulation using a smoothing kernel function. Firstly, the function $\mathscr{F}$ can be expressed using the Dirac delta function as:

$$\mathscr{F}(\mathbf{r}) = \int_\Omega \mathscr{F}(\mathbf{r}')\delta(\mathbf{r} - \mathbf{r}')d\mathbf{r}', \tag{3.1}$$

where δ_η is the Dirac delta function, $\mathbf{r}$ is the position where $\mathscr{F}(\mathbf{r})$ is calculated by interpolation of the known values $\mathscr{F}(\mathbf{r}')$ at position $\mathbf{r}'$ inside the solution space Ω. The fundamental principle of the SPH method is to approximate δ_η by an analytical weight function $W(\mathbf{r} - \mathbf{r}', h)$ as shown in Fig. 3.1 (h is the smoothing length or width of the kernel W), called a kernel function (Liu and Liu, 2010). If a kernel function is used instead of the Delta function, the approximation of $\mathscr{F}(\mathbf{r})$ is defined as:

$$\mathscr{F}(\mathbf{r}) \approx \int_\Omega \mathscr{F}(\mathbf{r}')W(\mathbf{r} - \mathbf{r}', h)d\mathbf{r}'. \tag{3.2}$$

Specifically, the kernel function should have the following properties:

- Normalization or unity condition: $\int W(\mathbf{r} - \mathbf{r}')d\mathbf{r}' = 1$.

- Compact condition: $W(\mathbf{r} - \mathbf{r}', h) > 0$ when $r' \in \Omega$, and zero otherwise.

- Monotonicity: $W(\mathbf{r} - \mathbf{r}', h)$ decreases as $|\mathbf{r} - \mathbf{r}'|$ increases.

- Symmetric property: W is an even function, and $\nabla_r W(\mathbf{r} - \mathbf{r}', h)d\mathbf{r}' = -\nabla_{r'} W(\mathbf{r} - \mathbf{r}', h)d\mathbf{r}'$.

- Delta function property: In the limit for $h \to 0$, the kernel function W becomes a Dirac delta function.

where ∇_r and $\nabla_{r'}$ denote the derivative at r and r', respectively. In the literature, there are several kernel functions, as described by Liu and Liu (2010). The most commonly used kernel functions are: Cubic Spline kernel, Wendland family kernels and Gaussian kernel. The Cubic spline kernel is given by (Monaghan, 1992):

$$W_C = \begin{cases} \sigma_c(1 - \frac{3}{2}q^2)(1 - \frac{q}{2}), & 0 \le q \le 1, \\ \frac{\sigma_c}{4}(2 - q)^3, & 1 < q \le 2, \\ 0, & otherwise, \end{cases} \tag{3.3}$$

where σ_c is a dimensional normalizing factor for the cubic spline function given by

$$\sigma_c = \begin{cases} \frac{10}{7\pi h^2}, & dim = 2, \\ \frac{1}{\pi h^3}, & dim = 3, \end{cases} \tag{3.4}$$

where dim is the number of dimensions. $q = \frac{|\mathbf{r}-\mathbf{r}'|}{h}$. The Cubic spline kernel satisfies the requirements and has a 2h radius compact support. However, it is a known issue that using this kernel may lead to particle clumping and thus the so-called tensile instability in SPH method (Brito, 2018).

To alleviate the particle clustering and improve the stability of the SPH method, a kernel based on one of the Quintic Wendland kernel suggested by Wendland (1995) has been used

$$W_w = \begin{cases} \sigma_w(1 - \frac{q}{2})^4(2q+1), & 0 \leq q \leq 2, \\ 0, & otherwise, \end{cases} \tag{3.5}$$

where

$$\sigma_w = \begin{cases} \frac{7}{4\pi h^2}, & dim = 2, \\ \frac{21}{16\pi h^3}, & dim = 3. \end{cases} \tag{3.6}$$

This kernel results in significantly reduced numerical dissipation and particle clumping (Robinson, 2009). The Wendland kernels have better numerical convergence than other kernels (Dehnen and Aly, 2012). The Gaussian kernel is expressed as

$$W_G = \begin{cases} \frac{1}{(\pi h)^{dim}}e^{-q^2}, & 0 \leq q \leq 3, \\ 0, & otherwise. \end{cases} \tag{3.7}$$

The Gaussian kernel does not have a compact support. Therefore, a cut-off limit is introduced. For the Gaussian type kernel, 3h is the typical value as in Eq. (2.7). The comparison between different kernel functions shows the cubic spline kernel's simplicity, the Gaussian kernel's stability and code efficiency (Morris, 1996). The Gaussian kernel is sufficiently smooth even for high orders of derivatives, and is regarded as a golden selection by Monaghan (1992) .Therefore, the Gaussian kernel both with 3h as the cut-off limit has been used for the cases studied in the latter chapter.

Formally, approximations for the derivative of function $\mathscr{F}$ can be deduced by

$$\nabla\mathscr{F}(\mathbf{r}) \approx \int_\Omega \nabla\mathscr{F}(\mathbf{r}')W(\mathbf{r}-\mathbf{r}',h)d\mathbf{r}', \tag{3.8}$$

Chapter3/Figs/fig_301.png

Fig. 3.1 Illustration of the SPH interpolation (Sampath et al., 2016).(Figure has been removed due to Copyright restrictions.)

which, after applying integration by parts, can be further expressed as:

$$\nabla \mathscr{F}(\mathbf{r}) \approx \int_{\partial \Omega} \mathscr{F}(\mathbf{r}')W(\mathbf{r}-\mathbf{r}',h)\mathbf{n}dS - \int_{\Omega} \mathscr{F}(\mathbf{r}')\nabla_{r'}W(\mathbf{r}-\mathbf{r}',h)d\mathbf{r}', \qquad (3.9)$$

where $\partial \Omega$ represents boundary of domain Ω, and n denotes normal direction toward outside of the domain Ω at the boundary. The surface integral contribution in Eq. (3.5) is negligible because the smoothing function value on the surface is zero. Therefore, ignoring the surface term, the approximations for the derivative of function $\mathscr{F}$ can be expressed only by the derivatives of the kernel function W as

$$\nabla \mathscr{F}(\mathbf{r}) \approx - \int_{\Omega} \mathscr{F}(\mathbf{r}')\nabla_{r'}W(\mathbf{r}-\mathbf{r}',h)d\mathbf{r}'. \qquad (3.10)$$

After applying the symmetric property of the kernel function, it can be rewritten as

$$\nabla \mathscr{F}(\mathbf{r}) \approx \int_{\Omega} \mathscr{F}(\mathbf{r}')\nabla_{r}W(\mathbf{r}-\mathbf{r}',h)d\mathbf{r}'. \qquad (3.11)$$

Particle Approximation

After the function $\mathscr{F}$ is described as the SPH kernel approximation formulation, the function $\mathscr{F}$ of a particle can be calculated as an interpolation formulation by other particles inside the support domain. The approximation $\mathscr{F}(\mathbf{r}_i)$ of particle i is given by:

$$\mathscr{F}(\mathbf{r}_i) \approx \sum_{j} \mathscr{F}(\mathbf{r}_j)W(\mathbf{r}_i-\mathbf{r}_j,h)V_j, \qquad (3.12)$$

where V_j is the finite volume of neighboring particle j, given by:

$$V_j = \frac{m_j}{\rho_j}, \qquad (3.13)$$

where m_j denotes mass of particle j, and ρ_j represents density of particle j.

The particle approximation for the spatial derivative of $\mathscr{F}$ is (Liu and Liu, 2010)

$$\nabla \mathscr{F}(\mathbf{r}_i) \approx \sum_{j} \mathscr{F}(\mathbf{r}_j)\nabla_i W(\mathbf{r}_i-\mathbf{r}_j,h)V_j. \qquad (3.14)$$

3.3   The Governing Equation

In this thesis, the interest is in using SPH model to simulate incompressible free-surface flows in the field of ocean engineering, where the characteristic Mach numbers are very moderate

and compressibility effects are small. In light of this, it is reasonable to assume a barotropic fluid, i.e. a fluid for which the pressure is a function of the density only and changes in the internal energy can thus be neglected. Although both approaches above are viable, the choice of WCSPH is preferred because of its simplicity over the more complicated ISPH, where the computational effort for solving the pressure equation can become considerable. The continuity and Navier-Stokes equations in Lagrangian form for a weakly-compressible fluid are:

$$
\begin{cases}
\frac{d\mathbf{u}}{dt} = -\frac{1}{\rho}\nabla p + \nu\nabla^2\mathbf{u} + \mathbf{g}, \\
\frac{d\rho}{dt} = -\rho\nabla\cdot\mathbf{u},
\end{cases}
\tag{3.15}
$$

where ρ, $\mathbf{u}$, t, ν and p denote density, velocity vector, time, kinematic viscosity and pressure, respectively. $\mathbf{g}$ represents the gravitational acceleration.

The governing equation can be discretized by an δ-SPH approximation. The original version of this diffusive term is presented by Molteni and Colagrossi (2009) to improve the pressure computation in WCSPH. The δ-SPH is a robust, accurate and reliable method, which has been proven to reduce pressure oscillation problems in a large number of applications (Antonio, 2010; Meringolo et al., 2015; Zhang et al., 2017; Sun et al., 2018b; Lyu and Sun, 2022; Huang et al., 2022). The δ-SPH formulation can be written as:

$$
\begin{cases}
\frac{d\rho_i}{dt} = -\sum_j(\mathbf{u}_j - \mathbf{u}_i)\cdot\nabla_i W_{ij}V_j + \delta hc\sum_j\Psi_{ij}\cdot\nabla_i W_{ij}V_j, \\
\frac{d\mathbf{u}_i}{dt} = -\frac{1}{\rho_i}\sum_j(p_j + p_i)\cdot\nabla_i W_{ij}V_j + \sum_j\alpha hc\Pi_{ij}\nabla_i W_{ij}V_j + \mathbf{g},
\end{cases}
\tag{3.16}
$$

where $W_{ij} = W(\mathbf{r}_i - \mathbf{r}_j, h)$ is the kernel function, c is numerical sound speed. If not specifically stated, δ and α are 0.1 and 0.01, respectively. The coefficients δ and α control the diffusion of density and velocity, respectively. As for the artificial viscosity, our experience is that the minimum value to stabilize the numerical scheme is $\alpha = 0.01$. Consequently, this value is constant in all simulations. Regarding the diffusion parameter, an in-depth analysis has been provided by Antonio (2010), which proves that this term does not affect the global evolution of the fluid, but only acts as a smoothing of the pressure field. In addition, the variation range of the diffusion parameter is limited and given in (Antonio, 2010). In all considered simulations δ was set equal to 0.1. For both the viscosity and diffusion parameters, small variations near these values do not imply a significant change in the numerical output.

The density diffusion is added in the continuity equation to avoid spurious numerical oscillations. The Ψ_{ij} in density diffusion is written as

$$
\begin{cases}
\Psi_{ij} = 2(\rho_j - \rho_i)\frac{\mathbf{r}_j - \mathbf{r}_i}{|\mathbf{r}_j - \mathbf{r}_i|^2} - (\langle\nabla\rho\rangle_i^L + \langle\nabla\rho\rangle_j^L), \\
\langle\nabla\rho\rangle_i^L = \sum_j(\rho_j - \rho_i)\mathbf{L}_i\nabla_i W_{ij}V_j, \quad \text{where } \mathbf{L}_i = \left[\sum_j(\mathbf{r}_j - \mathbf{r}_i)\otimes\nabla_i W_{ij}V_j\right]^{-1}
\end{cases}
\tag{3.17}
$$

where $\otimes$ denotes tensor product. The Π_{ij} in the viscosity term is given as

$$\Pi_{ij} = \frac{(\mathbf{u}_j - \mathbf{u}_i) \cdot (\mathbf{r}_j - \mathbf{r}_i)}{|\mathbf{r}_j - \mathbf{r}_i|^2}. \tag{3.18}$$

3.4 The Equation of State

In general, fluids whose density varies weakly with pressure or temperature can be treated as barotropic fluids, meaning that both pressure and internal energy are single-valued functions of density. When dealing with fluids like water, it is, therefore, possible to adopt a state equation that is only a function of density, $p = p(\rho)$. In the standard SPH formalism the fluid is treated as Weakly Compressible SPH (WCSPH) and the following equation of state is used to determine fluid pressure based on particle density:

$$p_i = \frac{c^2 \rho_0}{\gamma} \left[\left(\frac{\rho_i}{\rho_0} \right)^{\gamma} - 1 \right], \tag{3.19}$$

where $\gamma = 7$ is the polytropic constant and $\rho_0 = 1000 \text{ kg/m}^3$ is the reference density. A limit of c at least ten times faster than the maximum fluid velocity is required to keep the density variation to within 1% and therefore not introduce significant deviations from incompressible methods.

$$c^2 \geq \max \left\{ \frac{U_{max}^2}{0.01}, \frac{gH}{0.01} \right\}, \tag{3.20}$$

where U_{max} and H are the maximum velocity and the reference fluid depth, respectively. Nevertheless, artificial numerical sound speeds are not suitable if too large because this would lead to very small time steps. This can lead to significant computational expense, according to the CFL condition Eq. (3.43) required for stability and for this reason the small artificial speed of sound is used.

3.5 Boundary Condition

Free-Surface Boundary

A flow domain is usually composed of a solid boundary and a free-surface boundary. For free-surface conditions, both kinematic and dynamic boundary conditions should be considered. The kinematic conditions state that the fluid on the surface should maintain its evolution (Colagrossi, 2005).This condition is automatically achieved in the Lagrangian form.

Assuming that surface the tension is negligible, the free-surface pressure can be set as

$$p = p_e, \qquad (3.21)$$

where p_e is the external pressure at the free surface. Due to the truncation of the kernel support, the neighbouring particle numbers for a particle near the free surface are smaller than neighbouring particle numbers inside the fluid. This property is used to define the free-surface particles and to impose a free-surface boundary in the SPH method. The divergence of a particle position in SPH is used here (Lee et al., 2008). Once the free-surface particles are determined, Eq. (3.17) is applied to evaluate the pressure of these particles.

Wall Boundary

Here, a fixed ghost particles boundary proposed by Marrone et al. (2011) is employed. The solid boundary is described as a fixed ghost particles boundary. The number of layers of ghost particles depends on the size of the supporting domain. Each ghost particle has a corresponding interpolation node to calculate the physical properties. This interpolation node is obtained by mirroring the position of a fixed ghost particle into the fluid domain.

For the free-slip boundary case, the ghost particle has the same tangential velocity component as the interpolated node. For the no-slip boundary case, the tangential velocity components of the ghost particles and the interpolated nodes are in the same direction. The normal component of the fluid velocity is reversed in both conditions (free-slip/no-slip) to ensure the non-penetration condition. Here, the density is calculated by an SPH interpolation method,

$$\rho_{ip} = \sum_{j \in fluid} m_j W, \qquad (3.22)$$

where the label ip denotes the interpolation node. Then, using the equation of state, the pressure in interpolation nodes can be obtained. According to the Neumann condition, the pressure in ghost particle and its corresponding interpolation node should meet the following formulation,

$$p_{go} = p_{ip} + \rho_{ip}(\mathbf{g} - \mathbf{a_w}) \cdot (\mathbf{r}_{ip} - \mathbf{r}_{go}), \qquad (3.23)$$

where the label go denotes ghost particles, $\mathbf{a}_w$ is the acceleration of the wall. Conversely, the density of ghost particles is obtained.

3.6   Particle Shifting Algorithm

SPH is a Lagrangian particle method where the fluid is discretized as a series of particles, which means that the particles will be distributed along the streamline and in some cases stacking of particles with local area cavitation will occur. According to Lee's work, the accuracy of the SPH method calculation could be significantly reduced in the case of irregular distribution of particles (Oger et al., 2016). Xu et al. (2009) proposed a particle shifting algorithm (PSA) to prevent anisotropic particle distributions. An improvement was later proposed by Lind et al. (2012) by using Fick's law to control the shifting magnitude and direction.

First, Fick's law (law of diffusion) is introduced, i.e. the law of the rate of diffusion from a region of high concentration to a region of low concentration, the expression for which is

$$J = -DC, \tag{3.24}$$

where J is the diffusion flux, D is the diffusion coefficient and C denotes the concentration. Corresponding to the particle approach, it can be considered that J considers the number of particles per unit time passing through a unit area, which is proportional to the particle displacement velocity u_s

$$u_s = -D_s C_s, \tag{3.25}$$

where C_s represents the concept of particle concentration and D_s is the particle diffusion coefficient, which is obviously time step dependent. Also, the particle concentration and its gradient can be determined by the following equation in the SPH method

$$C_i = \sum_j \frac{m_j}{\rho_j} W_{ij}, \tag{3.26}$$

$$\nabla C_i = \sum_j (C_j - C_i) \frac{m_j}{\rho_j} W_{ij}. \tag{3.27}$$

Taking into account the CFL condition, the final displacement vector δr_s^i is obtained for particle i

$$\delta r_s^i = A_s h |u_i| \Delta t \nabla C_i, \tag{3.28}$$

where A_s is shifting coefficient for control of particle displacement, Δt is the time step. While moving the particles, the corresponding physical quantities should be corrected accordingly

$$\Phi_a^{i'} = \Phi_a^i + \nabla \Phi_a \delta r_s^i, \tag{3.29}$$

where Φ_a represents the particle's physical properties at the initial position, $\Phi_a^{i'}$ is the particle physics at the corrected position, and the physical quantities include: density, velocity, and pressure. After the position of the particle is changed, its corresponding physical properties at the neXu et al. (2009) and Lind et al. (2012)w position need to be interpolated. Here the process originally proposed by Xu et al. (2009) and Lind et al. (2012) is followed in the present work. Similar treatments were also used in the work of some other researchers, e.g., see Khayyer et al. (2017); Sun et al. (2017); Huang et al. (2018). Yet some more recent studies (Sun et al., 2018b) showed that when particles are rather small in resolution, ignoring updating particle properties has little influence on the solution.

PSA is found to be effective in regularising particle distribution, however, large errors occur when dealing with free surface problems due to incorrect shifting vector resulting from the kernel truncation. To handle this problem some treatments have been proposed in Khayyer et al. (2017). These corrections aim at removing the shifting component normal to the free surface to fulfill the kinematic boundary condition. To this aim, the improved particle displacement method proposed by Khayyer et al. (2017) is used. The improved particle displacement method is founded on calculation of a corrected unit normal vector, $\mathbf{n}^*$, as follows:

$$\mathbf{n}_i^* = \frac{\mathbf{L}_i \cdot \nabla C_i}{|\mathbf{L}_i \cdot \nabla C_i|}. \tag{3.30}$$

Since diffusion normal to the interface must be theoretically zero, the particle shifting displacement vector for free-surface and free-surface vicinity particles is obtained as follows:

$$\delta r_s^i = A_s h |u_i| \Delta t \nabla_s C_i = A_s h |u_i| \Delta t (\nabla C_i - \nabla_n C_i), \tag{3.31}$$

where $\nabla_n C_i$ and $\nabla_s C_i$ represent the normal and tangential components of ∇C_i with respect to the interface, respectively.

Considering basic definitions for normal components of a gradient vector, the normal and tangential components of concentration gradient can be expressed as:

$$\nabla_n C_i = (\mathbf{n}_i^* \cdot \nabla C_i)\mathbf{n}_i^*, \tag{3.32}$$

$$\nabla_s C_i = \nabla C_i - \nabla_n C_i. \tag{3.33}$$

As mentioned above, the particle displacements are different in different regions. Here, the particles are distinguished as inner, free-surface vicinity, free-surface and splash particles.
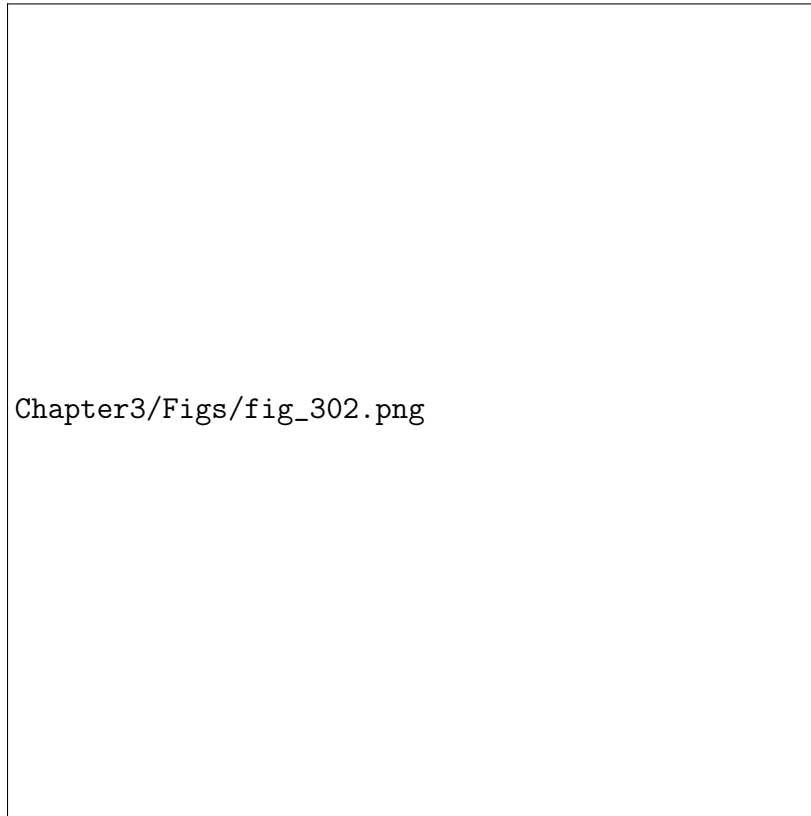
Fig. 3.2 Different types of particles (a) and their detection criteria (b) (Khayyer et al., 2017).(Figure has been removed due to Copyright restrictions.)

First, free-surface particles are detected based on position vector divergence criterion, i.e. $\nabla \mathbf{r} < 1.5$ exactly similar to that used in (Lind et al., 2012). Once free-surface particles are detected, free-surface vicinity particles are flagged on the basis of two criteria, i.e. 1) $1.5 < \nabla \mathbf{r} < 2$ and 2) $|\mathbf{r}_{jk} < h$ such that k is the nearest free-surface neighbor of j. For a particle with full compact support and regularly distributed neighbors,$\nabla \mathbf{r}$ would be equal to 2 in two dimensions (Lee et al., 2008). A splash particle, is a particle for which $\nabla \mathbf{r} < 1.5$ but it does not have any free-surface vicinity neighboring particles in its kernel domain and will not be shifted. Inner fluid particles are particles that have not been flagged either as free-surface, free-surface vicinity or splash particles. A summary of particle shifting displacement vectors implemented is presented in Fig. 3.2 .

3.7 Time Integration

For the SPH equations, which are explicit linear systems of equations, the computational solution process is an integration over time to solve for physical changes over time. In

numerical simulations, the SPH model spends a lot of time on particle scanning, and therefore the time-integration method should minimise the particle search process while ensuring accuracy. In this work, the prediction correction method is used (Monaghan, 1989), which requires only one search at each time step, from which second-order accuracy can be obtained. The prediction correction method is divided into two steps:

1. prediction step:

$$\mathbf{u}_i^{n+\frac{1}{2}} = \mathbf{u}_i^n + \frac{\Delta t}{2}\left(\frac{d\mathbf{u}_i^n}{dt}\right), \tag{3.34}$$

$$\mathbf{r}_i^{n+\frac{1}{2}} = \mathbf{r}_i^n + \frac{\Delta t}{2}\mathbf{u}_i^n, \tag{3.35}$$

$$\rho_i^{n+\frac{1}{2}} = \rho_i^n + \frac{\Delta t}{2}\left(\frac{d\rho_i^n}{dt}\right), \tag{3.36}$$

2. correction step

$$\mathbf{u}_i^{n+\frac{1}{2}} = \mathbf{u}_i^n + \frac{\Delta t}{2}\left(\frac{d\mathbf{u}_i^{n+\frac{1}{2}}}{dt}\right), \tag{3.37}$$

$$\mathbf{r}_i^{n+\frac{1}{2}} = \mathbf{r}_i^n + \frac{\Delta t}{2}\mathbf{u}_i^{n+\frac{1}{2}}, \tag{3.38}$$

$$\rho_i^{n+\frac{1}{2}} = \rho_i^n + \frac{\Delta t}{2}\left(\frac{d\rho_i^{n+\frac{1}{2}}}{dt}\right). \tag{3.39}$$

Finally, the physical values of the particles after one time step are obtained by:

$$\mathbf{u}_i^{n+1} = 2.0\mathbf{u}_i^{n+\frac{1}{2}} - \mathbf{u}_i^n, \tag{3.40}$$

$$\mathbf{r}_i^{n+1} = 2.0\mathbf{r}_i^{n+\frac{1}{2}} - \mathbf{r}_i^n, \tag{3.41}$$

$$\rho_i^{n+1} = 2.0\rho_i^{n+\frac{1}{2}} - \rho_i^n. \tag{3.42}$$

An appropriate time step should be chosen to satisfy the CFL conditions and ensure the stability of the time integral. The time step needs to satisfy the numerical sound velocity

condition as

$$\Delta t \leq \frac{h}{c},$$ (3.43)

the viscous diffusion condition,

$$\Delta t \leq 0.125 \frac{h^2}{v},$$ (3.44)

and the body force condition,

$$\Delta t \leq 0.25 \sqrt{\frac{h}{g}}.$$ (3.45)

3.8 Wave Generation and Absorption

To study the OWC device, a numerical wave tank (NWT) is need to simulate its response in wave conditions. In NWTs, wave generation is a necessary feature. In the SPH method, the wave generation approach includes: piston-type (Altomare et al., 2017), flap type techniques (Gomez-Gesteira et al., 2012), source generation (Liu et al., 2015), open boundary (Verbrugghe et al., 2019), and relaxation zone (Altomare et al., 2018; Zhu et al., 2021). The piston-type approach is used here to generate waves as this type of wave generation techniques is the most widely used in an SPH-based NWT and it is particularly well suited for the generation of waves in shallow water. The Bissell transfer function expresses the relationship between wave amplitude and wave maker displacement. For a piston wavemaker, the Bissell transfer function Φ can be expressed as follows

$$\Phi_B = \frac{H_{wave}}{S_0} = \frac{4\sinh^2(kd)}{2kd + \sinh(2kd)},$$ (3.46)

where H_{wave}, S_0, k and d are the wave height, piston Stroke number, wave number and the water depth, respectively. Once the piston stroke is defined, the velocity $U(t)$ of piston movement is given:

$$U(t) = \frac{dX(t)}{dt} = \frac{\omega}{\Phi_B} \eta(t),$$ (3.47)

where $X(t)$ is the position of the wave maker plate. ω is the angle wave frequency. $\eta(t)$ is the target water surface elevation. To improve accuracy, an active absorption wave creation method is introduced (Altomare et al., 2017). The error of free-surface elevation η_e is reduced by comparing the free surface η_{sph} near the wavemaker plate (4h from the wavemaker: This distance is selected to ensure that fluid particles used to measure free-surface elevation are

not neighbours of the boundaries of the piston.) with the theoretical free surface η_{theo}:

$$\eta_e = \eta_{theo} - \eta_{sph}. \tag{3.48}$$

The wavemaker velocity $U(t)$ has to be modified to match the velocity induced by the wave that will be absorbed. For a piston-type wavemaker, characterised by uniform horizontal velocity along the water depth, the wave absorption is performed using linear long wave theory. The correction velocity of the wavemaker plate can be calculated as:

$$U_c(t) = \eta_e \sqrt{gd}. \tag{3.49}$$

Thus, wavemaker velocity $U_n(t)$ with correction velocity can be expressed as:

$$U_n(t) = U_c(t) + U(t), \tag{3.50}$$

Finally, the wavemaker position x_{maker} is then corrected using the following expression:

$$x_{maker}(t + \Delta t) = x_{maker}(t) + U_n(t) * \Delta t, \tag{3.51}$$

Monochromatic waves are not representative of sea states that characterize real wave storm conditions. Sea waves are mostly random or irregular. In order to generate random waves, the Pierson-Moskowitz spectrum and the JONSWAP spectrum are used to simulate irregular waves. The JONSWAP spectrum is shown as following:

$$S(f) = \alpha_{ir} H_s^2 f_p^4 f^{-5} \gamma^\beta e^{-\frac{5}{4}\left(\frac{f_p}{f}\right)^4}, \tag{3.52}$$

$$\alpha_{ir} = \frac{0.0624}{0.23 + 0.0336\gamma - \left(\frac{0.185}{1.9+\gamma}\right)}, \tag{3.53}$$

$$\beta = e^{-\frac{(f-f_p)^2}{2\sigma^2 f_p^2}}, \tag{3.54}$$

$$\sigma = \begin{cases} 0.07 & f \leqq f_p \\ 0.09 & f > f_p \end{cases} \tag{3.55}$$

where $\gamma = 3.3$ here. The wave spectrum can be defined through its characteristic parameters (peak frequency f_p and spectrum shape H_s). An example of a wave spectrum is shown, where the y-axis represents the spectral density and the x-axis the frequency. The characteristic parameters of each spectrum can be assigned by the user together with the value of N (number

of parts in which the spectrum is divided). A phase seed is also used and can be changed to have different random series of δ_i. Therefore changing the phase seed allows different irregular wave time series to be generated both with the same significant wave height H_s and peak period f_p. The procedure to generate irregular waves can be summarised as follows [83, 84]:

1. Divide the spectrum into N parts ($N > 50$) in the interval (f_{start}, f_{stop}), where generally the values assumed by the spectrum (S_η) at the extremes of this interval is smaller than the value assumed for the peak frequency, $S_\eta(f_{start}) \leqq 0.01S_\eta(f_p)$ and $S_\eta(f_{stop}) \leqq 0.01S_\eta(f_p)$.

2. The frequency bandwidth is so-defined as$\Delta f = \frac{(f_{stop}-f_{start})}{N}$. The irregular wave is so decomposed into N linear waves.

3. Determine the angular frequency ω_i, wave height H_i and initial phase δ_i of each linear wave:

$$f_i = f_{start} + i\Delta f - \Delta/2, \tag{3.56}$$

$$\omega_i = 2\pi f_i, \tag{3.57}$$

$$H_i = 2\sqrt{2S_\eta(f_i)Deltaf}, \tag{3.58}$$

$$\eta_0(x,t) = \sum_{i=1}^{N} \frac{H_i}{2}cos(\omega_i t - k_i x + \delta_i), \tag{3.59}$$

where k_i can be obtained by the dispersion relationship $\omega^2 = gktanh(kh)$, h is water depth.

Wave absorption is essential to reduce/remove the unwanted wave reflection from the tank boundary. Sponge layers (Altomare et al., 2017; Molteni et al., 2013; Ni and Feng, 2013) are used at the end of NWT. By limiting the motion of the particles, the sponge layer is able to absorb waves and dissipate the wave energy. In the sponge layer, the velocity of the particles can be modified as,

$$u_c = u \cdot f(x, \Delta t), \tag{3.60}$$

where u_c is the corrected particle velocity; $f(x, \Delta t)$ is the reduction function introduced by Altomare et al. (2017) to reduce the velocity of the particles at each time step according to their location

$$f(x, \Delta t) = 1 - \Delta t \cdot 10 \left(\frac{x - x_0}{x_1 - x_0} \right)^2, \tag{3.61}$$

where x_0 and x_1 are the starting and ending positions of the sponge layer, respectively.

3.9 Summary of the Introduction to SPH Model

In this chapter, the mathematical basis of SPH has been briefly introduced. The discrete version of the Navier Stokes equation is presented in WCSPH form. In particular, the δ-SPH model is used in our work. Particle shifting techniques that regularise the particle distribution according to criteria used to measure particle anisotropy are also introduced. Boundary conditions in the SPH model, including free-surface boundary condition and solid wall boundary condition are described. Finally, a description of the wave-making methods used in SPH is given.

Chapter 4

SPH with Pneumatic Model

4.1   Introduction

A typical OWC device consists of water body and the air overhead. This is a semi-confined space formed by the submerged wall wrapping, with the water body open below. Incident waves cause the water body to drive the movement of the air. The moving air passes through a turbine in the opening above the device and generates electricity. Therefore, numerical models need to consider both air and water in order to complete the reproduction of the entire power generation process of power take-off (PTO) systems in an OWC device. The SPH method is known to have a very expensive computational cost. Therefore, the use of an air-water phase SPH model to simulate an OWC device is very time consuming. Furthermore, OWC devices often need to be simulated in a numerical water tank. Tens of metres of numerical flume make the whole calculation extremely costly. Therefore, a single-phase SPH method with a pneumatic model is developed to simulate OWC devices with PTO system.

4.2   Pneumatic Model

The rapid changes in the water volume inside the chamber result in changes in the air volume. The change in air volume leads to a change in air pressure. At this point, the difference between the air pressure in the chamber and the atmospheric pressure leads to air flow through the opening of the turbine. According to numerous experimental and numerical studies, the air pressure in the chamber is linearly related to the air flow rate at the opening for the Wells turbine.(e.g. see (Koo and Kim, 2010), Ning et al. (2015, 2016))

$$p_a = K_{dm}^l q_d,\qquad(4.1)$$

where p_a is air pressure in the chamber and K_{dm}^l is the pneumatic damping coefficient for the linear expression and q_d is the air velocity within the duct. In contrast, for OWC installations with impulse turbines, or for physical models of OWC with orifices (where orifices are used to represent air turbines), a quadratic expression between the flow rate in the duct and the pressure drop of the air in the chamber is used (López et al., 2016), i.e.,

$$p_a = \begin{cases} K_{dm}^q(q_d)^2, & q_d > 0, \\ -K_{dm}^q(q_d)^2, & q_d \leq 0, \end{cases} \tag{4.2}$$

where K_{dm}^q is the damping coefficient for the parabolic expression. $q_d > 0$ denotes that air flows into the chamber. $q_d \leq 0$ denotes that air flows out. The velocity of the air q_d near the duct can be calculated as following

$$q_d = \frac{\Delta V}{A^l \Delta t}, \tag{4.3}$$

where ΔV denotes the volume change of air phase inside the chamber within time Δt. A^l is the cross-sectional area of the duct. The instantaneous volume of air can be obtained by subtracting the volume of water from the volume of the chamber. The change of water volume can be directly evaluated by measuring the free-surface level inside the chamber. Finally, the air pressure inside the chamber can be expressed in terms of the free-surface level.

The change in air volume is obtained by the evolution of the free surface. However, the compressibility of the air is not considered here. Therefore, the air fluxes obtained from the model in the present model are inaccurate. The effect of air compressibility on the performance of an OWC device was theoretically analysed by Thakker et al. (2003), under the hypothesis of isentropic compression/decompression processes. A 5–8 % reduction in the device conversion efficiency was found because of the compressibility of the flow. Sheng et al. (2013) conducted an experimental study considering the airflow through an orifice connected to a chamber pressurized and depressurized by the motion of a piston. In their work, a power loss due to air compressibility of about 2 % was found for a relative pressure in the chamber of about 2.2 kPa. The scaling and air compressibility effects on the performance of an offshore stationary OWC were simulated by Elhanafi et al. (2017b). It is found that air compressibility effects can be neglected without significant differences in the device performance for small-scale OWC models scaled (1:10). Simonetti et al. (2017) studied the effect of air compressibility in modelling OWC devices at scale 1:1 (prototype) and at four different scales (1:50, 1:25, 1:10 and 1:5). The results confirm that compressibility effects are not reproduced in the small-scale model tests (less than 1:25). The above studies
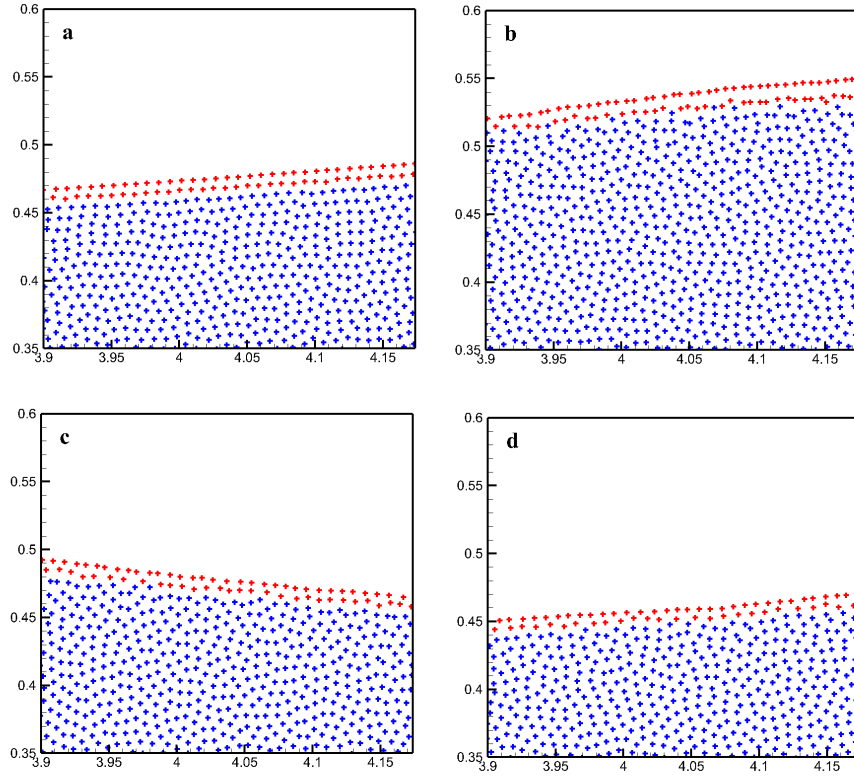
Fig. 4.1 Free surface particles (red dots) at $t = 4.0$ s (a), 6.0 s (b), 8.0 s (c), and 10.0 s (d).

show that the compressibility of the air is negligible when the model scale is small. The laboratory simulations discussed in this thesis are considered to be small-scale devices, i.e. the compressibility of air is ignored.

To begin with, the free surface particles should be detected in the simulation. Once the air pressure is obtained, it needs to apply it to the free surface. In SPH, the divergence of particle positions $\nabla \cdot \mathbf{r}$ is usually 2 for a two-dimensional problem (Lee et al., 2008). However, this value becomes smaller near the free surface. Based on our numerical tests, 1.89 was chosen as this criterion. Numerical tests are the simulation of regular wave as introduced in Section 4.5. Different values of $\Delta \cdot \mathbf{r}$ are selected to detect whether particles near the free liquid level have been correctly selected. When $\nabla \cdot \mathbf{r}$ is less than 1.89, air pressure is applied

$$\forall \text{ particle } i \in [\nabla \cdot \mathbf{r}_i = \sum_j (\mathbf{r}_i - \mathbf{r}_j) \cdot \nabla_i W_{ij} V_j \leq 1.89] \Longrightarrow \text{particle } i \in \mathscr{F}_f, \qquad (4.4)$$

where $\mathscr{F}_f$ is free-surface particles. Fig. 4.1 illustrates the capture of free-surface particles when this criterion is used. Two layers of fluid particles are captured close to the free surface.

Finally, the governing equations need to consider the air pressure when solving for the gradient of pressure of free surface particles

$$-\frac{1}{\rho_i}\nabla p_i = \begin{cases} -\frac{1}{\rho_i}\sum_j\left[(p_j+p_a)+(p_i+p_a)\right]\cdot\nabla_i W_{ij}V_j, & i\in\mathscr{F}_f \\ -\frac{1}{\rho_i}\sum_j(p_j+p_i)\cdot\nabla_i W_{ij}V_j, & \text{otherwise.} \end{cases} \tag{4.5}$$

Only the free-surface particles inside the chamber are directly affected by the air pressure. Also, it is important to note that there are cases where the air pressure is lower than the atmospheric pressure. A negative pressure may exist inside the chamber. However, the free-surface boundary condition is imposed by setting the pressure at the free-surface to zero in the SPH method (Lee et al., 2008). Therefore, the free-surface condition is not considered inside the chamber.

4.3   Regional Ghost Particle Approach

In the current SPH approach, fixed ghost particles are used to simulate wall boundary conditions. In general, the number of layers of fixed ghost particles is determined based on the kernel function. For example, a Gaussian kernel function needs three layers of ghost particles to avoid errors due to kernel truncation. Therefore, for a front wall partly submerged in water, one layer of ghost particles could lead to the effect of water particles on both sides Fig. 4.2(a). For a single resolution simulation, this would undoubtedly require smaller particle spacing to simulate the entire flow field. Thanks to the development of multi-node ghost particle technology (Meringolo et al., 2015), this allows the simulation of a front wall with only three layers of dummy particles, as shown in Fig. 4.2(b). The multi-node ghost particle technique does not completely escape the limitation of wall thickness on particle resolution. Therefore, the region ghost particle technique is proposed, where the fluid near a thin wall is divided into several regions. Each region has a unique corresponding ghost particle. This allows the ghost particles/fluid particles in different regions not to affect each other.

The approach for dividing the zones is critical to the regional ghost particle approach. Three different approaches (see Fig. 4.3) are investigated here. The same regional division approaches described by Meringolo et al. (2015) is used in approach (a). Approach (b) is another straightforward way, comparable to the one described in He et al. (2019b). For approach (c), the fluid domain is divided into five sections around the thin wall, which are two sections more compared with those of approaches (a) and (b), leading to a more complicated
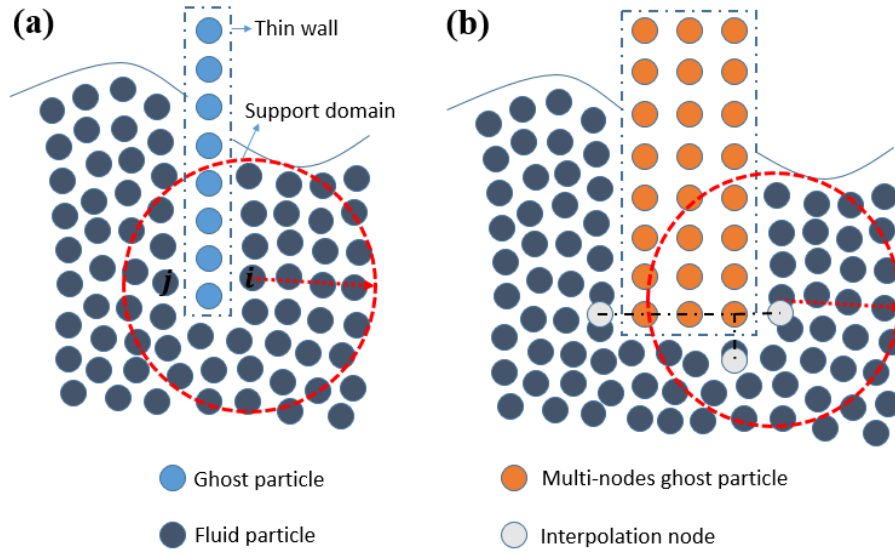
Fig. 4.2 Illustration of the front wall with one layer (a) and multi layers (b) of ghost particles.

code. It takes approach (b) as an example to demonstrate that the technique of region ghost particles, utilising the splitting strategy, works.

1. The fluid region near the thin wall is divided into three sections, each with corresponding ghost particles as well as interpolation nodes. This part is usually done during the initial setup and is fixed as shown in Fig. 4.4.

2. The physical properties of the interpolation nodes are obtained by interpolating the fluid particles in the region using SPH interpolation. The properties of the ghost particles are obtained by interpolating the nodes. This allows the ghost particles to not be influenced by other regions.

3. Only the fluid particles in the region, the ghost particles and the fluid particles in the adjacent regions are considered. This ensures that the problem of kernel truncation does not occur. It is also ensured that region Ω_a and region Ω_c do not influence each other.

The fluid particles in region Ω_c do not affect the particles in region Ω_a. The interpolation approach is based on the traditional fixed ghost method. As a result, the regional ghost particle technique may potentially approximate wall thickness with lower precision, overcoming the limit of ghost particles for thin structures. The other two splitting approaches are replicated using the same procedure except for the inconsistent ghost particle arrangement.

A communication vessel is simulated to evaluate the performance of the various region dividing approaches. As illustrated in Fig. 4.5, the communication vessel is made up of two
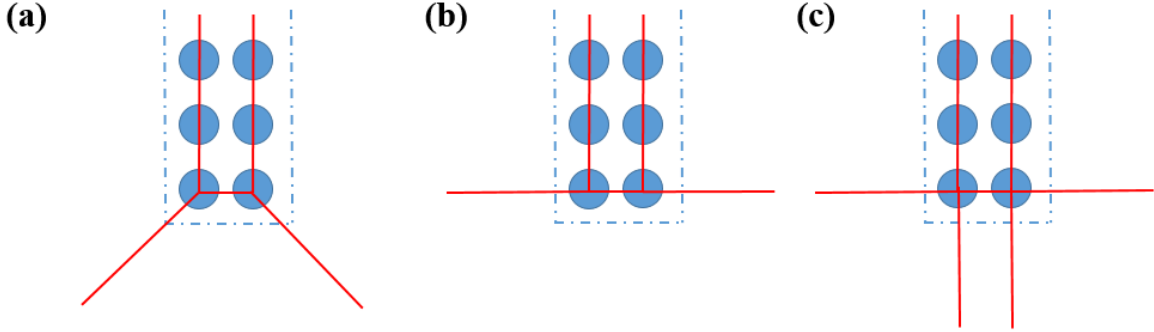
Fig. 4.3 Schematic diagram of the three different ways of splitting regions for the regional ghost particle approach. Approach (a) uses the same regional division approaches described by Meringolo et al. (2015). Approach (b) uses another straightforward method, described by He et al. (2019b). For approach (c), the fluid domain is divided into five sections around the thin wall, where fluid region at the bottom of the thin wall is divided into two parts according to the number of ghost particle layers.
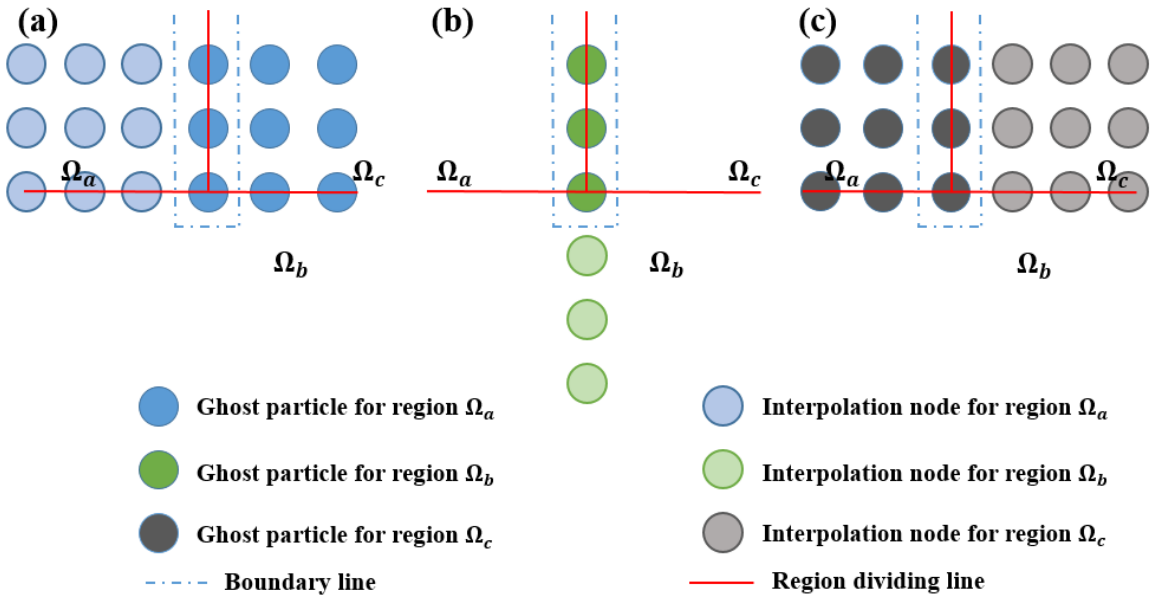
Fig. 4.4 Schematic illustration of the regional ghost particle approach.
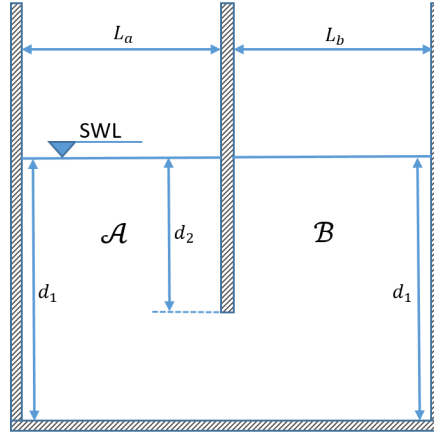
Fig. 4.5 Illustration of the communicating vessel case.

vessels connecting at the bottom. The widths of the two containers $\mathfrak{A}$ and $\mathfrak{B}$ are slightly different ($L_a = 0.35$ m and $L_b = 0.32$ m). The thickness of the mid wall in the middle is 0.01 m. Particle spacing is 0.01 m, implying that the wall is represented by a single layer of ghost particles. The initial particle spacing of 0.01 results in the middle wall having only one layer of imaginary particles. This can be used to examine the present regional ghost particle approach.

Figure 4.6 shows the pressure field of a communication vessel at $t = 10.0$ s using three different region approaches. The pressure field on both sides of the wall is quite unstable for the approach (a) and (c), comparing with approach (b), as shown in Fig. 4.6. Furthermore, the time series of kinetic energy for the three approaches, as illustrated in Fig. 4.7 shows that technique (b) produces a more stable solution after 0.2 s. Therefore, the approach (b) is employed for the following numerical simulation. Approach (a) has a ghost particle arrangement that may not fill the support field of the particles at the bottom of the middle wall. approach (b) is the simplest, with the two sides of the wall avoiding interaction. Approach (c) divides the area into five parts. This is probably too complex and introduces some errors instead.

4.4   Numerical Validation

Wave propagation and convergence analysis

The first step towards the investigation of OWC is to develop a robust NWT. This section is to verify the performance of a SPH–based NWT by comparing the numerical results with the analytical ones. Fig. 4.8 shows the 2D NWT, in which d and $L = 4\lambda$ represent the water
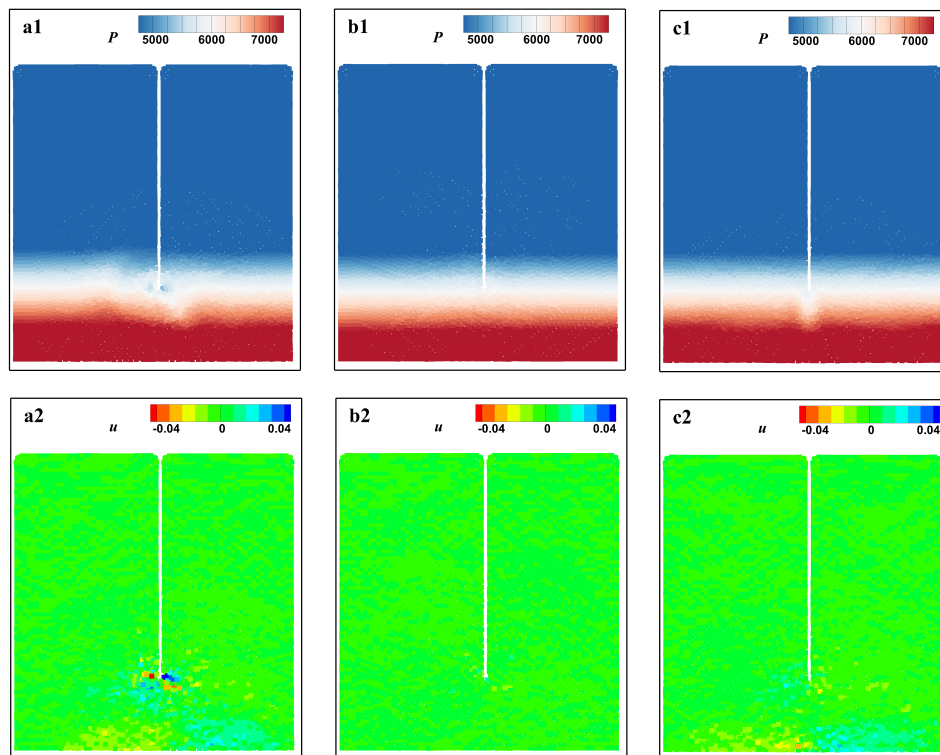
Fig. 4.6 The pressure (a1~c1) and horizontal velocity field (a2~c2) of the communicating vessel at t = 10 s using the regional division method (a) (a1, a2), method (b) (b1, b2) and method (c) (c1, c2).
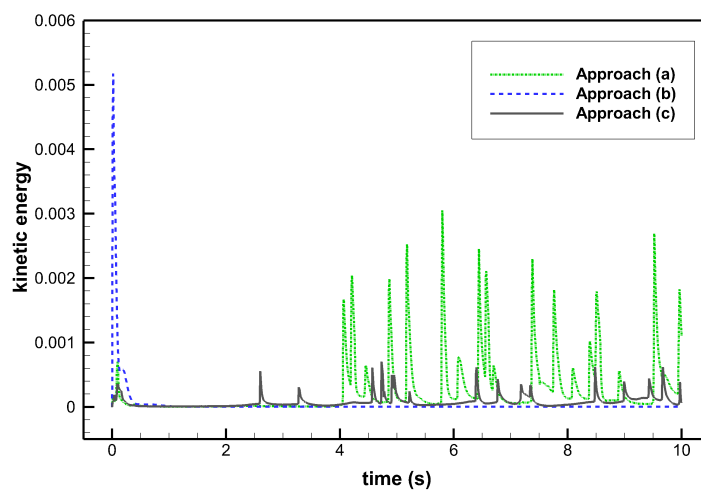
Fig. 4.7 Time series of the kinetic energy of the linker using the three regional division methods.
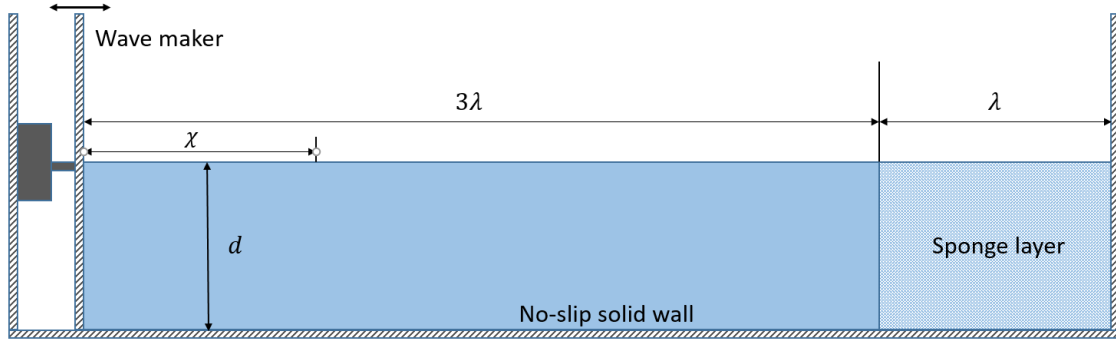
Fig. 4.8 Sketch of a NWT.

depth and the tank length, respectively, where λ denotes the incident wavelength. There is a sponge layer with the length of λ at the right end of the tank which is modeled to dissipate wave power. The incident wave height is denoted by H. A piston–type wavemaker located at the left boundary of the tank is used to generate waves. The solid walls of the tank are modelled using no–slip boundary conditions.

For quantifying and better evaluating the comparison between the reference results, the mean average errors for amplitude MAE_a and phase MAE_p are used, which are calculated according to equations

$$MAE_a = \frac{1}{N_a} \sum \frac{|\eta_{extr}^{ref} - \eta_{extr}^{sph}|}{A}, \tag{4.6}$$

$$MAE_p = \frac{1}{N_a} \sum \frac{|t_{extr}^{ref} - t_{extr}^{sph}|}{T}, \tag{4.7}$$

where $extr$ refers to the local extrema, A to the wave amplitude, T to the wave period and N_a to the number of wave crest. ref and sph denote reference data (e.g., theory or experimental data) and SPH results, respectively. The NWT is tested by the generation of regular waves with $T = 1.2$ s, $H = 0.1$ m and $d = 0.5$ m. Time series of the water surface elevation at $\chi = 0.5\lambda$ (a), λ (b) and 2λ (c) predicted by the SPH NWT with three different resolutions, i.e., $dx0 = 0.005$ m, 0.01 m and 0.02 m, together with the theoretical solutions, are illustrated in Fig. 4.9. The waves generated by the NWT are found to propagate steadily with satisfactory accuracy, except $dx0 = 0.02$ m. As shown in Fig. 4.9a, there are some small changes of the surface elevation between 4 s to 6 s for $dx0 = 0.02$ m. This is due to the method used to determine the free surface position being more sensitive to isolated particles when the spacing between particles is larger. Numerical results for the two finer resolutions overlay one another and agree well with the analytical results, indicating that a convergent solution seems to be achieved with $dx0 \leq 0.01$ m. It was found that the MAE_a are 5.9%, 6.1% and

5.6% for the resolution ($dx0 = 0.01$ m) at the position a, b and c , respectively, and MAE_p are 1.5%, 1.3% and 1.9%, respectively. It gives confidence in the present SPH NWT for generating and absorbing waves.

Communicating Vessels

To validate the effect from the pneumatic model, a communication vessel is simulated (Fig. 4.10). The two vessels with same width $L_c = 0.32$ m are connected at the bottom. The starting water depths in the two vessels are $d_1 = d_2 = 0.56$ m. The connecting wall's submergence d_3 and thickness are 0.33 m and 0.01 m, respectively. At the beginning, 1000 Pa air pressure is imposed into $\mathfrak{B}$. This is only achieved by applying air pressure directly to the governing equation. Under the pressure of the air, the water body begins to oscillate and eventually reaches a new steady state. According to hydrodynamic theory, in the new steady state, there is a height difference $H_d = 1000/(\rho g) = 0.102$ m between the two vessels due to the difference in air pressure.

Fig. 4.11 shows the time history of the height difference H_d for two vessels. It can be seen that H_d oscillates with time. There is a steady decay of oscillation over time. The final steady state agrees with the theoretical values. Two different resolutions both show stable and coincident results. Fig. 4.12 shows the pressure field at the initial moment as well as at 60 seconds. It can be noticed that the pressure in the vicinity of the free-surface level of vessel $\mathfrak{B}$ changes at 60 s. It shows that the change in air pressure not only leads to a change in the height of the free surface but also affects the pressure field of the water.

An Onshore OWC with Slope Bottom

An OWC device with a slope platform initially was investigated by López et al. (2014) (Fig. 4.13). The physical model is built based on the prototype designed on the A Guarda breakwater at a 1:25 scale. The numerical wave tank is 6 times the incident wavelength, and water depth is 0.42 m. In the laboratory experiment, a rectangular opening at the top is set up to simulate a turbine. The flow rate of the opening in this rectangular opening is expressed as a quadratic expression with respect to the air pressure in the chamber. According to López et al. (2014), a dimensionless damping coefficient B^* is expressed as

$$B^* = \frac{|p_a|^{0.5}}{|q_d|} \frac{b_1}{\rho_{air}^{0.5}}, \tag{4.8}$$

where ρ_{air} and b_1 are the reference density of air phase and the chamber length, respectively. The movement of the water body causes rapid changes in the volume of air inside the
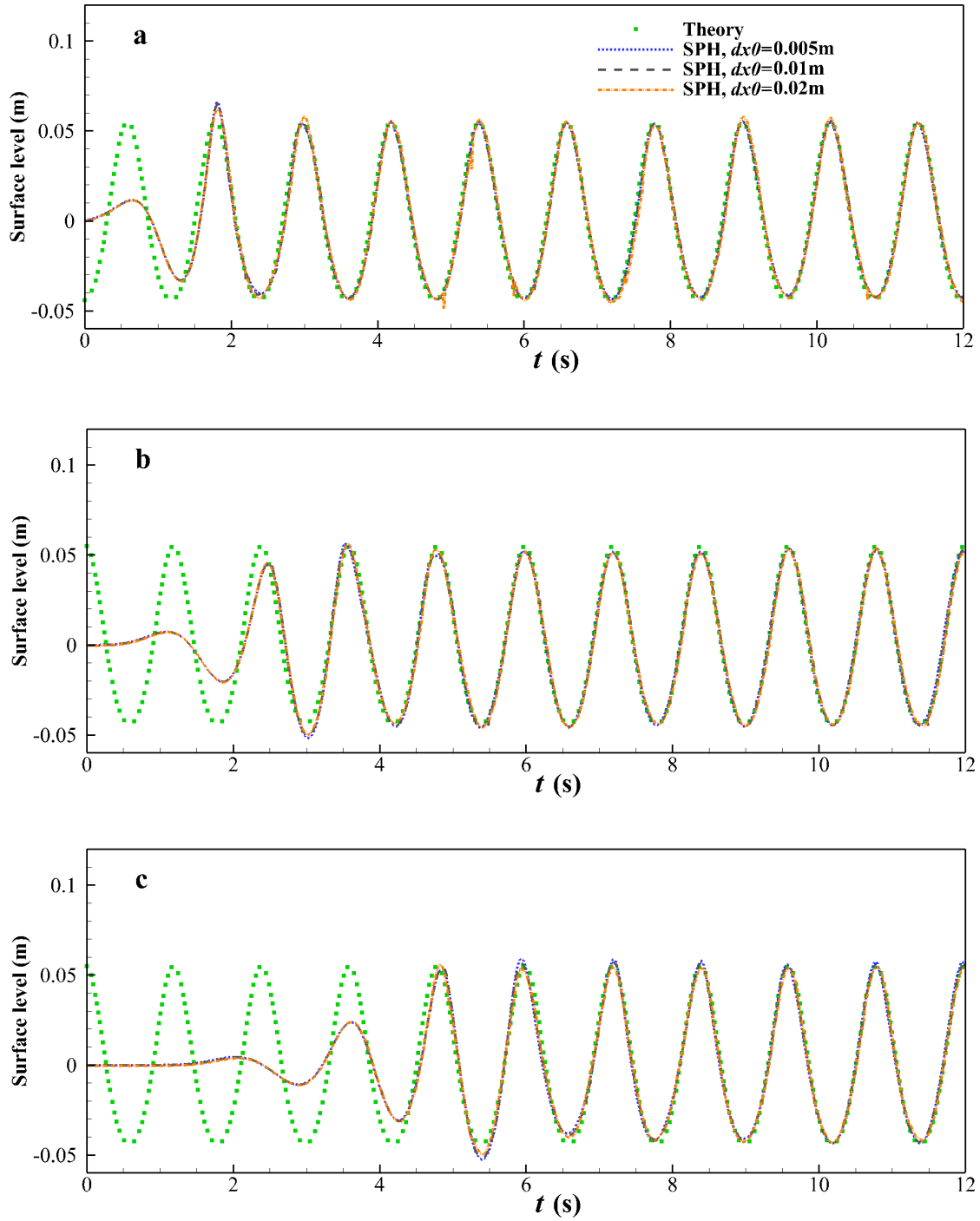
Fig. 4.9 Time evolution of the surface elevation of a propagating regular wave with T=1.2 s, λ=2.04 m and H=0.1 m at χ=0.5λ (a), λ (b) and 2λ (c).
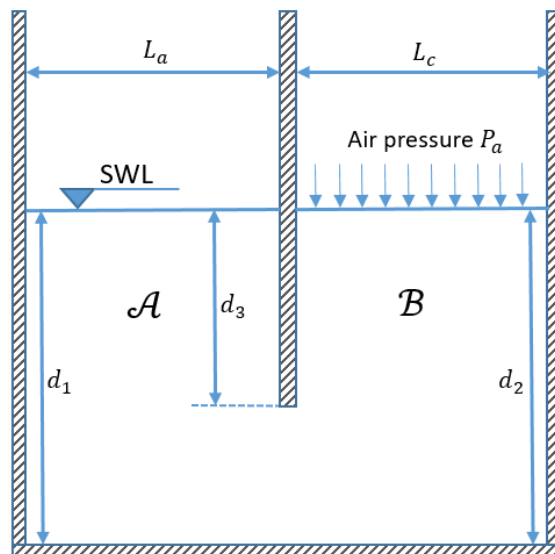
Fig. 4.10 Illustration of the communicating vessel case.
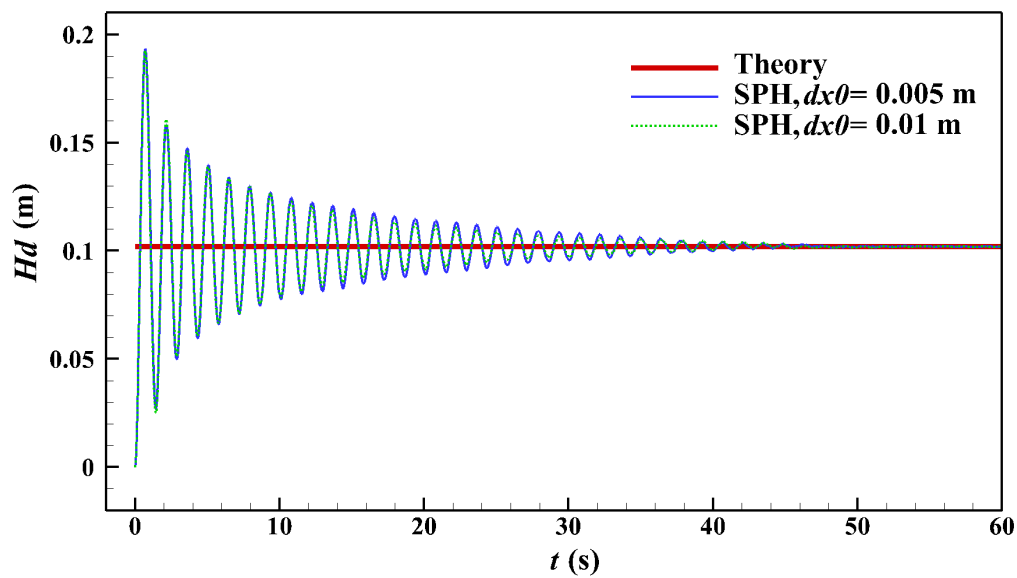
Fig. 4.11 Elevation of the free-surface level difference between containers $\mathcal{A}$ and $\mathcal{B}$.
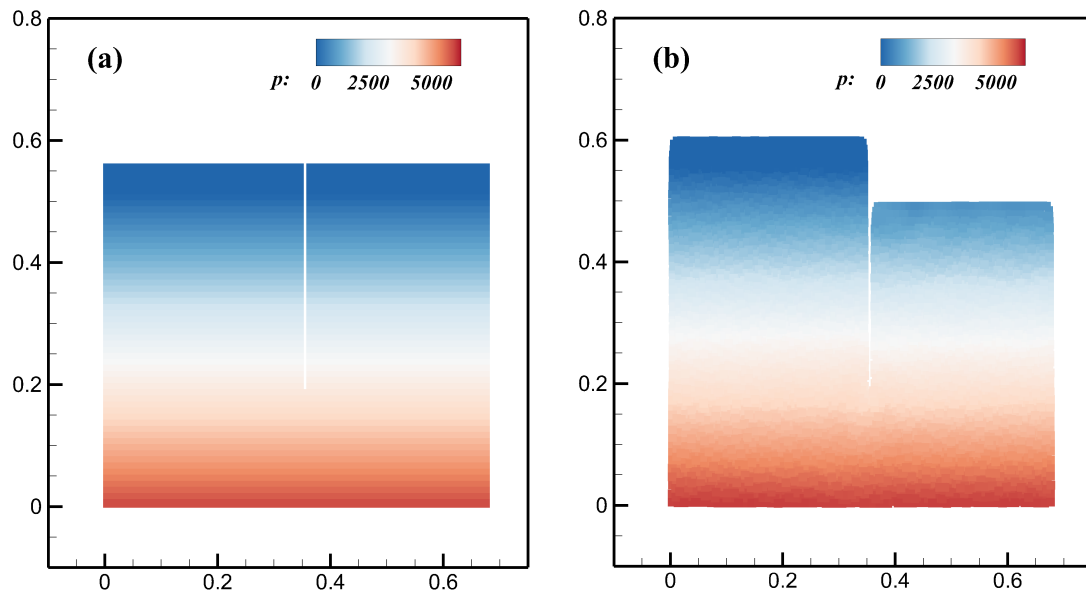
Fig. 4.12 The pressure field of communicating vessel at $t = 0$ s (a) and $t = 60$ s (b) ($dx0 = 0.005$ m).
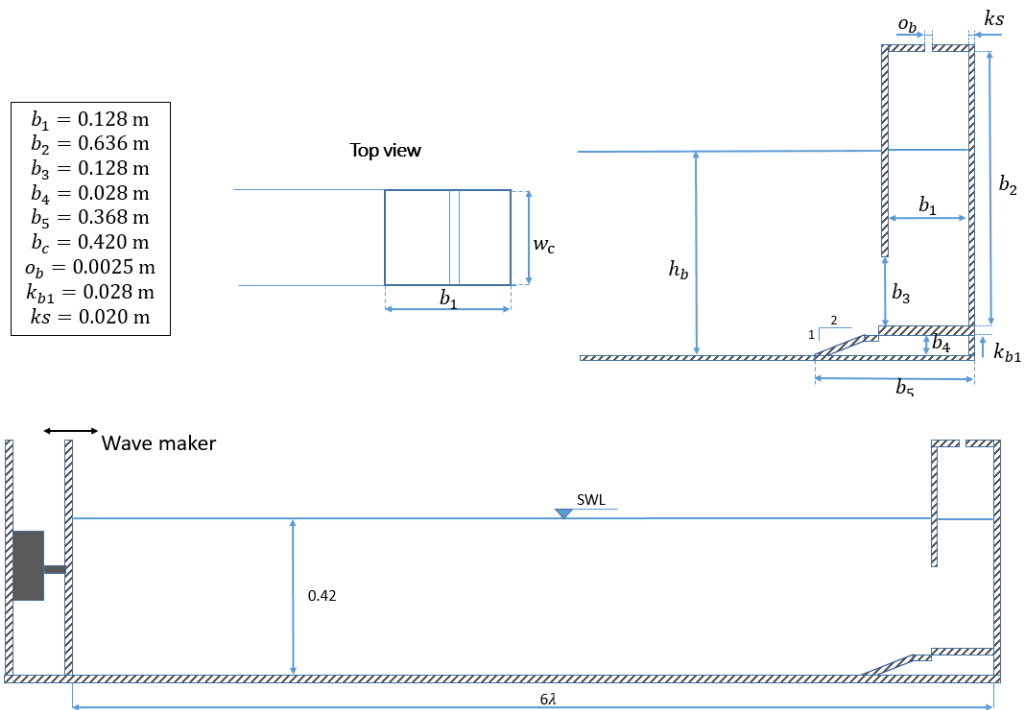
Fig. 4.13 Illustration of the OWC device and the numerical water tank, dimensions in (m).
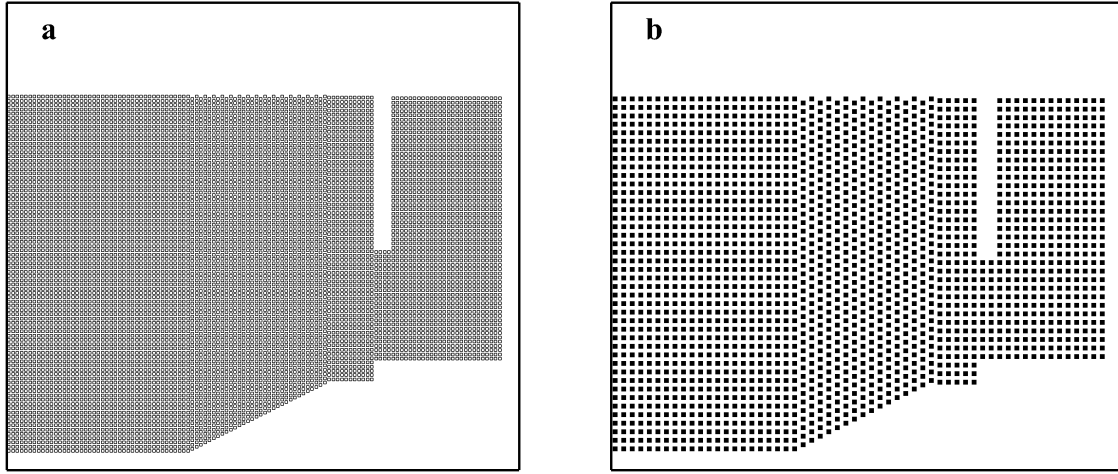
Fig. 4.14 The initial particle setup using the multi-node particle method (a), $dx0 = 0.005$ m; and the regional ghost particle method (b), $dx0 = 0.01$ m.

Table 4.1 Comparison of SPH setup and computational time between multi-node particle and regional ghost particle

Approach	Resolution (m)	Time step (s)	Physical time (s)	Calculation time (h)
Multi-node particle	0.005	0.00005	21	245.2
Regional ghost particle	0.01	0.0001	21	36.1

chamber. This in turn creates a pressure differential across the turbine that restricts/affects the movement of the water. Thus, the oscillating water body inside the chamber is being damped. Eq. (4.8) is from the dimensionless analysis proposed by López et al. (2014). Eq. (4.8) was used to obtain the damping coefficient of Eq. (4.2) from Lopez's experimental data (López et al., 2014). In the present model, the damping coefficient needs to be determined first before the OWC system can be simulated.

Combining Eq. (4.8) with Eq. (4.2), the damping factor K_{dm} in Eq. (4.2) is

$$K_{dm}^q = \left(\frac{B^* \rho_{air}^{0.5}}{b_1} \right)^2 . \tag{4.9}$$

Finally, the damping factor is $534.66 \text{ kg}^{-0.5}\text{m}^{-2.5}$ for the slot with 2.5 mm width.

Fig. 4.14 shows the initial particle setup for the multi-node ghost particle approach and the regional ghost particle approach. The thickness k_s of the thin front wall is 0.02 m as in Fig. 4.14. The multi-node ghost particle approach results in at least three layers of ghost particles for the wall. Thus, a particle spacing 0.005 m is used at the beginning. Besides

that, regional ghost particle approach is used here with particle spacing 0.01 m. Thus, it just employs two layers of ghost particles to describe the front wall. For these two particle spacings, the numerical wave tanks need 160 000 and 40 000 fluid particles, respectively. The numerical setup and time cost are shown in Table 4.1. The simulations are run on a desktop computer using an Intel(R) Core(TM) i5-7500T CPU Processor (Quad-Core, 2.71 GHz) under a WINDOWS 7 (64-Bit Edition) operating system. It is found that the reduction in the number of particles leads to a significant reduction in the computational cost. Fig. 4.15 shows the comparison of surface elevations and air pressure with experimental data (López et al., 2014). MAE_a and MAE_p are used to quantitatively assess the accuracy of the model. MAE_a and MAE_p represent the difference in amplitude and phase between the numerical solution and the reference solution at the wave position, respectively. Mean average errors MAE_a and MAE_p are calculated. Here, N_a is set to five due to the five wave peak in Fig. 4.14.

Fig. 4.15 shows the comparison of free-surface elevations and air pressure. The free surface height of Star-CCM+ is greater at the peak than in the experimental results. For both boundary approaches, the SPH solution exhibits similar free-surface level variations, although there is a small difference in the local peaks. Specifically, the errors (MAE_a and MAE_p) in amplitude and phase from the experimental data is 8.8% and 4.4% for the multi-node particle method. In contrast, these two errors are 8.1% and 4.5% for the regional ghost particle approach. In addition, the air pressures for the two different boundary approaches show similar results. Specific error data can be found in Table 4.2. The above results show that the current SPH model can capture the variation of free surface and air pressure in the chamber very well. The regional ghost particle approach can decrease the particle resolution and reduce the computational cost without reducing the computational accuracy.

The air flow rate at the opening and the capture power of the OWC can be calculated from the free surface of the chamber and the air pressure. To compare these data simultaneously, the numerical results are multiplied by fixed factors 2, 100, 0.05, and 200, respectively. Fig. 4.16 shows the variation of these data over a period of time. The SPH results agree with the Star-CCM+ data despite some slight differences. At t/T=13.60, the free surface is at its lowest point. The low rate of change of the free-surface level at this point leads to a zero air pressure. At t/T=13.85, the free surface rises rapidly resulting in a rapid flow of air out of the chamber. At this point, both air pressure and power obtain their maximum values. At t/T=14.1, the free-surface level is near its maximum value. The air flow rate is very low resulting in near zero air pressure and power. The free-surface level then drops. At this point, the air pressure in the chamber drops causing air to flow into the chamber. The change in free-surface level allows the air flow rate to be determined. Based on the relationship
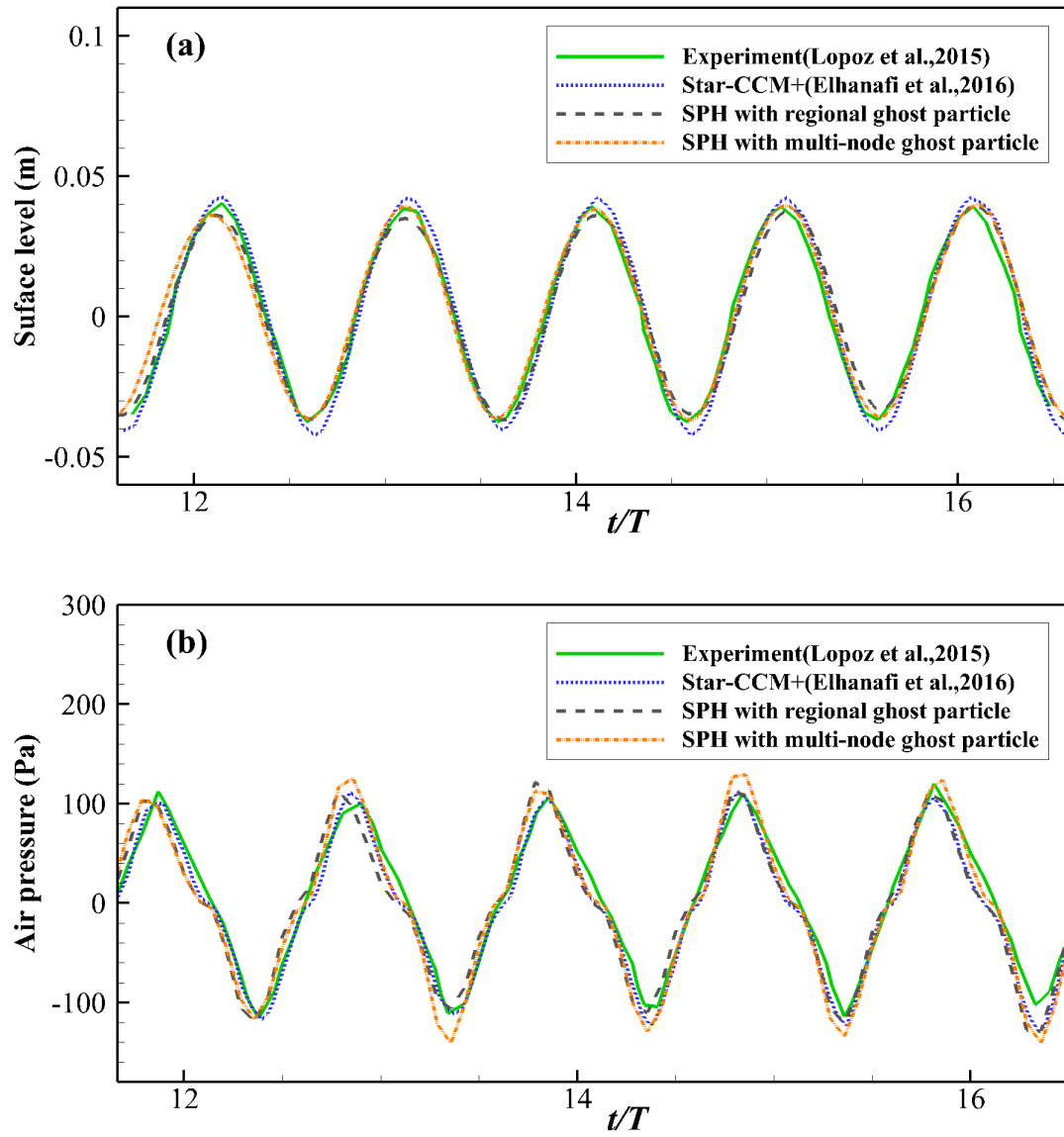
Fig. 4.15 Surface elevation (a) and air pressure drop (b) inside the chamber (Wave condition: $H_w = 0.04$ m, $\lambda = 2.42$ m and $T_w = 1.4$ s).
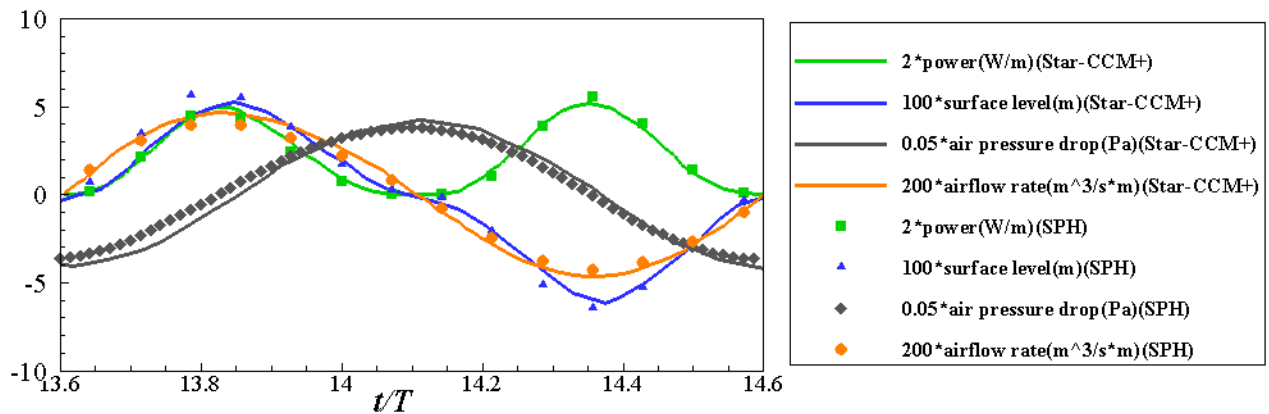
Fig. 4.16 Comparison of Power, surface elevation,air pressure drop, and air flow rate between SPH and STAR-CCM+ (Elhanafi et al., 2016).

Table 4.2 Comparison of boundary setup and errors between multi-node particle and regional ghost particle

Boundary approach	MAE_a (Surface evolution)	MAE_p (Surface evolution)	MAE_a (Air pressure)	MAE_p (Air pressure)
SPH with regional ghost particle	7.8%	3.8%	8.1%	4.5%
SPH with multi-node ghost particle	7.2%	3.7%	8.8%	4.4%

between pressure and flow rate, the air pressure can be obtained. Finally, the capture power can be calculated from the flow rate and air pressure.

An Onshore OWC with Step Bottom

'Lid-off' Cases

An OWC device with a step bottom, as experimentally studied by Vyzikas et al. (2017) is simulated. The numerical tank had the same length of 28 m as the experimental data. Fig. 4.17 depicts a schematic of the OWC. The OWC spans the whole width of the flume and is made up of three similar independent chambers, each chamber having an orifice in the centre of the top wall. In the absence of a PTO, the top-wall of the OWC was removed and ambient pressure was permitted to enter the OWC. For the cases that no PTO was considered, they are known as 'Lid-off' cases. The thickness for the thin front wall of this OWC device is 0.024 m, as depicted in Fig. 4.17. When the thickness of the front wall is taken into account, two starting particle resolutions (0.008 m and 0.012 m) are chosen, as illustrated in Fig. 4.18. For particle resolutions of 0.008 m and 0.012 m, respectively, about 160000 and 330000 fluid particles are required, respectively, for the whole computational domain.

Fig. 4.17 Illustration of the OWC device and the numerical water tank, dimensions in (m).

Fig. 4.18 The initial particle setup using the multi-node particle method (a), $dx0 = 0.008$ m; and the regional ghost particle method (b), $dx0 = 0.012$ m.
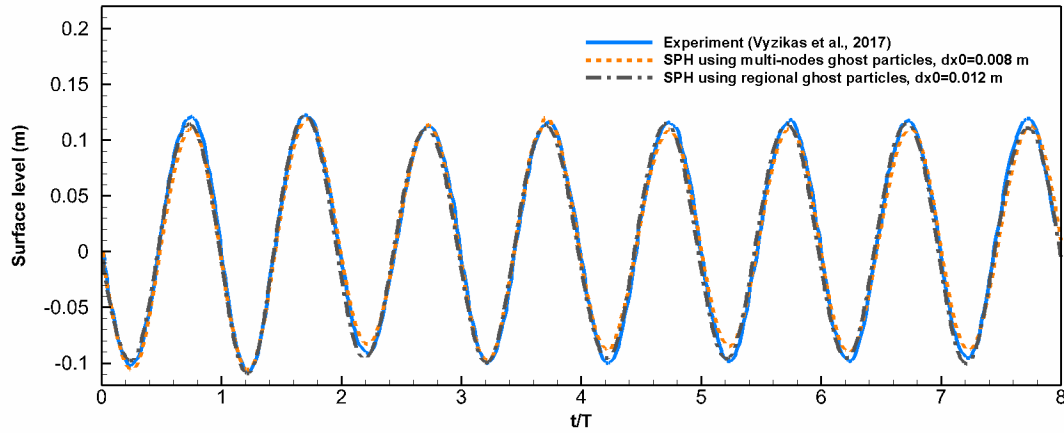
Fig. 4.19 Surface elevation (a) and air pressure drop (b) inside the chamber (Wave condition: $H_w = 0.088$ m, $\lambda = 5.03$ m and $T_w = 2.15$ s).

Table 4.3 Boundary approach and errors

Approach	MAE_a (Surface evolution)	MAE_p (Surface evolution)
SPH with regional ghost particle	5.8%	1.3%
SPH with multi-node ghost particle	6.2%	1.5%

Fig. 4.19 compares the surface elevations for the 'Lid-off' situation. For both ghost particle approaches, SPH obtained similar results and both approaches agreed well with the experiment, as shown in Table 4.3. Table 4.4 shows the particle spacing settings and the time spent. It can be observed that the regional virtual particles result in larger particle spacing and time steps, and less time spent.

'Lid-on' Cases

When considering the OWC with a PTO system (also known as the 'Lid-on' case), the pneumatic damping coefficient must first be established. The velocity of the free surface can be calculated in terms of the partial derivatives of the free surface with respect to time. The link between the air velocity and air pressure is thus obtained, as shown in Fig. 4.20. To

Table 4.4 Numerical setup and cost

Approach	Resolution (m)	Time step (s)	Physical time (s)	Calculation time (h)
Multi-node particle	0.008	0.00005	33	310
Regional ghost particle	0.012	0.0001	33	157
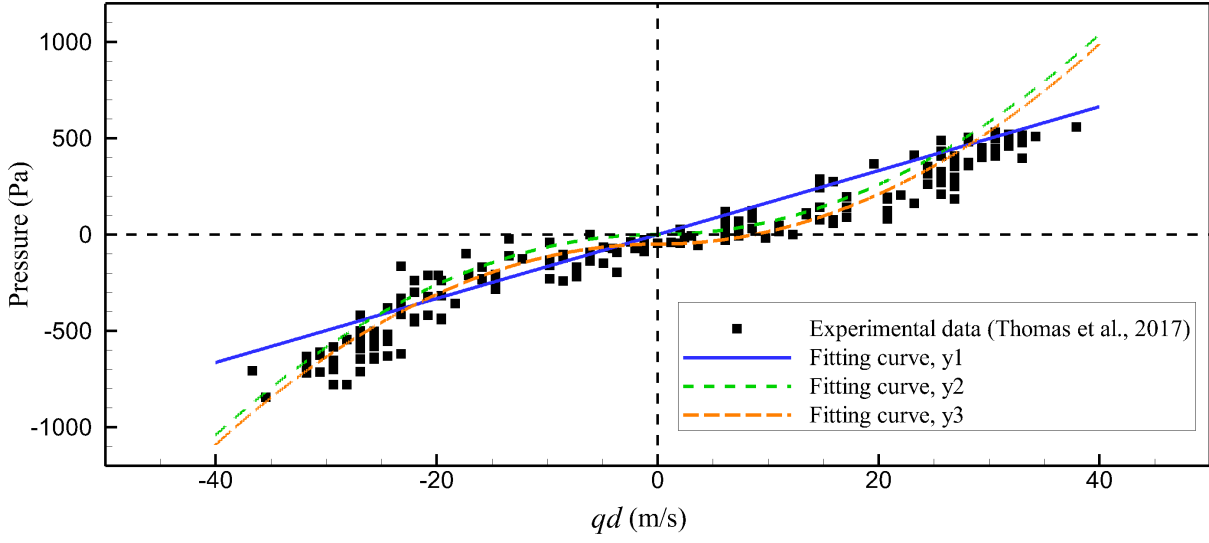
Fig. 4.20 Pressure drop versus free surface velocity.

represent the connection between air velocity and air pressure, the linear (y1) and quadratic (y2) formulae are obtained. These two expressions are assumed to pass through the origin. Nevertheless, it is discovered from the measurement data that when the flow velocity is zero, the air pressure is not zero. The experiment shows the air pressure are unsymmetrical data, and the difference between the absolute values is about 200 Pa. Therefore, the quadratic expression (y3), which does not pass through the origin, is also included to produce a better fitting relationship between air pressure and air velocity. In this section, the effects of these three expressions are compared. The exact expressions $y1$, $y2$, and $y3$ are as follows:

$$p_{a1} = 16.6q_d, \tag{4.10}$$

$$p_{a2} = \begin{cases} 0.65(q_d)^2, & q_d > 0, \\ -0.65(q_d)^2, & q_d \le 0, \end{cases} \tag{4.11}$$

$$p_{a3} = \begin{cases} 0.65(q_d)^2 - 50, & q_d > 0, \\ -0.65(q_d)^2 - 50, & q_d \le 0, \end{cases} \tag{4.12}$$

The squared value of the correlation coefficient R^2, which indicates the fit of the expression to the data, for these three fitting lines are 90.12, 89.49 and 93.13, respectively. The best fit can be found in (y3), and there is less than 1% difference between expressions (y1) and (y2).

The air pressure drop of the corresponding experimental results and the SPH results for the 'Lid-on' case are compared in Fig. 4.21. The pressure peak of expression 1 is the smallest.
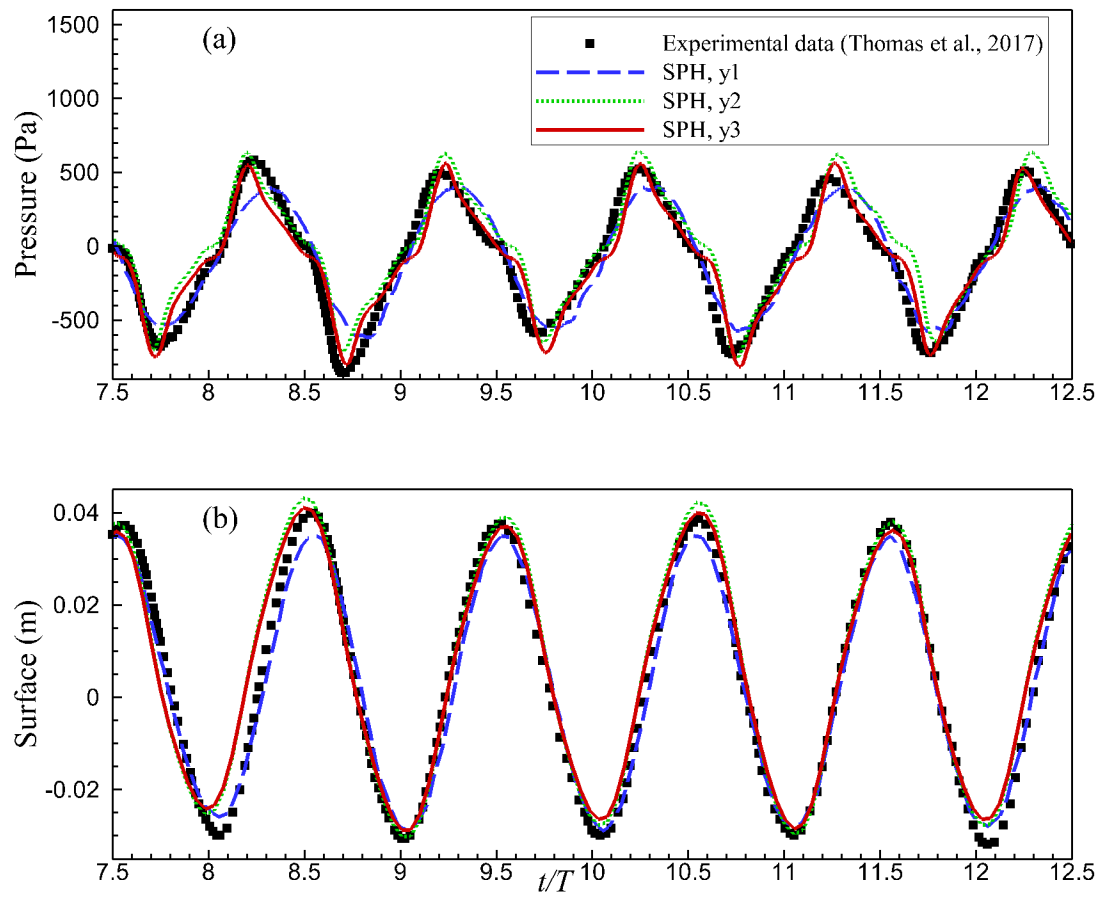
Fig. 4.21 Comparison of relative free surface elevation (a) and air pressure drop (b) inside the chamber, for H_w=0.088 m, λ=5.03 m and T_w=2.15 s, with experimental data.

Table 4.5 Various expressions and errors

Approach	MAE_a (Surface evolution)	MAE_p (Surface evolution)	MAE_a (Air pressure)	MAE_p (Air pressure)
SPH, y1	19.1%	9.3%	20.0%	9.3%
SPH, y2	12.5%	4.4%	14.0%	4.4%
SPH, y3	8.5%	4.4%	9.8%	4.4%

The peak air pressure drop of the expression SPH(y2) is smaller than the peak values of the expression SPH(y3). In Fig. 4.21, the surface elevation inside the chamber of the OWC is compared. Table 4.5 shows the relative errors in the results of these three expressions. The result of the quadratic expression is better than the result of the linear expression. The squared value of the correlation shows that the quadratic expression expresses the relationship between air pressure and flow rate better. The expression (y3), which does not go through the dots, shows a better result than the expression (y2). The quadratic expressions can show better results compared to the linear expressions. In addition, the form of the expressions have a significant influence on the results.

4.5   Summary of the SPH with Pneumatic Model

In this chapter, a single-phase SPH model is proposed to simulate OWC devices with a PTO system. To consider the effect of air phase, the relationship between the air flux and air pressure is employed. The change in volume of air in the chamber is calculated from the change in free surface and thus the flow rate of the opening is obtained. The instantaneous air pressure can also be obtained from the relationship between air flow rate and pressure. To simulate the front wall of OWC devices, a regional ghost particle approach is developed. The fluid near the thin wall is divided into three regions and configured with ghost particles and interpolation nodes. The ghost particles in each region do not affect the numerical calculations in the other regions. The fluid particles in the regions that are not in direct contact also do not affect each other. The regional ghost particle technique, therefore, avoids the interaction of fluid particles on both sides of the thin wall. The present model is validated by simulations with a linker as well as two different OWC devices. Finally the following conclusions can be drawn.

1. The proposed single-phase SPH with pneumatic model can capture the evolution of the free surface and air pressure inside the chamber. This model demonstrates that the single-phase SPH model can also be used to simulate OWC devices with power take-off systems.

2. The expressions for air flow rate and pressure are important for the accuracy of the results. The quadratic expressions show better results than the linear expressions.

3. The regional ghost particle technique eliminates the limitations of thin wall thickness on particle resolution. The regional ghost particle technique can simulate thin walls with greater particle resolution and results in less computation time.

Chapter 5

Parallel SPH Framework

5.1   Introduction

When simulating an OWC in a numerical tank, hundreds of thousands of particles or even millions of particles are usually required in two/three dimensions. In order to perform larger-scale SPH numerical wave tank simulations, it is therefore necessary to develop efficient parallel SPH models for large-scale computing. This chapter aims at developing a MPI-based parallel SPH model. One of the essential procedures is domain decomposition consisting of geometrically subdividing computational domain into as many smaller subdomains as desired, and performing solutions in a processor corresponding to a subdomain. Using (Message Passing Interface) MPI data communications among processes, the SPH numerical results can be reconstructed on the whole domain.

5.2   Parallelization SPH Framework

Contrary to Eulerian grid-based methods, SPH is a Lagrange mesh-free method with particles. This specificity causes some problems: (i) The kernel interpolation is based on based neighbouring particles within support domain. The size of the support domain depends on the smoothing length. For a particle near the subdomain boundary, there is an interpolation truncation due to domain decomposition, and so it requires adjacent subdomains to allow particle-to-particle interactions. The particle searching process for a particle in one subdomain should include particles in neighbouring subdomains. (ii) The particles in one subdomain may move into another one, and so some strategies should be introduced to transfer particles. (iii) Load balance strategy. The transfer of particles between different processors may result in various numbers of particles per processor. Simulating a complex free-surface flow with

the SPH model usually results in irregularly distributed across the computational domain. Different numbers of particles lead to different computational costs for each processor. Load-unbalance affects parallel efficiency. Therefore, in the development of a parallel SPH framework, it needs to address several of these issues.

Domain Decomposition

Firstly, it needs to decompose the entire computational domain into several subdomains. Each subdomain corresponds to a core. Domain decomposition is achieved by using a fictitious background Cartesian grid. Here, it does not consider load balancing strategies, but rather focus on the completion of a parallel framework. Thus, the background grid is fixed in time during the entire simulation, as shown in Fig. 5.1. Each grid denotes a subdomain. K and M denote the number of grids in x and z directions of the whole simulation domain. The length and height of the whole domain are denoted by L_x and L_z, respectively. If the region decomposition is homogeneous over the entire computational domain, the size (l_x, l_z) of each grid can be determined by

$$(l_x, l_z) = \left(\frac{L_x}{K}, \frac{L_z}{M} \right). \tag{5.1}$$

The parallelisation of the background meshes is not straightforward. It needs to determine each mesh to prevent race conditions for the particle input process, i.e., multiple threads inputting the same particle at the same time. To overcome this issue, the subdomains should be marked and each of them shall correspond to a unique core. Here, the index sort method is used to get grid index $C_i(k,m)$ ($i = 0, 1, \cdots, N_c - 1$, $k = 0, 1, \cdots, K - 1$, $m = 0, 1, \cdots, M - 1$, $N_c = K * M$ is the total core numbers). The grid index $C(k,m)$ is computed as

$$C(k,m) = k * M + m. \tag{5.2}$$

Note that the index $C(k,m)$ of each sub-domain is unique. In the basic uniform grid, particle i with position $r_i = (x_i, z_i)$ is inserted into one spatial grid with coordinates $C(k,m)$. After determining the boundary for each sub-domain, it can find a unique corresponding grid C for every particle according to the position r_i. Based on the position of each particle and the position of the sub-domain boundary, the particles will be placed in different arrays. Thus, each array represents a set of particles in a sub-domain. Then, the numerical solution process for the particles belonging to different array can be implemented in different cores in parallel. Thus, with the above strategy, all particles are marked and assign them to the corresponding subdomains.
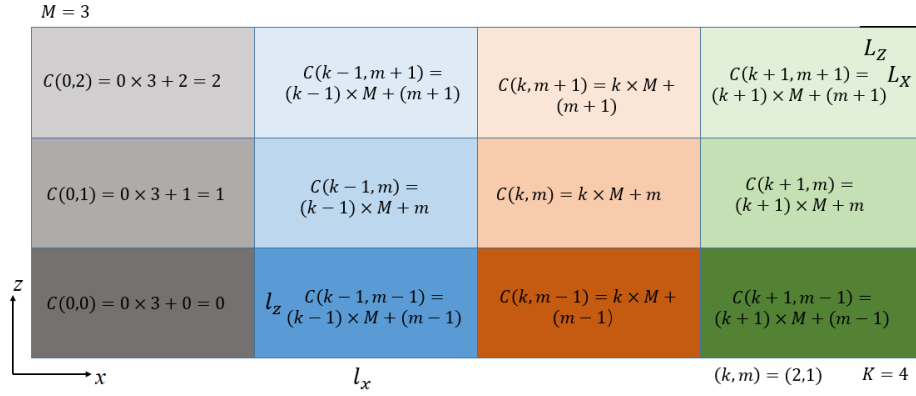
Fig. 5.1 Sketch of the 2-D domain decomposition and grid index list.

Message Passing

In the SPH method, the interpolation of a particle requires contributions from its neighbouring particles. Thus, a particle around the subdomain boundary requires message from particles in adjacent subdomains to ensure kernel support integrity. It needs to be identified: (i) lists of adjacent sub-domains and (ii) the particles in each sub-domain that need to be passed.

Lists of Adjacent Sub-domains

According to the domain decomposition method, a fixed regularly distributed background grid is used, and each grid has a unique sort index $C(k,m)$. Adjacent sub-domains for grid $C(k,m)$ represent all surrounding grids that are in contact with this grid, and their sort indexes are $C(k-1,m-1)$, $C(k-1,m)$, $C(k-1,m+1)$, $C(k,m-1)$, $C(k,m+1)$, $C(k+1,m-1)$, $C(k+1,m)$ and $C(k+1,m+1)$ for a grid $C(k,m)$. For some subdomains near the boundary of the entire computational domain, which are not fully surrounded by other subdomains, the rule should be adjusted accordingly. This strategy is entirely based on the grid index list. If the subdomain division does not change, then this list of adjacent grids applies to the entire calculation process.

Local neighbouring mesh list

In the SPH method, the search for the neighbouring particles is based on the mutual distance of the interpolation points (Ferrari et al., 2009). With the help of the background mesh, the links between particles and their neighbouring particles are locally constructed, which are used in the calculation, as shown in Fig. 5.2. The minimum side length of a mesh must equal the size of the support domain. Thus, there is a local neighbouring mesh list in each subdomain, which has the same sort index $\mathbf{C}(\mathbf{k},\mathbf{m})$ as introduced in the work of domain
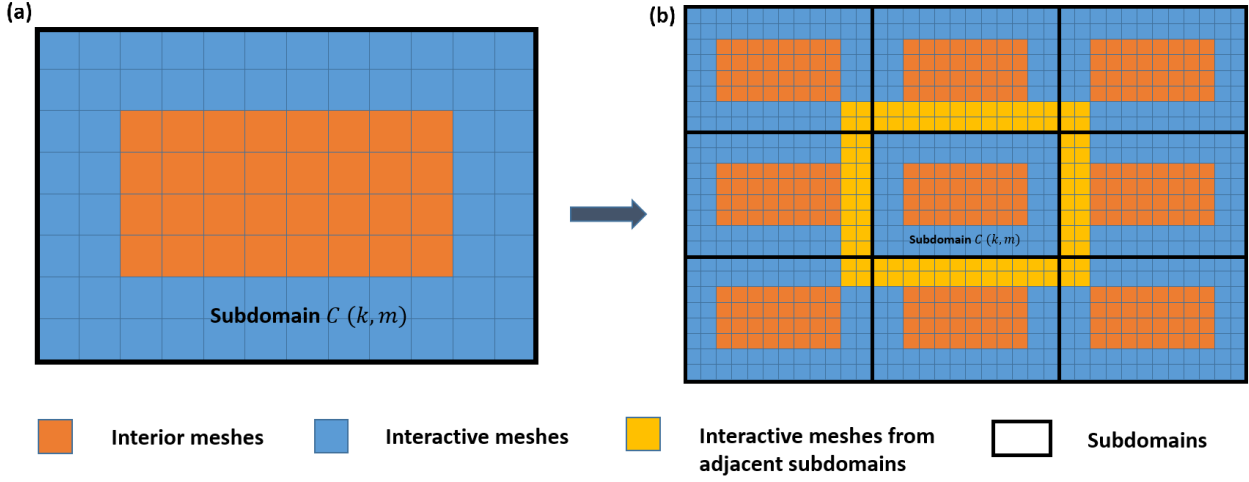
Fig. 5.2 Illustration of message passing. (a) Local neighbouring particle list, interior meshes and interactive meshes; (b) Interactive meshes message passing from adjacent sub-domains.

decomposition. The grid index $\mathbf{C}(\mathbf{k}, \mathbf{m})$ is computed as

$$\mathbf{C}(\mathbf{k}, \mathbf{m}) = \mathbf{k} * \mathbf{M} + \mathbf{m}, \tag{5.3}$$

where $\mathbf{k} = 0, 1, \cdots, \mathbf{K} - 1$, $\mathbf{m} = 0, 1, \cdots, \mathbf{M} - 1$. $\mathbf{k}$ and $\mathbf{m}$ denote the list numbers along x direction and z direction, respectively. $\mathbf{K}$ and $\mathbf{M}$ are the numbers of mesh along x direction and z direction, respectively. $\mathbf{K}$ and $\mathbf{M}$ can be calculated as

$$\mathbf{K} = \frac{L^x_{max} - L^x_{min}}{h}, \mathbf{M} = \frac{L^z_{max} - L^z_{min}}{h}, \tag{5.4}$$

where L^x_{max} and L^x_{min} denote the maximum and minimum position along x direction, respectively. L^z_{max} and L^z_{min} denote the maximum and minimum position along z direction, respectively. The local neighbouring mesh list can be used to search for neighbouring particles for kernel interpolation calculations. It also allows ready searching for particles that need to be passed in different sub-domains.

Interaction Particles

In SPH, the calculations are performed based on kernel function interpolation. A particle near the subdomain boundary requires the particle information from adjacent subdomains to solve the governing equation. However, the size of the support domain is determined by the kernel function. Therefore, message passing is only required for particles in the meshes besides subdomain boundaries. The meshes that do not have any interaction with

adjacent subdomains are named as 'interior meshes', and the meshes that influence adjacent subdomains are, called 'interactive meshes'. Each sub-domain needs to be divided by a small grid in order to perform particle searches. However, the sub-domain size is sometimes not exactly divided by the grid. This means that the local meshes of neighbouring sub-domains are not perfectly matched. Therefore, the two-layer mesh near the subdomain boundary needs to be considered. As the local neighbouring particle list, the interactive meshes as shown in Fig. 5.3 can be determined by

$$\mathbf{C}(\mathbf{k},\mathbf{m}) \begin{cases} \mathbf{k} < 2, \quad Left, \\ \mathbf{k} > (\mathbf{K}-3), \quad Right, \\ \mathbf{m} < 2, \quad Down, \\ \mathbf{m} > (\mathbf{M}-3), \quad Up, \end{cases} \in \text{Interactive meshes.} \qquad (5.5)$$

The interactive meshes are restricted to the vicinity of the boundaries of the four directions (left, right, down, up) of each sub-domain. As a result, this procedure dedicated to finding the interactive meshes should be completed just before the message passing. Then particles in the interactive meshes are interaction particles.

The algorithm of the message passing is shown in Algorithm 1. In line 2, p_i^z is interaction particles along z direction. In line 9, p_i^x is interaction particles along z direction.

According to the region decomposition strategy, any subdomain is a regular quadrilateral. All subdomain boundaries are uniquely determined. Particle information can be reloaded into a new core based on the particle's position. At same time, the particle information is deleted from the previous core. Thus, the transfer of particles among cores is carried out by the deletion and addition of particle information. Since the displacement of the particle at each time step is small relative to the subdomain size, the transfer of particles only takes place in adjacent subdomains, which further narrows the choice of new subdomains for particles.

5.3   Dynamic Load Balance

As a Lagrangian particle-based method, SPH particles could move from one processor to another processor. In some particular cases, particles will be present in large numbers in one processor and in small numbers in other processors. In the numerical calculation of SPH, the number of SPH particles is related to the calculation load. At the same time, the computational time spent on the whole calculation process depends on the processor with the longest computational time. The uneven distribution of computational effort between processors is called 'load imbalance'. One of the biggest problems with load imbalance is that it reduces the speed of computation. This is because when a processor with a small
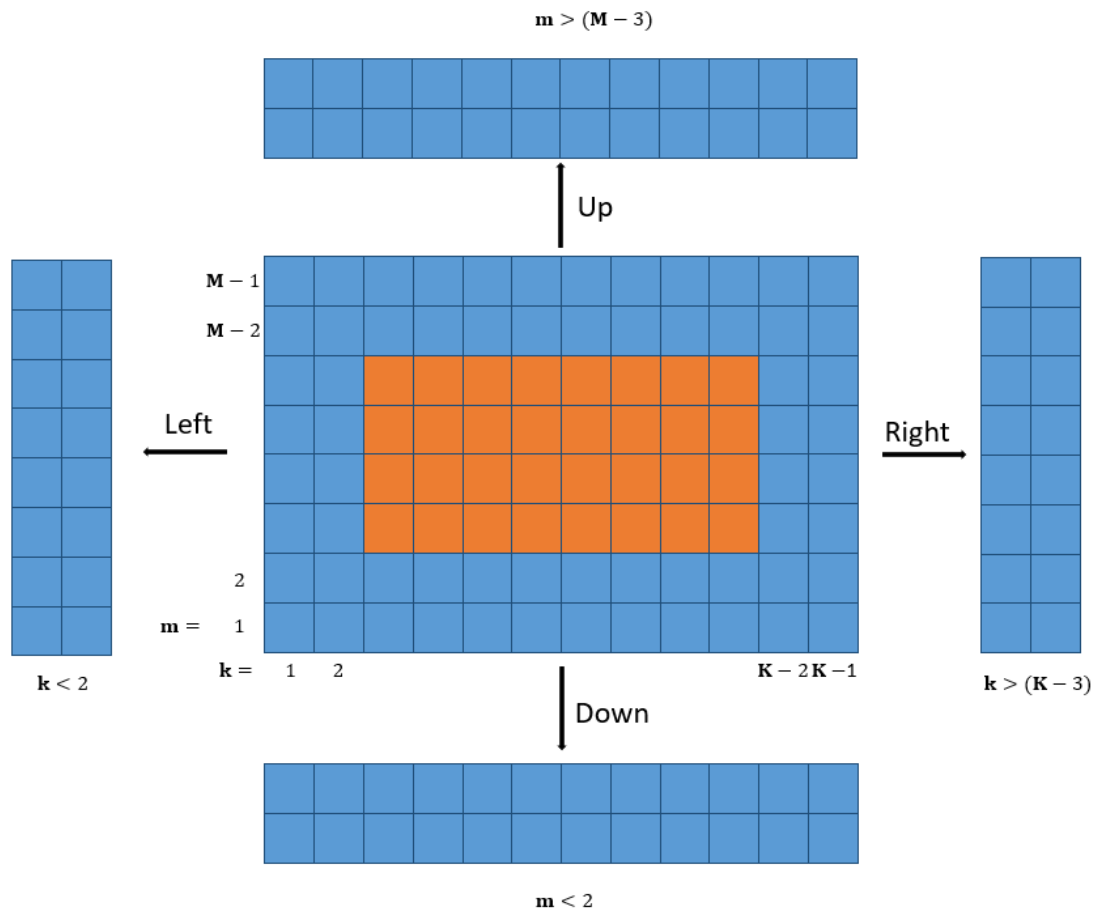
Fig. 5.3 Illustration of the interactive meshes.

Algorithm 1 Message passing

1: Initialization: determine position of the subdomain based on $C(k,m) = k * M + m$;
2: Determine interaction particles p_i^z along z direction ($\mathbf{m} < 2$ and $\mathbf{m} > (\mathbf{M} - 3)$) as Eq. (5.5);
3: **if m** > 0 **then**
4:    p_i^z is transferred to $\mathbf{C}(\mathbf{m}, \mathbf{m} - 1)$;
5: **end if**
6: **if m** $< (\mathbf{M} - 1)$ **then**
7:    p_i^z is transferred to $\mathbf{C}(\mathbf{m}, \mathbf{m} + 1)$;
8: **end if**
9: Determine interaction particles p_i^x along x direction ($\mathbf{k} < 2$ and $\mathbf{k} > (\mathbf{K} - 3)$) as Eq. (5.5);

10: **if k** > 0 **then**
11:    p_i^x is transferred to $\mathbf{C}(\mathbf{k} - 1, \mathbf{m})$;
12:    **for m** $= 0, \mathbf{M} - 1$ **do**
13:       Determine whether p_i^x is within the boundary of $\mathbf{C}(\mathbf{k} - 1, \mathbf{m})$;
14:    **end for**
15: **end if**
16: **if k** $< (\mathbf{K} - 1)$ **then**
17:    p_i^z is transferred to $\mathbf{C}(\mathbf{k} + 1, \mathbf{m})$;
18:    **for m** $= 0, \mathbf{M} - 1$ **do**
19:       Determine whether p_i^x is within the boundary of $\mathbf{C}(\mathbf{k} + 1, \mathbf{m})$;
20:    **end for**
21: **end if**

---

number of particles has completed calculation, it needs to wait for a processor with a larger load to complete the computation before it can start the next time step. Therefore, it needs to specify special methods to ensure that each processor is loaded equally at each time step in order to maximise the efficiency of parallelism.

Computation Load

Computation Particle Numbers

The distribution of the number of particles has a direct relationship to the computational loading. Thus, the measurement of the calculation load in each core is translated into a measurement of the number of particles. The load balancing problem is converted into a geometric problem, i.e. the number of particles in each region is guaranteed to be balanced by geometric division. Computational load balance strategies based on the number of particles are widely considered in published works (Ferrari et al., 2009; Ihmsen et al., 2011; Cherfils et al., 2012; Oger et al., 2016; Guo et al., 2018). In these works, the entire computational domain is discretized into regular meshes. The meshes are grouped into subdomains by means of space-filling curves or division methods. The load balance of the subdomains is balanced taking into account the number of particles in these meshes.

In the present SPH model, the calculation particle numbers N_{cn} can be calculated as

$$L = N_{cn} = N_f + N_w + N_{in} + N_{ip}, \tag{5.6}$$

where N_f, N_w, N_{in}, and N_{ip} are the numbers of fluid particles, wall particles, interpolation nodes, and interaction particles from other processors. L denotes computation load.

However, there are several problems with the division based on calculating the number of particles. Firstly, the computational cost of various nodes/particles is inconsistent. For example, fixed ghost particles need an additional cost to determine their physical quantities. Thus, fluid particles near walls and fixed ghost particles require more computational effort. In addition, the correlation between the calculation load and the number of particles decreases if there are severe inhomogeneous distributions in the subdomains such as fragmentation, splashes, complex interface, etc. In the case of irregular distribution, the support domain of an particle is not fully filled with neighbouring particles. Even if the number of particles is the same, it does not mean that the number of particle pairs is the same. A parallel strategy based on computation particle numbers cannot guarantee a consistent computational cost in each core.

Running Time

At each time step, the parallel SPH code is divided into two main parts: MPI communication and SPH solver. MPI communication represents the transfer of particle data between different cores. The SPH solver represents the numerical solution of the SPH model, including neighbouring particle search, boundary conditions and solution of the Navier-Stokes equation. The load balance needs to take into account all of these components to achieve perfect results. However, in the current SPH code, $MPI - Send$ and $MPI - Recv$ are used for point-to-point communication. Communication load is not only affected by the number of transfer particles, but also communication blocks, which make it difficult to take into account the load balance of MPI communication for large-scale MPI parallel problems.

A more simple and reliable way to evaluate computational loading is to use running time. The main purpose of dynamic load balance is to improve parallel efficiency, i.e., to ensure that the computation time cost is consistent in each core. Running time based load balance ignores the complexity of the SPH process (code) and directly considers the primary purpose of load balance strategy. Moreover, the variability of core performance is already implicitly included. In 2013, Domínguez et al. (2013) carried out an investigation into the particle numbers and computation time-based balancing schemes in the context of multi-GPU (multi-node with MPI). The results show that a time-based loading balancing scheme has better computational efficiency than a balancing scheme based on the number of particles. The calculation load L can be calculated as

$$L = t_S, \tag{5.7}$$

where t_S denotes the time cost for SPH process (not including communication cost) in each core. The greater the time consumption, the more the computational load. However, the time cost of each code is required before implementing the dynamic load balancing strategy. The update of particle position is small due to small SPH time step. Thus, the information about the time cost of each core at the previous time step can be used as a computational load distribution to optimise sub-domain partitioning

$$L^n = t_S^{n-1}, \tag{5.8}$$

where L^n is the computational load at n^{th} time step. t_S^{n-1} is the time cost at $n^{th} - 1$ time step. The message of subdomain division at previous time is also recorded as a reference.

Subdomain Update
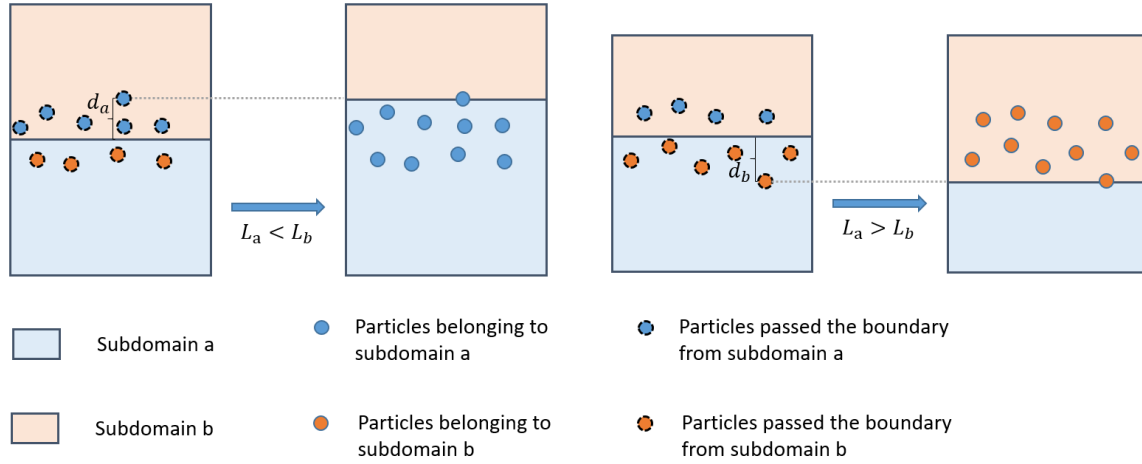
Fig. 5.4 Illustration of dynamic load balance strategy along *y* direction.

In some previously published studies (Ferrari et al., 2009; Ihmsen et al., 2011; Guo et al., 2018), the entire computational domain was divided into small grids. These small grids are then searched using space-filling curves. The combination of small meshes along the space-filling curve can achieve load balance. However, this approach would result in a completely new subdomain division, which cannot refer to the SPH time of the previous time step when considering the SPH time balance. In the present parallel strategy, the computational domain has been delineated as regular subdomains and marked by grid index list. Therefore, to achieve dynamic loading balance, subdomains are updated by changing the subdomain boundaries (size). This leads to the adjustment of its neighbouring subdomain boundaries, to ensure subdomains have no overlapping parts.

At each time step, many particles flow into and out of the subdomain. The inflow and outflow of particles at the boundary of a subdomain are shown in Fig. 5.4. The calculation loads are L_a and L_b for subdomain a and b, respectively. The change of boundary requires the determination of a reference position. For this purpose, the position of the particle furthest from the boundary is regarded as the reference position. The positions of the inflow and outflow particles furthest from the subdomain boundary are denoted as d_a and d_b, respectively. However, there is no inflow and outflow particle along subdomain boundary sometimes, a particle spacing is used as a reference position. When $L_a > L_b$, the boundary along the y-axis direction should be shifted inside the subdomain a to d_a in order to reduce the size of the subdomain A to ensure there is a load balance between subdomains a and b. When $L_a < L_b$, the boundary should be moved inside the subdomain b to d_b in order to decrease calculation loads in subdomain b. The change in boundaries causes the division of subdomains to become irregular. To be able to continue using the grid index list, the subdomains of the same column
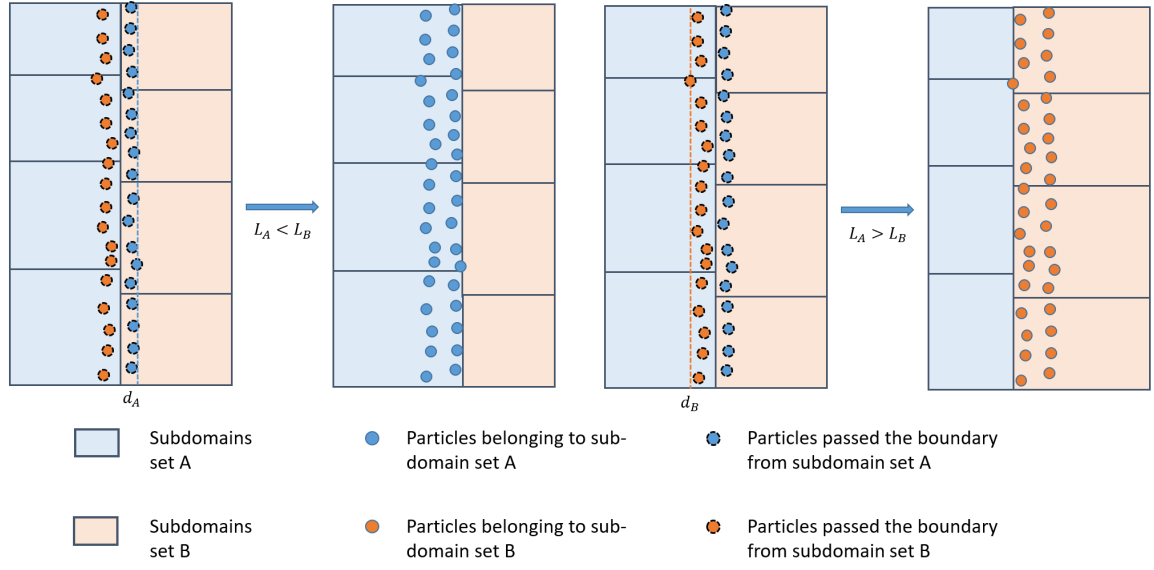
Fig. 5.5 Illustration of dynamic load balance strategy along x direction.

have the same boundaries along the x-axis. When considering changes in the boundaries of subdomains along the x-axis, consider all subdomains in the same column are regarded as a whole, called set A and B as shown in Fig. 5.5. The rules of sub-domain boundaries along x-axis direction are the same as the those along y-axis direction, as shown in Fig. 5.5. Total calculation particle numbers in set A and B are considered as the computation load for the balance strategy based on calculation particle numbers. While the maximum SPH time in set A and B is used as computation load for load balance strategy based on running time. The algorithm of the Subdomain update is shown in Algorithm 2. In line 9, $L_{C(k,0)}$ and $L_{C(k+1,0)}$ are the computational load at subdomain $C(k,0)$ and $C(k+1,0)$, respectively. In line 13, 'set $k-1$, k and $k+1$' are the subdomain set $k-1$, k and $k+1$. In line 16, p_i^x is interaction particles along z direction. In line 16, $L_{C(k,m)}$ and $L_{C(k,m+1)}$ are the computational load at subdomain $C(k,m)$ and $C(k,m+1)$, respectively.

Once the new sub-domain boundaries are obtained, the particles need to be updated to the corresponding sub-domains. The algorithm of the Update particles to new cores is shown in Algorithm 3. In line 3, p_t^z is interaction particles along z direction. In line 11, p_t^x is interaction particles along z direction.

To achieve load balance of the system, an accurate evaluation of load is important. Evaluation of the load situation allows the determination of whether to implement the dynamic load balancing strategy. An imbalance monitoring tag is defined as

$$E_{i,max} = \frac{L_S^{max} - L_S^{min}}{L_S^{avg}} < e_d, \tag{5.9}$$

Algorithm 2 Subdomain update

1: Initialization: determine position of the subdomain based on $C(k,m) = k*M+m$;
2: Determine the calculation load and communicate globally;
3: Transfer all information of load L to the first processor of a subdomain set and maximum value is selected to be the load for the whole column;
4: **if** $m > 0$ **then**
5:    L of $C(k,m)$ is transferred to $C(k,0)$;
6: **end if**
7: Compare local computational load along x direction;
8: **if** $k < (K-1)$ **then**
9:    **if** $L_{C(k,0)} < L_{C(k+1,0)}$ **then**
10:       Subdomain boundary is shifted as shown in Fig. 5.5;
11:    **end if**
12: **end if**
13: Message of update subdomain boundary is transferred to subdomain at the set $k-1$, k and $k+1$;
14: Update subdomain boundaries along z direction;
15: **if** $m < (m-1)$ **then**
16:    **if** $L_{C(k,m)} < L_{C(k,m+1)}$ **then**
17:       Subdomain boundary is shifted as shown in Fig. 5.4;
18:    **end if**
19: **end if**
20: the message of update subdomain boundary is transferred to subdomain at the set $k-1$, k and $k+1$;

Algorithm 3 Update particles to new cores

1: Initialization: determine position of the subdomain based on $C(k,m) = k*M + m$;
2: Update particles to new cores along z direction;
3: Determine particles p_t^z needed to be transfer along z direction;
4: **if** $m > 0$ **then**
5:     p_t^z is transferred to $C(k, m-1)$;
6: **end if**
7: **if** $m < (M-1)$ **then**
8:     p_t^z is transferred to $C(k, m+1)$;
9: **end if**
10: Update particles to new cores along x direction;
11: Determine particles p_t^x needed to be transfer along x direction;
12: **if** $k > 0$ **then**
13:     p_t^x is transferred to $C(k-1, m)$;
14:     **for** $m = 0, M-1$ **do**
15:        Determine whether p_t^x is within the boundary of $C(k-1, m)$;
16:     **end for**
17: **end if**
18: **if** $k < (K-1)$ **then**
19:     p_t^x is transferred to $C(k+1, m)$;
20:     **for** $m = 0, M-1$ **do**
21:        Determine whether p_t^x is within the boundary of $C(k+1, m)$;
22:     **end for**
23: **end if**

---

where $E_{i,max}$ is max error for all cores, e_d is user defined error tolerance. L_S^{max}, L_S^{min}, and L_S^{avg} denote max, min, and average calculation load for all cores. Once max error $E_{i,max}$ is greater than the set value, the dynamic load balancing strategy can be implemented. The imbalance monitoring tag has been used by many other researchers (Oger et al., 2016; Guo et al., 2018; Ji et al., 2019) in SPH.

In addition, this criterion also applies to the local load balance distribution E_i as following

$$E_i = \frac{L_a - L_b}{L_a} < e_d, \tag{5.10}$$

This means that the load balance between local cores is not simultaneous, but depends on the local load balance distribution.

It takes some time to obtain load balance for initially unstable fluid problems. Thus, an initial load balance strategy is developed to maintain the initial homogeneous load balance. Initially, the entire computational domain is divided evenly. The subdomain boundary positions are then updated according to calculation loads. This approach is the same as the dynamic loading balance strategy described above. The subdomain boundaries are continuously adjusted until the conditions are met Eq. 5.9. The maximum number of iterations (Number of adjustments) to 1000, and the physical information of the particles is not updated in the initial homogeneous load balance. This initialisation of the subdomains was previously investigated by parallelSPHysics (Rogers et al., 2011). The current model extends it to two dimensions (x, z directions). Movement of subdomain boundaries may lead to overlapping subdomain boundaries (subdomain disappearance). To prevent this from happening, the distance between subdomain boundaries is limited to be greater than the supporting domain

A detailed flowchart of the developed framework is presented in Fig 5.6 to summarize all the algorithms. The code is written in FORTRAN using open source libraries OpenMPI. If not specifically stated, studies in this work are conducted on the Fotcluster2 in High Performance Computer Centre in University of Plymouth. Fotcluster2 is a 752 core distributed-memory cluster, which is comprised of: a 3U combined head & storage node, plus 56 compute nodes. The tests are conducted on the phase2 consisting of 36 Viglen $HX425T^2i$ HPC 2U Compute Nodes, equipped with Dual Intel Xeon E5650 (Westmere) Six Core 2.66GHz processors and 12 GB of memory per motherboard.
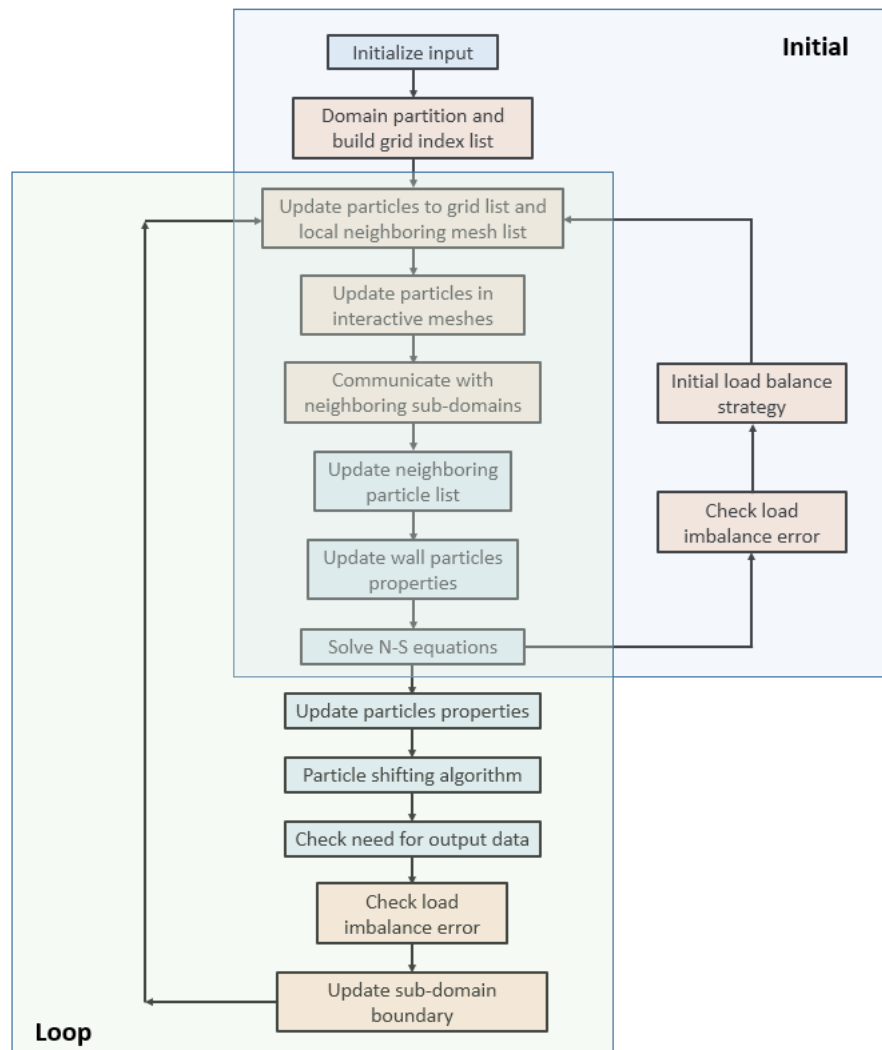
Fig. 5.6 Flowchart of SPH parallel framework.
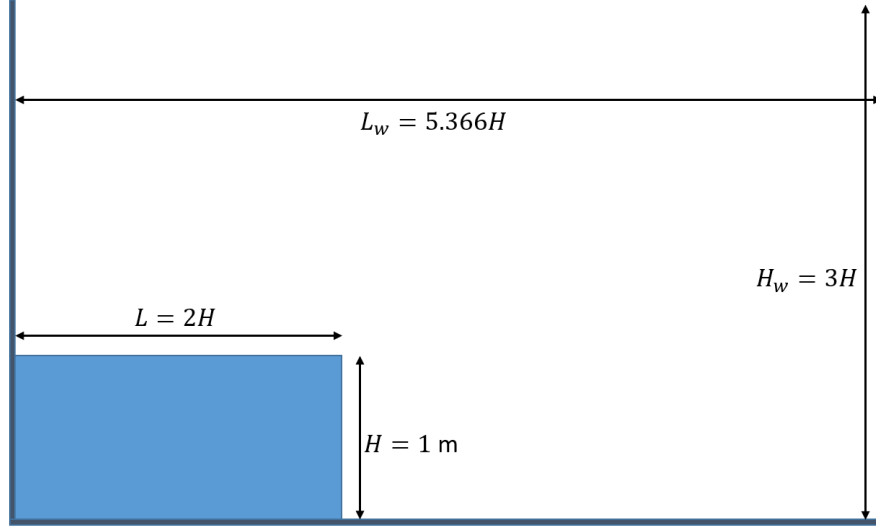
Fig. 5.7 Sketch for two-dimensional dam break problem.

5.4   Numerical Performance Analysis

Dam Breaking

Dam breaking is widely investigated in the SPH literature, since this case shows the ability of SPH models to deal with large deformation problems. The deformation of the water phase can be used to validate the dynamic load balance strategy. Fig 5.7 shows a sketch of the initial setup, where the reservoir height is $H = 1.0$ m, length and height of the tank are $d = 5.366H$ and $D = 3.0H$. Initial particle spacing is 0.01 m, and 20,000 fluid particles are used. Time step is 0.0005 s, and numerical sound speed is $c_0 = 10\sqrt{gH}$. A total of 12 cores, 6 cores along the x-direction and 2 cores along the y-direction, are used. Four tests are employed here for a comprehensive assessment of the performance: (a) dynamic load balance strategy based on calculation particle number, fluid domain uniformly divided at the beginning; (b) dynamic load balance strategy based on calculation particle number with initial homogeneous load balance; (c) dynamic load balance strategy based on running time, fluid domain uniformly divided at the beginning; (d) dynamic load balance strategy based on running time with initial homogeneous load balance. $e_{i,max}$ is 0 for all these four cases.

Fig 5.8 compares the division of the computational domain for test (a), (b), (c), and (d) at $t = 0$ s , 1 s , and 1.9 s. Although the initial divisions are the same for tests (a) and (c), the division of subdomains showed some differences at 1.0 s and 1.9 s because of different load balance strategies. Although tests (a) and (b) ((c) and (d)) use the same load balance strategy,

there are still some differences between the divisions at 1.0 s and 1.9 s due to the different divisions initially.

Fig 5.9 shows the time series of calculation particle numbers $Ntol$ in each core for tests (a), (b), (c), and (d). Tests (a) and (b) show small oscillations around the mean value generally after $t = 4.0$ s. Although tests (c) and (d) show relatively stable changes after $t = 4.0$ s, the stability interval for N_{cn} in each core is not consistent. The changes of N_{cn} in tests (b) and (d) are relatively stable compared to tests (a) and (c) in the beginning, respectively. Note that, the dynamic load balance strategy based on the calculation particle numbers N_{cn} ensures that calculation particle number in each core is balanced.

Fig 5.10 shows the time series of SPH time T_s in each core for tests (a), (b), (c), and (d). Although N_{cn} in tests (a) and (b) reach the steady state after $t = 4.0$ s, the stability interval for T_s varies in each core. Moreover, the difference between the maximum (about 0.031 s) and minimum (about 0.021 s) running times is approximately 0.01 s. In comparison, the running time for tests (c) and (d) are stable around 0.025 s after $t = 4.0$ s. The time spent for a time step depends on the core that consumes the longest amount of time. Obviously, the time consumption of a time step for a loaded balancing strategy based on the number of particles computed is greater than that of a balancing strategy based on the running time after $t = 4.0$ s. Furthermore, the initial load balancing strategy ensures that the running time is relatively balanced at the start of the calculation.

Sharp changes in calculation particle numbers N_{cn} and running time T_s are observed before $t = 4.0$ s. It can be seen that the use of load balancing strategies does not instantly result in perfect load balancing when loading is most unbalanced. The update of the subdomain boundaries is based on the gradual adjustment of the particle position changes. Nevertheless, the load balance strategy avoids an exacerbation of the load unbalance condition. The load balance strategy guarantees almost perfect balance at each time step, in terms of the both running time or the number of calculated particles after $t = 4.0$ s.

Wall particles and particles close to walls, require additional computational tasks to impose wall conditions. In addition, the number of wall particles also affects the number of particle pairs. The number of wall particles is shown here to explain the difference in computation time due to inconsistent particle types, even though the number of particles is the same. Fig 5.11 shows the time series of wall particles in each core for tests (a), (b), (c), and (d). The colours of the core time histories correspond to those of the domain decomposition presented in Fig. 5.8. Cores 2 and 4 are associated to the upper left and upper right subdomains, respectively, of the computational domain. Wall particles are not balanced in tests (a) and (b), even for the load balance strategy based on calculation particle numbers used in these two cases. Notice that, for all four cases the distribution of wall particles ends
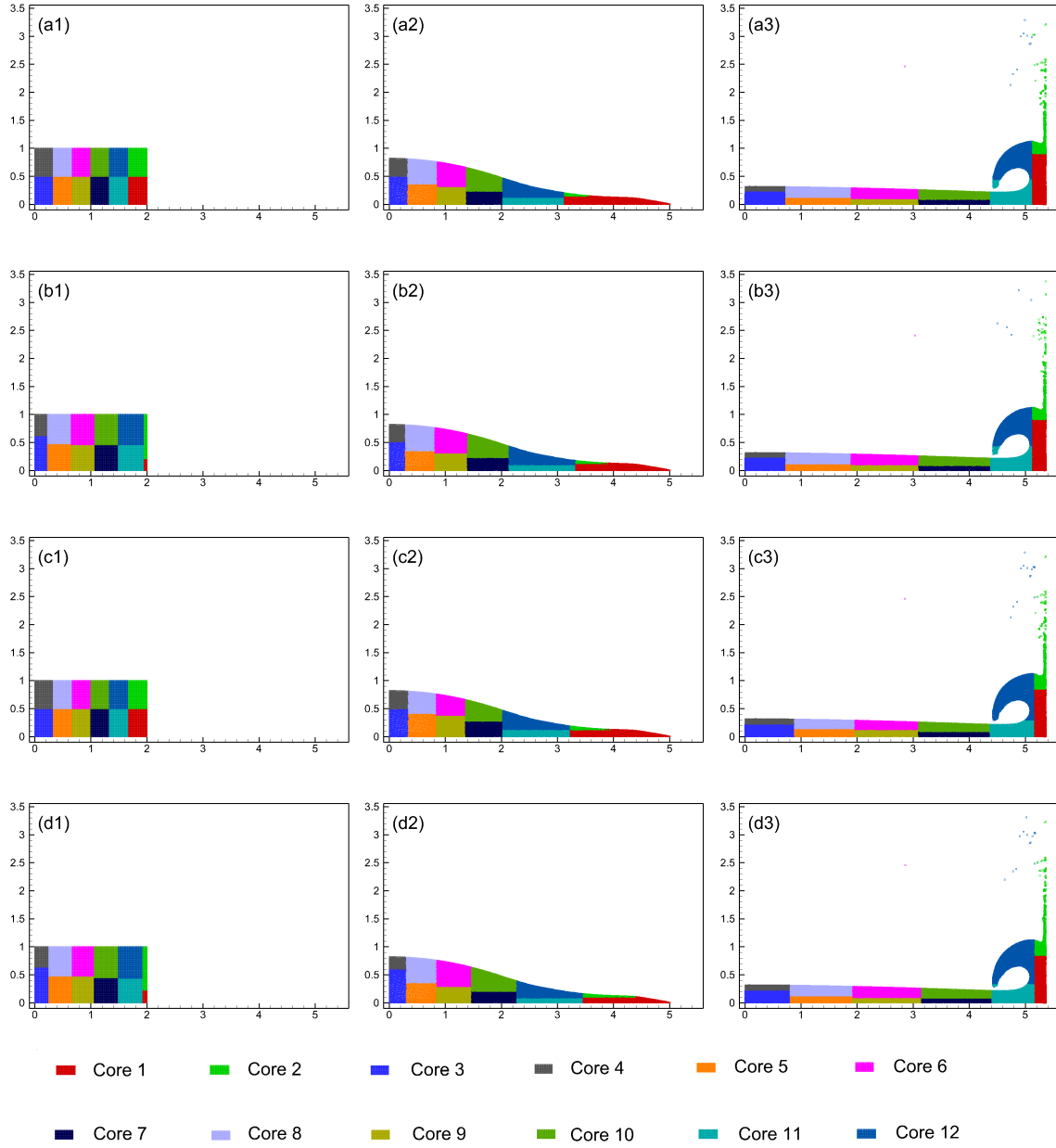
Fig. 5.8 Domain decomposition for test (a), (b), (c), and (d) at $t = 0$ s, 1.0 s, and 1.9 s. (Label '1', '2', and '3' denote $t = 0$ s, 1.0 s, and 1.9 s, respectively). Each subdomain is shown in a different color.
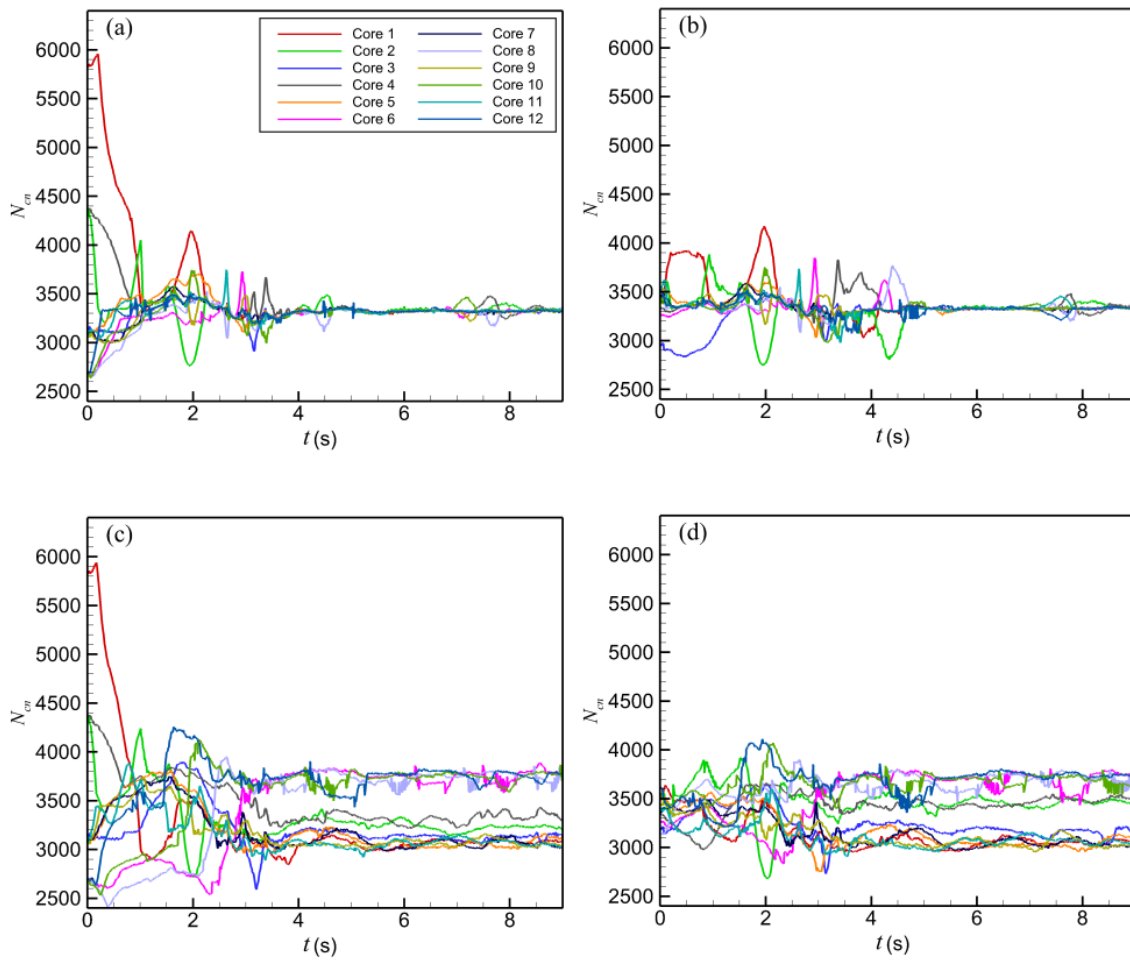
Fig. 5.9 History of calculation particle numbers N_{cn}.(Label 'a', 'b', 'c' and 'd' denote tests (a), (b), (c), and (d), respectively).
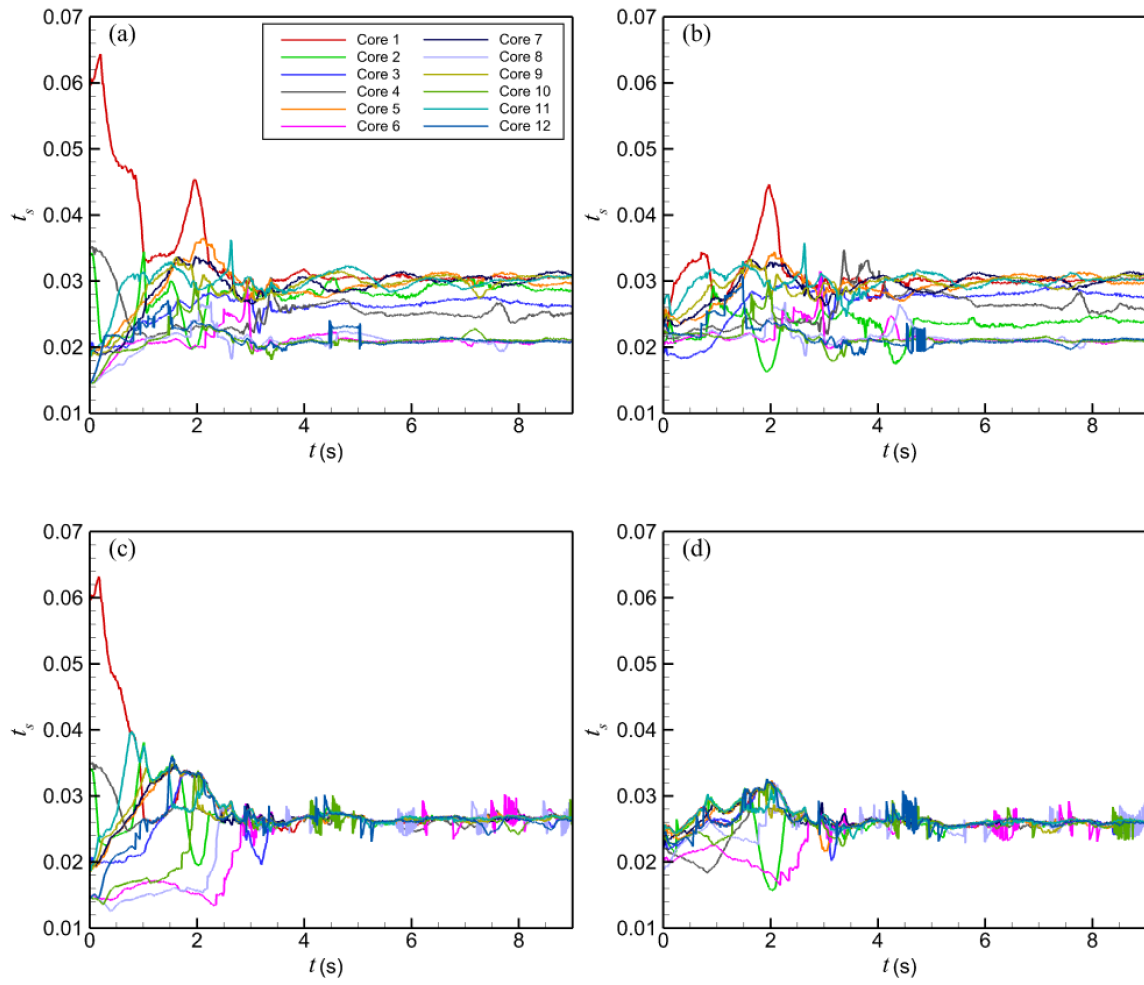
Fig. 5.10 History of running time t_s in each core.(Label 'a', 'b', 'c' and 'd' denote tests (a), (b), (c), and (d), respectively).
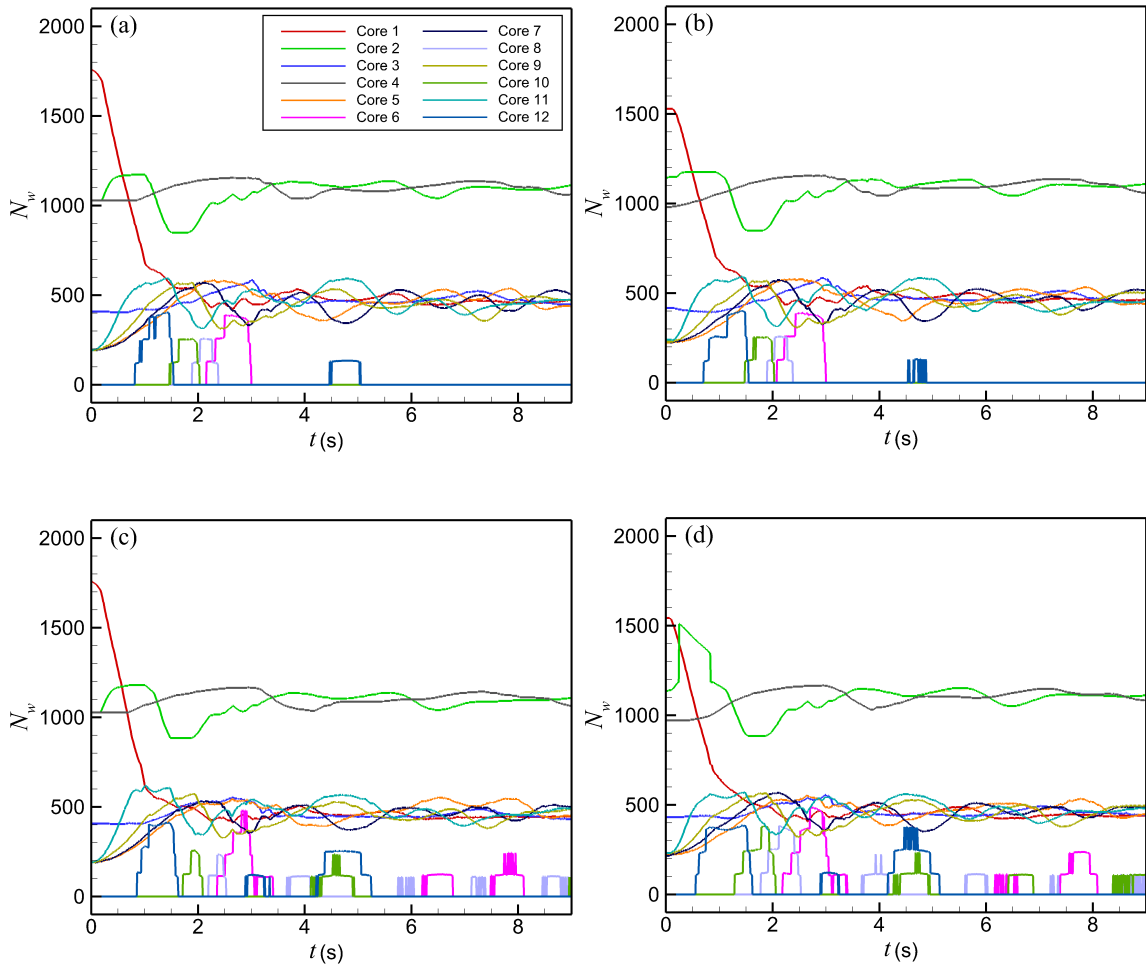
Fig. 5.11 History of wall particle numbers N_w in each core. (Label 'a', 'b', 'c' and 'd' denote tests (a), (b), (c), and (d), respectively).
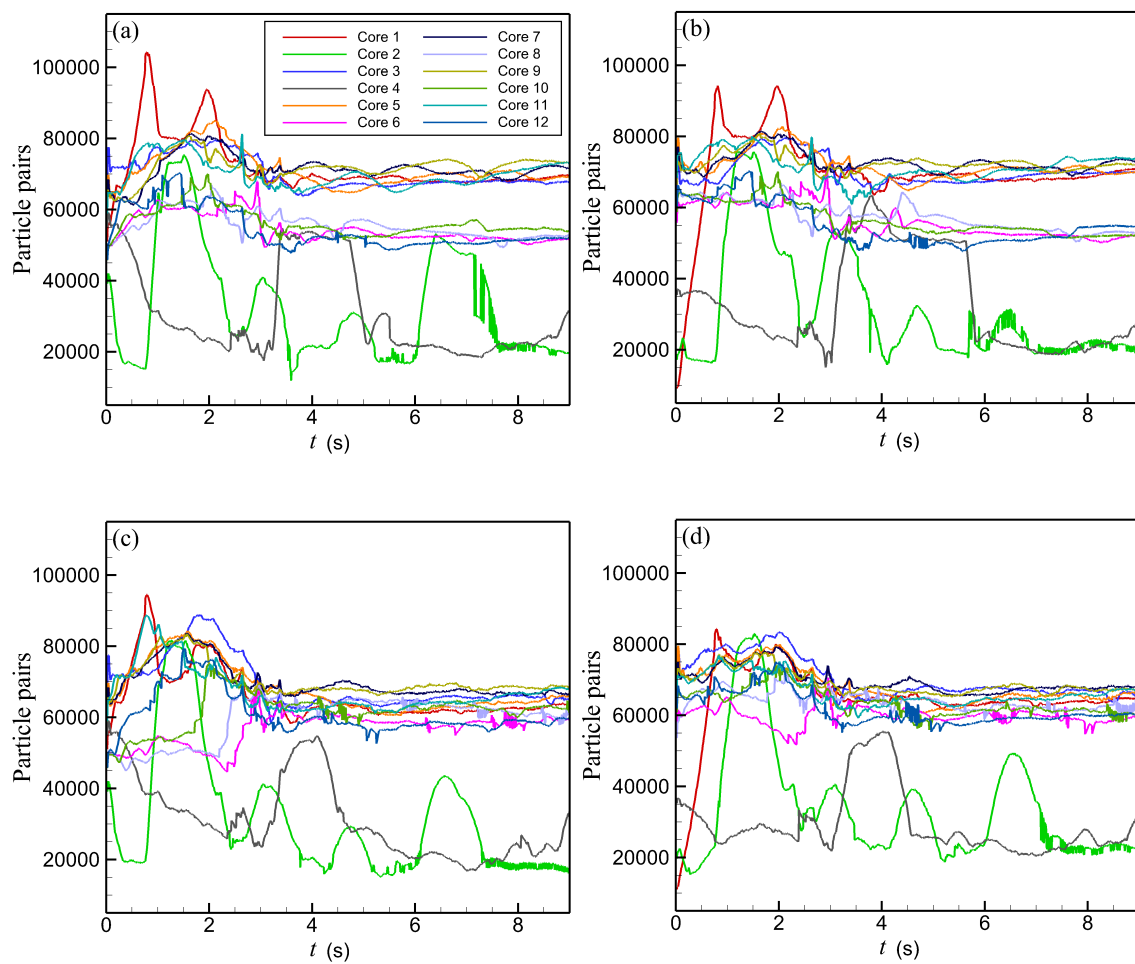
Fig. 5.12 History of the number of particle pairs in each core. (Label 'a', 'b', 'c' and 'd' denote tests (a), (b), (c), and (d), respectively).

Table 5.1 SPH setup and computational time

Test	Fluid particle number	Time step (s)	Number of Cores	Physical time (s)	Wall time (s)
(a)	20000	0.0005	12	9	1836.33
(b)	20000	0.0005	12	9	1784.83
(c)	20000	0.0005	12	9	1646.83
(d)	20000	0.0005	12	9	1549.16

up in three similar states: cores 2 and 4 are stable around 1000 wall particles, cores 1, 3, 5, 7, 9, and 11 have a stable number of wall particles around 400, whereas cores 6, 8, 10, and 12 have a stable number of wall particles around 0. Although cores 2 and 4 have maximum fixed ghost particles due to vertical walls, they have the smallest number of particle pairs as shown in Fig 5.12. This is because a switch for the wall particle calculation is set (Bouscasse et al., 2013), i.e., the wall particles are not involved in the calculation when there are no fluid particles nearby. Considering the consistent calculation particle numbers, the number of particle pairs decreases substantially when a large number of wall particles are not involved in the computation for cores 2 and 4.

In a time step, the SPH time can be divided into two main parts: the time of neighbouring particle search T_{se} and the solution of the N-S equation T_{ns}, as shown in Fig 5.13 and Fig 5.14, respectively. Comparing Fig 5.12 and Fig 5.13, the number of particle pairs shows a correlation with the time of neighbouring particle search T_{se}. Although the number of particle pairs and the particle search time T_{se} are lower for cores 2 and 4, the time spent in solving the N-S equation T_{ns} does not show such a large difference. The reason for this may be that the wall particles and the fluid particles near the wall particles require an additional computational effort to account for the boundary conditions. Table 5.1 shows the time cost in these four cases. The load balance strategy based on running time can improve computational efficiency more, compared to the one based on calculation particle numbers. For example, test (d) is 15.2% more efficient than test (b). Although the initial load balancing strategy requires extra computational effort at the initial moment, the overall computational cost is effectively reduced.

The dam break then is extended to be simulated with 1 million fluid particles (Initial particle spacing is 0.002 m) to test the performance of present model at a scale of the hundreds of cores and millions of particles. A total of 200 cores, 40 cores along the x-direction, 5 cores along the y-direction, are used. The time step is 0.0001 s. This case uses the proposed dynamic load balance strategy based on running time with initial homogeneous load balance. The physical time was 9 s, taking a total of 9.5 hours to complete the calculation. Fig 5.15 shows the subdomain snapshots at six moments. The complex free surface can be observed
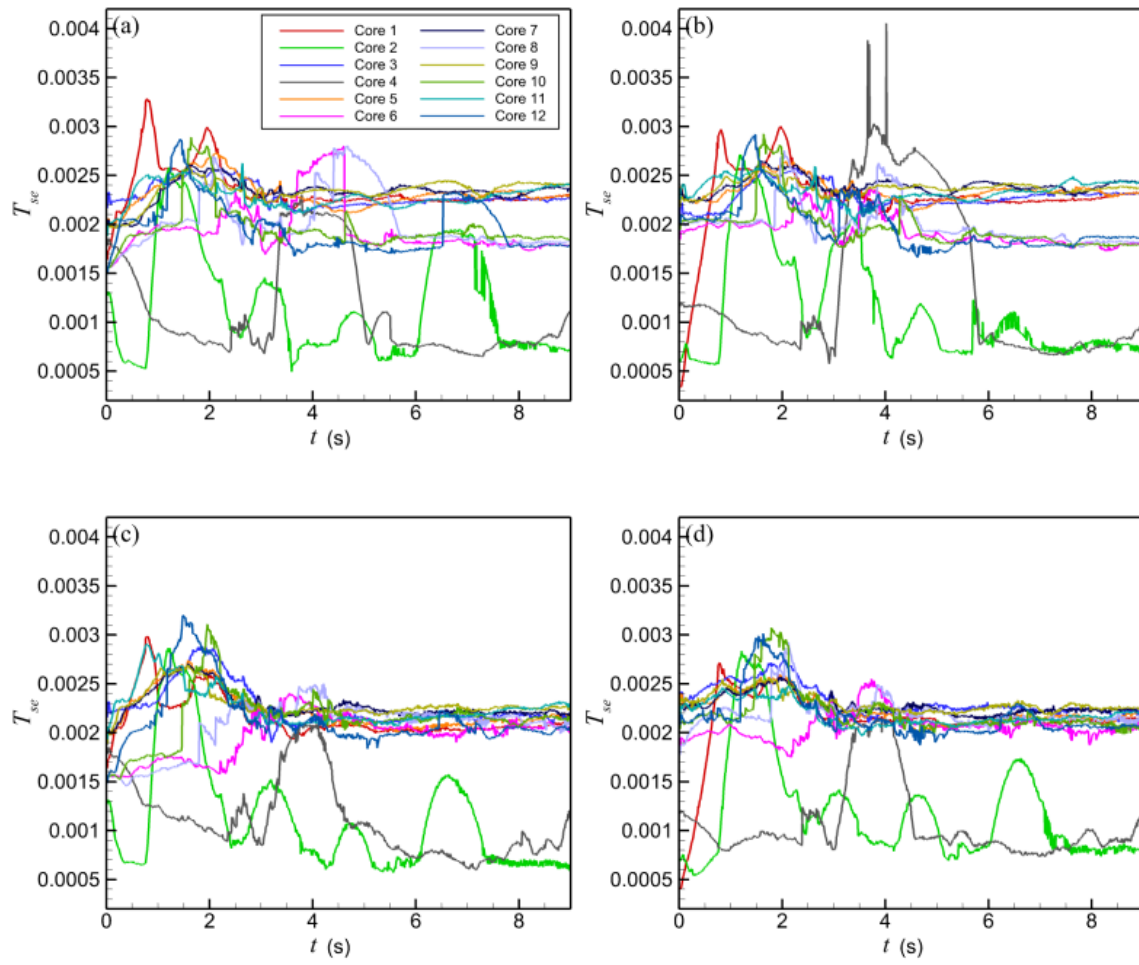
Fig. 5.13 History of running time at each time step for neighbouring particle search T_{se}. (Label 'a', 'b', 'c' and 'd' denote tests (a), (b), (c), and (d), respectively).
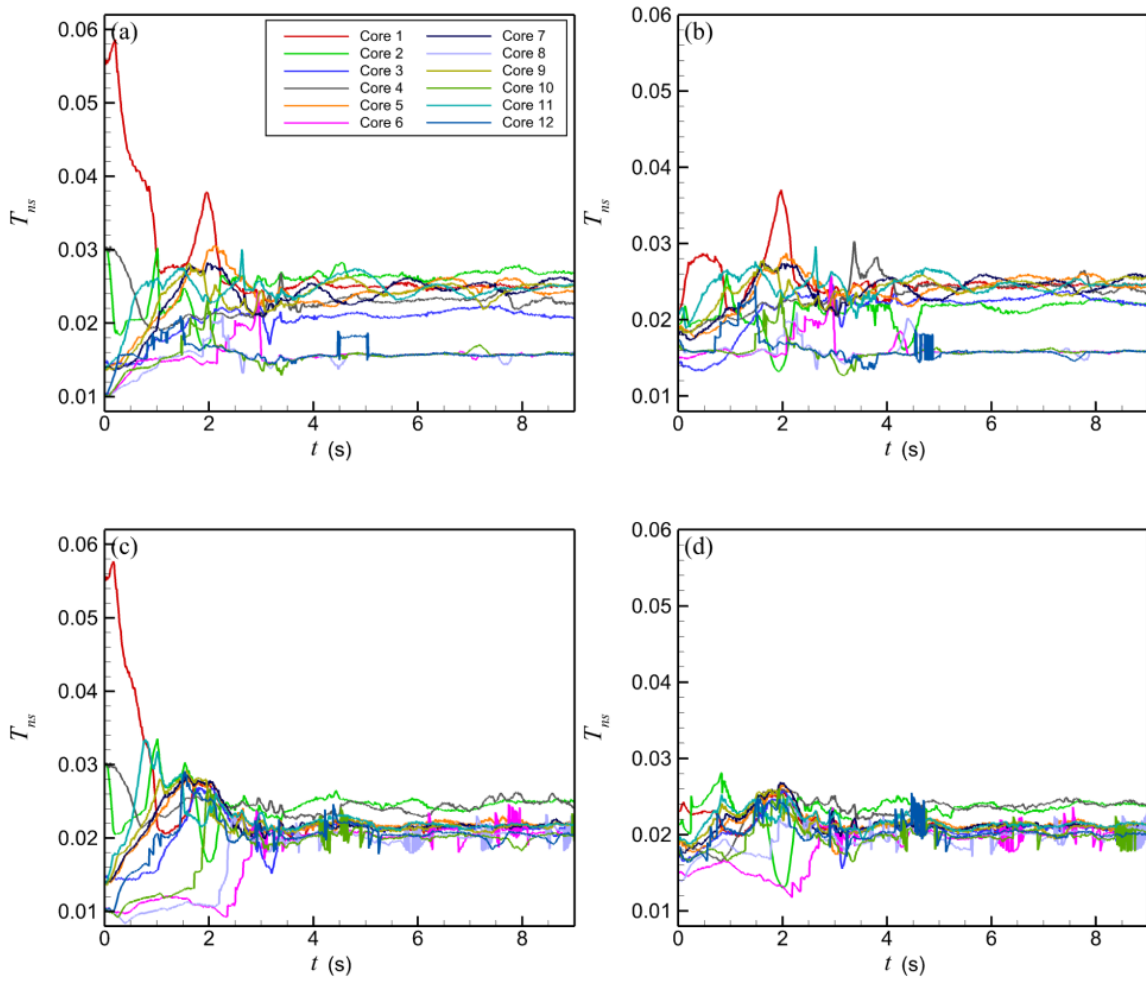
Fig. 5.14 History of running time at each time step for the solution of the N-S equation T_{ns}. (Label 'a', 'b', 'c' and 'd' denote tests (a), (b), (c), and (d), respectively).

at 2.5 s, where the upwardly deflected fluid then falls violently onto the wet deck under the recovering action of gravity producing a large splash at 3.0 s. Eventually, it reaches a relatively stable state at 9 s, i.e., no strong slamming with large splashes occuring. The complex free surface is divided into 200 non-overlapping sub-domains by regular small rectangles. Fig 5.16 shows the heat map, where The *y*-axis represents the number of cores and the *x*-axis represents physical time, colour indicates SPH time. An imbalance in running time can be observed until 3 s. After 3 s, the SPH time is fairly even across the 200 cores. In particular, the balancing running time at 3.5 s corresponds to Fig 5.15, showing the performance of the current parallel model with dynamic load balancing. A good dynamic load balancing should ensure that the time spent by each processor is consistent during runtime, e.g., see Figure 5.16, which shows the time heat map of the 2D wet bed dam breaking test (Guo et al., 2018). It shows that within 7000 time steps, the time spent by each processor is almost the same. The current model uses a simple geometry (rectangle) to divide the complex free surface flow. The adjustment of each sub-domain affects the surrounding sub-domains. At the same time, the adjustment of one sub-domain is limited by the surrounding sub-domains. The parallel strategy at each time step takes into account the results of the previous time step and is only adjusted once. This means that the adjustment at each time step is limited. Before 3 seconds, the fluid flow slammed against the right wall producing a rolled flow situation. For such a rapidly deforming free surface flow, the current model may not be able to achieve loading balance. By adjusting the dynamic load balancing strategy, it is possible to adjust the boundaries iteratively to alleviate this problem.

Fig 5.18 shows the time series of the water front. The agreement with the reference solution demonstrates the accuracy of the parallel model.

Wave Structure Simulation

Physical experiments of a focused wave group interacting with a truncated vertical wall are modelled in this section (Mai et al., 2015; Hu et al., 2017). The wave flume is 35 m long, 0.6 m wide in cross-section, 1.2 m high and operates at a still water depth of 0.7 m. The plate is 26.9m from the wave maker and submerged to a depth of 0.15m. An incident wave set (focused wave) was used in the experiment. A theoretical focus time is 42 s and a theoretical focus position is at 31.90m. The values of still water level, position of the plate and wave condition were set in general agreement with the experiment as shown in Fig 5.19. In particular, the plates are fixed during the experiment. The numerical flume length is 36 m. A sponge layer located between 31 m and 36 m is used to absorb the wave to prevent wave reflection. The free surface level is measured at 26.885 m from the wave maker for comparison with the experimental data. The convergence of the wave simulations in Section
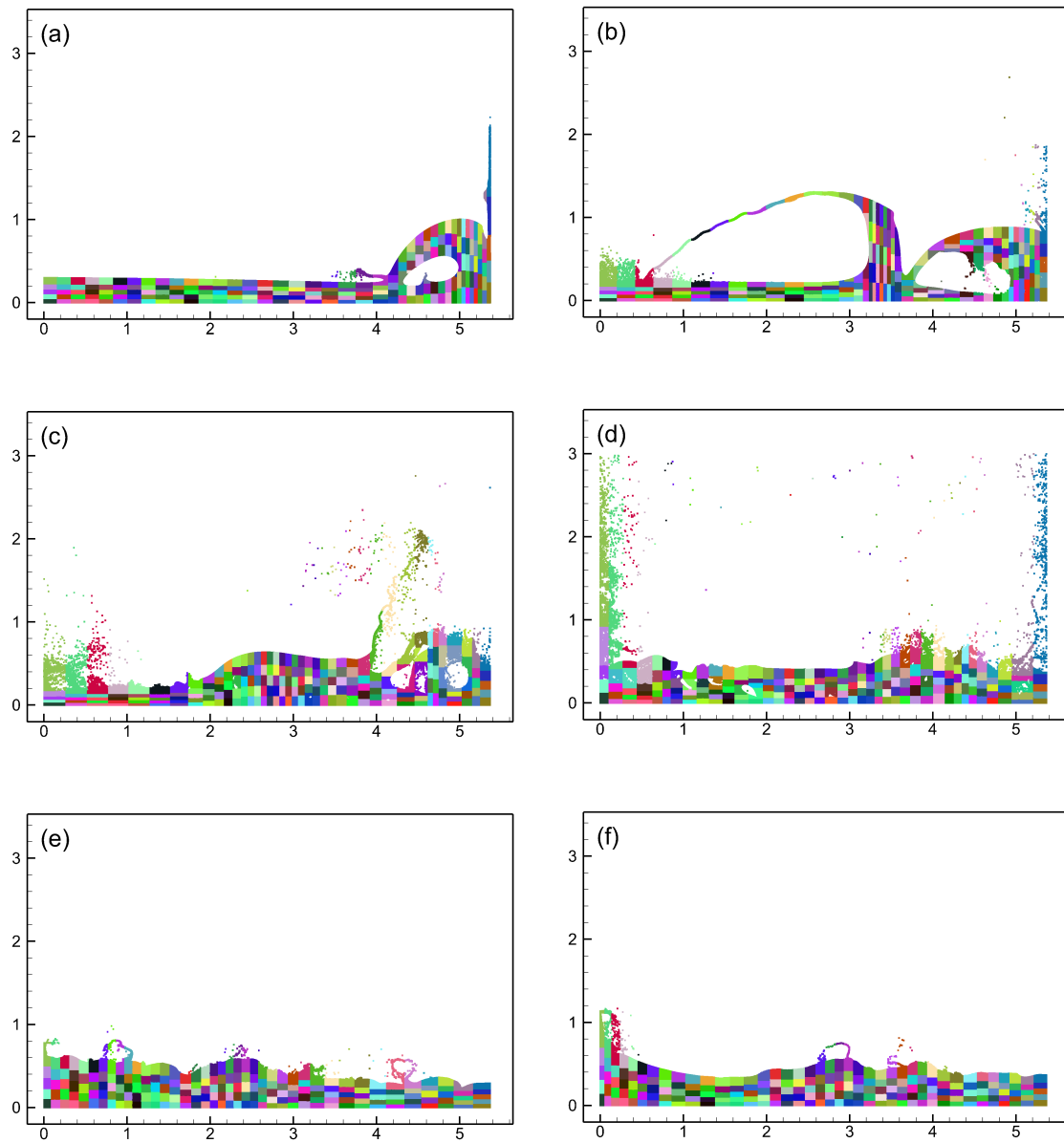
Fig. 5.15 Subdomain distribution at $t = 2.0$ s (a), 2.5 s (b), 3.0 s (c), 3.5 s (d), 5.0 s (e) and 9.0 s (f).
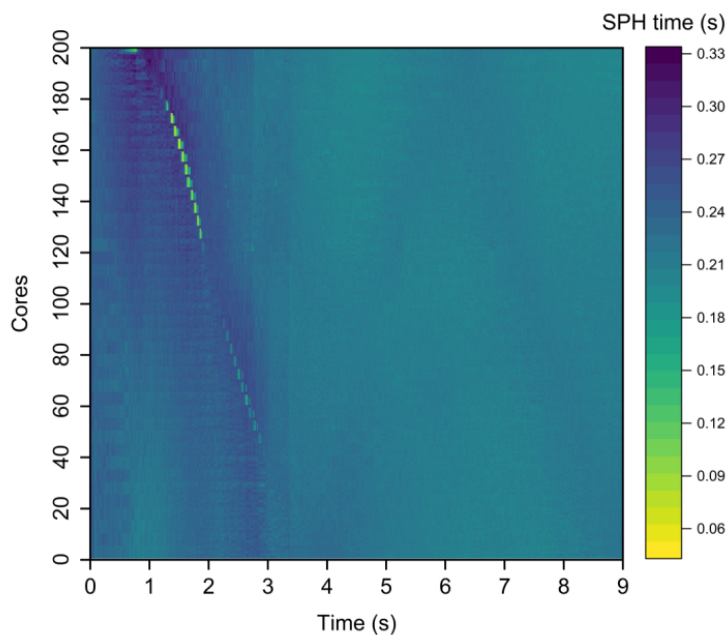
Fig. 5.16 The heat map of SPH time for the dam break case with 1,000,000 fluid particles and 200 cores.

4.5.1 shows that the results tend to stabilise when the particle spacing is less than 0.01 m. To simulate particle numbers greater than one million, the initial particle spacing was 0.004 m with a total of 1,575,000 fluid particles. $e_{i,max}$ is set to 0.05, and the time step was set to 0.0002 s. The physical time was 45 seconds, taking a total of 31.5 hours to complete the calculations.

As shown in Fig 5.20(a), a total of 200 cores are used in this example, with 2 cores in the vertical direction and 100 cores distributed along the horizontal direction. The smooth pressure distribution in the whole flume at 35.1 s can be observed in Fig 5.20(b). Fig 5.20(c) and Fig 5.20(d) show the locally smooth pressure distribution as well as the horizontal velocity distribution. Splashing shows the ability of SPH to reconstruct the nonlinear free liquid surface. Fig 5.21 shows the free surface elevation in front of the plate in comparison with the experiment. The peak free surface predicted by SPH near 36.7 s is overestimated by 0.05 m. After 38 s, there is a phase shift of the free surface, which may be due to the effect of the sponge layer not absorbing waves well.

Chapter5/Figs/fig_532.png
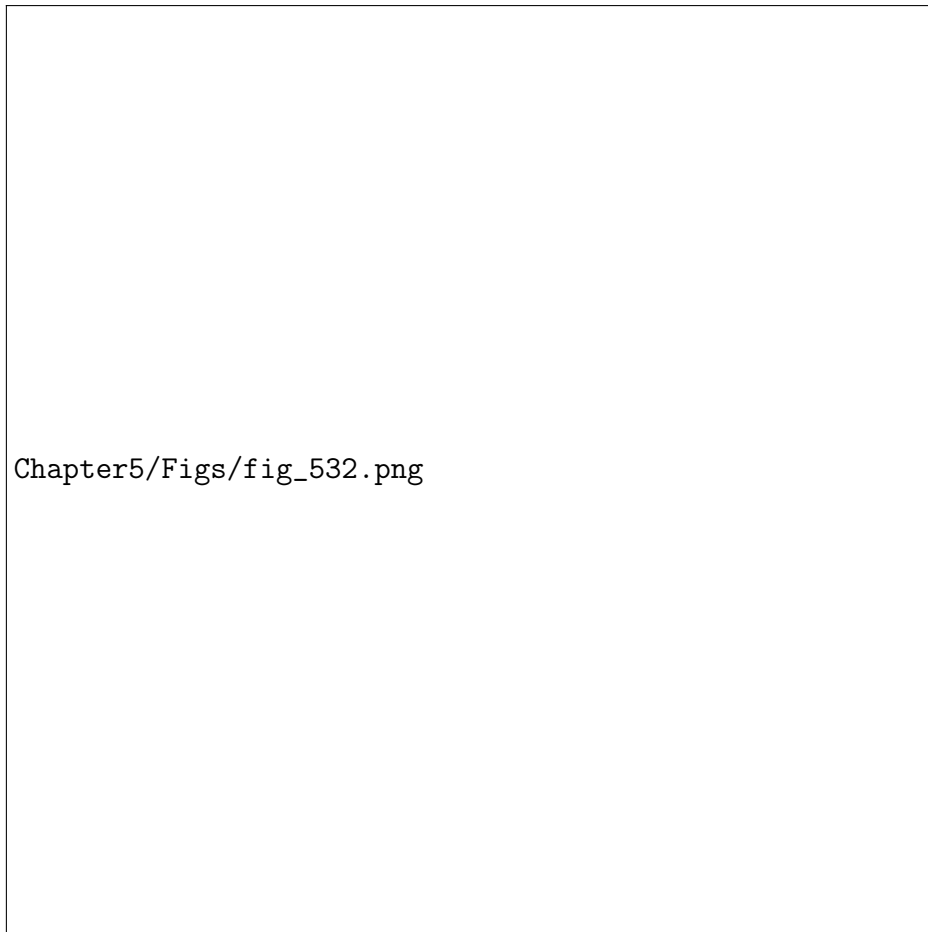
Fig. 5.17 The heat map of ISPH dynamic load balancing for the dam break test case. The vertical axis is number of time steps, and the horizontal axis is MPI partitions, totally 768 MPI partitions has been used here, the colour bar represents wall time (seconds) spent in each timestep (Guo et al., 2018). (Figure has been removed due to Copyright restrictions.)
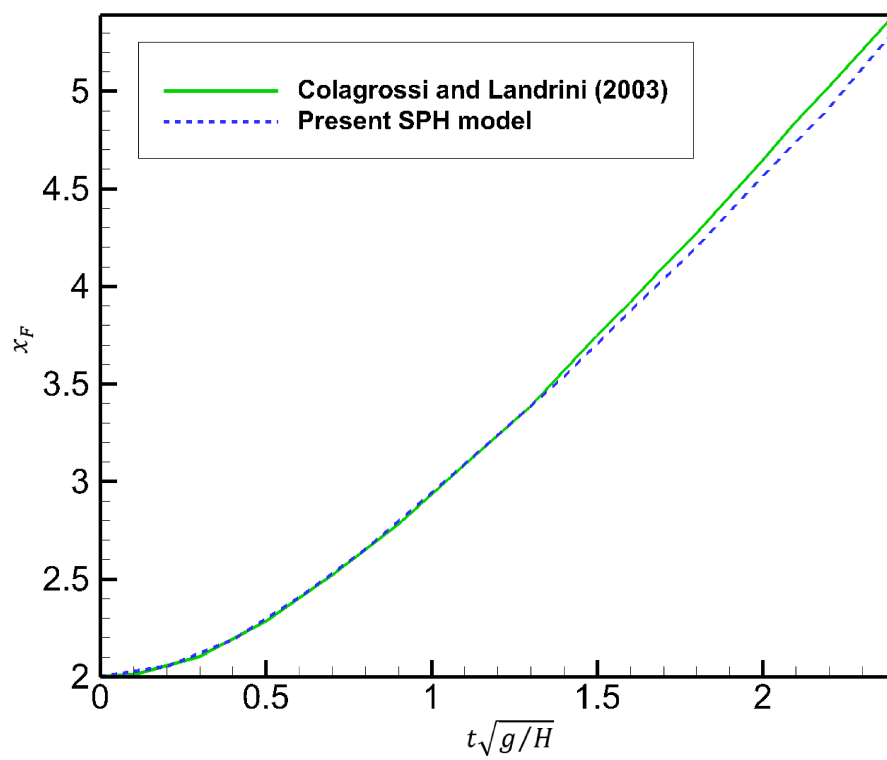
Fig. 5.18 Time series of water front.

Chapter5/Figs/fig_520.png

Fig. 5.19 Side view sketch of physical model (Hu et al., 2017). (Figure has been removed due to Copyright restrictions.)
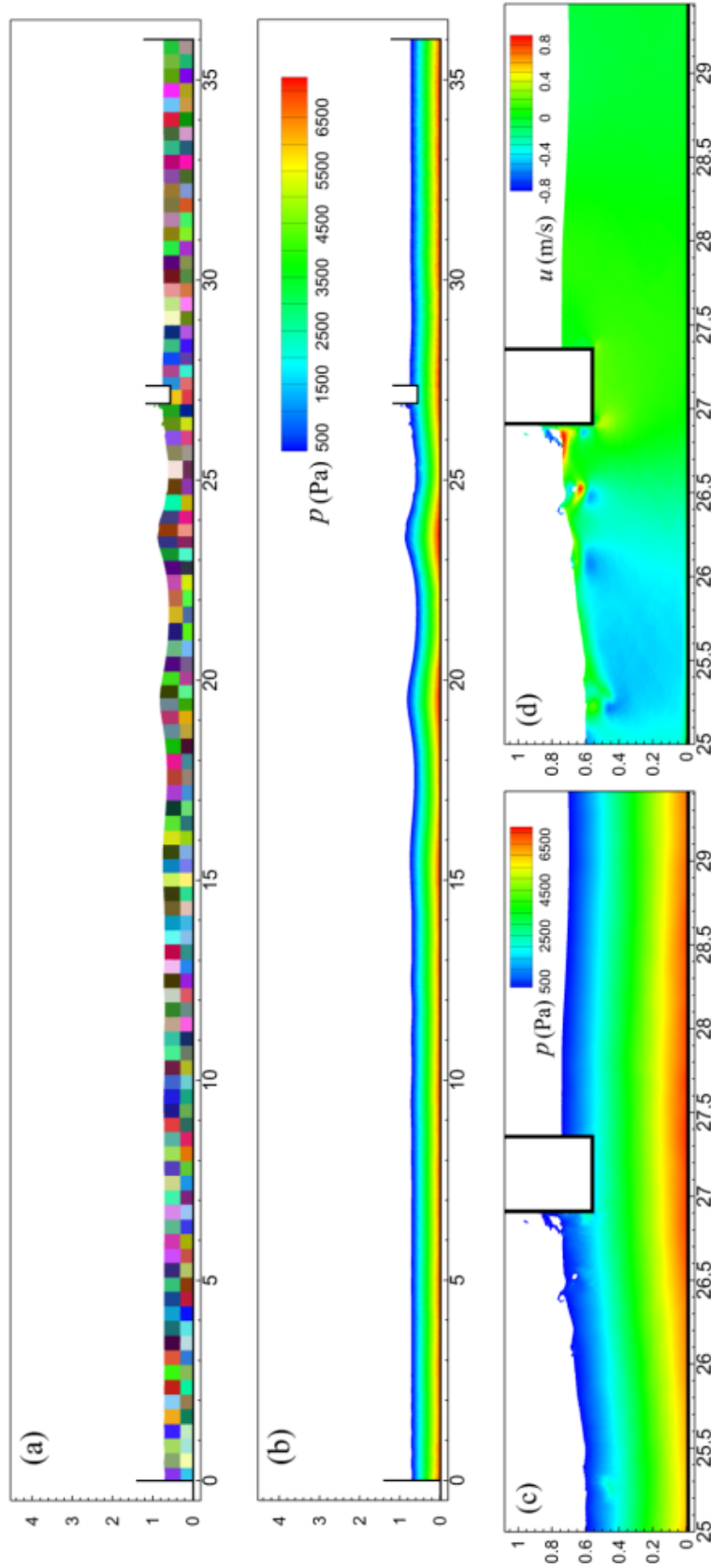
Fig. 5.20 Subdomain distribution at 35.1 s (a); Pressure field in the whole flume at 35.1 s (b); Local pressure field at 35.1 s (c); Local horizontal velocity field at 35.1 s (d).
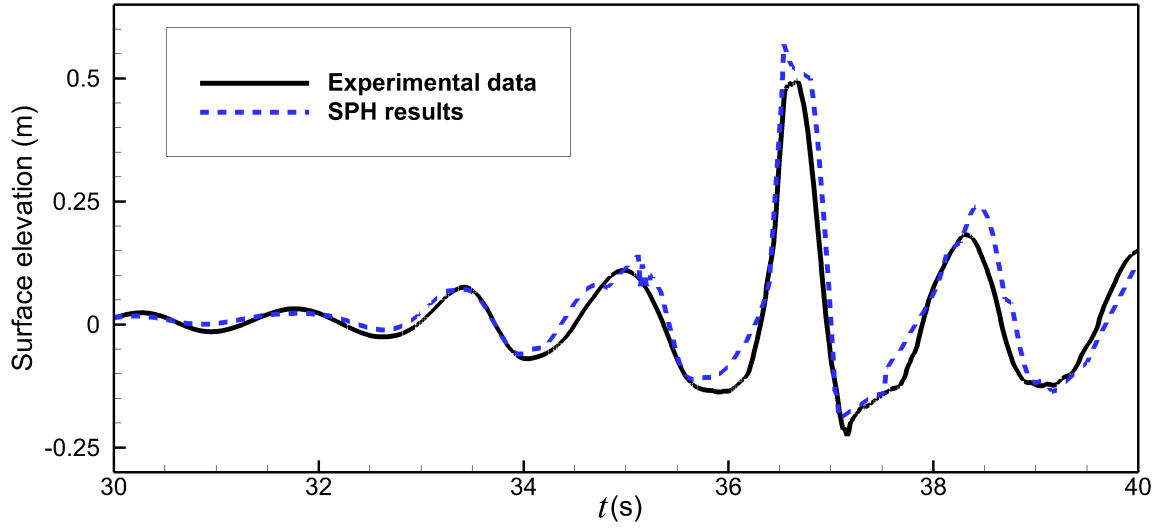
Fig. 5.21 Comparison of wave elevation at a position 26.885 m.

In Fig 5.22, all cores spend a similar amount of time at the beginning, due to the implementation of the initial load balancing strategy. Before 30 seconds, the time spent increases for an increasing serial number of cores. The larger the core serial number, the later the increase in SPH time occurs. This may be due to the fact that the wave propagates gradually from the wave maker (on the left side) to the right side. Thus, when the wave propagates on the left side of the tank, the complications of the flow condition (the motion of free surface, particles transfer between adjacent cores, etc.) make the corresponding processors slower compared to those of the still water related ones. In spite of this, the maximum difference in time consumption for the 200 cores over the entire 45 seconds is approximately 0.0255 seconds (5.1% relative to the minimum run time), which is a very slight loading imbalance. The current parallel model still achieves relatively good load balance.

Water Entry of a Wedge

This case simulates the free fall of a wedge in initially calm water (Zhao et al., 1996). The width of the wedge is 0.5 m with an angle 30° and mass 72.5 kg, as shown in Fig 5.23. The depth and the width of water tank are 1.5 m and 3 m, respectively. Initial vertical velocity of the wedge is 6.15 m/s. The convergence of the present SPH model is checked via three different particle resolutions in this part: 0.01 m, 0.002 m, and 0.0005 m, resulting in 45 thousand, 1.125 million, and 18 million fluid particles, correspondingly. $e_{i,max}$ is 0.05 for this case. The tests are conducted on the China Science and Technology Cloud (CSTC), which
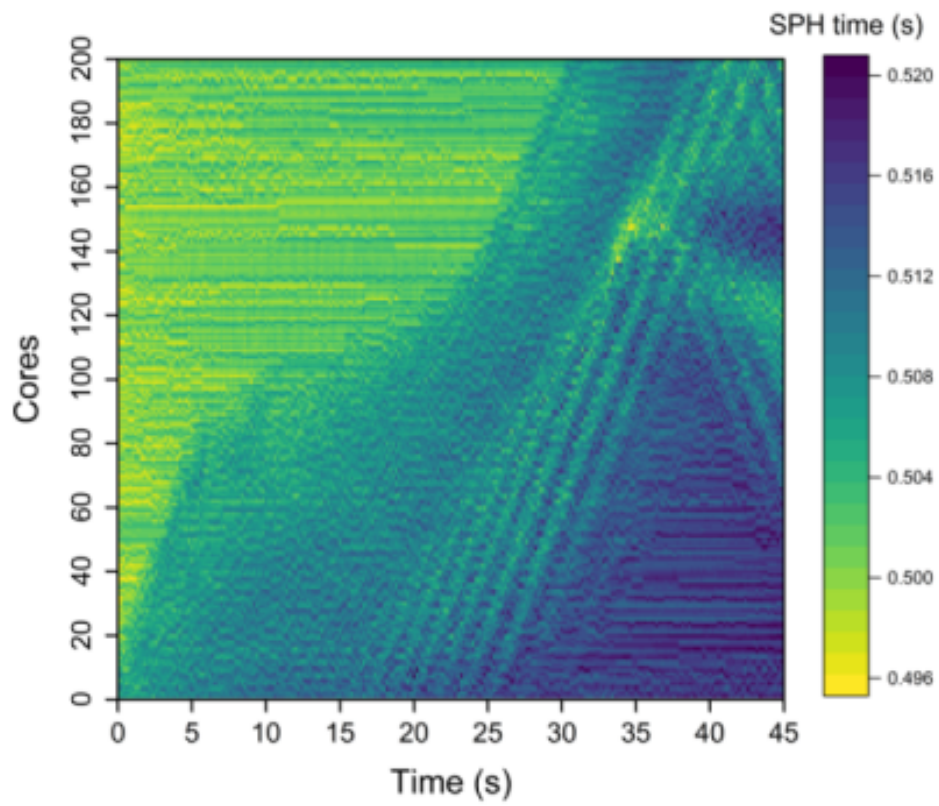
Fig. 5.22 The heat map of SPH time for the wave structure case with 1,575,000 fluid particles and 200 cores.
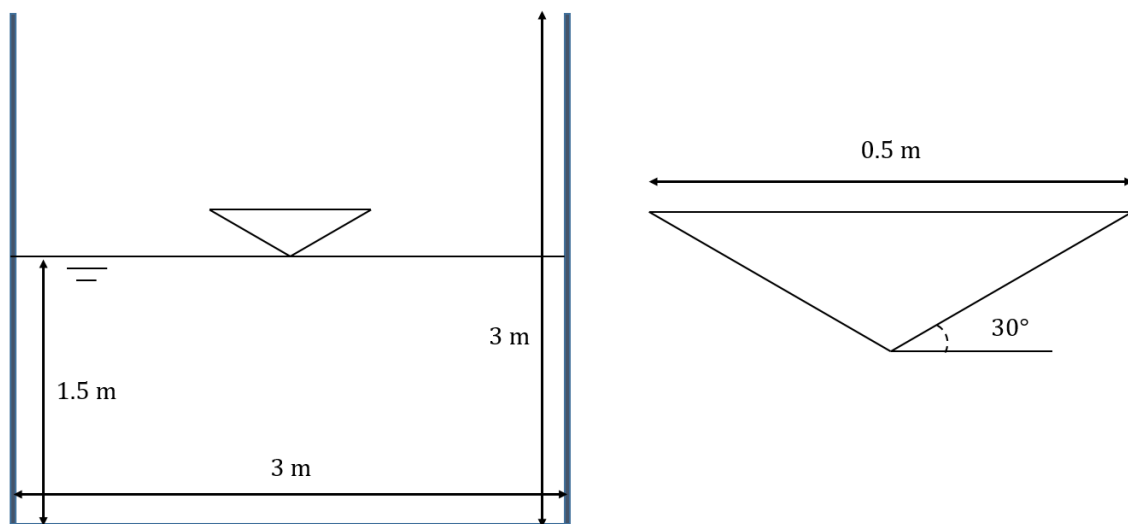
Fig. 5.23 Geometry of water tank and wedge.

Table 5.2 CPU data of water entry of a wedge

Test	Resolution (m)	Fluid particle number	Timestep (s)	Number of timestep	CoreS	Serial CPU time (s/particle/time-step)
(a)	0.01	4.5×10^4	0.00005	100	12	1.7×10^{-4}
(b)	0.002	1.125×10^6	0.00001	500	288	2.4×10^{-4}
(c)	0.0005	1.8×10^7	0.0000025	2000	1920	4.6×10^{-4}
(d)	0.002	1.125×10^6	0.00001	500	144	2.0×10^{-4}

consists of 823688 cores on 858 compute nodes. The tests are conducted on 96 core CPU nodes each using Intel Xeon Platinum 9242@2.3GHz.

A snapshot at $t = 0.005$ s is illustrated in Fig 5.24, where the effect of particle resolutions on the free surface jet capture can be observed. As particle resolution increases, splashes are better captured. Table 5.2 presents the numerical set up and time cost for three particle resolutions. The number of time steps varies from resolution to resolution because to the Courant-Friedrichs-Levy (CFL) condition; it is inversely proportional to the particle resolution. Table 5.2 shows the comparable serial CPU time for each resolution. A complete parallelization should provide an equivalent serial CPU time. This value rises with spatial resolution, as seen in Table 5.2. This difference may mostly be attributed to communication blockage. The additional time caused by blocking communication becomes more obvious as the number of cores rises.

Speedups and efficiencies

Weak and strong scaling tests are conducted to evaluate the parallel performance of present model. The test case examined is the 2D 2nd Stokes wave (wave height 0.1 m and wave period 2.0 s) in a numerical wave flume. Each simulation is run for 1000 time steps. The initial set-up is as shown in Fig. 5.25. The regular numerical tank facilitates the setting up of numerical cases to meet the needs of strong and weak scale tests. The tests are conducted on CSTC, and $e_{i,max}$ is 0.05.

The weak scale test is a test to ensure that the number of particles in each core is consistent while increasing the number of cores. Ideally, as the number of core increases, the computation time should remain constant. However, due to communication load, as the number of cores increases, the computation time also increases. The computational cost t_s for 60 cores is defined as a reference and calculate the weak scale efficiency e_w for different numbers of cores

$$e_w = \frac{t_i}{t_s}. \tag{5.11}$$
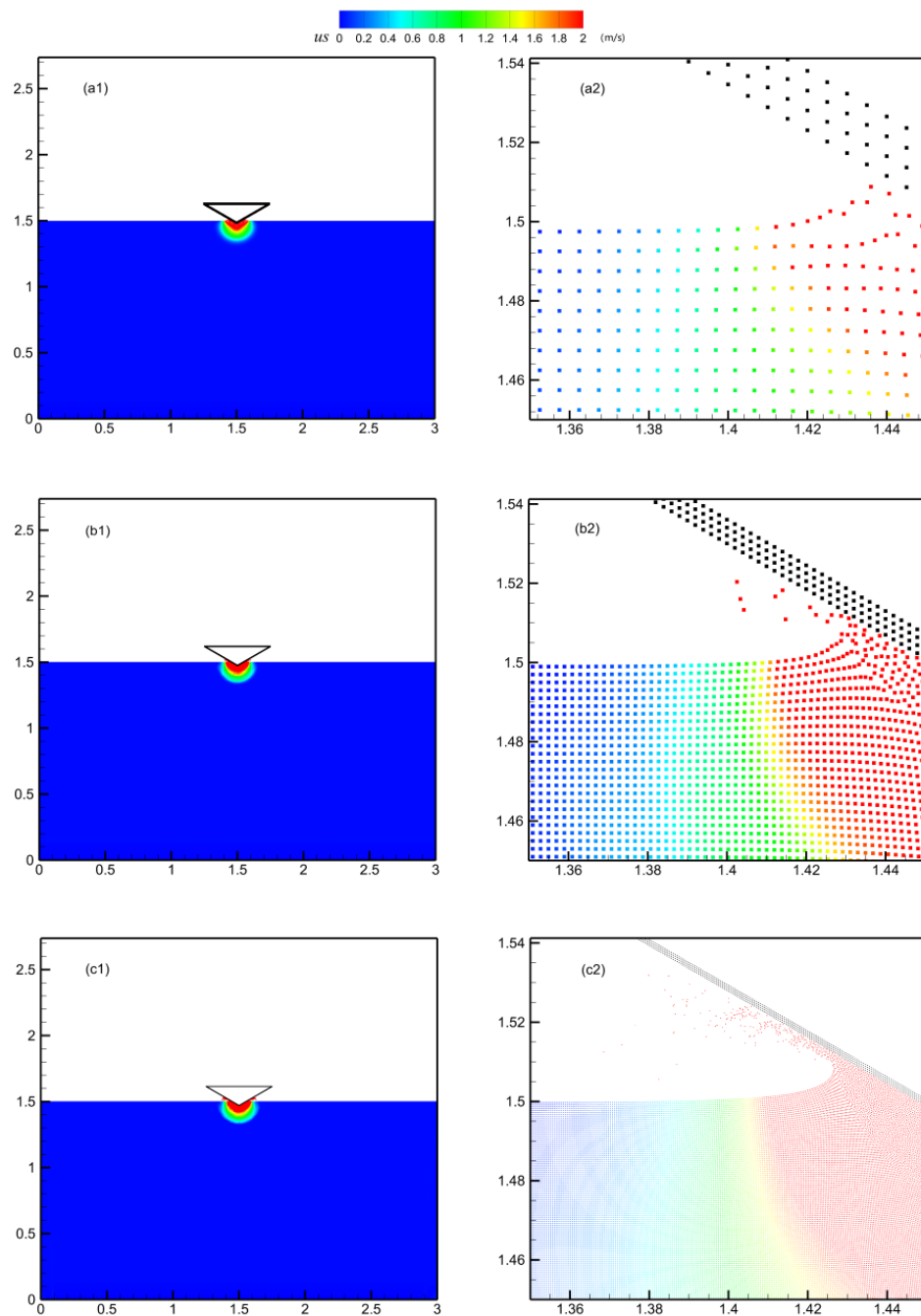
Fig. 5.24 The velocity of wedge impact simulation involving various particle resolution at $t = 0.005$ s. (Label 'a', 'b', and 'c' denote tests 45 thousand, 1.125 million, and 18 million, respectively; '1' and '2' denote whole water wank and local domain, respectively.)
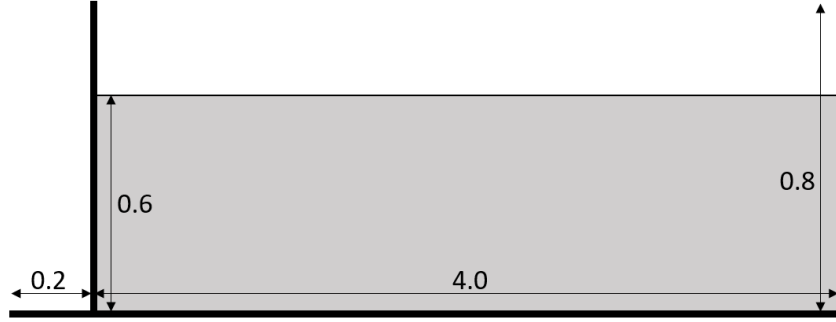
Fig. 5.25 Simulation setup for scaling tests.
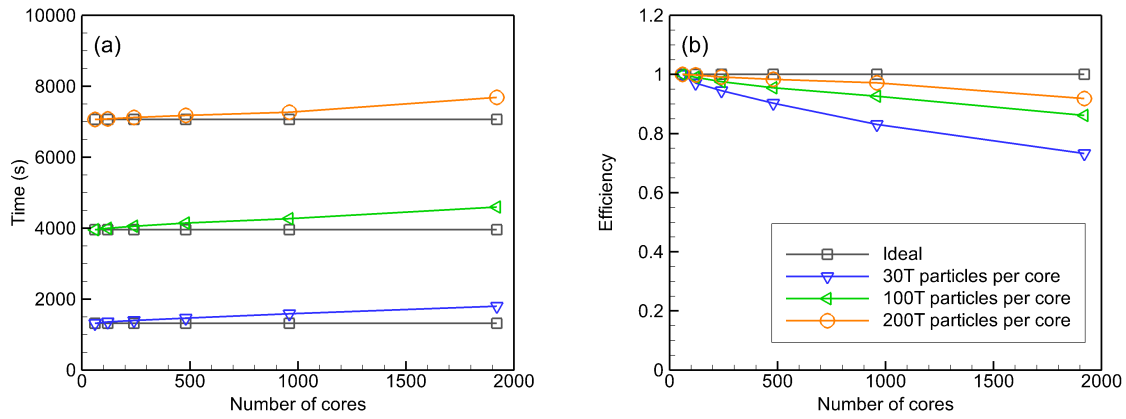
Fig. 5.26 Time cost (a) and efficiency (b) of weak scaling tests.

where t_i is the time cost for the number i of cores. Three different groups of single core particle numbers of 30,000, 100,000, and 200,000 (written as 30T, 100T, and 200T) were tested at 60, 120, 240, 480, 960, and 1920 cores, respectively. Fig. 5.26 shows the time spent and the efficiency of the weak scale tests. As the number of cores increases, the calculation time increases, whereas the efficiency decreases as expected. Ultimately, for the cases run in 1920 cores, the efficiencies are only 0.73, 0.86, and 0.92 for 30, 100, and 200 thousand particles per core, respectively. Although the number of particles in each core remains the same, the increase in communication time due to the increased number of cores affects the overall computational efficiency. For the case of more particles in each core, the communication time takes up less of the overall time, leading to a higher computational efficiency.

In the case of strong scaling, the number of cores is increased while the problem size remains constant, resulting in a reduced workload per core. Speedup S_s and efficiency e_s for strong scaling studies are calculated from
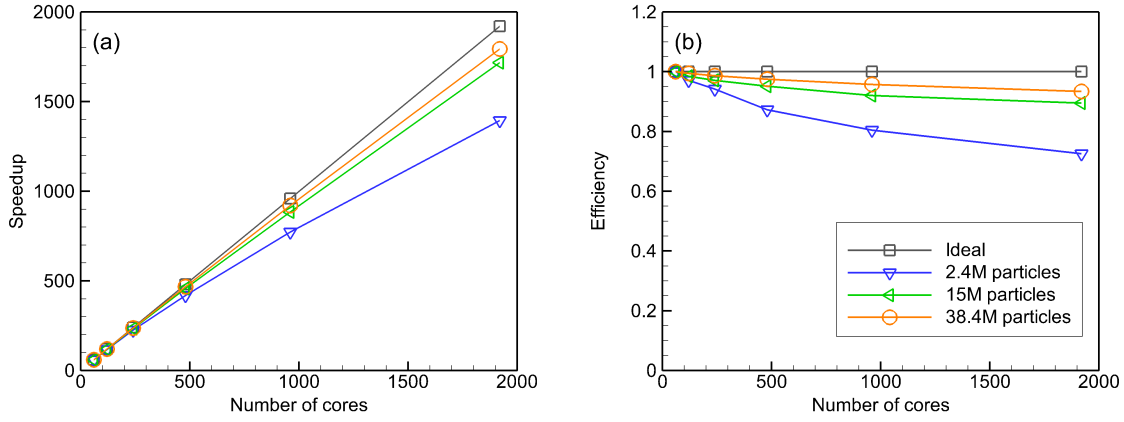
Fig. 5.27 Speedup (a) and efficiency (b) of strong scaling tests.

$$S_s = \frac{N_r \times T_r}{T_s}, \tag{5.12}$$

$$e_s = \frac{N_r \times T_r}{N_s \times T_s}. \tag{5.13}$$

Three different sets of total particle numbers of 2.4, 15 and 38.4 million (written as 2.4M, 15M, and 38.4M) were tested at 60, 120, 240, 480, 960, and 1920 cores, respectively. Fig. 5.27 shows the computational speedups as well as the efficiencies under the strong scale tests. Increasing the number of cores can reduce the number of particles per cores. This leads to a reduction in the cost per core calculation. However, the cost for overhead computation and communication of information also increases. For the cases run in 1920 cores, the efficiencies are 0.72, 0.89 and 0.93 for the cases with 2.4, 15 and 38.4 million particles, respectively. It is expected that the efficiency could be improved. Meanwhile, higher efficiency can be obtained by introducing a data decomposition of particle interaction loops through a shared memory parallel framework.

Comparison with other parallel codes

To compare the present method, the same dam-breaking case with the one published in Cherfils et al. (2012) is simulated. Fig. 5.28 shows the subdomain distribution for this case with 5000 fluid particles using 4 cores. Particle spacing is 0.02 m. The numerical set up is the same as that used in Cherfils et al. (2012). The time step is 0.0004 s, a total computation time cost is 6.1 mins, whereas Cherfils et al. (2012) quoted 15 mins.
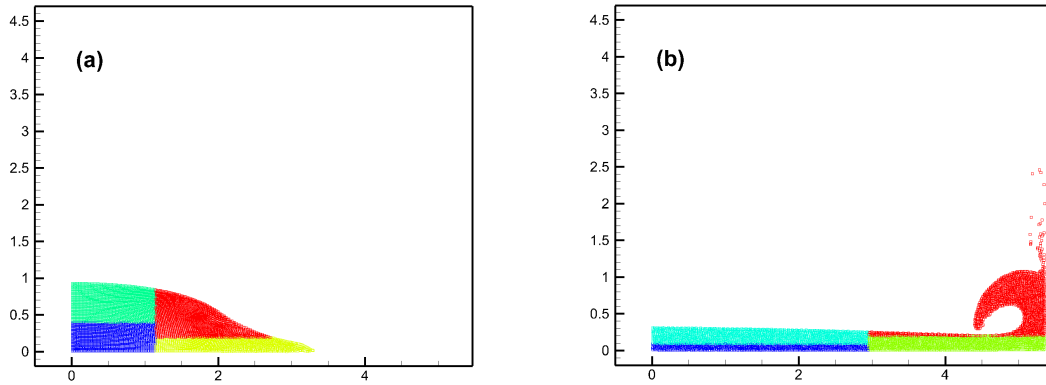
Fig. 5.28 Subdomain distribution for dam breaking case with 5000 fluid particles at $t = 0.4$ s (a) and 1.9 s (b)

It seems that the current method is much more efficient. However, this may be not rigorous. First, the two SPH numerical models are different and the Rusanov flux is taken into account in JOSEPHINE Cherfils et al. (2012), which may require additional computational effort. Secondly, the computation using JOSEPHINE is tested on a Xeon W3520, 2.67 GHz. While, the current SPH model is simulated on a computing environment with a Dual Intel Xeon E5650 (Westminster). The above calculations show that many factors need to be considered when comparing different SPH-MPI models in order to reach a rigorous conclusion.

The ISPH parallel solver (Guo et al., 2018) was used to simulate 100 million particles when it was slightly less than 80% efficient at 1536 cores. In the case of 100 million particles used by Oger et al. (2016), 72% efficiency was observed on 16,384 cores. When the number of cores is 2000, the efficiency is even greater than 100%. Ji et al. (2019) used a multi-resolution SPH model to simulate 128 million irregularly distributed particles using 1,792 cores. Its computational efficiency is around 90%. However, the efficiency drops to around 60% when the cores increase to 7,168. The current model uses 1,920 cores to simulate 38 million particles with an efficiency of 93%. The above comparison shows the computational efficiency of the different models. However, it is difficult to say qualitatively which model is more efficient (scalable). The performance of different models under different HPC architecture is different. However, as the number of cores increases, the efficiency of all models decreases significantly. This is the main problem that MPI parallelism has to face when it is extended to the extreme scale.

5.5   Summary of the Parallel SPH Framework

This chapter has presented a new MPI-based parallel SPH framework with a dynamic load balance strategy for free-surface flow. The new framework uses a background Cartesian grid to decompose the domain, and a grid list to map the entire domain. Meanwhile, within each subdomain there exists a local mesh for neighbouring particle search as well as determining the particles that need to be transferred. In the dynamic load balance strategy, two evaluation criteria are considered, i.e., computation particle numbers and running time are considered. The update of the subdomain divisions is achieved by updating the subdomain boundary according to the workload/subdomain division from the previous time step. An initial load balance strategy is developed to maintain the initial homogeneous load balance. Results show that the present parallel SPH framework can efficiently simulate free-surface flow.

In the dam breaking cases, the load balance strategy based on the calculation particle number can achieve the balance of the calculation particle number. The load balancing strategy based on running time ensures that the running times in each core are almost uniform, regardless of different particle numbers. In terms of overall time cost, the load balancing strategy based on running time achieves better parallel efficiency. The complex free surface in the dam breaking cases can be captured, demonstrating that the current parallel framework can guarantee dynamic load balance even in the face of large deformations. The wave-structure case demonstrates the ability of the present SPH model to simulate the numerical wave tank with millions of particles for tens of seconds. The wedge of water entry are simulated with various particle resolutions, which involved up to 18 million particles as well as 1920 cores. The results show that higher resolutions allow for better capture of the nonlinear free-surface condition. However, the difference in equivalent serial CPU time at different resolutions and cores shows the extra cost of blocking communication. This parallel SPH model was then tested on a large scale uniform particle distribution of up to 1920 cores. Nevertheless, it still shows a decrease in efficiency in the case of 1920 cores. Future work should consider the extension of the model to three dimensions. In the meantime, the development of non-blocking MPI parallel strategies has the potential to further improve parallel efficiency.

Chapter 6

Coupled SPH with OceanWave3D

6.1 Introduction

SPH is highly advantageous method for simulating strongly nonlinear free-surface conditions with large deformations. Nevertheless, one of the drawbacks of the SPH method is its low computational efficiency. In comparison, OceanWave3D, based on fully nonlinear potential flow theory, is a very efficient and accurate simulation of surface waves and velocity fields from the deep sea, with satisfactory results both in the open ocean and nearshore. Therefore, a two-way coupled model between SPH and OceanWave3D is proposed. The linear region can be solved using the efficient OceanWave3D solution in order to reduce the computational cost. Meanwhile, in the nonlinear region the expensive SPH model is used to simulate the nonlinear phenomena. This coupled model therefore aims to further improve the computational efficiency of the numerical model without compromising the ability of the SPH model in dealing with nonlinear problems.

6.2 OceanWave3D

OceanWave3D was proposed by Engsig-Karup et al. (2009); Bingham and Zhang (2007) for large-scale modelling of wave problems in coastal and offshore environments, based on a fully nonlinear potential flow theory. OceanWave3D numerically solves the potential flow governing equations (Currie, 2016) for gravity waves at the water surface in a 3D Eulerian reference system using a right-angle coordinate system (x, y, z). Fluids are assumed to be incompressible, inviscid and non-rotating flows. The problem of non-breaking free surface waves can be described in terms of the velocity potential energy ϕ and the z position η of the free surface. At a free surface, nodes should remain at the surface with a pressure equal to

the atmospheric pressure. At the bottom, the no penetration condition is set. The kinematic and dynamic boundary conditions of the free surface, and bottom boundary condition are

$$\frac{\partial \eta}{\partial t} = -\frac{\partial \eta}{\partial x}\frac{\partial \tilde{\phi}}{\partial x} - \frac{\partial \eta}{\partial y}\frac{\partial \tilde{\phi}}{\partial y} + \tilde{w}\left[1 + \left(\frac{\partial \eta}{\partial x}\right)^2 + \left(\frac{\partial \eta}{\partial y}\right)^2\right], \tag{6.1}$$

$$\frac{\partial \tilde{\phi}}{\partial t} = -\frac{1}{2}\left[\left(\frac{\partial \tilde{\phi}}{\partial x}\right)^2 + \left(\frac{\partial \tilde{\phi}}{\partial y}\right)^2\right] + \frac{1}{2}\tilde{w}^2\left[1 + \left(\frac{\partial \eta}{\partial x}\right)^2 + \left(\frac{\partial \eta}{\partial y}\right)^2\right] - g\eta, \tag{6.2}$$

$$\frac{\partial \phi}{\partial z} + \frac{\partial h_o}{\partial x}\frac{\partial \phi}{\partial x} + \frac{\partial h_o}{\partial y}\frac{\partial \phi}{\partial y} = 0, \quad z = -h_o, \tag{6.3}$$

where $h_o = h_o(\mathbf{x})$ is the water depth from the seabed to the still water level. $\tilde{\phi} = \phi(\mathbf{x}, \eta, t)$ is the velocity potential of the free surface, $\mathbf{x} = (x, y)$ represents the horizontal position and $\tilde{w}$ is the vertical velocity of the free surface.

The σ coordinate transformation allows a fixed grid distribution to be obtained taking into account free surface variations

$$\sigma = \frac{z + h_o(\mathbf{x})}{\eta(\mathbf{x}, t) + h_o(\mathbf{x})}. \tag{6.4}$$

Then the Eq. (6.1 Eq. (6.2) and Eq. (6.3) is rewritten as:

$$\Phi = \tilde{\phi}, \quad \sigma = 1; \tag{6.5}$$

$$\frac{\partial^2 \Phi}{\partial x^2} + \frac{\partial^2 \Phi}{\partial y^2} + \left(\frac{\partial^2 \sigma}{\partial x^2} + \frac{\partial^2 \sigma}{\partial y^2}\right)\frac{\partial \Phi}{\partial \sigma} + 2\left[\frac{\partial \sigma}{\partial x}\frac{\partial}{\partial x}\left(\frac{\partial \Phi}{\partial \sigma}\right) + \frac{\partial \sigma}{\partial y}\frac{\partial}{\partial y}\left(\frac{\partial \Phi}{\partial \sigma}\right)\right] +$$
$$\left(\frac{\partial^2 \sigma}{\partial x^2} + \frac{\partial^2 \sigma}{\partial y^2} + \frac{\partial^2 \sigma}{\partial z^2}\right)\frac{\partial^2 \Phi}{\partial \sigma^2} = 0, \quad 0 < \sigma < 1; \tag{6.6}$$

$$\left(\frac{\partial \sigma}{\partial z} + \frac{\partial h_o}{\partial x}\frac{\partial \sigma}{\partial x} + \frac{\partial h_o}{\partial y}\frac{\partial \sigma}{\partial y}\right)\frac{\partial \Phi}{\partial \sigma} + \frac{\partial h_o}{\partial x}\frac{\partial \Phi}{\partial x} + \frac{\partial h_o}{\partial y}\frac{\partial \Phi}{\partial y} = 0, \quad \sigma = 0. \tag{6.7}$$

The classical fourth-order Runge-Kutta method is used as the numerical integration algorithm. Wave generation and absorption are achieved using the relaxation zone method proposed by Larsen and Dancy (Larsen and Dancy, 1983).
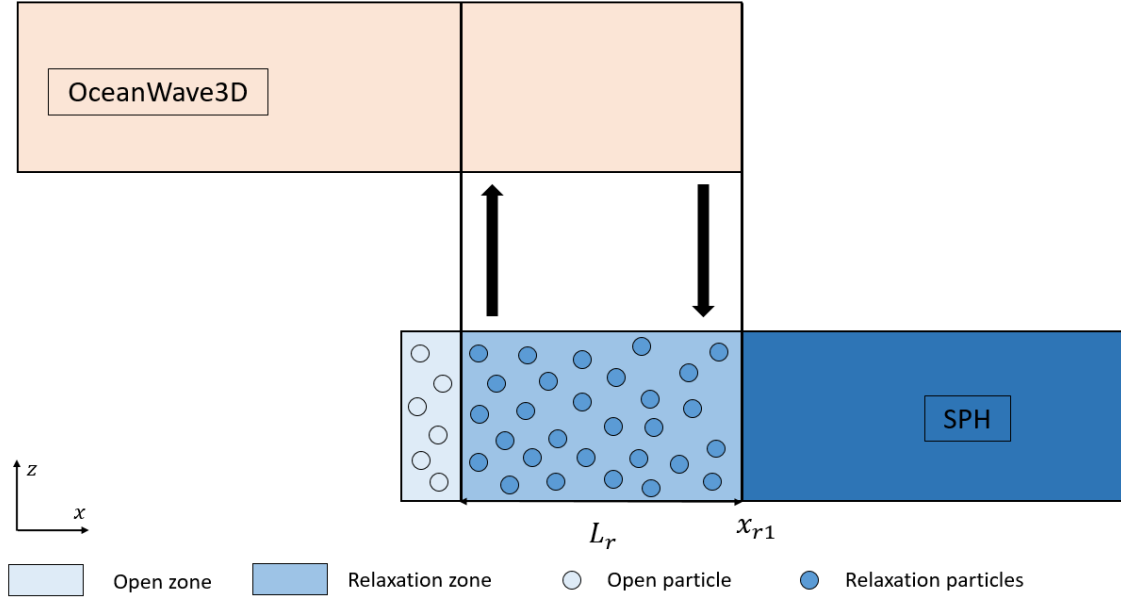
Fig. 6.1 Sketch of coupling sub-domain.

6.3 Coupling Strategy

The coupled model is based on the decomposition of a global domain into separated Ocean-Wave3D and SPH domains. The exchange of information between OceanWave3D and SPH domains is performed by a two-way coupling algorithm, and the couplings take place by using relaxation functions to the physical properties in the coupling region. This is presented in four main sections: coupling strategies in space and time, Open relaxation region in SPH model, OceanWave3D solver for the coupled model, and coupling strategies for the parallel system.

Coupling Strategies in Space and Time

In the current coupled model the whole computational domain is spatially divided into several overlapping sub-domains. Fig. 6.1 shows an example of the coupled model. The computational domain is divided into OceanWave3D and SPH regions. The coupling regions are fixed and carry out information transfer. The OceanWave3D and SPH models have different requirements for time steps. For accurate and stable calculations, models need to be coupled at the same moments in time. The time step (t_o) for OceanWave3D is typically several orders of magnitude higher than (t_s) for SPH. In general, the OceanWave3D is less
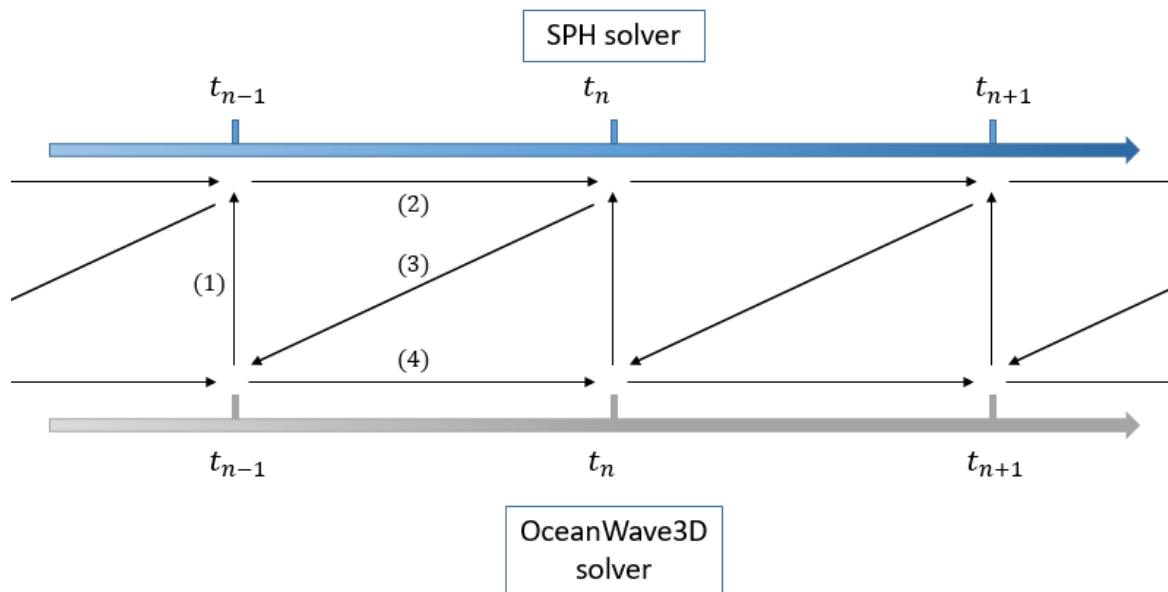
Fig. 6.2 Sketch of calculation process under one time step.

expensive than the SPH domain. Therefore, the unique time step is used

$$t_o = t_s. \tag{6.8}$$

The coupling strategy here is to complete the calculation at each time step and then couple the results of the two models, as shown in Fig. 6.2. At the beginning of a time step, the results of OceanWave in the coupled region are passed into the SPH model. After SPH has completed its calculations for a time step, its data is passed back into OceanWave3D. OceanWave3D then completes the calculation for one time step.

Open Relaxation Boundary in SPH Model

The length of a numerical flume is often tens or even hundreds of metres. The SPH computational domain can be truncated and coupled with OceanWave3D. The development of the coupled model shortens the size of the SPH computational domain. It is necessary to develop open boundaries at the SPH coupling interface. The open boundary can be transformed between the incoming and outgoing flow boundaries because of the periodicity of wave flow. In many articles the authors treat inlet and outlet boundaries separately, but it needs to develop stable inlet/outlet flow open boundaries. According to the wave motion properties, the velocity is not uniform over a cross section that propagates along the wave. This means that the open flow field particle generation/deletion is not uniformly distributed perpendicular

to the open boundary, and appear at the open boundary. Irregular particle distributions may lead to calculation errors. As the free-surface level is always constantly changing in the coupling area, the increase and decrease of particles in the vertical direction should be considered.

In order to achieve the above, an open relaxation boundary is developed. The open relaxation boundaries are implemented as open and relaxation zones. Particles in these zones are called open particles and relaxation particles, respectively. Physical quantities from OceanWave3D can be applied to these particles. A sketch of the open relaxation boundary is depicted in Fig. 6.1. The relaxation zone, where a relaxation function is used, can obtain a smooth transitional region from the results of OceanWave3D to SPH simulations. The open zones are placed in the inflow/outflow regions to cover the truncated kernel area. The number of open particle layers is determined by the kernel function. Therefore, the SPH model achieves coupling in the coupled region by the open relaxation boundary. Meanwhile, the open relaxation boundary ensures that the SPH model does not suffer from kernel truncation in the coupling interface. In the following, the treatments of open particles and relaxation particles are discussed in detail.

Particle Creation/Deletion/Transformation

At the open relaxation boundary, particles transform between open and relaxation particles. At the same time, the mass flux at the coupling interface is achieved by the production and deletion of the open particles. The position is used as a basis to distinguish particle species. An open particle entering the relaxation region is transformed into a relaxation particle. Relaxation particles and fluid particles are updated based on the change of position. Meanwhile, the positions of each kind of particle are updated according to the velocity in the time integration method.

Particle generation and deletion at coupling interfaces can lead to sharp changes in mass at the interface. To solve that, the interface is subdivided into segments of equal size (Ferrand et al., 2017). Mass flux at each segment is obtained from OceanWave3D. Meanwhile, the change in mass due to the creation and deletion of particles is applied to the interface segment to ensure a continuous change in mass at the interface over time. The mass flux m_f across each segment from OceanWave3D is given by:

$$m_f = \rho_s \Delta x_s \mathbf{u}_{sg} \mathbf{n}_s \Delta t, \tag{6.9}$$

where $\mathbf{u}_{sg}$ and ρ_s are the velocity and density at the center of the segment from the underlying OceanWave3D field, respectively. The symbols $\mathbf{n}_s$ and Δx_s represent the normal vector

pointing to the interior of the SPH and the width/area of each segment, respectively. The symbols for mass fluxes indicate mass inflow and outflow into the SPH region. The mass of each segment at each time step is calculated as (Chiron et al., 2018; Ferrand et al., 2017)

$$m_s^{n+1} = m_s^n + m_f^n + m_{d/a}^n, \tag{6.10}$$

where $n + 1$ and n denote $n + 1$ time step and n time step, respectively. m_f^n and $m_{d/a}^n$ denote mass flux and the change of mass due to particle generation and deletion at n time step. Fig. 6.3 shows the process of particle generation and deletion. When the segmented mass m_s exceeds the mass of a reference particle, a new particle is injected and the value of the resulting mass is subtracted from the corresponding segmented mass. Conversely, when this mass is lower than the mass of the reference particle, the particle closest to the segment is removed and its mass is added to the mass of the segment. Furthermore, particles that move outside the open boundary are removed and, again, their mass is added to the nearest segment. A weight w_s (Ferrand et al., 2017) is associated to these mass change in Fig. 6.3, can be calculated as

$$w_{s1} = \frac{r_1}{r_s}, \tag{6.11}$$

$$w_{s2} = \frac{r_2}{r_s} = 1 - w_{s1}, \tag{6.12}$$

where r_s, r_1, and r_2 are the length of the segment, the vertical distance between the particle and the centre of segment 1, and the vertical distance between the particle and the centre of segment 2. The presence of weights ensures that changes in mass are distributed over adjacent segments.

Relaxation Particles

Relaxation zones are implemented to establish the smooth continuum of horizontal velocity and free surface level in the relaxation region from the Oceanwave3D to the SPH results. Horizontal velocity and free surface level from OceanWave3D are imposed on these relaxation particles. The relaxation domain builds smooth transitions. A relaxation function is applied here, which is an extension to that of Mayer et al. (1998) and has been used in Jacobsen et al. (2012). The relaxation function is

$$\alpha_r(i) = 1.0 - \frac{\exp(\chi_{rs}^\beta) - 1}{\exp(1) - 1}, \quad i \in R1, \tag{6.13}$$
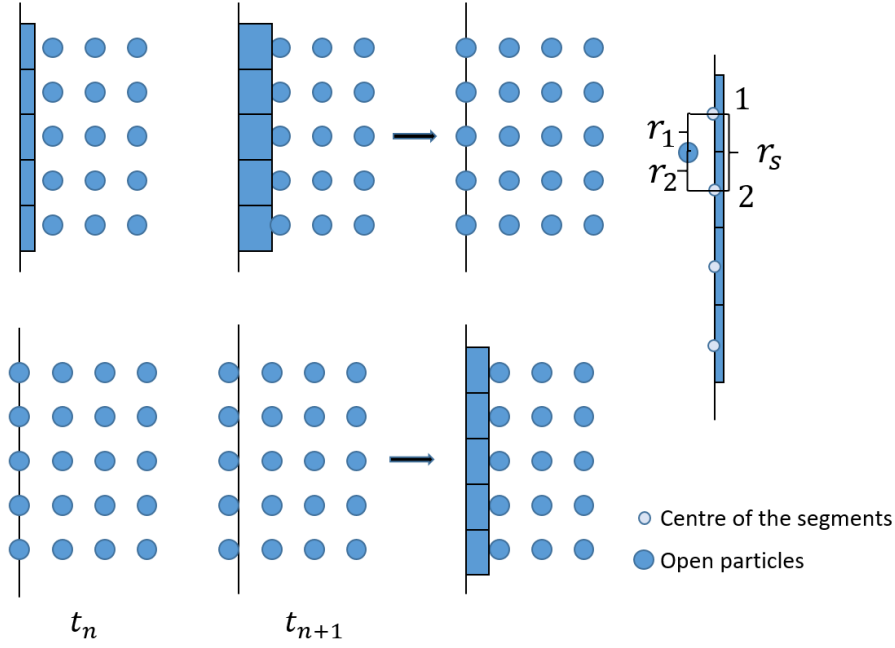
Fig. 6.3 Sketch of particle generation and deletion at coupling interface.

where $\beta = 3.5$ is the relaxation coefficient (Referring to the selection in Jacoben et al.'s work Jacobsen et al. (2012)) and $\chi_{rs} = \frac{|x_i - x_{r1}|}{L_r}$. x_{r1} are the horizontal positions of the interfaces between the relaxation particle zone and the fluid zone, as shown in Fig. 6.1. $R1$ denotes coupling region. x_i is the horizontal position of particle i. L_r denotes the length of the relaxation zone. The definition of χ_{rs} ensures that α_r is always 1 at the interfaces between the fluid zone and the relaxation zones, and α_r is always 0 at the interfaces between the open zones and the relaxation zones. Then the horizontal velocity u_x and free-surface level η is modified in the following way

$$\Phi_a = \alpha_r(\Phi)_a^{SPH} + (1 - \alpha_r)(\Phi)_a^{OceanWave3D}. \tag{6.14}$$

where Φ_a denotes horizontal velocity and free-surface level. Once the corrected free-surface level η_i is obtained, η_i is imposed on relaxation particles. In the relaxation zone, the fluid particles near the free surface are generated or removed in reference to the corrected free-surface level η_i as shown in Fig. 6.4. To achieve that, all free-surface particles need to be detected inside the relaxation zone using the method proposed by Marrone et al. (2010). The height of each free-surface particle is compared with the corrected free-surface level η_i at the corresponding position. A free-surface particle is removed if it goes up above η_i with a longer distance than the initial particle spacing. If the free-surface particle goes down below η_i with a longer distance than the initial particle spacing, a new open particle is generated. The new
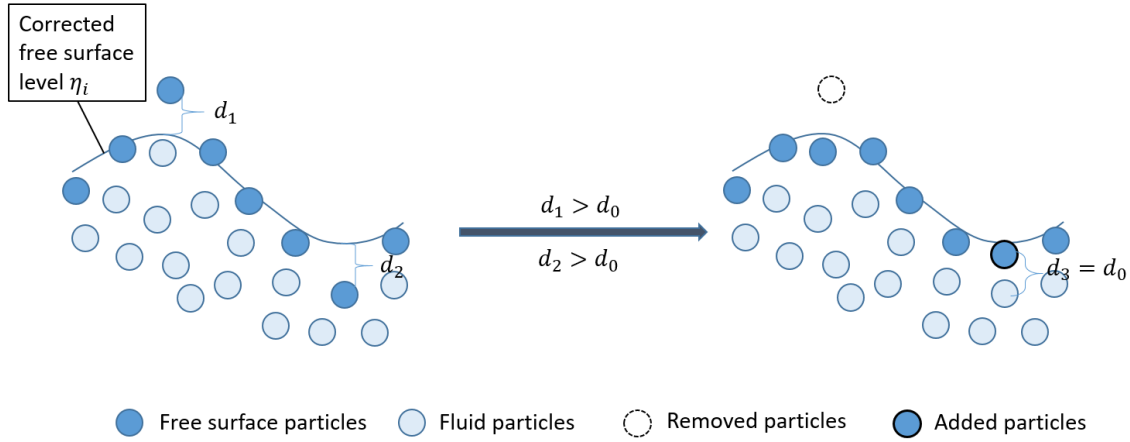
Fig. 6.4 Sketch of generation and removal of free surface particles in the relaxation zone.

fluid particle has the same horizontal coordinates as the previous free-surface particle, but the vertical height is one initial particle spacing greater than the previous free-surface particle. The velocity of this new particle is the same with the previous free-surface particle.

Due to the use of relaxation functions in the relaxation zone, a smooth result is constructed between the SPH results and the OceanWave3D results. The different results produced by the two numerical models will gradually be harmonized. As the reflected wave passes into the relaxation region, the motion of the particles gradually converges to the OceanWave3D solution due to the relaxation function.

Open Particles

The main purpose of open particles is to avoid the effects of kernel truncation. Due to the use of the relaxation zone, the horizontal velocity of the flow field, at the interface between the relaxation zone and the open zone, achieves the same solution as OceanWave3D. To obtain the vertical velocity and density of the open particles, interpolation nodes are used. Along the normal direction of the open boundary, the interpolation nodes are arranged at the open boundary line as shown in Fig. 6.5. In the vicinity of the interpolation node, SPH interpolation does not give good results due to the presence of kernel truncation. Thus, a moving least-squares (MLS) reconstruction (Lancaster and Salkauskas, 1981) is used to obtain the physical properties of open particles.

Suppose that $f(\mathbf{r})$ is the local pressure or velocity field function in the support domain of interpolation nodes. The approximation of $f(\mathbf{r})$ at the position of relaxation particles is
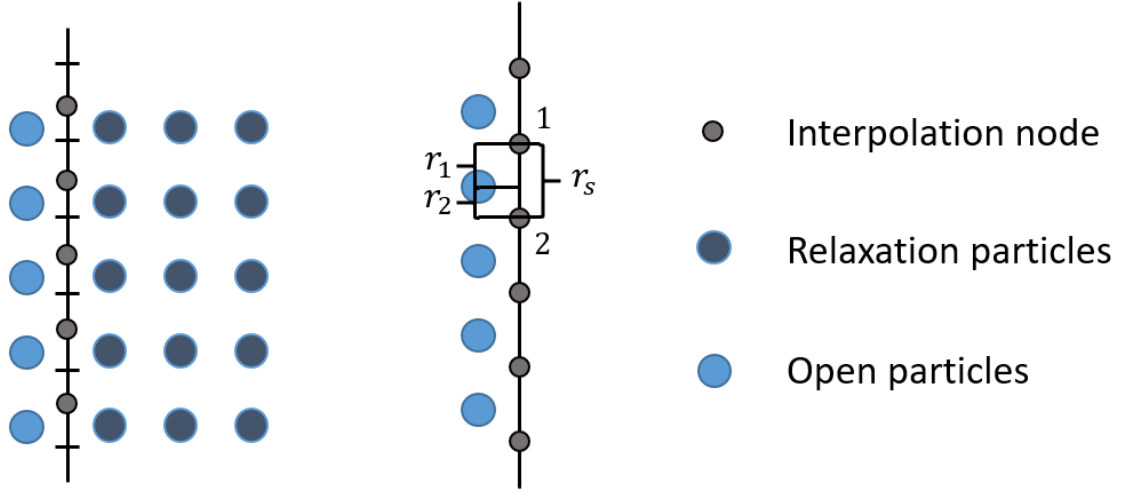
Fig. 6.5 Sketch of interpolation for open particles.

denoted as $f_h(\mathbf{r})$, which can be calculated with the help of a basis as:

$$f_h(\mathbf{r}) = \sum_{i=1}^{mn} q(\mathbf{r}_i)c_m(\mathbf{r}_i) = q^T(\mathbf{r})c_m(\mathbf{r}), \qquad (6.15)$$

where $q(\mathbf{r})$ is the basis function and mn is the term numbers of the basis function, c_m is the factor of the basis function. In this work, the quadratic basis is used as

$$q^T(\mathbf{r}) = [1, x, y, x^2, xy, y^2], mn = 6. \qquad (6.16)$$

Since pressure and velocity are interpolated, $f_h(\mathbf{r})$ can denote the local pressure and velocity reconstruction field here and is influenced by the nearby relaxation particles. Thus, it can construct a function of weighted residual Q:

$$Q = \sum_{j=1}^{n} W_q(\mathbf{r}_j)(f_h(\mathbf{r}_j) - f(\mathbf{r}_j))^2 = \sum_{j=1}^{n} W_q(\mathbf{r}_j)[(q^T(\mathbf{r}_j)c_m(\mathbf{r}_j) - f(\mathbf{r}_j))^2], \qquad (6.17)$$

where $W_q(\mathbf{r})$ is a weight function, n is the number of the relaxation particles inside the support domain of weight function.

For an arbitrary relaxation particle, the value of $c(\mathbf{r})$ can be determined by minimizing the weighted residual Q

$$\frac{\partial Q}{\partial c} = \mathbf{G}(\mathbf{r})c_m(\mathbf{r}) - \mathbf{H}(\mathbf{r})\mathbf{F}_q = 0, \tag{6.18}$$

where $\mathbf{G}(\mathbf{r})$ is given as

$$\mathbf{G}(\mathbf{r}) = \sum_{j=1}^{n} W_q(\mathbf{r}_j)q^T(\mathbf{r}_j)q(\mathbf{r}_j), \tag{6.19}$$

and $\mathbf{H}(\mathbf{r})$ is given as

$$\mathbf{H}(\mathbf{r}) = q^T(\mathbf{r})W_q(\mathbf{r}) = [q(\mathbf{r}_1)W_q(\mathbf{r}_1), q(\mathbf{r}_2)W_q(\mathbf{r}_2), ..., q(\mathbf{r}_n)W_q(\mathbf{r}_n)], \tag{6.20}$$

and $\mathbf{F}_q$ is field value

$$\mathbf{F}_q = [f_1, f_2, ..., f_n], \tag{6.21}$$

Solving for $c_m(\mathbf{r})$ from Eq. (6.18) and substituting it into Eq. (6.15) leads to

$$f_h(\mathbf{r}) = q^T(\mathbf{r})\mathbf{G}^{-1}(\mathbf{r})\mathbf{H}(\mathbf{r})\mathbf{F}_q = \Upsilon^T(\mathbf{r})\mathbf{F}_q, \tag{6.22}$$

where $\Upsilon^T(\mathbf{r})$ is the shape function. The pressure and vertical velocity of interpolation nodes can be obtained from $f_h(\mathbf{r})$. Meanwhile, the pressure gradient of interpolation nodes can be calculated by the gradient of $f_h(\mathbf{r})$ as

$$f_h'(\mathbf{r}) = (\Upsilon^T(\mathbf{r}))'\mathbf{F} = ((q^T(\mathbf{r}))'\mathbf{G}^{-1}(\mathbf{r})\mathbf{H}(\mathbf{r}) +$$
$$q^T(\mathbf{r})(\mathbf{G}^{-1}(\mathbf{r}))'\mathbf{H}(\mathbf{r}) + q^T(\mathbf{r})\mathbf{G}^{-1}(\mathbf{r})(\mathbf{H}(\mathbf{r}))')\mathbf{F}_q. \tag{6.23}$$

The pressure field at the open boundary enforces the Neumann boundary condition. Considering the right-hand sketch of Fig. 6.5, the pressure of an ordinary ghost particle is evaluated as follows

$$p_o = (p_{i1} + r_{io}p_{i2}^n\rho_{i1})W_{i1} + (p_{i2} + r_{io}p_{i1}^n\rho_{i1})W_{i2}, \tag{6.24}$$

where w_{i1} and w_{i2} are the weights of interpolation nodes. The weights in Fig. 6.5 are calculated in the same way as in Fig. 6.3. p_{i1}^n and p_{i1}^n denote the gradient of pressure at interpolation nodes 1 and 2, respectively. p_{i1} and p_{i2} denote the pressure at interpolation node 1 and 2, respectively. The vertical velocity of the ghost particle can be obtained using the same method.

SPH Results for OceanWave3D

In addition to coupling physical quantities from OceanWave3D, the SPH model also needs to interpolate physical quantities and pass them into OceanWave3D. In OceanWave3D, only free surface quantities can be coupled. Thus, the coupling is limited to the surface elevation and the vertical free surface velocity, yielding satisfactory results. The vertical free surface velocity $\tilde{w}^u$ can be obtained by SPH interpolation

$$\tilde{w}_i^u = \frac{\sum w_j^u W_{ij} V_j}{\sum W_{ij} V_j},\tag{6.25}$$

where i is the node located at the free surface in OceanWave3D, j is the fluid particle in SPH, and w_j^u is the vertical velocity of particle j.

OceanWave3D for Coupled Model

In the coupling region, the SPH solver needs velocity and free-surface level data from OceanWave3D. In order to transfer the OceanWave3D results to SPH, the interpolation of the data in the coupling region should be calculated. Generally, the particle positions of SPH and the node positions of OceanWave3D do not coincide in the coupled region. Therefore, the reference physical properties of the particles need to be obtained by interpolation at the nodes. Following the approach in Paulsen et al. (2014), the native pre-computed finite difference stencils of the solver are utilized for efficient evaluation of the following finite Taylor series:

$$\aleph_t(\mathbf{x_i} + \Delta\mathbf{x_i}) = \sum_{n=0}^{2a} \frac{\Delta^n}{n!} \frac{\partial^n \aleph}{\partial \mathbf{x_i}^n}(\mathbf{x_i}),\tag{6.26}$$

where $\aleph_t(\mathbf{x_i} + \Delta\mathbf{x_i})$ is the reference value of the SPH particle i at the position $\mathbf{x_i} + \Delta\mathbf{x_i}$. $\mathbf{x_i}$ is the position of the OceanWave3D node, which is the nearest neighbour node to SPH particle i. In the interpolation kernel, $2a + 1$ terms are applied ($a = 2$). Generally speaking, there is some error between the free-surface height of SPH and the OceanWave3D results. This means that SPH particles may exist outside the OceanWave3D grid nodes. If so, the grid in the vertical direction is directly selected as the highest node point.

As mentioned previously, the SPH particles in the open relaxation zone require velocity and free-surface level from OceanWave3D. When the velocity potential Φ is obtained in the σ-domain, the velocities can be calculated as follows:

$$u(\mathbf{x}, z) = \frac{\partial \Phi(\mathbf{x}, z)}{\partial x} = \frac{\partial \Phi(\mathbf{x}, \sigma)}{\partial x} + \frac{\partial \sigma}{\partial x} \frac{\partial \Phi(\mathbf{x}, \sigma)}{\partial \sigma},\tag{6.27}$$

$$v(\mathbf{x}, z) = \frac{\partial \Phi(\mathbf{x}, z)}{\partial y} = \frac{\partial \Phi(\mathbf{x}, \sigma)}{\partial y} + \frac{\partial \sigma}{\partial y} \frac{\partial \Phi(\mathbf{x}, \sigma)}{\partial \sigma}, \tag{6.28}$$

$$w(\mathbf{x}, z) = \frac{\partial \Phi(\mathbf{x}, z)}{\partial z} = \frac{\partial \sigma}{\partial z} \frac{\partial \Phi(\mathbf{x}, \sigma)}{\partial \sigma}. \tag{6.29}$$

In the present coupled model, the free-surface level and vertical free-surface velocity inside the open relaxation boundary are transferred, as shown in Fig. 6.1. To ensure a smooth transition from SPH results to OceanWave3D data, the same relaxation function as that used in Eq. (6.13) for the SPH model is used.

Coupling Strategies for Parallel System

Both the SPH and OceanWave3D codes are written in Fortran. However, the current SPH code is MPI-parallel and the OceanWave3D code is not parallel. Therefore, when coupling the two models, the coupling strategies under a parallel system is achieved. Since OceanWave3D is much more computationally efficient than SPH, a processor is used to run the OceanWave3D results separately. In the parallel SPH model, it can determine which processors in the SPH model have information that needs to be passed to OceanWave3D, based on the location of those processors. Therefore, point-to-point MPI communication can be achieved. The data is passed using *MPI − send* and *MPI − receive*. A detailed flowchart of the developed framework is attached in Fig 6.6.

Highlighting the differences from the published coupling model

Although a coupled SPH-OceanWave3D model (Verbrugghe et al., 2018, 2019) has been developed previously, the coupled model developed here uses different coupling techniques, mainly in terms of:

1. different particle generation/deletion methods on the coupling interface. In Verbrugghe et al. (2019), particle generation/ deletion at the coupling interface is based on the position of particle. This can lead to sudden changes in mass at the interface. The model in Verbrugghe et al. (2018) uses the moving wavemaker boundaries, and does not need to generate/delete particles.

2. different coupling physical properties. In Verbrugghe et al. (2018, 2019), only horizontal velocity at the coupling region (relaxation region) was considered. Only buffer particles (open particle here) were considered in their SPH region to correct the horizontal velocity, and no relaxation function was used (Verbrugghe et al., 2018, 2019).
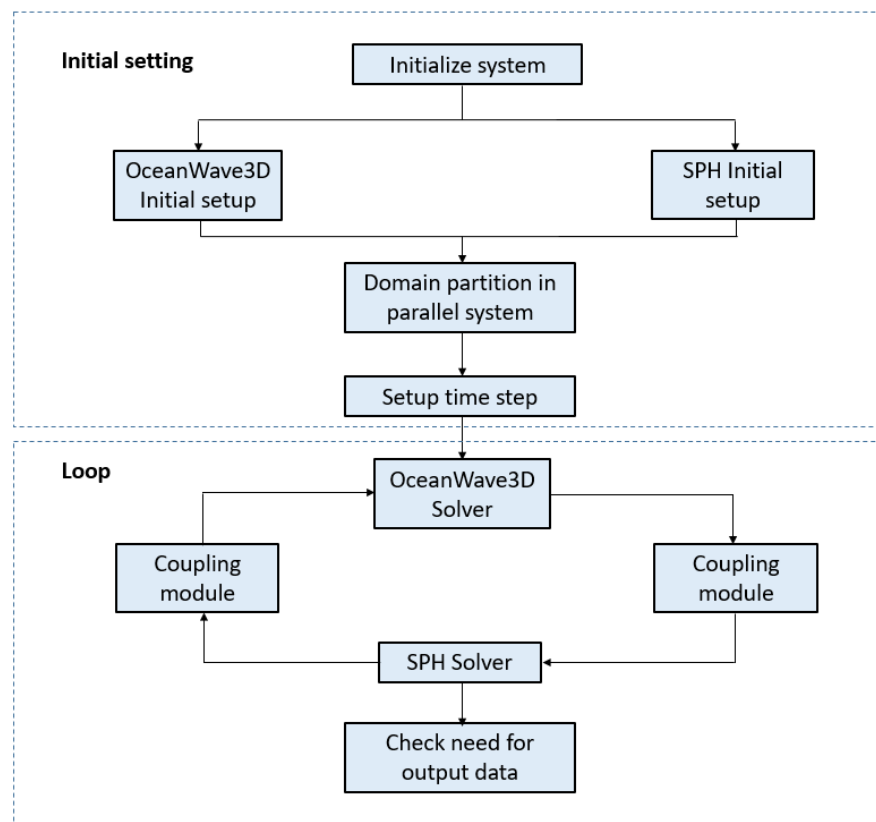
Fig. 6.6 Flowchart of coupled model framework.

In the present model, the horizontal velocity and free-surface level are both corrected based on the relaxation function.

3. different interpolation approach for open zone. In Verbrugghe et al. (2019), the density of buffer particles (open particles) was obtained using SPH kernel interpolation method proposed by Liu et al. (2005). While MLS reconstruction is used in the present model.

4. different parallel frameworks. The SPH code and OceanWave3D are both programmed by FORTRAN. While PYTHON was used to build the message transfer between those two codes in (Verbrugghe et al., 2018, 2019).

6.4   Numerical Validation

Regular Wave

The simulation of nonlinear regular waves is to verify the accuracy of the coupling scheme. Another important part is to demonstrate the contribution of coupled models in reducing computational cost by comparing the simulation time of different models. The numerical domain for the coupled model is shown in Fig. 6.8, where a 40 m long wave tank is defined. On the right side of the tank, a 5 m-long sponge layer is applied to absorb waves. On the left side of the tank, part of the OceanWave3D region, a 4 m long relaxation area is used to generate waves. L_a and L_b are the beginning and ending position of coupling region. A regular wave with wave height 0.1 m and wave period 2.0 s is used to validate the coupled model. The wave conditions have been chosen to be representative of Stokes' second order wave (as can be seen in Fig. 6.7). The mean average errors for amplitude MAE_a and phase MAE_p (Zhu et al., 2020) are calculated. Fig. 6.11 show the free surface elevation for various regular wave cases. Table 6.1 summarises the numerical settings, errors and costs of regular wave cases.

Comparing the results of cases (1), (2), (3), (4), and (5), it can be found that the variation in mesh size of OceanWave3D does not show much effect on the coupled simulation results. By comparing case (1), (6), and (7), it is found that as the particle spacing decreases, it gradually approximates the analytical solution. When the particle spacing is less than 0.01 m, it does not show a higher MAE_a and phase MAE_p with theoretical solution. The results of cases (1), (6), and (7) are presented in Fig. 6.9 which shows all MAE_a and MAE_p converging at lower first order for the range of resolutions tested. The coupled model is believed to give converged results when the particle spacing is 0.01 m. The coupled model is believed to give converged results when the particle spacing is 0.01 m. The comparison between cases (1), (8),
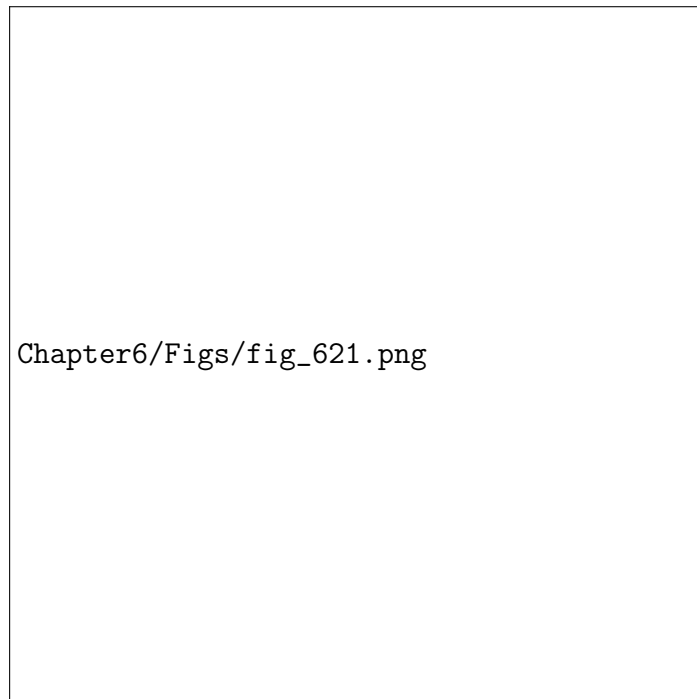
Fig. 6.7 Wave conditions on Le Mehaute abacus (Le Méhauté, 2013).(Figure has been removed due to Copyright restrictions.)
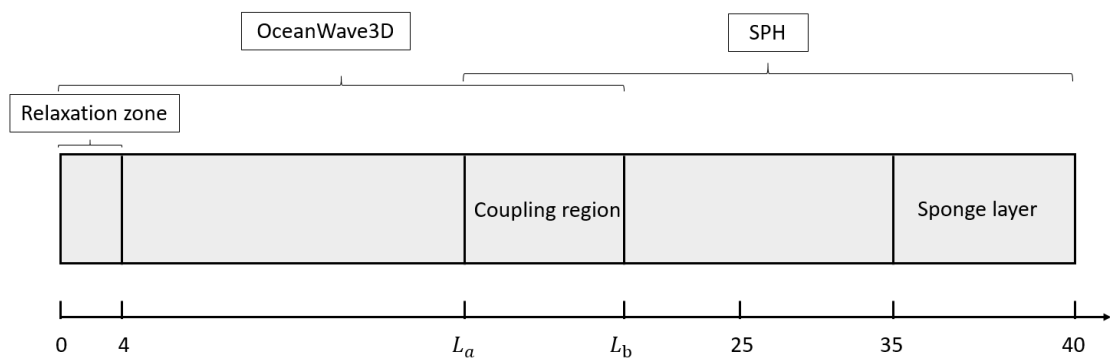
Fig. 6.8 Computation domain for wave simulation cases.
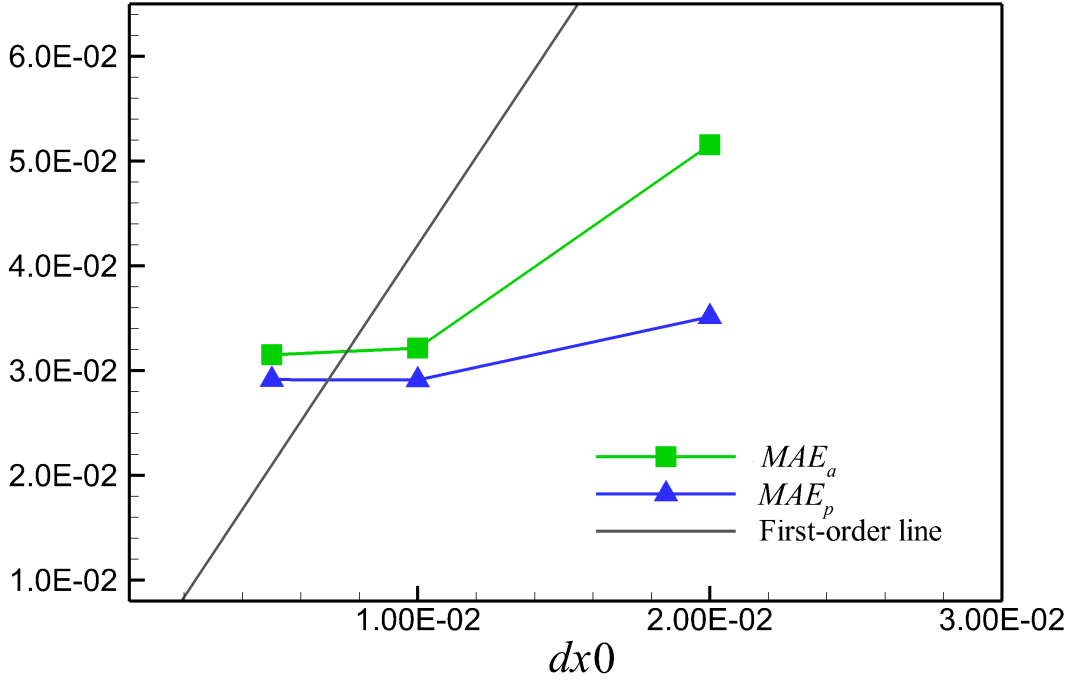
Fig. 6.9 Convergence of MAE_a and MAE_p with different initial particle spacing for regular waves.

and (9) is shown in Fig. 6.10. In cases (1), (8), and (9), different length of coupling region are selected, responding to 0.5λ, λ and 1.5λ (where λ denotes wave length). The results indicates that the accuracy improves as the length of the coupling region increases. The one wavelength long coupling region is believed to give satisfactory results, hence hereinafter it is applied in all the case studies unless otherwise specified.

The wave case simulated solely by OceanWave3D is better matched to the theoretical solution then those simulated by SPH or the coupled model according to cases (1), (10), and (11). SPH model is based on the NSE, which takes into account fluid viscosity and rotation. In the simulation of wave propagation, the results gradually deviate from the theoretical solution over time in these cases, due to the fluid viscosity as well as numerical dissipation (Zago et al., 2021). Fig. 6.12 shows the pressure field of cases (1), (10), and (11) at 11 s. It is found that the coupled model, SPH-only, and OceanWave3D have the smooth pressure field. Fig. 6.13 shows the velocity field of cases (1). Smooth horizontal and vertical velocity field is found near the coupling interface. The computational time of the coupled model is reduced relative to the SPH model. The above results indicate that using a coupled model to reduce the simulation area of the SPH can save computational costs.
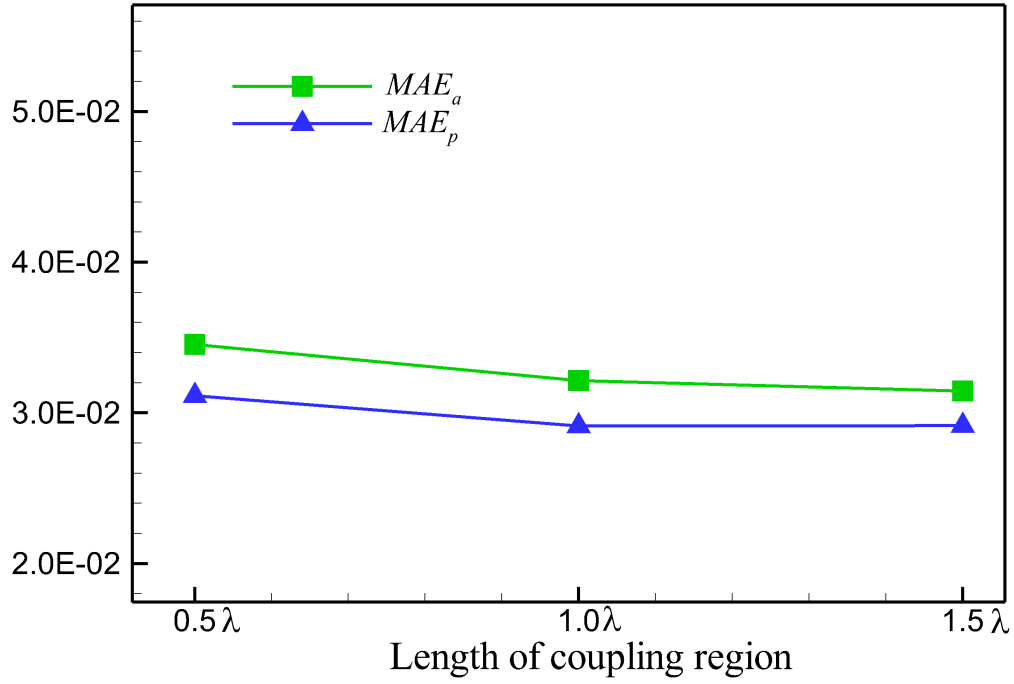
Fig. 6.10 MAE_a and MAE_p with different lengths of coupling region for regular waves.

Table 6.1 Numerical setup, errors and cost of the regular wave cases.

case	mesh numbers (x, y)	particle size (m)	particle number	L_a (m)	L_b (m)	MAE_a	MAE_p	Cores	Cost (h)
1	900×10	0.01	175 000	15.0	19.6	3.2%	2.9%	49	11.3
2	1800×10	0.01	175 000	15.0	19.6	3.2%	2.9%	49	12.0
3	450×10	0.01	175 000	15.0	19.6	5.2%	3.0%	49	11.0
4	900×20	0.01	175 000	15.0	19.6	3.2%	2.9%	49	11.6
5	900×5	0.01	175 000	15.0	19.6	3.2%	2.9%	49	11.0
6	900×10	0.02	43 750	15.0	19.6	5.0%	3.5%	49	3.1
7	900×10	0.005	700 000	15.0	19.6	3.1%	2.9%	49	47.5
8	900×10	0.01	175 000	15.0	17.3	3.4%	3.1%	49	11.3
9	900×10	0.01	175 000	15.0	21.9	3.1%	2.9%	49	11.3
10	2400×10	–	–	15.0	19.6	2.5%	2.3%	1	0.6
11	–	0.01	280 000	15.0	19.6	3.6%	2.9%	48	23.2
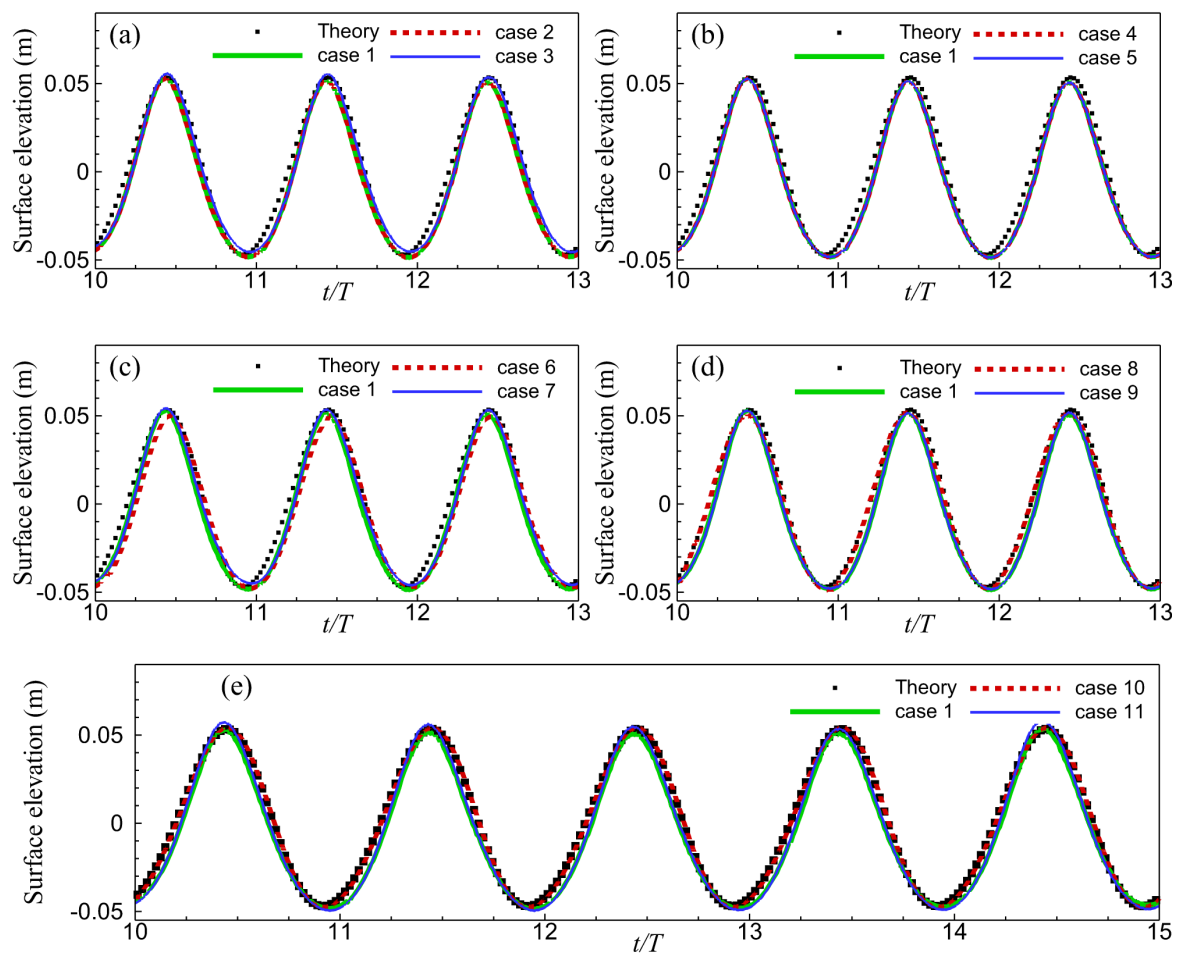
Fig. 6.11 Free surface comparison between numerical simulation and theory solution for regular waves.
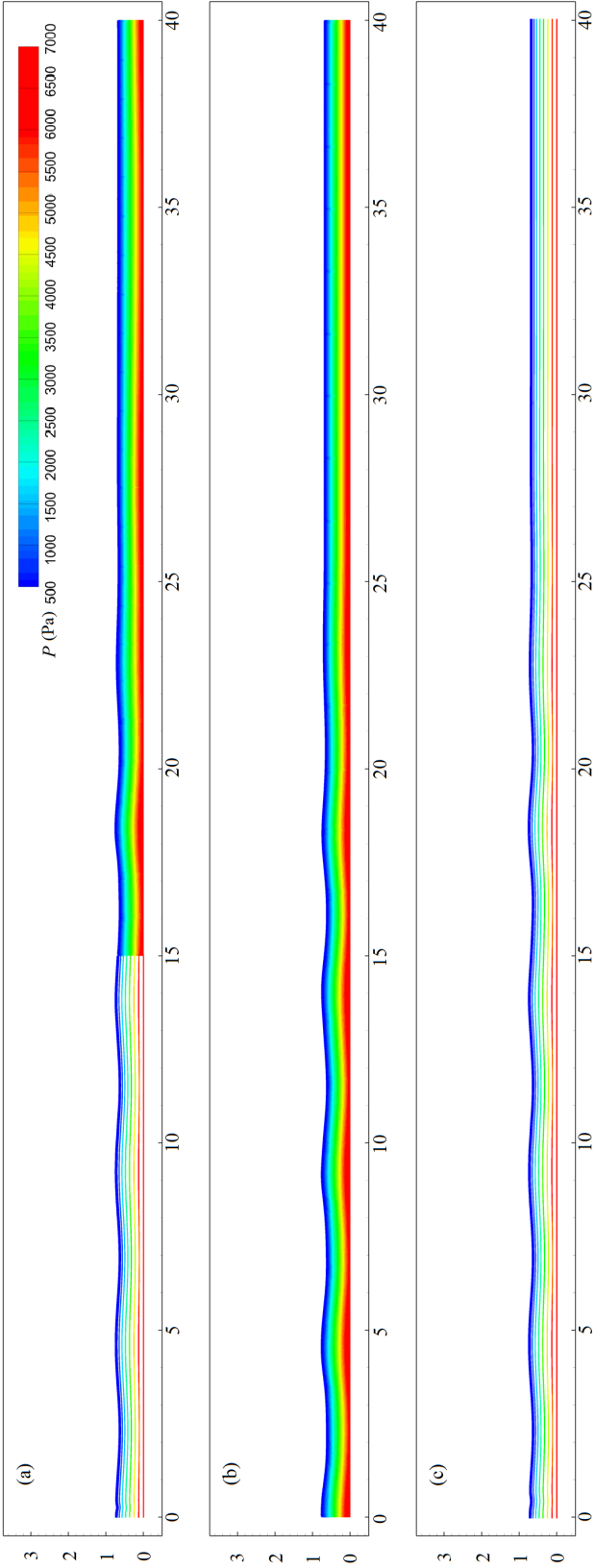
Fig. 6.12 Pressure field comparison between coupled model (a), SPH (b), and OceanWave3D (c) for regular waves.

Irregular Waves

To examine the performance of the coupled model in modelling irregular waves, a JONSWAP spectrum is selected to generate irregular waves with significant wave height $H_s = 0.15$ m, peak period $T_p = 2.0$ s for a water depth $d = 0.66$ m. Initial particle spacing is 0.01 m, and the time step is 0.0001 s. The initial particle spacing was chosen with reference to the conclusions on particle convergence in Table 6.1. Particle spacing less than 0.01m has less variation in error. The initial time step refers to Section 3.7 for the time step requirements. The numerical domain for the coupled model is shown in Fig. 6.5. Coupling interface is at $L_a = 6.0$ m. Mesh numbers is 900×10 ($x \times y$).

The water surface elevation measured at 15.0 m is plotted in Fig. 6.14. The theoretical time series is also represented for comparison. At local peaks, SPH results differ from theoretical values. There are two possible reasons for this: insufficient particle resolution and choice of relaxation domain length. Altomare et al. (2017) suggested that wave height should be less than ten times of particle resolution to achieve accurate modelling of regular waves. For the modelling of irregular waves, this condition may not be satisfied all over the free surface, affecting the accuracy of small wave heights in the irregular wave spectrum. The length of the relaxation domain may not be appropriate for all waves, either. Fig. 6.15 presents the contour of the velocity field at two representative moments. The velocity fields of the two numerical models are matched together at the coupling interface. The black lines indicate the free surface level in OceanWave3D. It can be found that the free surface evolution of OceanWave3D in the relaxation region is in good agreement with the SPH results.

Waves over a Submerged Bar

Regular wave propagation over a submerged bar (Beji and Battjes, 1993) was simulated. The numerical flume, the geometric setup of the bar, and the position of four wave gauges (WG1–WG4) are shown in Fig. 6.16. Two regular waves of the same period $T_w = 2.5$ s are simulated with different wave heights H_w of 0.022 m and 0.042 m. Non-breaking and spilling are observed, respectively, for the two examined wave conditions. Different from the coupled SPH model for the empty wave tank as reported in Sections 5.1 and 5.2, three regions (except for the coupling regions) are applied for the present case: one SPH region in the middle of the wave tank covering the submerged bar, and two OceanWave3D regions occupying the remainder of the tank. The SPH region is from 6 m to 23 m. Regions simulated by OceanWave3D are from 0 m to 9 m and from 20 m to 40 m. Coupling regions are from 6.65 m to 9 m, and from 20 m to 22.35 m. Initial SPH particle spacing is 0.005 m. The numerical setup is shown in Table 6.2. The mesh spacing in OceanWave3D is much larger
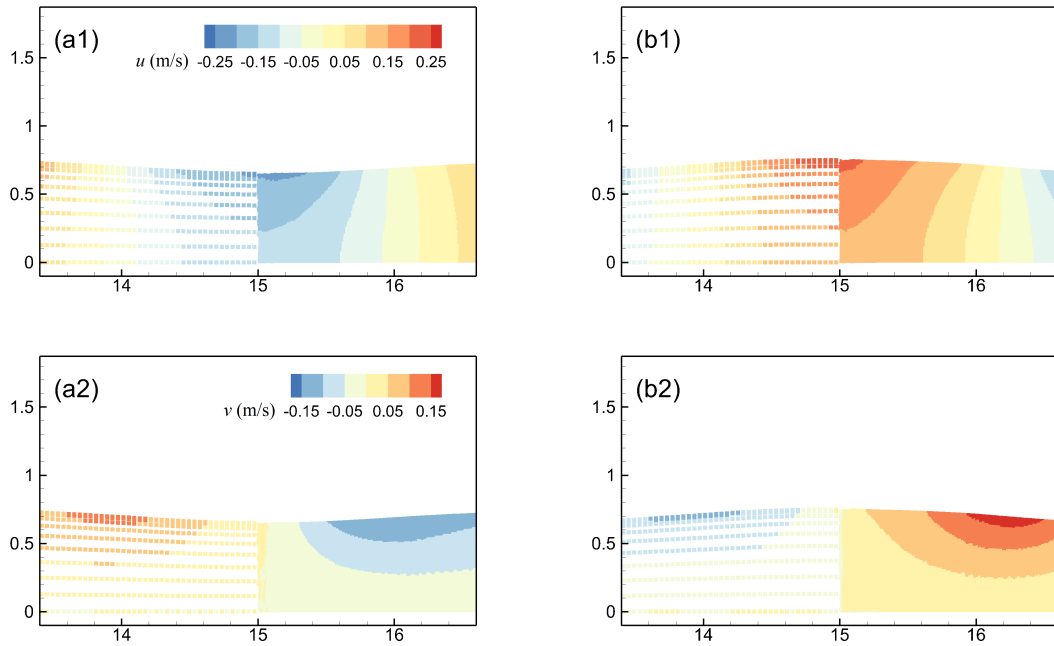
Fig. 6.13 Velocity field of regular waves near coupling region at $t = 13.5$ s and 14.5 s. (Labels 'a' and 'b' denotes 13.5 s and 14.5 s, respectively; Label '1' and '2' denotes horizontal velocity and vertical velocity, respectively.)
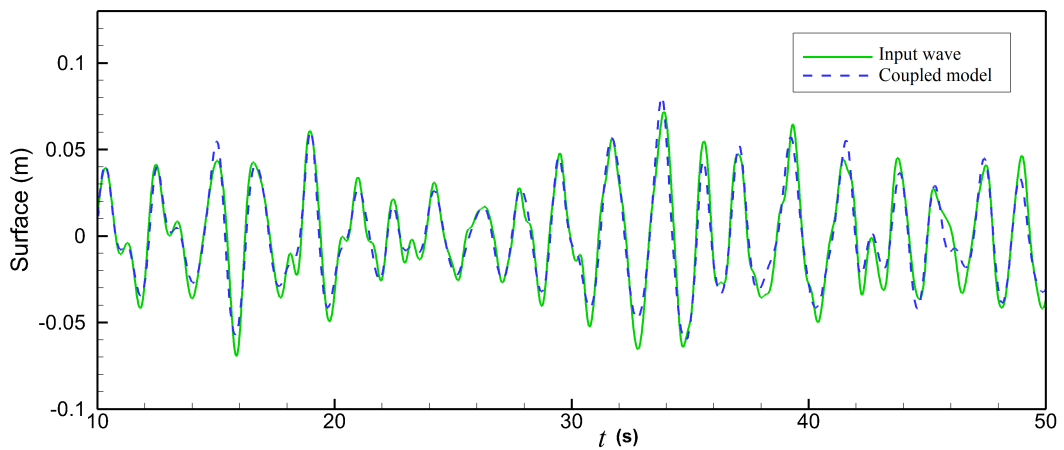
Fig. 6.14 Free surface comparison between coupled model and theory solution for irregular waves.
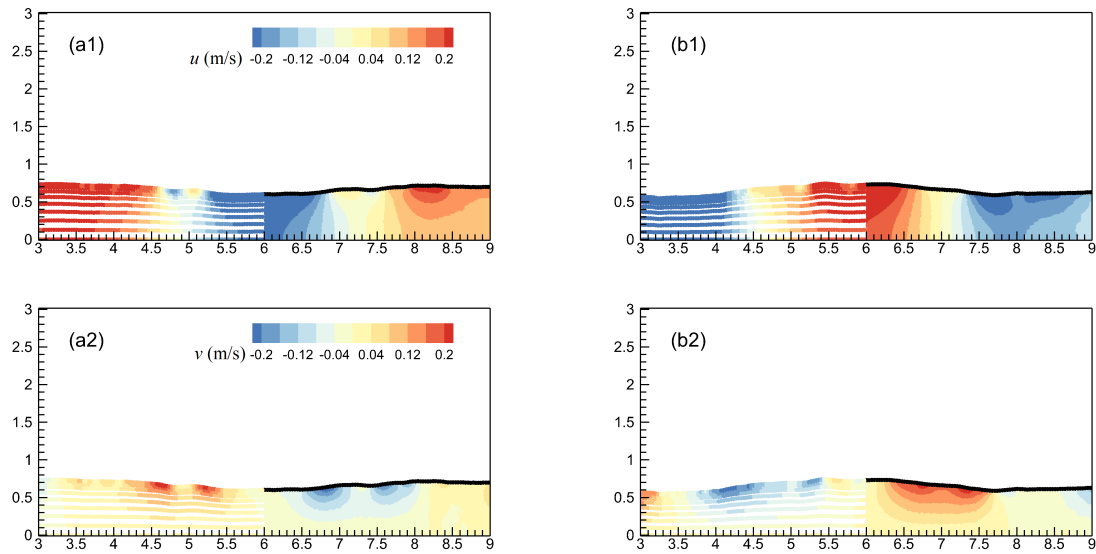
Fig. 6.15 Velocity field of regular waves near coupling region at $t = 28.2$ s and 29.2 s. (Labels 'a' and 'b' denotes 28.2 s and 29.2 s, respectively; Label '1' and '2' denotes horizontal velocity and vertical velocity, respectively.)

Table 6.2 Summary of the numerical setup of waves over a submerged bar.

case	mesh numbers (x, y)	particle size (m)	Time step (s)	H_w (m)	T_w (s)	Breaking type	Cores	Cost (min)
s1	500×10	–	0.01	0.022	2.5	Non-breaking	1	1
s2	$225 \times 10, 500 \times 10$	0.005	0.00001	0.022	2.5	Non-breaking	33	1217
s3	500×10	–	0.01	0.042	2.5	Spilling	1	1
s4	$225 \times 10, 500 \times 10$	0.005	0.00001	0.042	2.5	Spilling	33	1217

than the initial particle spacing in SPH. This is because the program crashes when it tries to use a denser particle spacing for case 3. A warning occurs when simulating wave breaking at higher resolutions.

Table 6.3 Table 6.3 shows the time spent on the three parts, i.e., OceanWave3D, SPH and coupling, for case s2. It demonstrates that Oceanwave3D takes the least amount of time (0.04%). Coupling takes about 12.8% of the time. The main cost is the SPH module, which accounts for 87.5% of the total time.

Table 6.3 Time cost of each module in the coupled model for case s2.

	OceanWave3D Module (min)	Coupled Module (min)	SPH Module (min)	Total cost (min)
s2	0.48	151	1065	1217
%	0.04	12.8	87.5	100
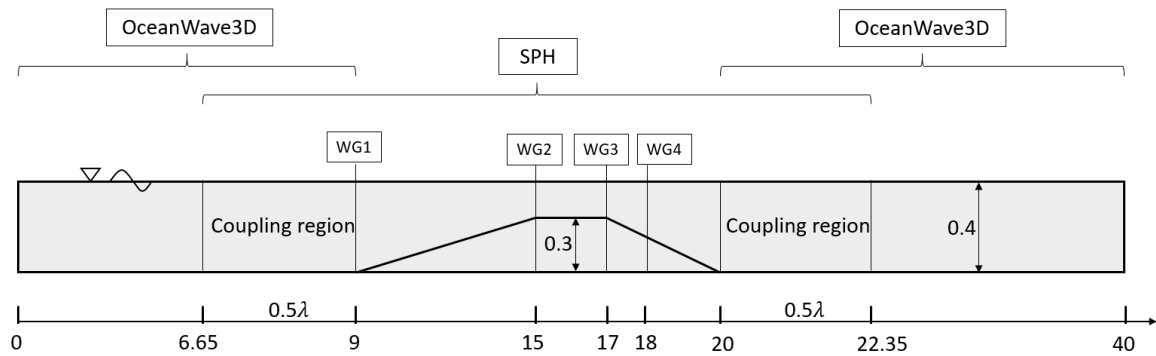
Fig. 6.16 Numerical setup for waves over a submerged bar.

Figure 6.17 compares the free-surface elevation at the four wave gauges (WG1–WG4). As the wave passes over the dam, the wave profile can be seen to be deformed. Comparing the coupled model, OceanWave3D and experimental results, it shows that the coupled model produces more accurate results at the local wave crests than the OceanWave3D. The high computational speed makes OceanWave3D attractive, although there is a slight decrease in computational accuracy. It is also important to note that the coupled model uses a much denser initial particle spacing than the grid employed in. This shows that OceanWave3D can achieve same results at this grid size (much larger than the particle spacing in SPH) with coupled SPH model. Thus, the larger grid size is not the main reason of the large errors of OceanWave3D for the breaking wave cases in Figure 6.18.

Figure 6.18 illustrates the evolution of the free surface for the regular wave with a higher wave height of 0.042 m. Fig. 6.19 illustrates the pressure field as well as the pressure field of the interface attachment. It shows that the interface pressure field remains smooth and stable at different moments in time. In Fig. 6.18 (c) and (d), it can be observed that there is a large discrepancy between the OceanWave3D results and the experimental results, while the coupled model shows better agreement. Wave breaking occurs between $x = 15.0$ m and 17.0 m. Fig. 6.20 shows the snapshots at different times of the coupled model and the OceanWave3D model at the bar. It can be seen that OceanWave3D's calculation nodes do not change in the horizontal direction, but move in the vertical direction to simulate a wave passing over the bar. OceanWave3D is therefore not appropriate for simulating wave breaking. When the incident wave height is 0.022 m, OceanWave3D and SPH show similar wave propagation processes over the submerged bar. Overall, in the absence of non-breaking conditions, OceanWave3D's high efficiency makes it very competitive. In the case of wave breaking, OceanWave3D's results deviate far from the experimental results and the coupled model is the better choice. Also, as the SPH domain is reduced in the coupled model, the coupled model can further improve the efficiency compared to the SPH model.
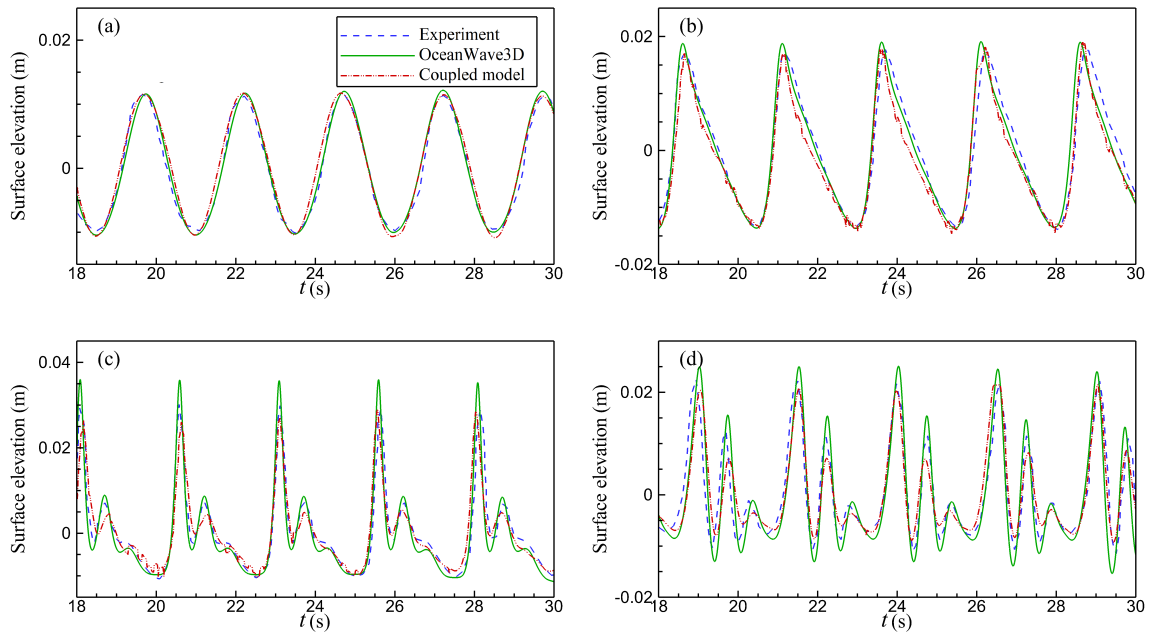
Fig. 6.17 Free surface elevations at the wave gauges WG1 (a), WG2 (b), WG3 (c), WG4 (d) for regular waves with wave period 2.5 s and wave height 0.022 m.
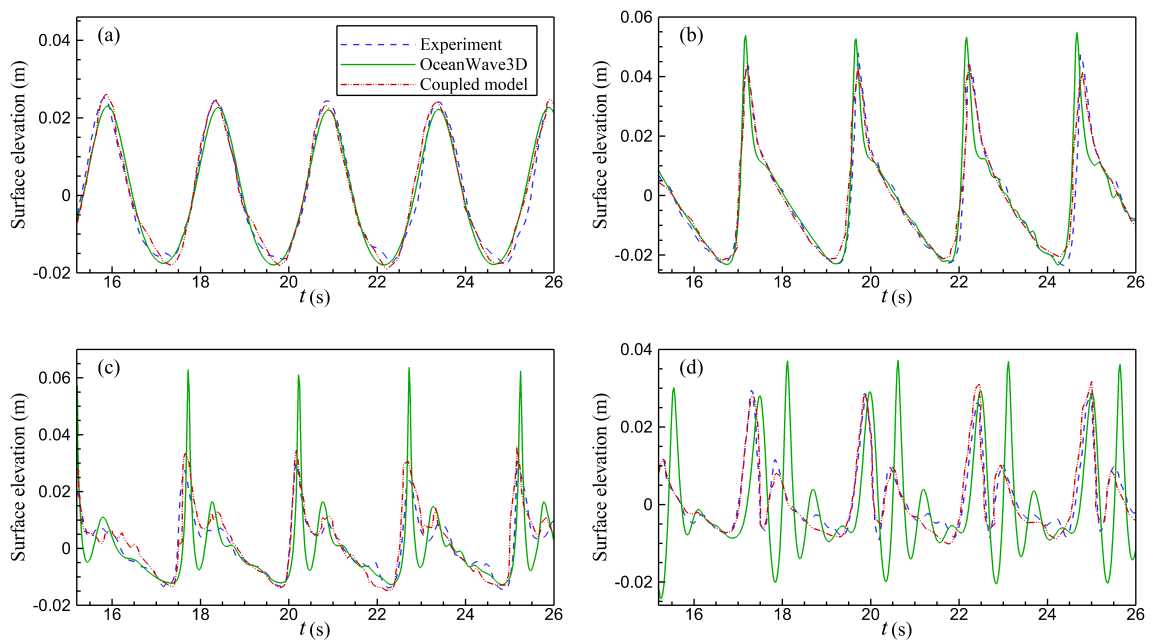
Fig. 6.18 Free surface elevations at the wave gauges WG1 (a), WG2 (b), WG3 (c), WG4 (d) for regular waves with wave period 2.5 s and wave height 0.042 m.
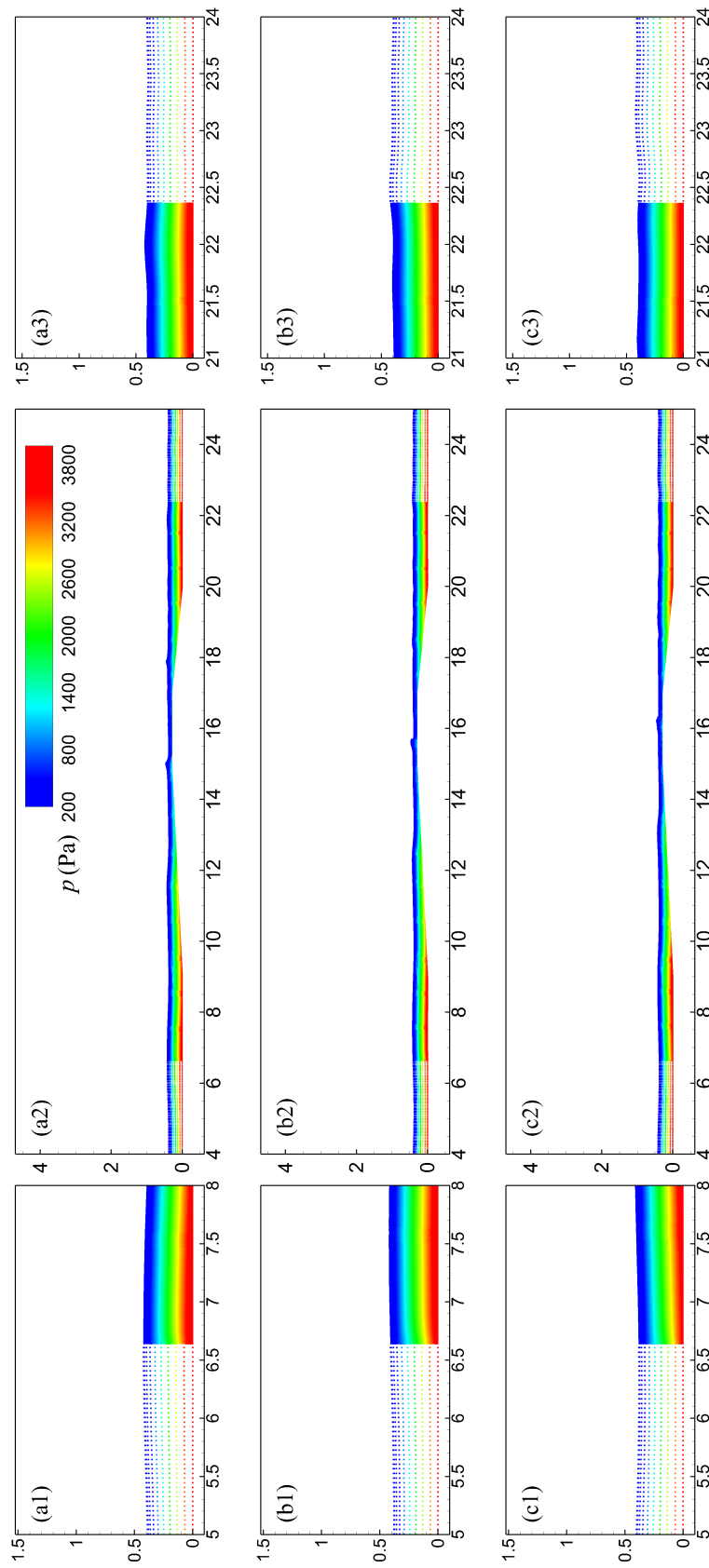
Fig. 6.19 Pressure field near the left coupling interface (1), near the bar region (2), and near the right coupling interface (3) at $t = 18.5$ s (a), 19.0 s (b), and 19.5 s (c) predicted by the coupled model for wave period 2.5 s and wave height 0.042 m.
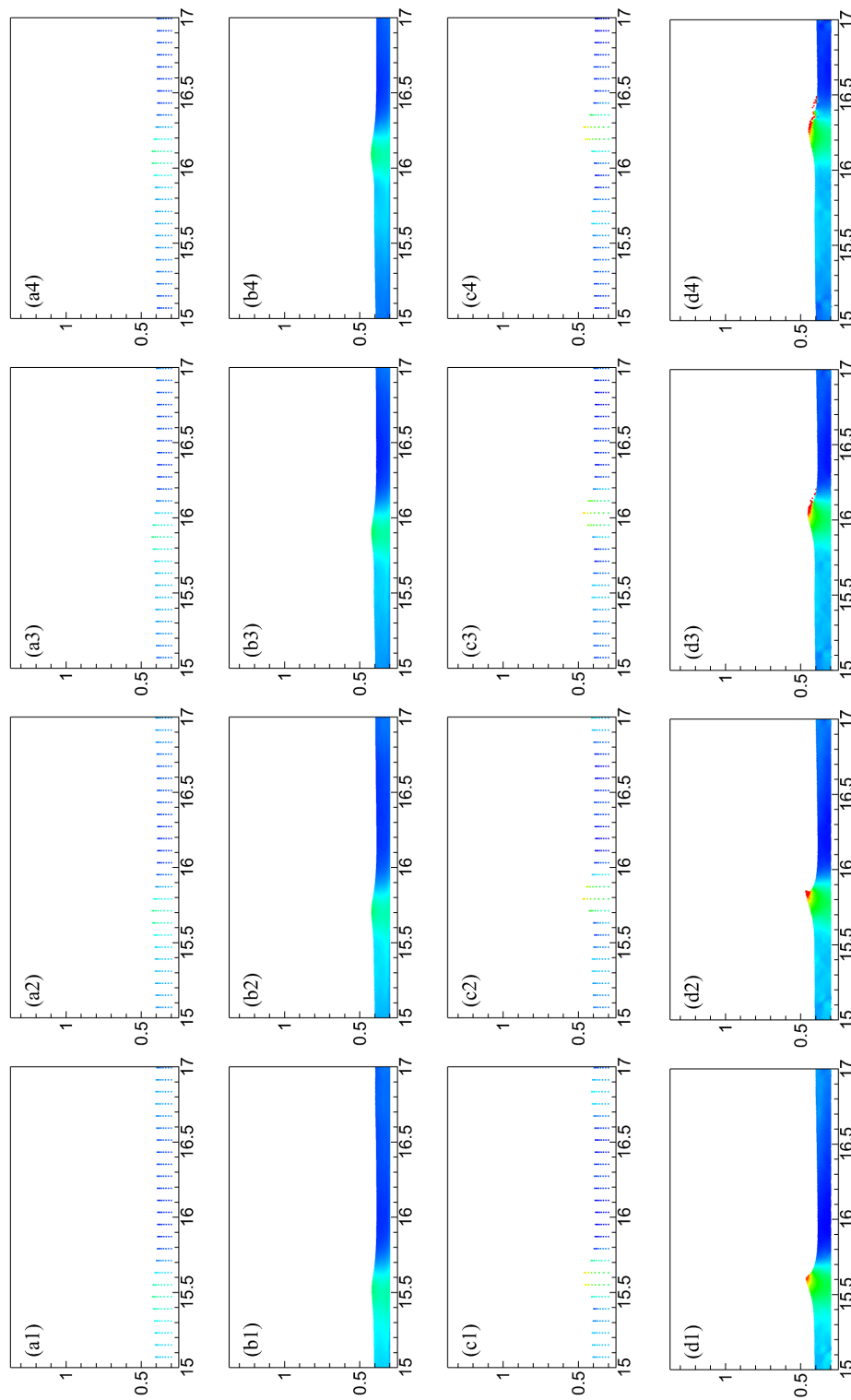
Fig. 6.20 Contour plot of the horizontal velocity above the submerge bar for wave period 2.5 s and wave height 0.042 m: OceanWave3D (a) and (c), coupled model (b) and (d) at $t = 22.75$ s (1), 23.05 s (2), 23.25 s (3), and 23.75 s (4).

6.5   Summary of the Coupled SPH with OceanWave3D

In this work, a two-way coupled model is proposed to hybridize the SPH model with OceanWave3D. The SPH model is used to simulate the nonlinear regions, while the remainder of the domain is simulated with the OceanWave3D, which is based on a fully nonlinear potential flow theory with less computational expense. The development of coupled models has shortened the SPH computational domain. SPH and OceanWave3D are overlapping at the coupling region. In the SPH model, the open relaxation boundary is used in the coupling region. Horizontal velocity and free-surface elevation in the open zone are obtained from OceanWave3D, while vertical velocity and density are obtained from the relaxation region by moving least square reconstruction. The coupling region builds smooth transitions thanks to the relaxation function. The entire coupled model is calculated in a parallel framework, where OceanWave3D is assigned only one processor to calculate it, while the MPI-based parallel SPH model is calculated using multiple processors in the SPH region.

The coupled model is tested for several cases including regular waves, irregular wave and waves over a submerged bar. In terms of computational accuracy, the coupled model results are better than the SPH model but not as good as the OceanWave3D results. This is probably because the shortened SPH region reduces the error due to the numerical dissipation of the SPH. The coupled model is less computational expensive than the SPH-only model, but far more expensive than OceanWave3D. This means that the additional computation time required for coupling the SPH and OceanWave3D models is much smaller than the reduced computation time due to the shortened SPH region. Furthermore, the results show that the longer the length of the coupling region the higher the accuracy. The coupled model can also reproduce the surface elevation of irregular waves. For cases of waves over a submerged bar, OceanWave3D is far less expense than the coupled model. However, the coupled model shows a better agreement with the experimental free-surface elevation for the wave-breaking condition. Finally, it can be concluded that the coupled model can be highly accurate and less computational expensive for wave hydrodynamics. The coupled model preserves the ability of the SPH model to handle nonlinear surfaces while being computationally cheaper than an SPH-only model.

Chapter 7

Investigation of the U-OWC Device

7.1 Introduction

U-shaped oscillating water column (U-OWC) device was initially developed by Boccotti (2003). Compared with typical OWC devices, U-OWC devices have a vertical duct resulting from a submerged wall on the outside of the chamber (as shown in Fig. 7.1). For U-OWC devices, wave loads on the U-OWC devices has not yet been widely explored. The present SPH model was utilised to simulate a U-OWC device in this chapter, and validated by comparing results with experimental data. Following that, the wave loads on the U-OWC device with different geometric parameters and wave conditions were predicted. The numerical findings are intended to serve as a guide for U-OWC device dependability design.

7.2 Experimental and Numerical Setup

The experiments of a U-OWC device were carried out at University of Plymouth.The experiments of a U-OWC device were carried out by Dr. John Samuel at the University of Plymouth. The wave tank is 35 m long and 0.75 m high. An U-OWC device placed before the end of the flume with the back wall of the structure at a distance of 27.0 m from the wave paddle. An orifice is used to simulate the damping of the turbine. Four wave heights and three periods were combined, as shown in Table. 7.1. Finally, two orifice radii, corresponding to two values of turbine damping, were used in the tests: $e = 3$ mm and 4 mm. These two open radii correspond to an open rate O_r of 0.4% and 0.7%. O_r represents the ratio of the top opening to the area of the entire top cover. Eight pressure sensors were placed on the lip wall facing outside (P1-P6) and inside the chamber (P7 and P8), as shown in Fig. 7.1. P5, P7,
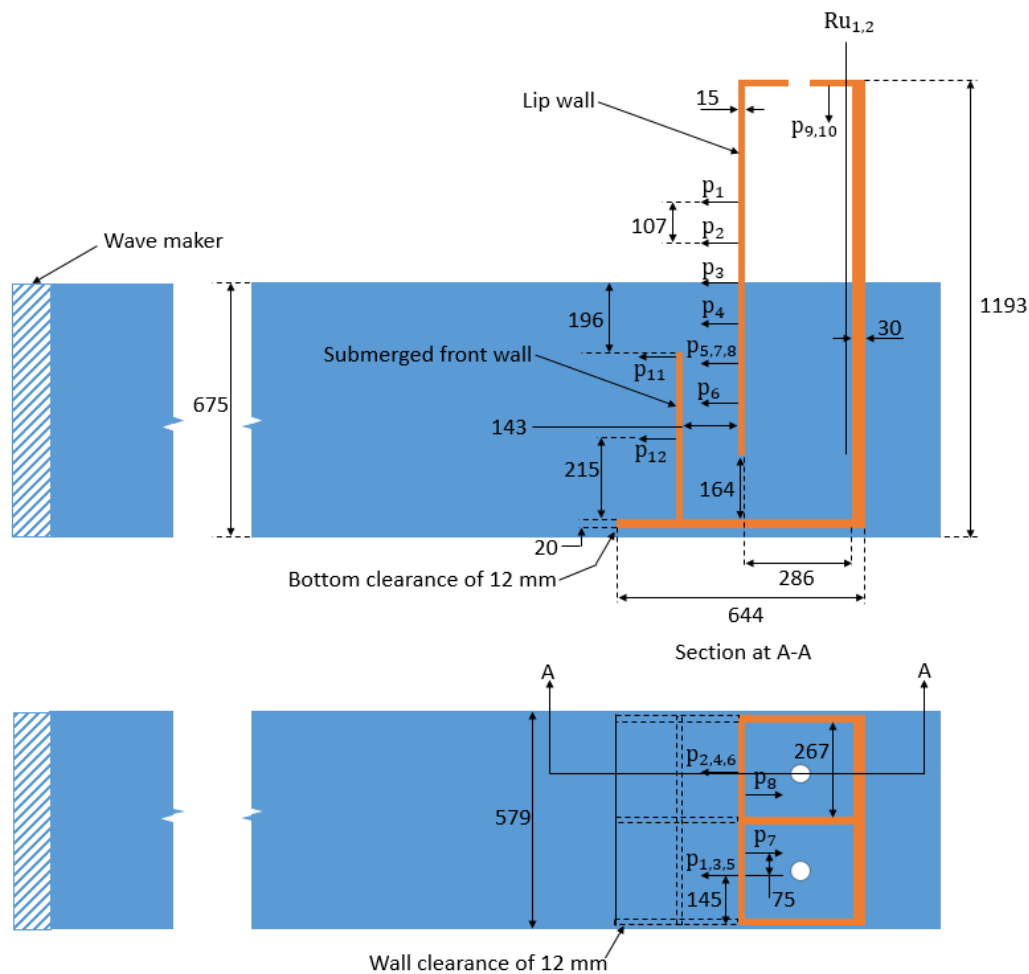
Fig. 7.1 Cross sectional and plan view of the U-OWC in the wave tank adapted from Dr. John Samuel.

and P8 have the same vertical position. The capture frequency of pressure sensor and wave gauge are 1920 Hz and 128 Hz. All wave conditions are recalibrated before the tests.

Current experimental data on sea conditions are limited. The experiment is limited to regular waves. For more complex wave conditions, such as irregular waves, more experiments are needed. Only two opening sizes were considered for the top opening. Different opening sizes have different effects on air compressibility. Therefore, more opening sizes need to be considered. In addition, the air flux at the top opening is still obtained by measuring the height change of the free surface. In the future, more reasonable ways of measuring open air fluxes may be needed.

The numerical simulations have the same setup (including location of measurement points) as experiments. The numerical wave tank is shown in Fig. 7.2. The entire computational domain is divided into two parts: the SPH region and the Oceanave3D region. The

Table 7.1 Wave parameters and open rate for investigating related hydrodynamic performance.

Case	Wave period (s)	Wave height H_s (m)	Wave length L_s (m)	Wave steepness H_s/L_s	Open rate (%)
1	2.15	0.050	4.96	0.010	0.7
2	2.15	0.100	4.96	0.020	0.7
3	2.15	0.150	4.96	0.030	0.7
4	2.15	0.247	4.96	0.050	0.7
5	1.96	0.100	4.42	0.052	0.7
6	1.70	0.100	3.67	0.027	0.7
7	1.70	0.100	3.67	0.027	0.4
8	1.96	0.100	4.42	0.023	0.4
9	2.15	0.100	4.96	0.020	0.4
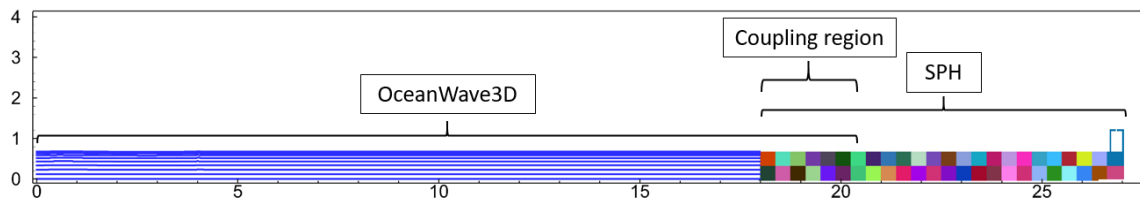
Fig. 7.2 Sketch of the numerical setup and subdomain distribution in the SPH-based wave tank.

coupling interface should not be too close to the OWC unit because of the presence of the nonlinear free surface condition. Thus, numerical regions from 18 m to 27 m are simulated using SPH. 18 m is the beginning of the coupling region, and the length of the overlapping region is half the incident wave wavelength. Fig. 7.2 shows 49 sub-domain divisions using 49 cores. 1 core is used for the Oceanwave3D solver, whereas the remaining 48 cores are used for the SPH solver. Firstly, the validation was carried out by comparing the data from both physical and numerical models. Once the numerical model has been validated, the model is used to analyse the effect of the geometry on the wave loads of the U-OWC device. Different incident waves are considered for wave loading, including five different wave heights and five different wave periods. Then, different geometrical designs of the U-OWC are modelled. The influences of the width and height of the U-shaped structure on the wave loading are considered.

7.3   Model Validation

Damping Factor

Before proceeding with the model validation, it is necessary to determine the damping factor. The damping factor is used to obtain the instantaneous air pressure from the flow rate/pressure relationship in the pneumatic model. The velocity ΔV_f of the free surface is calculated using the following equation,

$$\Delta V_f = \frac{\eta_{n+1} - \eta_n}{t_{n+1} - t_n}, \tag{7.1}$$

where η_n and t_n denote the free-surface level and the time, respectively, at the n time points. Based on the opening rate, it can obtain the air flow velocity q_d at the orifice

$$q_d = \frac{\Delta V_f}{O_r}. \tag{7.2}$$

The relationship between the flow rate and the air pressure inside the chamber is shown in Fig. 7.3. To represent the connection between air velocity and air pressure inside the chamber, the quadratic formulas are utilised

$$P_a = \begin{cases} K_{dm}(q_d)^2, & q_d > 0, \\ -K_{dm}(q_d)^2, & q_d \leq 0, \end{cases} \tag{7.3}$$

where $K_{dm} = 1.25$ and 1.47, respectively, for open rate 0.4% and 0.7%. Although some of the experimental data deviated from the fitted curve, especially at higher flow rates, the correlation coefficient of the two curve fits was 0.912 and 0.932, respectively. Thus, 1.25 and 1.47 are used as damping factors for open rate of open rate 0.4% and 0.7%.

Validation

Fig. 7.4 and Fig. 7.5 show the time histories of free surface and air pressure drop inside the chamber for wave case 2 and case 4, respectively. The MAE_a and MAE_p of the free-surface elevation from the numerical simulation for case 2 are 4.1 % and 1.9%, respectively. While the MAE_a and MAE_p of the free-surface elevation from the numerical simulation for case 4 are 1.5 % and 2.3%, respectively. The MAE_a and MAE_p of the air pressure from the numerical simulation for case 2 are 8.2 % and 2.0%, respectively. While the MAE_a and MAE_p of the air pressure from the numerical simulation for case 4 are 5.0 % and 4.6%, respectively.

R²=
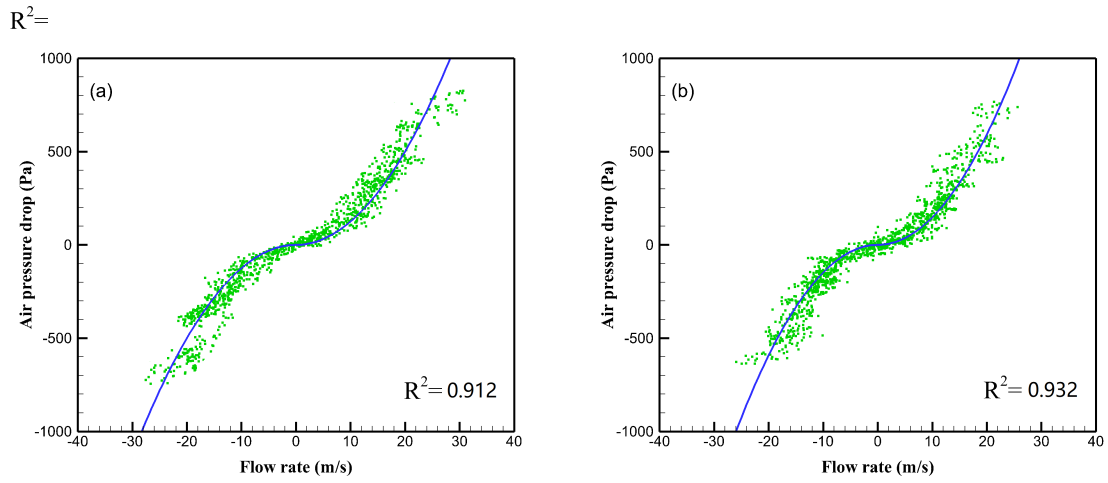
Fig. 7.3 Pressure drop versus flow rate for open rate 0.4% (a) and 0.7% (b). Green dots: experimental data; Blue line: fitting curve.
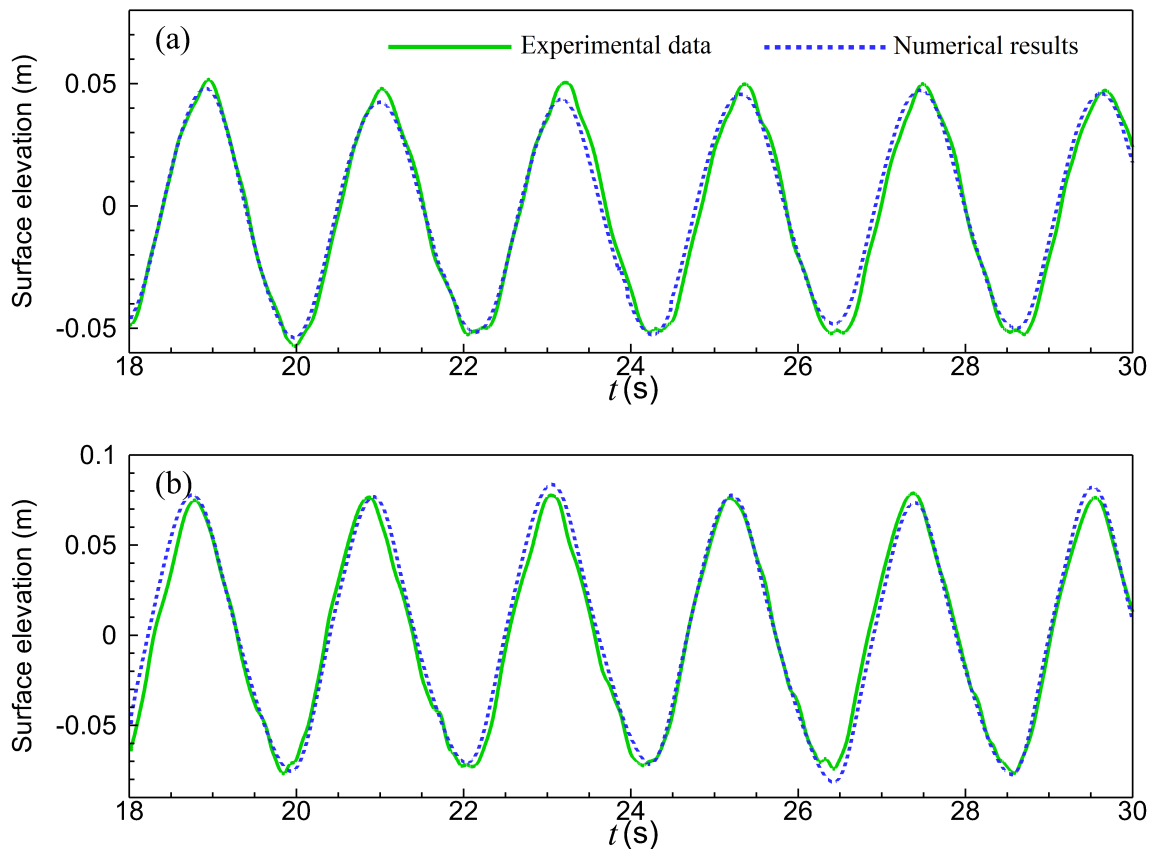
Fig. 7.4 Time series of surface elevation inside the chamber for case 2 (a) and case 4 (b). Experimental data of surface elevation from Ru 1 as Fig. 7.1.
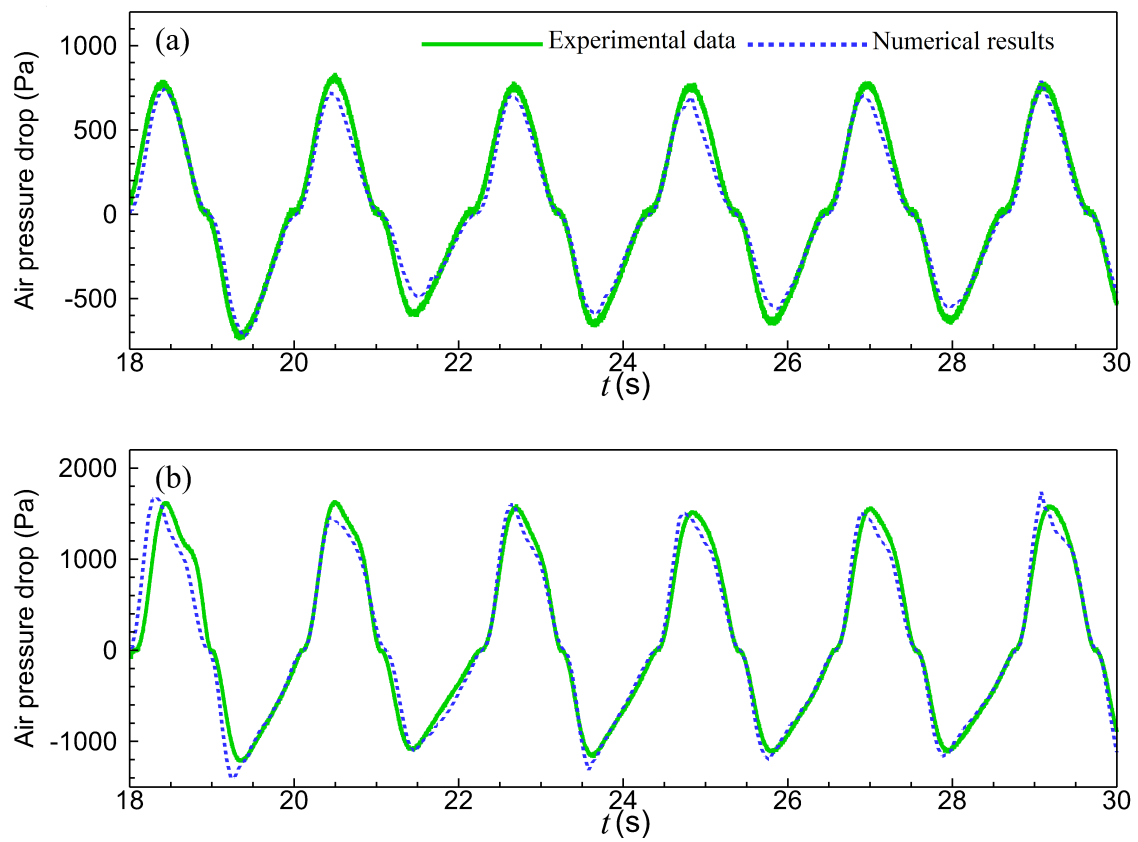
Fig. 7.5 Time series of air pressure drop inside the chamber for case 2 (a) and case 4 (b). Experimental data of air pressure from P9 as Fig. 7.1.
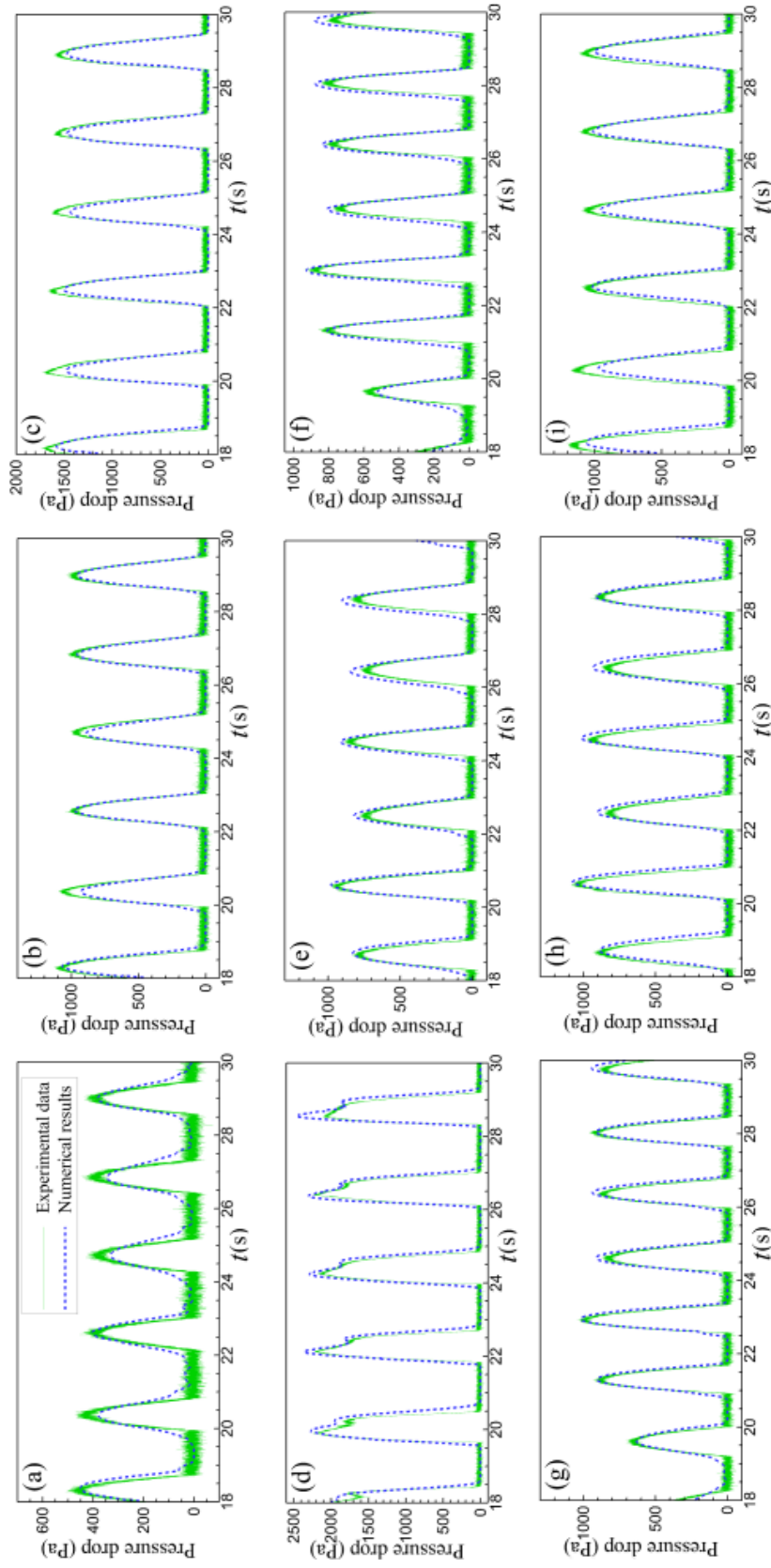
Fig. 7.6 Time series of pressure at sensor 3 for case 1 (a), case 2 (b), case 3 (c), case 4 (d), case 5 (e), case 6 (f), case 7 (g), case 8 (h), and case 9 (i).

The time series of pressures at pressure sensors for case 2 and case 4 are shown in Fig. 7.7 and Fig. 7.8, respectively. Good agreements between the simulations and the experiments of the wave pressure for case 2 on the inner and outer side of the front wall are achieved as shown in Fig. 7.7. For case 4, pressure peaks generally have an error of less than 10% at each pressure measurement point. Figure 7.10 shows the pressure, horizontal and vertical velocity fields. Smooth numerical solutions can be found near the coupling interface. Also, the variation of the velocity field from 15 m to 18 m in OceanWave3D region shows that the two-way coupled model can transfer reflected wave effects into OcanWave3D. In Fig. 7.11, the complex free-surface condition qualitatively agrees well with the experiment at $t = 21.4$ s and 22.4 s for case 4. At $t = 21.4$ s, a rolling wave in front of the submerged wall can be observed. The height of the free surface level inside the chamber is greater than the height of the free-surface level in front of the lip wall at 21.4 s. At 22.4 s, the splash generated by the wave slamming against the lip wall is reproduced. Figure 7.11 demonstrates the good capability of SPH in modelling nonlinear free surfaces.

In Fig. 7.6, it can be seen that a double pressure peak phenomenon occurs in case 4, and similar phenomenon is not observed in cases 1, 2 and 3. The wave height for case 4 is 0.247 m, much larger than that in the other cases. The larger the wave height, the higher the incident wave power. In case 4, splashing occurs due to strong wave-structure interactions, as shown in Fig. 7.11. The splashdown will cause slamming of the water surface. However, smaller splashes generate less slamming pressure as shown in Fig. 7.11. Figure 7.9 shows the velocity direction of the fluid particles in front of the front wall at three moments for cases 2 and 4. It can be noticed that as the water falls, vortices are generated near the wall. This could be a reason why the double peaks of pressure are observed in case 4 only.
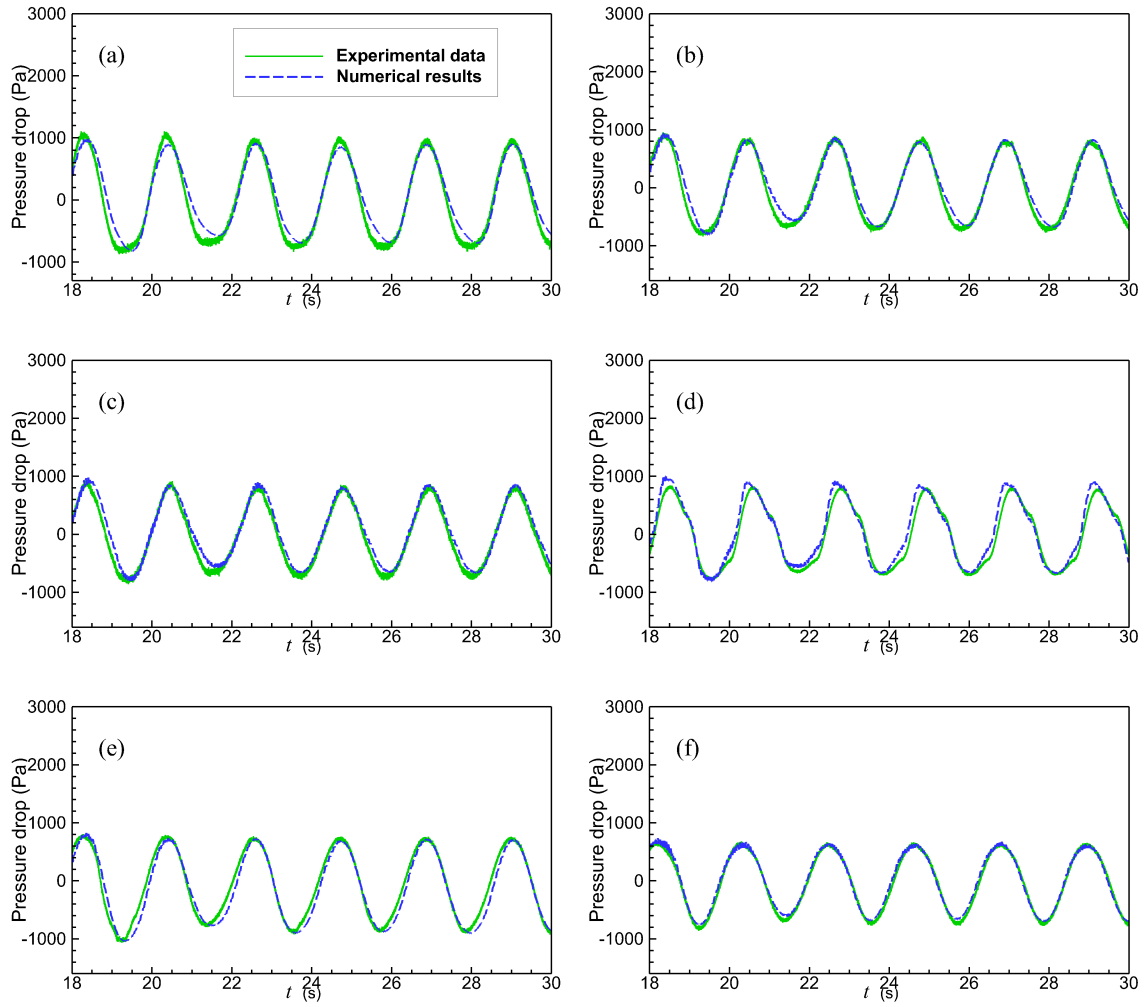
Fig. 7.7 Time series of pressure at sensor 4 (a), 5 (b), 6 (c), 7 (d), 11 (e), and 12 (f) for case 2.
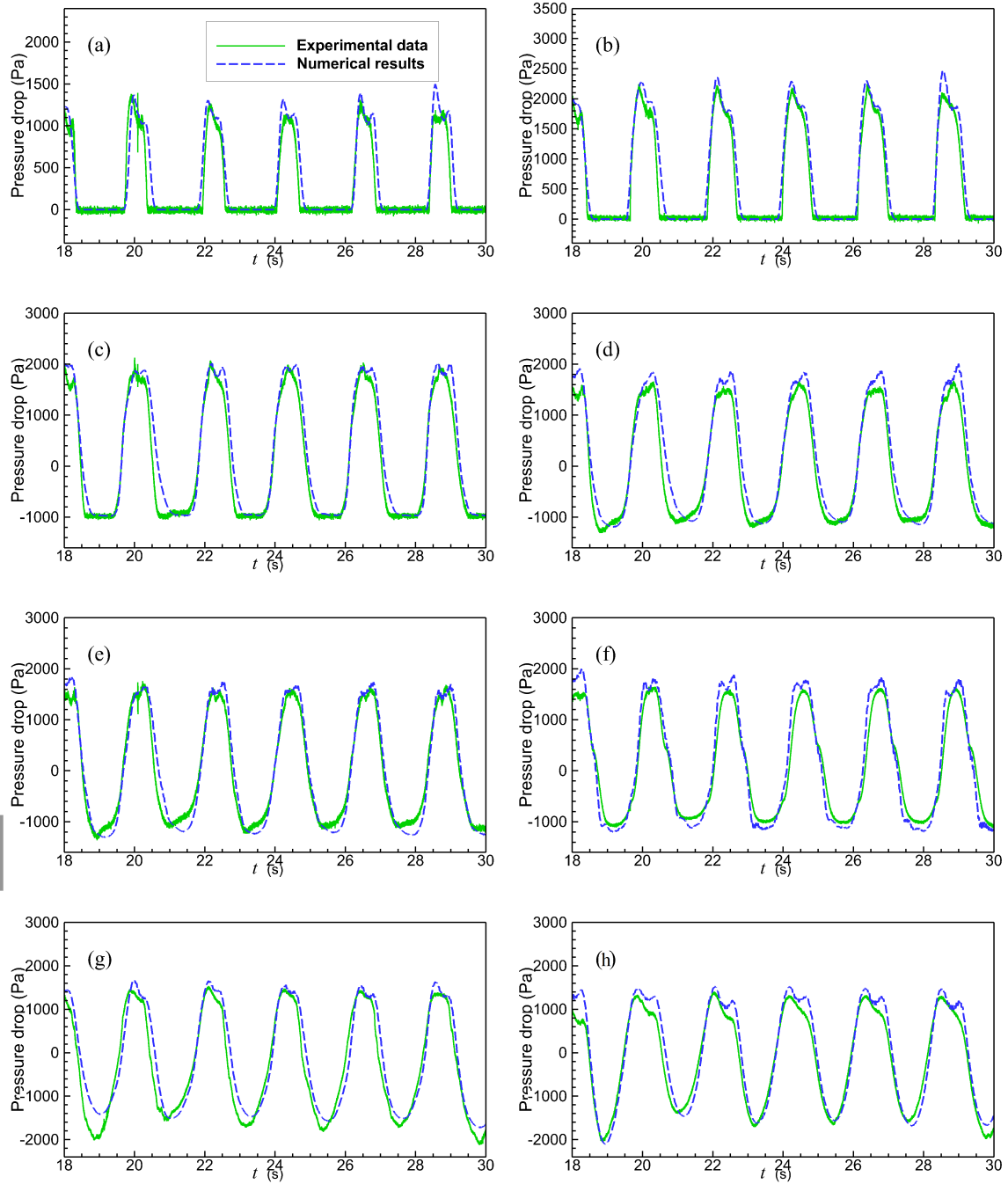
Fig. 7.8 Time series of pressure at sensor 2 (a), 3 (b), 4 (c), 5 (d), 6 (e), 7 (f), 11 (g), and 12 (h) for case 4.
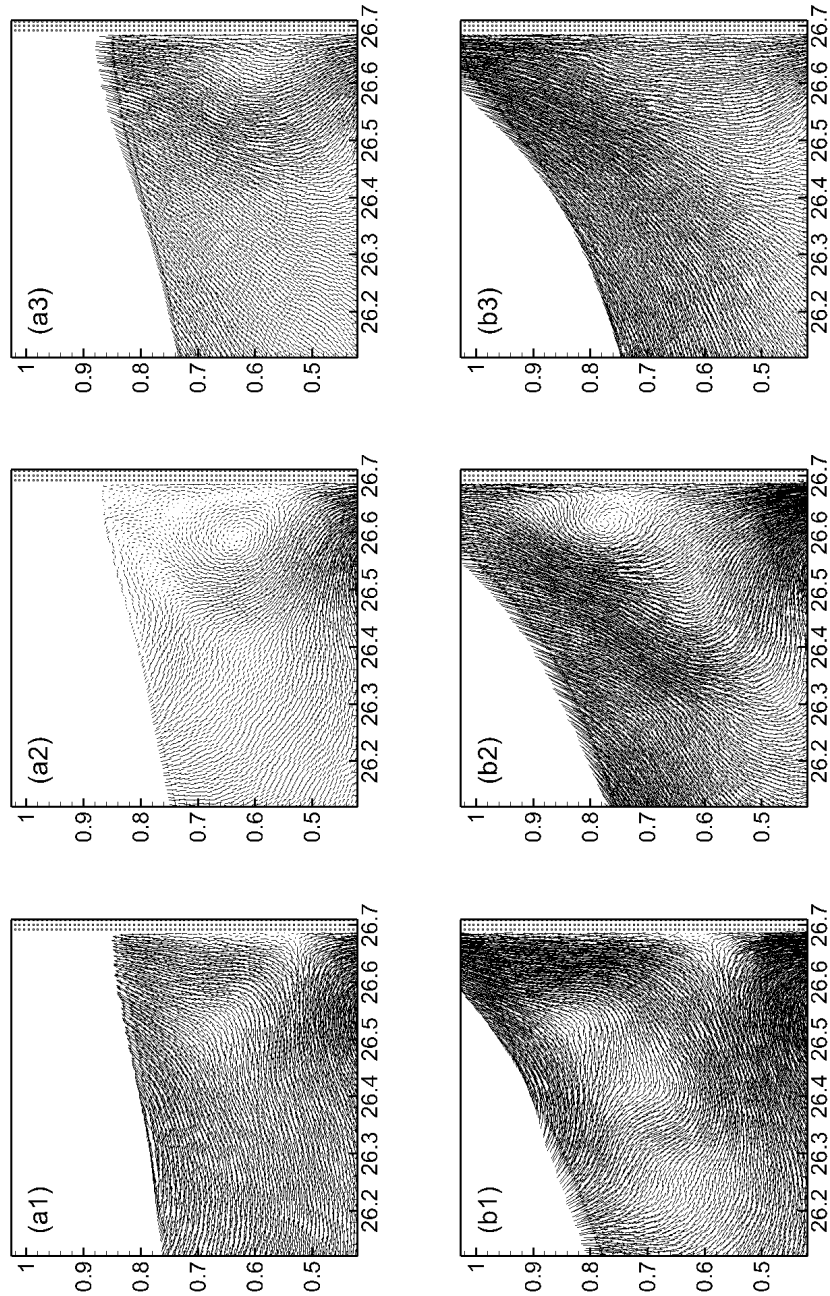
Fig. 7.9 velocity direction of the fluid particles in front of the front wall at 22.3 s (1), 22.4 s (2), and 22.5 s (3) for cases 2 (a) and 4 (b).
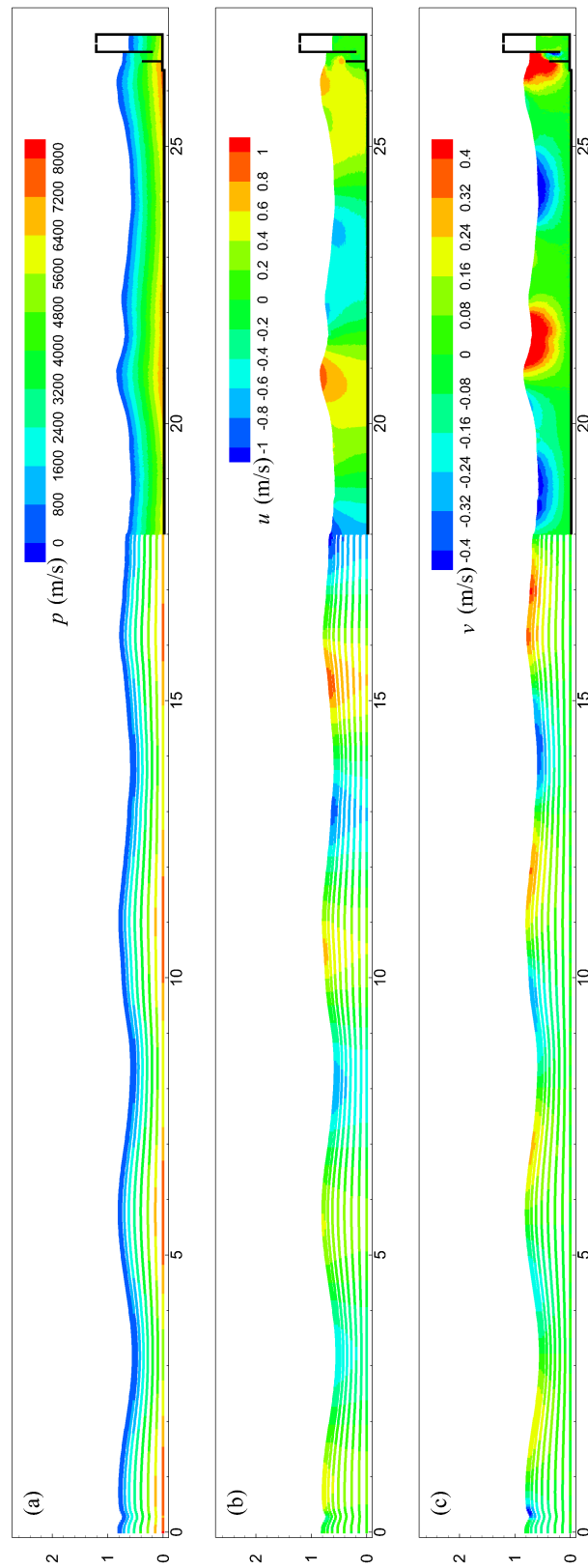
Fig. 7.10 Pressure (a), horizontal velocity (b) and vertical velocity (c) field at 22.0 s.

7.4   Results and Discussions

In the above section, the reproducibility of the SPH model for pressure at the measurement point has been verified. For the survivability of U-OWC under rough wave conditions, sliding or overturning due to wave loads need to be considered in the structural design phase. For an onshore U-OWC installation, more attention needs to be placed on the lip wall (Wall 1). Wall 2 is completely submerged in water and encounters relatively few hazardous situations. Therefore, only the forces as well as the moments of wall 1 are discussed. Wave force and bending moment on lip wall are shown in Fig. 7.12. The inflection points 1 of the device are subjected to local maximum loads for wall 1. The point is taken as the rotational centers of wave bending moments. The total horizontal wave force F_1 and wave moment M_1 are the sums of the seaward and shoreward surface components:

$$\mathbf{F_1} = \mathbf{F_{1o}} + \mathbf{F_{1i}} = \sum_j p_j^{out} * \Delta x_0 + \sum_j p_j^{in} * \Delta x_0, \tag{7.4}$$

$$\mathbf{M_1} = \sum_j p_j^{out} r_{j1} \Delta x_0 + \sum_j p_j^{in} r_{j1} \Delta x_0, \tag{7.5}$$

where $\mathbf{F_{1o}}$ and $\mathbf{F_{1i}}$ denote wave force on the wall 1 from outside and inside the chamber, respectively. Δx_0 is initial particle spacing. r_1 denotes the distance to the corner 1. In addition to the pressure from the water, the effect of air pressure on the wall 1 also needs to be considered. The directions of p^{out} and p^{in} are different. Positive values of $\mathbf{F^1}$ and $\mathbf{M^1}$ indicate horizontal forces to the right and counterclockwise, respectively.

Effects of Wave Condition on Wave Loads

In this subsection, the effect of wave period and height on the horizontal wave forces and wave moments acting on the wall 1 is investigated. Water depth d of 0.675 m, the geometries of the chamber, and the damping factor K_{dm} of 1.47 are constant. Various wave heights and periods are examined here.

Effects of Wave Height

Firstly, the cases of the incident wave with the same wave period of 2.15 s, and various wave heights (0.05 m, 0.10 m, 0.147 m, 0.198 m, and 0.247 m) are simulated. Fig. 7.13 shows the time series of horizontal wave forces and wave moments at wall 1. The symbols for wave forces as well as moments indicate the direction (Positive values indicate horizontal forces to the right; positive bending moments are counterclockwise). As the wave height increases, the
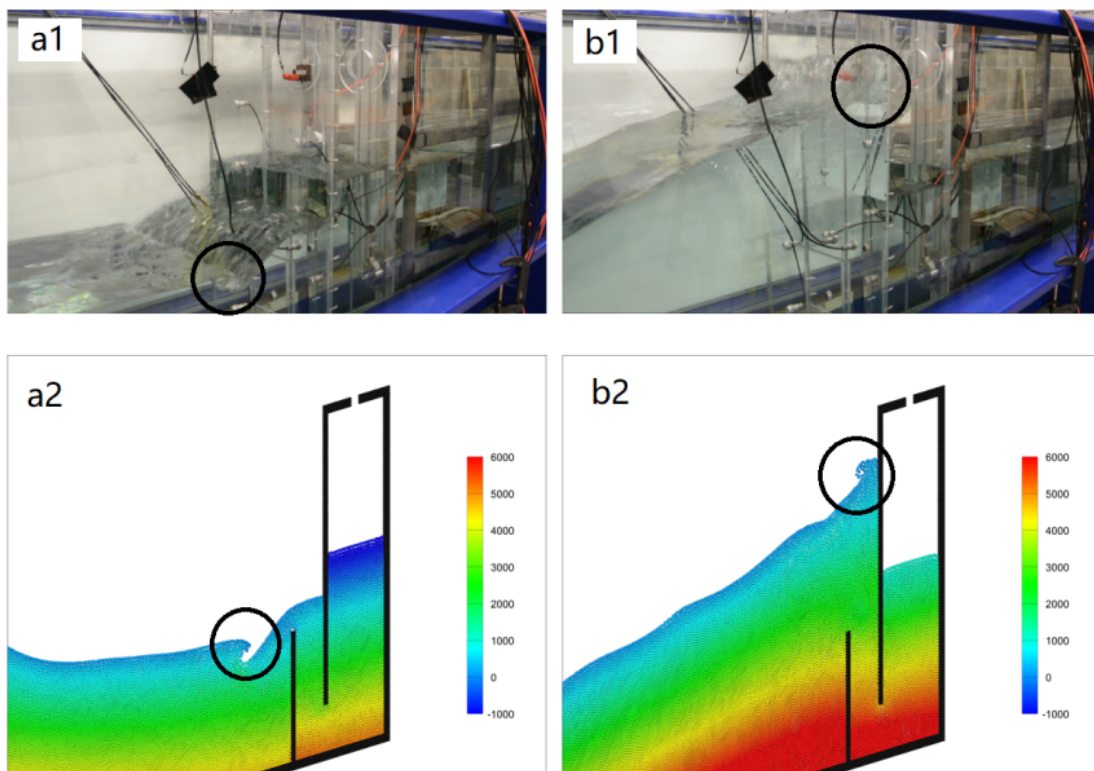
Fig. 7.11 Comparisons of nonlinear free surface between the SPH and experiment at $t = 21.4$ s and 22.4 s for case 4. (Labels 'a' and 'b' denotes 21.4 s and 22.4 s, respectively; Label '1' and '2' denotes experiment photos and numerical screenshots, respectively)
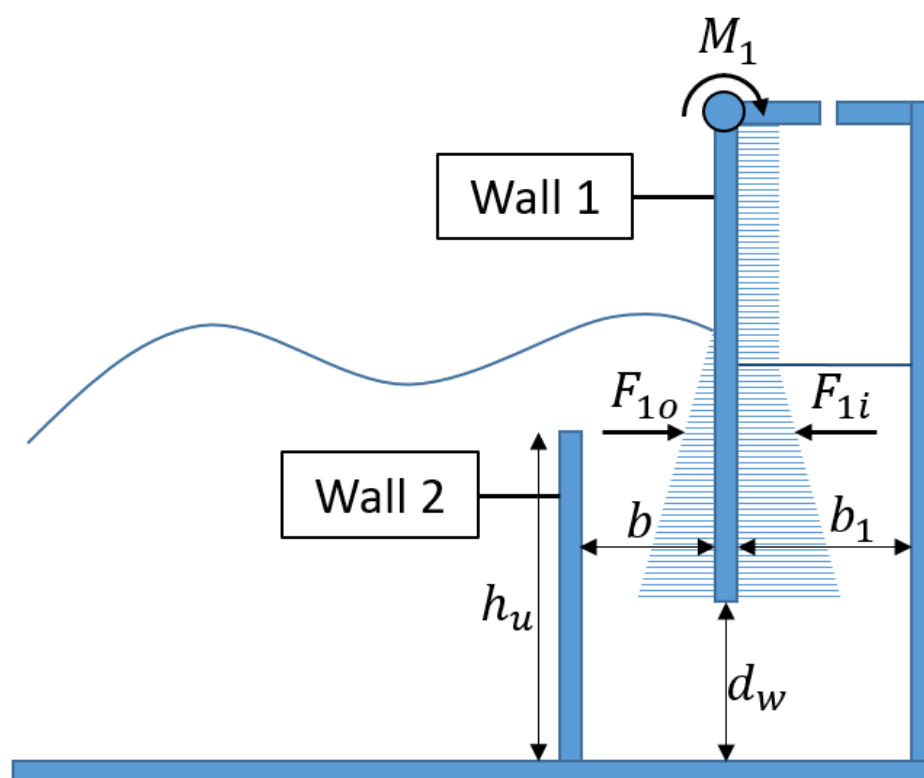
Fig. 7.12 Schematic of wave force and moment on the U-OWC device.

time profiles of the wave forces, as well as moments, at wall 1 become more complex. Two local peaks in the positive wave force occur as the wave height increases, named $FP1$ and $FP2$. While one local peak in the negative wave force occurs as the wave height increases, called $FP3$. The moments also show two local peaks $MP1$ and $MP2$. The frequency is not affected by wave height.

As the wave height increases, the two components of the horizontal wave force also gradually increase as shown in Fig. 7.14. F_{1i} and F_{1o} are around their lowest values when $FP1$ occurs. In Fig. 7.15, an instantaneous screenshot of the three peak pressures at a wave height of 0.20 m is shown. The air pressure in the chamber is lower than the atmospheric pressure, resulting in a larger positive wave force. Therefore, $FP1$ occurs mainly due to the air pressure. The part of the lip wall that is exposed to air is closer to corner 1. This explains why the moment does not show a local peak while $FP1$ occurs in Fig. 7.16. After $FP1$ happens, F_{1i} continues to increase and F_{1o} remains at its lowest value for a while. This explains the locally low values of F_1 between $FP1$ and $FP2$. Then F_{1o} becomes larger gradually. As a result, F_1 gradually increases with a local peak $FP2$. $FP2$ occurs when F_{1i} is near its initial value. In the model, a quadratic expression is used to represent the relationship between the air flow rate and the air pressure in the chamber. As a result, the air pressure changes more slowly around the zero point as shown in Fig. 7.17. This variation in air pressure is also reflected in F_{1i}, i.e., pressure growth becomes slow around the initial value. However F_{1o} shows a linear increase i.e., the growth rate of F_{1o} around air pressure zero point is greater than the value of F_{1i} . This is partly responsible for the appearance of the local peak $FP2$. In Fig. 7.15, the height of the free surface of the external water column (the wave peaks reach the lip wall) results in $FP2$ as well as $MP2$. In Fig. 7.13, $FP3$ (Wave force direction pointing out of the chamber) occurs when the internal air pressure is greater than the atmospheric pressure. Although the free surface levels are similar on both sides of the lip wall in Fig. 7.16, the air pressure affects the water pressure and results in local peaks $FP3$ as well as $MP2$.
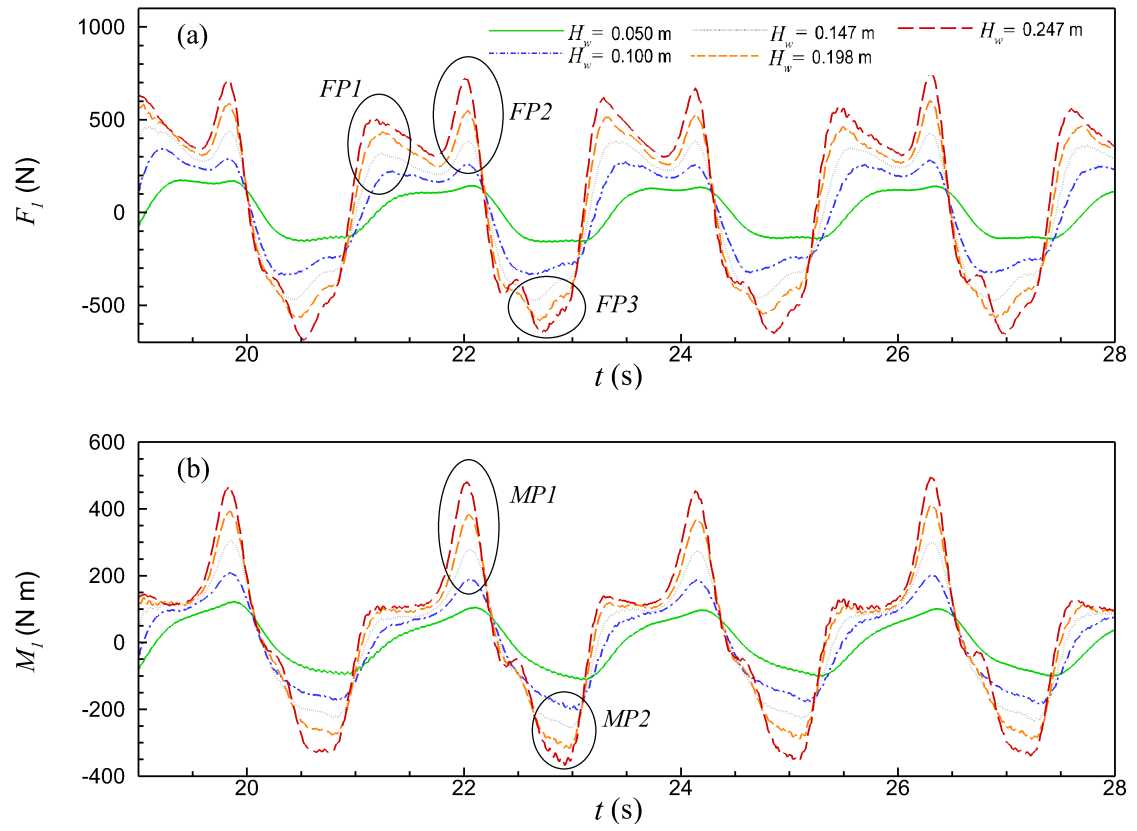
Fig. 7.13 Time histories of the horizontal wave forces F_1 (a) and wave moments M_1 (b) at wall 1 for different wave heights.
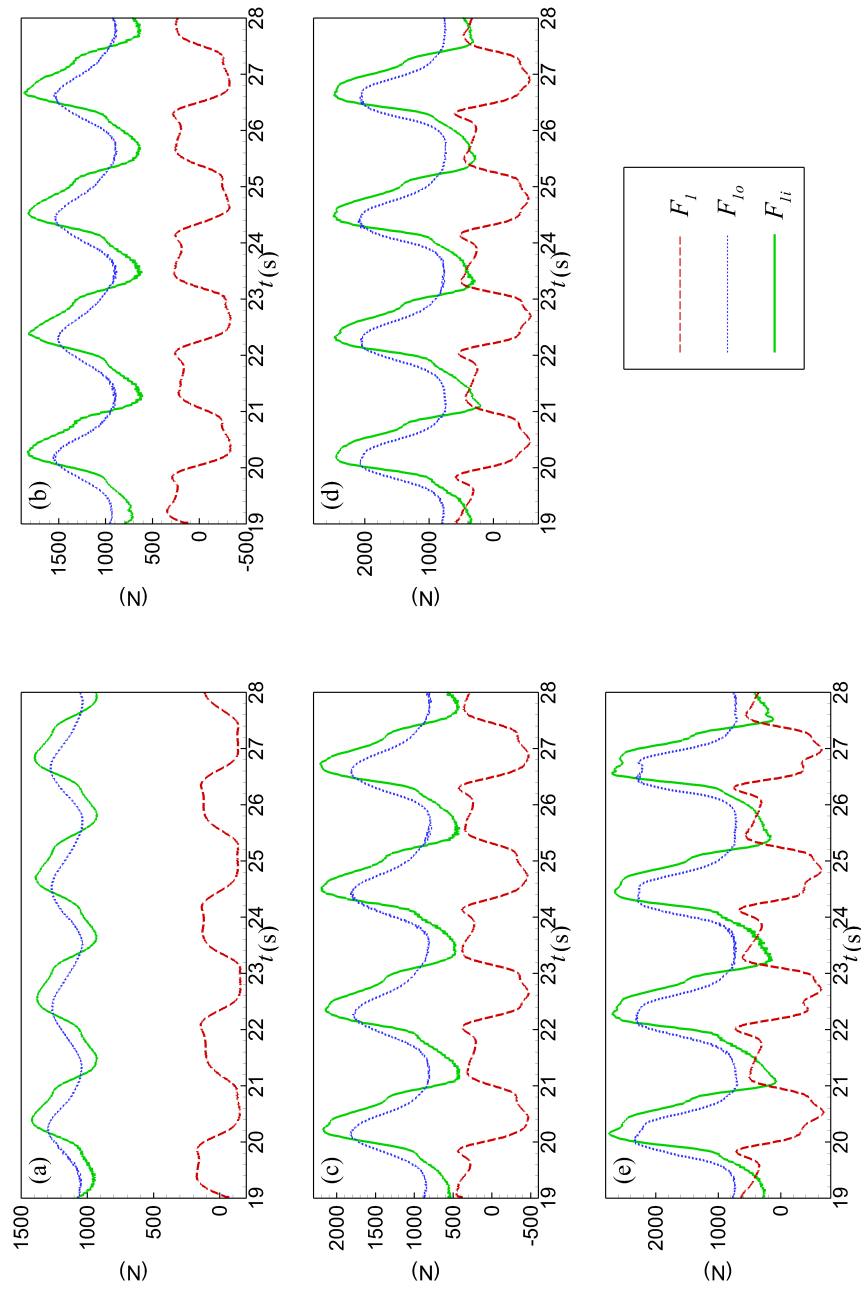
Fig. 7.14 Time histories of the horizontal wave forces F_1, wave forces on the outer F_{1o} and inner F_{1i} side of the wall 1 for wave height $H_w = 0.05$ m (a), 0.10 m (b), 0.15 m (c), 0.20 m (d) , and 0.25 m (e).
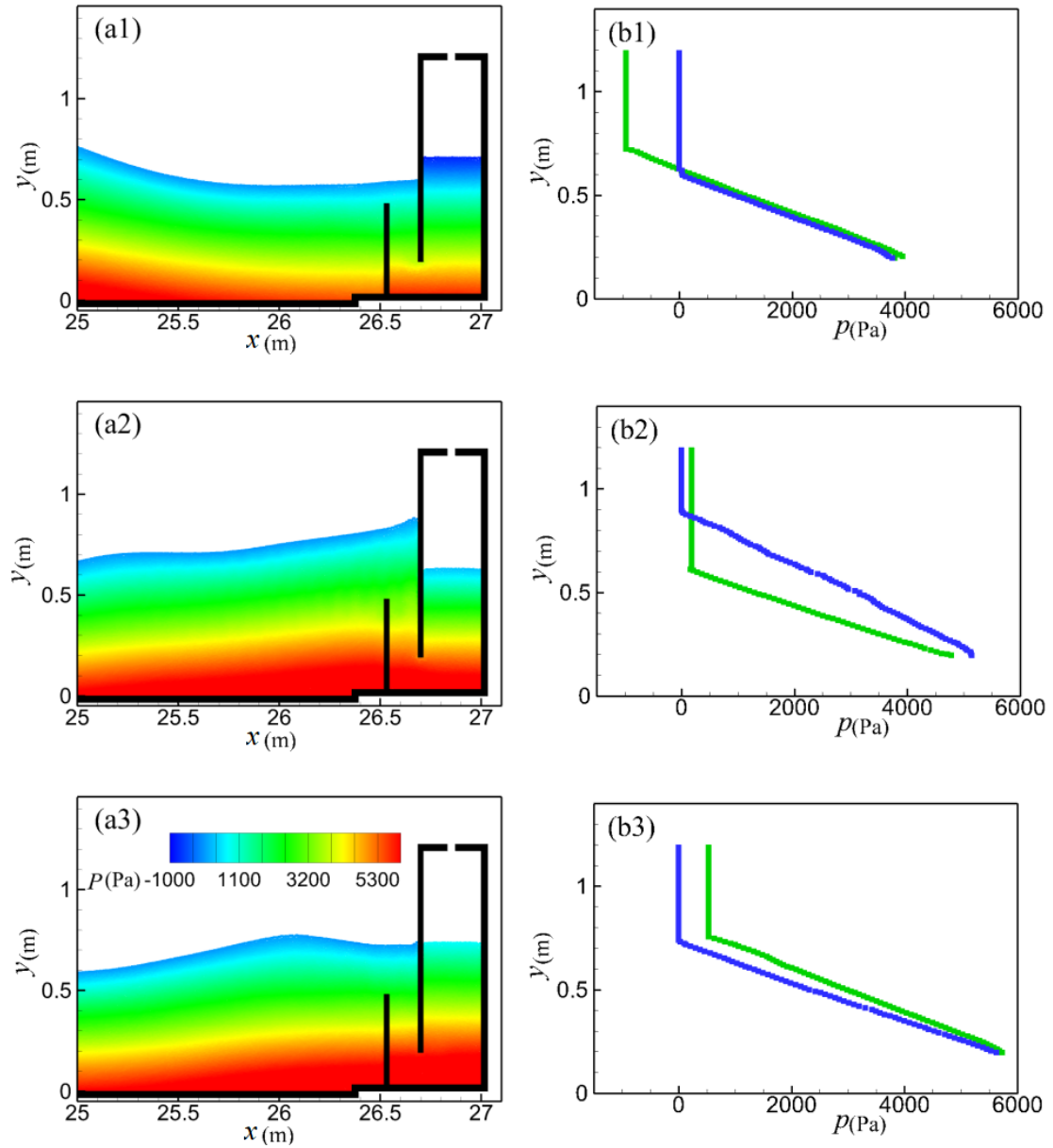
Fig. 7.15 Pressure field (a) and pressure distribution (b) (blue dots: outer; green dots: inner) on both sides of wall 1 for wave height $T_w = 0.20$ m at $t = 23.2$ s (1), 24.1 s (2), and 24.7 s (3).
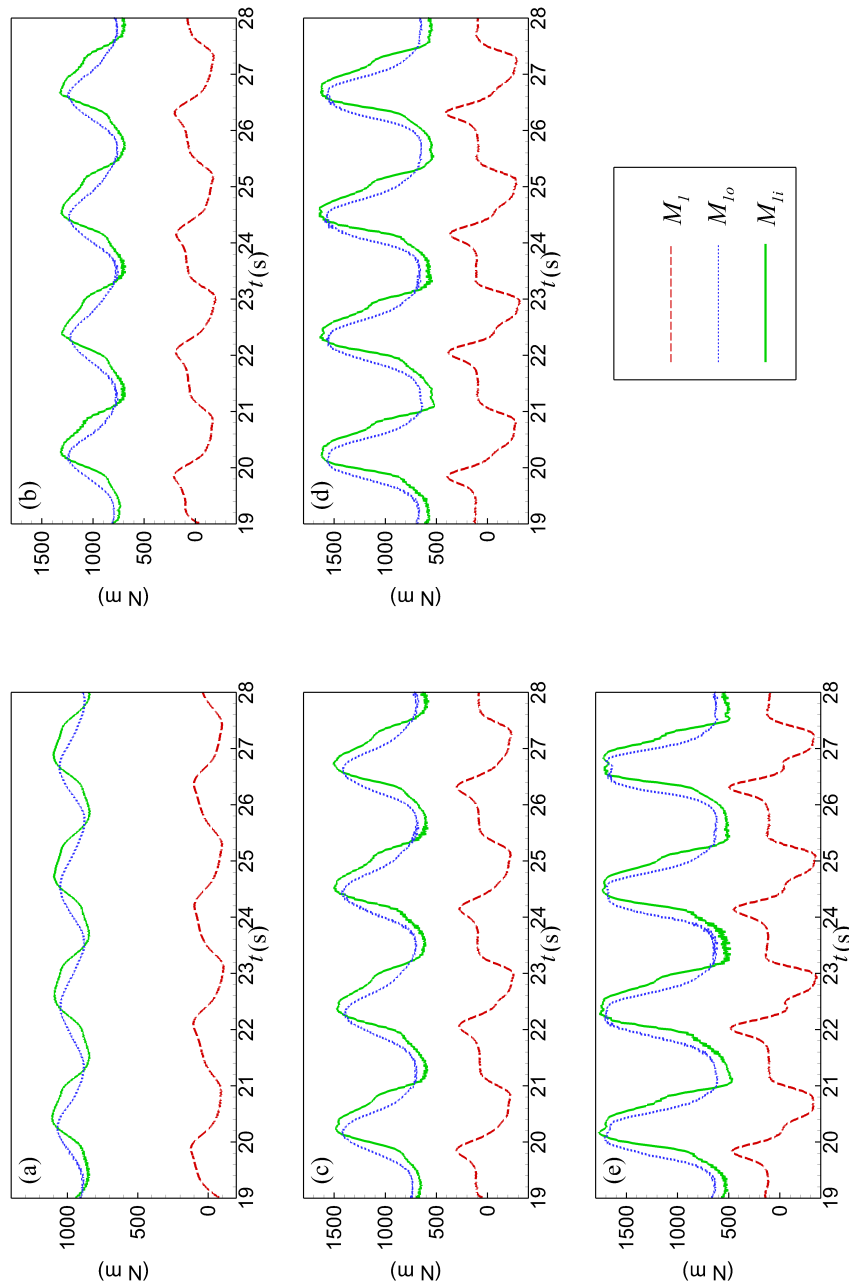
Fig. 7.16 Time histories of the wave moment M_1, wave moments on the outer M_{1o} and inner M_{1i} side of the wall 1 for wave height $H_w = 0.05$ m (a), 0.10 m (b), 0.15 m (c), 0.20 m (d), and 0.25 m (e).
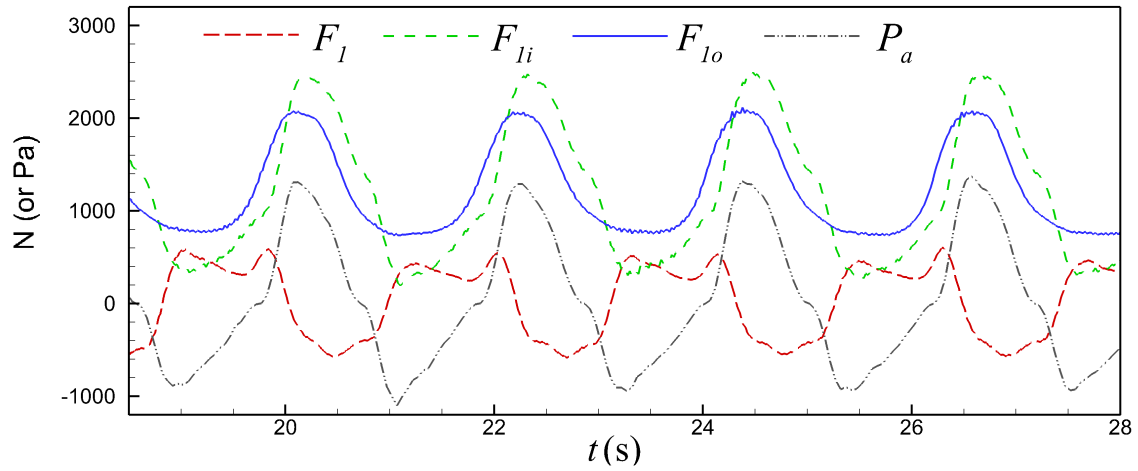
Fig. 7.17 Time histories of the horizontal wave forces F_1, air pressure P_a inside the chamber, wave forces on the outer F_{1o} and inner F_{1i} side of the wall 1 for wave height $H_w = 0.20$ m .

Effects of Wave Period

The cases of the incident wave with the wave height of 0.20 m, and various wave periods (1.75 s, 1.95 s, 2.15 s, 2.35 s, and 2.55 s) were simulated. The wave periods can be expressed as the dimensionless wave number $Kh = kh\tanh(kh)$, $K = \omega^2/g$, ω is wave frequency (1.75 s, 1.95 s, 2.15 s, 2.35 s, and 2.55 s correspond to 0.893, 0.722, 0.593, 0.497 and 0.422).

Figure 7.18 shows the time series of horizontal wave forces and wave moments. The time is nondimensionalised as t/T_w to facilitate the comparison of the results for different wave periods. When the period is greater than 0.722, $FP1$ decreases as the period increases. When the period is less than 0.722, $FP1$ increases with the increasing wave period, and $FP2$ decreases with increasing wave period. $FP3$ has a minimum value at wave number of 0.593, and a maximum value at 0.422. The moment $MP1$ decreases with increasing period. $MP2$ decreases as the period increases when the period is greater than 0.593. When the period is less than 0.593, $MP2$ increases as the period increases. Also, the the value of $MP2$ is greater than $MP2$ when Kh is less than 0.497. When $Kh = 0.593$, the maximum wave forces and moments are minimum for all periods. Variations in wave period lead to changes of wave forces and moments on both sides of wall 1 in terms of both amplitude and phase as illustrated in Fig. 7.19 and Fig. 7.20. The phase change also leads to a change in the total wave force and the moment. For example, $FP2$ becomes smaller due to slight phase difference between F_{1i} and F_{1o} for $Kh = 0.422$.
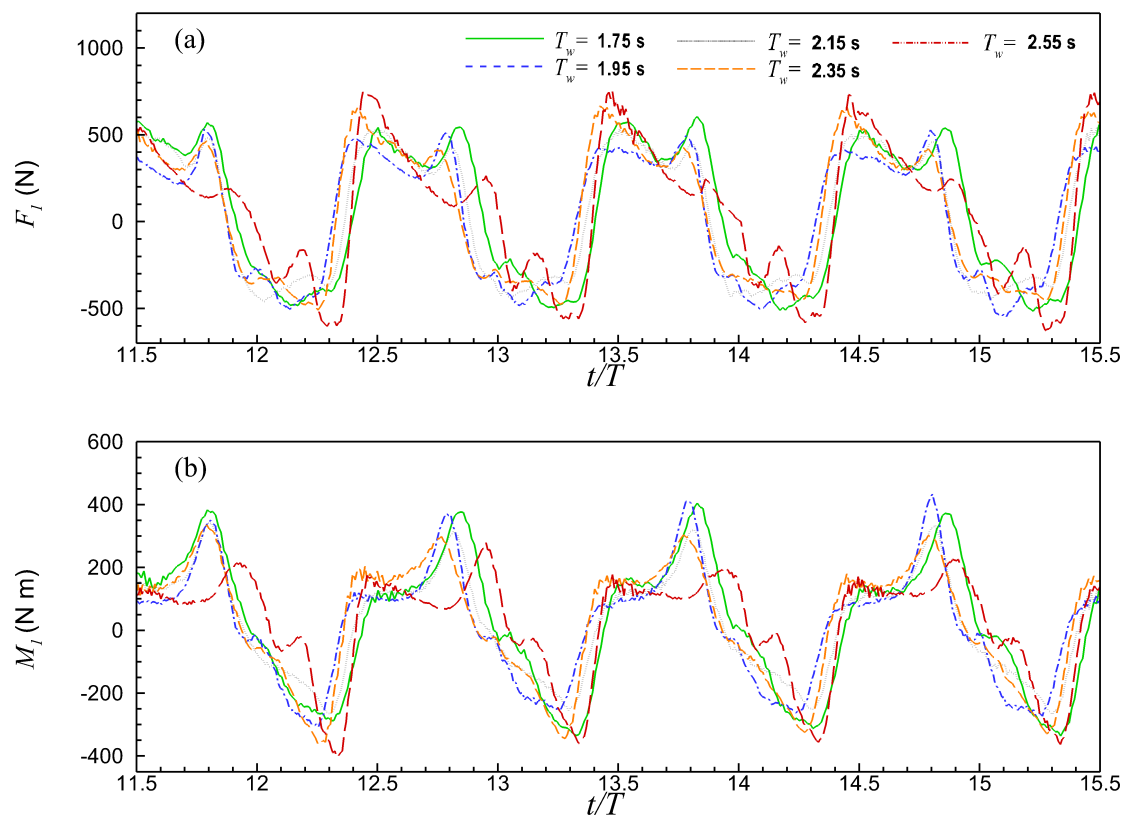
Fig. 7.18 Time histories of the horizontal wave forces F_1 (a) and wave moments M_1 (b) at wall 1 for different wave periods.
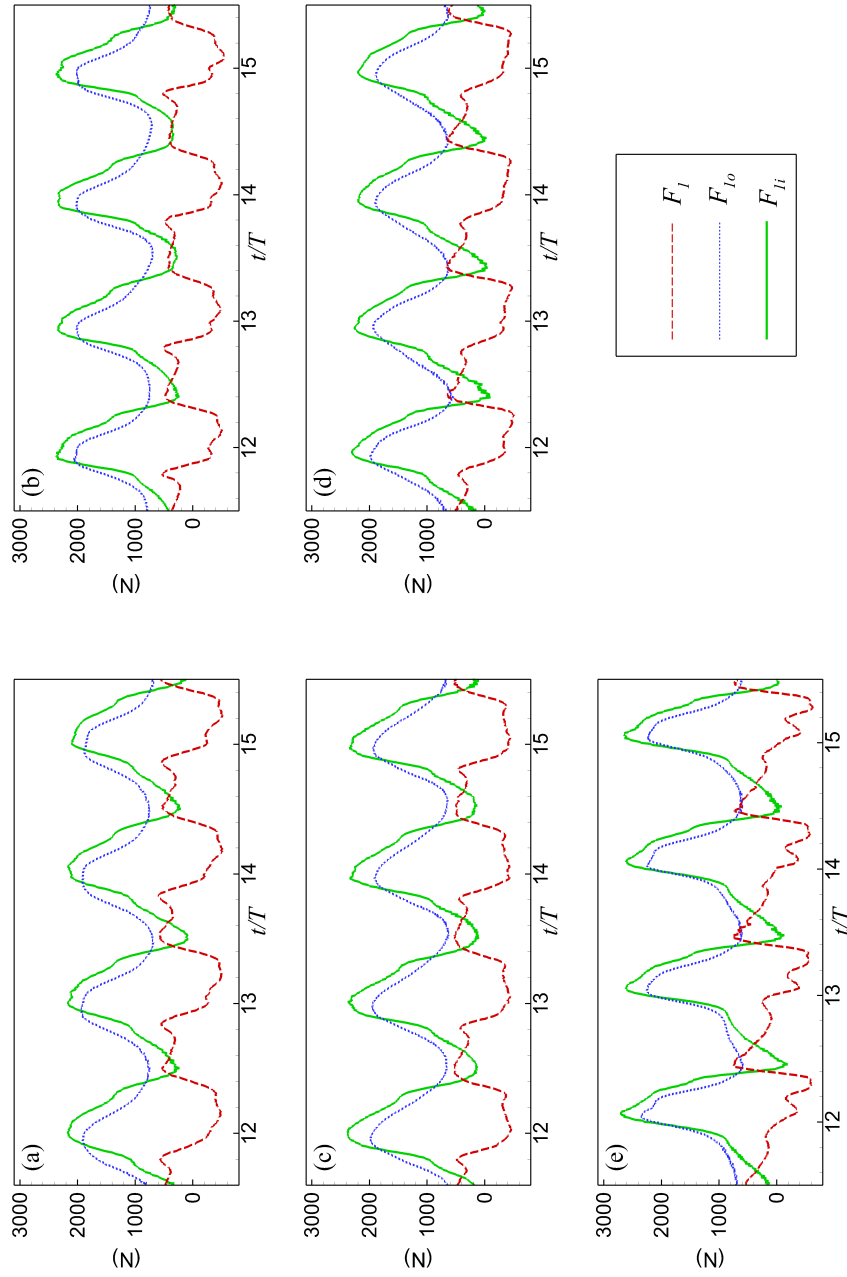
Fig. 7.19 Time histories of the horizontal wave forces F_1, wave forces on the outer F_{1o} and inner F_{1i} side of the wall 1 for wave period $T_w = 1.75$ s (a), 1.95 s (b), 2.15 s (c), 2.35 s (d), and 2.55 s (e).
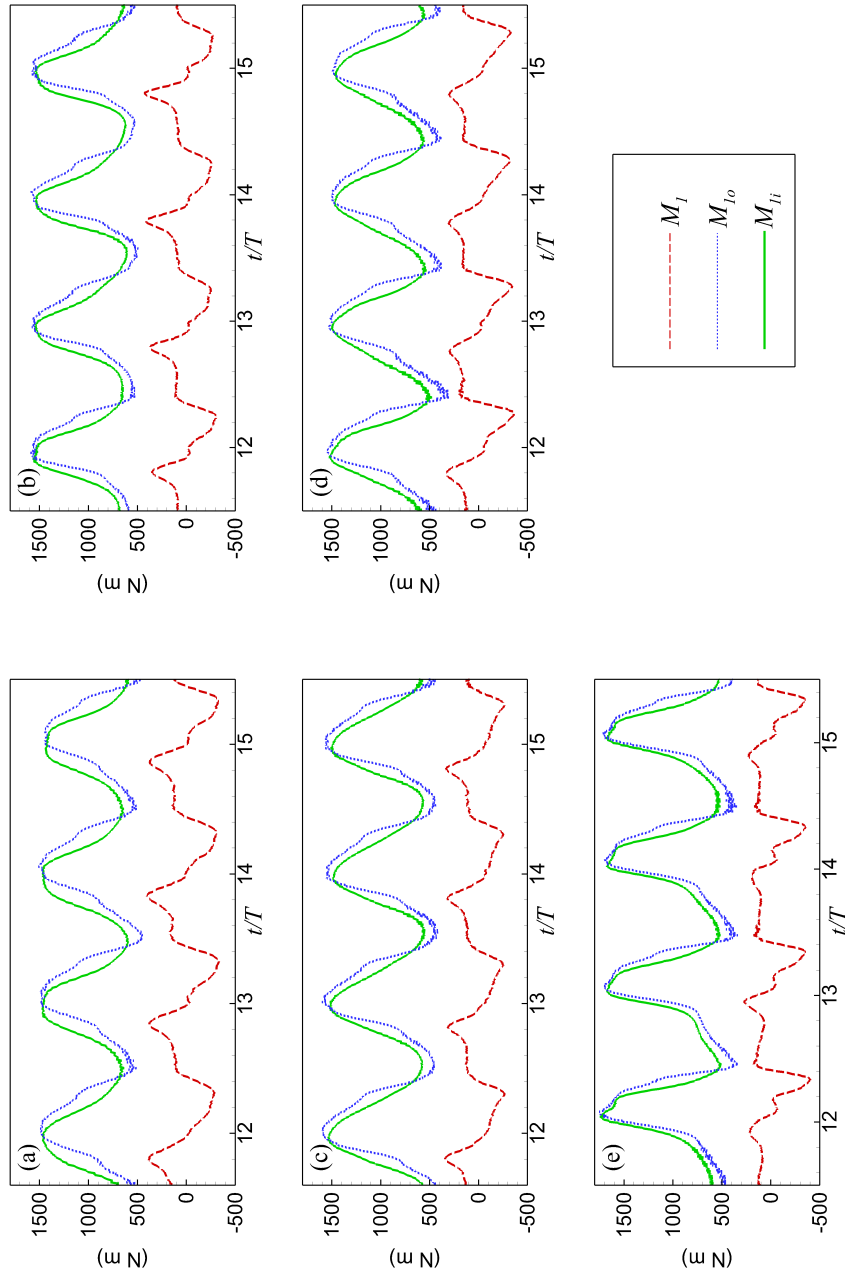
Fig. 7.20 Time histories of the wave moment M_1, wave moments on the outer M_{1o} and inner M_{1i} side of the wall 1 for wave period $T_w = 1.75$ s (a), 1.95 s (b), 2.15 s (c), 2.35 s (d), and 2.55 s (e).

Table 7.2 Wave conditions for the investigation of geometry parameters.

	1	2	3	4	5	6	7	8	9	10
Wave period (s)	1.75	1.85	1.95	2.05	2.15	2.25	2.35	2.45	2.55	2.65
Kh	0.893	0.800	0.722	0.652	0.593	0.542	0.497	0.457	0.422	0.391

Effect of Geometry Parameters on Wave Loads

As mentioned in previous sections, the U-OWC system investigated here is composed of a submerged wall in the front of the chamber. The hydrodynamic properties of U-OWC vary with the change of the position as well as the height of the submerged wall. The vertical duct width b and duct height h_u are introduced to better represent the variation of the shape as shown in Fig. 7.12. Hereinafter, the influences of two geometry parameters: the duct width and the duct height, on wave forces acting on the lip wall are investigated. When the influence of one of these factors is investigated, the other parameters are kept constant. Simulations are performed for a constant wave height of 0.20 m, a damping factor of $K_{dm} = 1.47$ and ten incident wave periods T_w varied evenly from 1.75 s to 2.65 s. The wave periods can be expressed as the dimensionless wave number as shown in Table 7.2.

Effects of Vertical Duct Width

To investigate the effects from the variation of vertical duct width b on wave load, five different cases are considered, i.e., $b = 0.063$ m, 0.103 m, 0.143 m, 0.183 m, and 0.223 m (the relative vertical duct width $b/b_1 = 0.220, 0.360, 0.5, 0.640$ and 0.78, where b_1 is the width of the chamber). The maximum horizontal force peak F_1^{max} and wave moment peak M_1^{max} for wall 1 are shown in Fig. 7.21. When the dimensionless wave number is 0.893, The minimum value of F_1^{max} for wall 1 occurs at the relative vertical duct width $b/b_1 = 0.5$. The minimum F_1^{max} for wall 1 is achieved when $b/b_1 = 0.5$ for Kh from 0.542 to 0.893. When Kh is less than 0.497, the maximum horizontal forces peak for wall 1 decreases as the vertical duct width b increases. When Kh is greater than 0.542, the minimum value of M_1^{max} for wall 1 occurs at $b/b_1 = 0.5$. When Kh is less than 0.457, the minimum M_1^{max} for wall 1 occurs at $b/b_1 = 0.78$. When $b/b_1 = 0.22$, the M_1^{max} for wall 1 is maximal for all wave conditions. In general, when Kh is greater than 0.542, $b/b_1 = 0.5$ should be chosen from the perspective of survivability. When Kh is less than 0.457, the changes of wave force and moment peak with b/b_1 show an opposite trend.

Fig. 7.22 also shows the time histories of the wave forces of the inner and outer side of wall 1 for $Kh = 0.893$. The variation in air pressure from the width b/b_1 affects the pressure on the inner wall of wall 1. At the same time, the pressure on the outer wall of wall
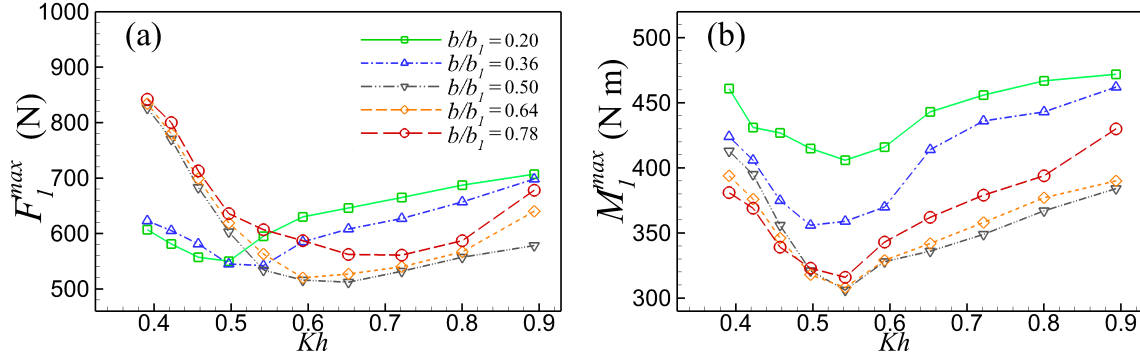
Fig. 7.21 Maximum horizontal forces F_1^{max} and wave moments M_1^{max} for different vertical duct widths.

1 also has some influence. In addition, the phase of the peak of the pressure changes. When $Kh = 0.893$, the first force peak $FP1$ is not obvious for $b/b_1 = 0.2$. As mentioned above, the air pressure affects the first force peak $FP1$. Therefore, $FP1$ is not significant when $b/b_1 = 0.2$. The maximum horizontal force occurs at $FP2$ when b/b_1 is less than 0.5. When b/b_1 is greater than 0.5, the maximum horizontal force occurs at $FP1$.

Effects of Vertical Duct Height

To investigate the effects of the variation of vertical duct height h_u on wave load, five different cases are considered, i.e., $h_u = 0.079$ m, 0.179 m, 0.279 m, 0.379 m, and 0.479 m (the relative vertical duct heights are $h_u/d_w = 0.50$, 1.12, 1.74, 2.36 and 2.98, where d_w is distance between the bottom of the lip wall and the seabed, see Fig. 7.12). Fig. 7.23 shows the horizontal force peak F_1^{max} and wave moment peak M_1^{max} for duct width $b = 0.143$ m.

When $Kh = 0.893$, F_1^{max} for the relative vertical duct height $h_u/d_w = 2.36$ is lowest for different vertical duct heights. While F_1^{max} for $h_u/d_w = 1.74$ is smallest for Kh from 0.593 to 0.893. When Kh is less than 0.542, the horizontal forces peak for wall 1 decreases as the vertical duct height h_u increases. When Kh is less than 0.652, the minimum value of M_1^{max} for wall 1 occurs at $h_u/d_w = 2.36$. When Kh is less than 0.593, M_1^{max} increases as the vertical duct height h_u increases. When Kh is less than 0.457, the vertical duct height has little impact on the wave moment peak for wall 1.
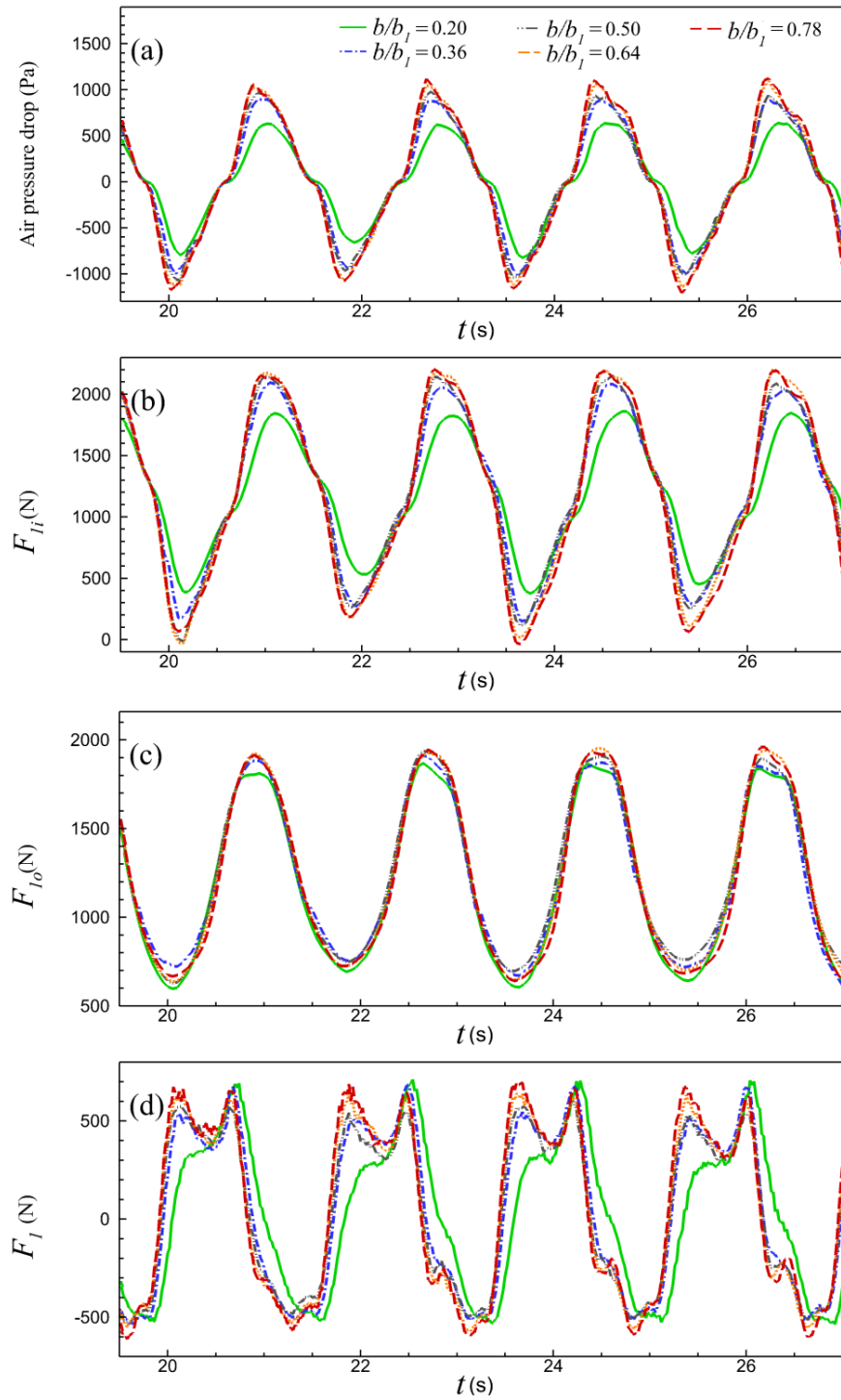
Fig. 7.22 The comparison of air pressure drop inside the chamber for different vertical duct widths for $Kh = 0.893$.
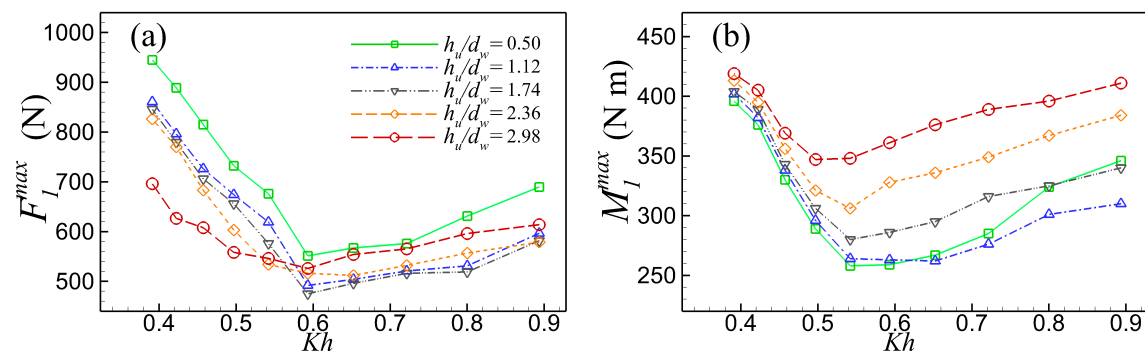
Fig. 7.23 Maximum horizontal forces F_1^{max} and wave moments M_1^{max} for different vertical duct heights.
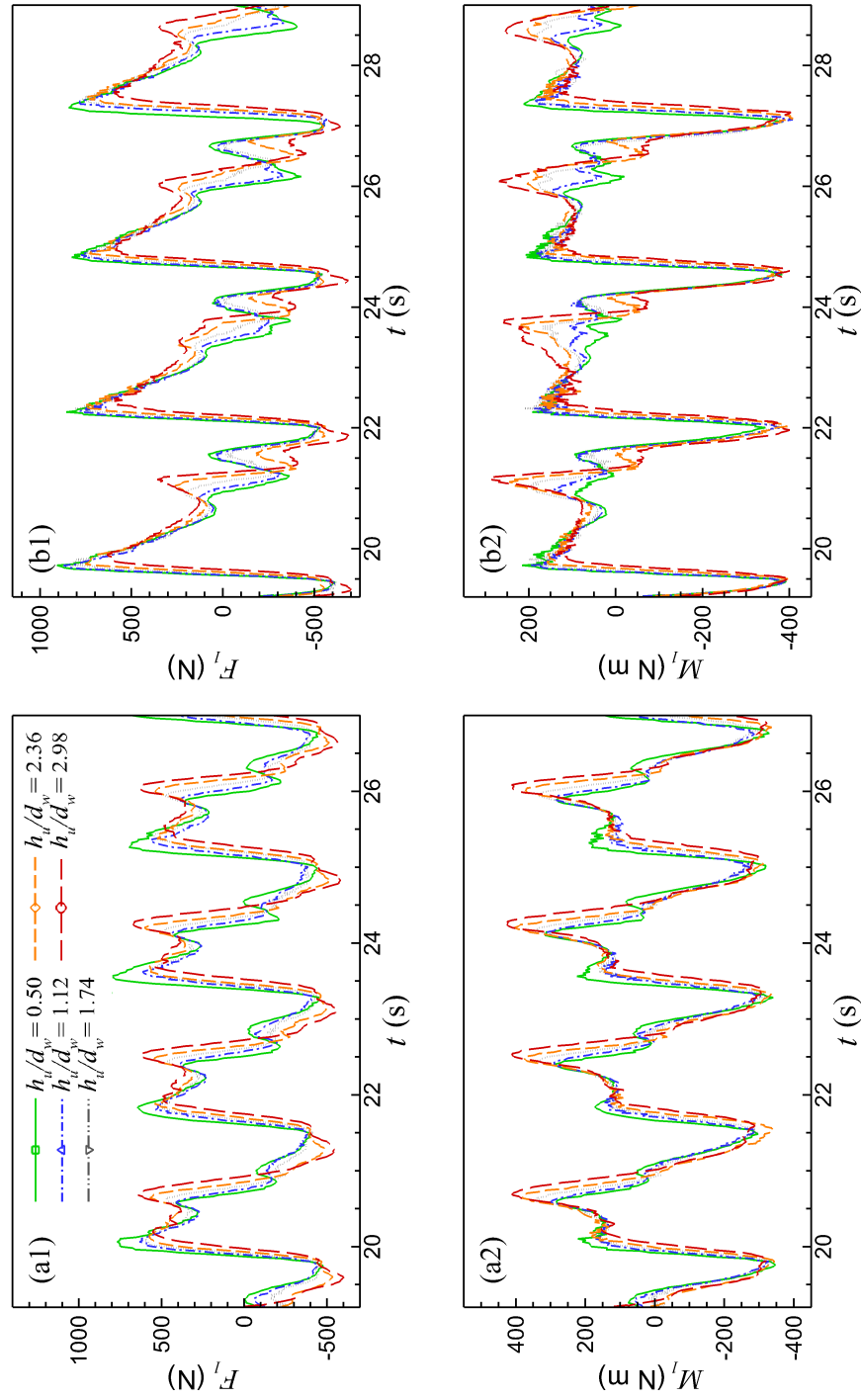
Fig. 7.24 Time history of wave forces F_1 (1) and wave moments M_1 (2) of wall 1 for $Kh = 0.893$ (a) and $Kh = 0.422$ (b).

Fig. 7.24 shows the time history of the wave force as well as the moment for wall 1 when Kh are 0.893 and 0.422. When $Kh = 0.893$, the first force peak $FP1$ decreases as the vertical duct height h_u increases. While the second force peak $FP2$ increases as the vertical duct height h_u increases. When h_u/d_w is less than 1.739, the maximum horizontal force happens at the first force peak $FP1$. While the maximum horizontal force happens at the second force peak $FP2$ when h_u/d_w is greater than 2.360. For $Kh = 0.422$, maximum horizontal force occurs at the first force peak $FP1$ when h_u/d_w is less than 2.36. While maximum horizontal force occurs at $FP3$ when $h_u/d_w = 2.98$. When $Kh = 0.893$, the first moment peak $MP1$ increases as the vertical duct height h_u increases. While the maximum wave moment occurs at the second moment peak $MP2$ when $h_u/d_w = 0.50$. The maximum wave moment occurs at the first moment peak $MP2$ when h_u/d_w is greater than 1.12. When $Kh = 0.893$, the maximum wave moment occurs at the second moment peak $MP2$, and is much less affected by vertical duct height. Fig. 7.25 shows the time series of air pressure drop, wave forces on the inner and outer side of the wall 1. The change in geometry affects the phase difference between the inner and outer walls. This results in a change in the total horizontal wave force on wall 1 (as shown in Fig. 7.24).

Finally, the relative vertical duct height h_u/d_w can be set at 1.12 to achieve relatively small forces and moments for Kh greater than 0.593. The value of maximum wave force peak and moment peak exhibit an opposite tendency with the increasing vertical duct height h_u when Kh greater than 0.593. However, the change of the wave force peak between $h_u/d_w = 0.50$ and 2.98 is 26% for $Kh = 0.391$. While the change of wave moment peak is only 6% in the same condition. Thus, the height of wall 1 should be higher for large wave periods.

From the experimental test, the natural period is found to be in the range of approximately 2.2 seconds ($Kh = 0.54$). In order to make the conclusions general, several specific wave periods (the dimensionless wave number) above are reformulated in the conclusions section based on the natural period.

7.5   Summary of optimization of the U-OWC device

In this chapter, the coupled SPH model is applied to optimize the U-OWC breakwater. First, the experiments as well as the numerical setup are briefly described. Numerical simulations are performed to assess dependence on the U-OWC geometry. The numerical free surface level in the chamber, the air pressure and the pressure measurement points are compared with the experimental data. The results showed that the model can reproduce the loading and hydrodynamic efficiency of the U-OWC breakwater in a regular wave well. Then, the wave forces and bending moments acting on the lip wall for various wave heights and periods
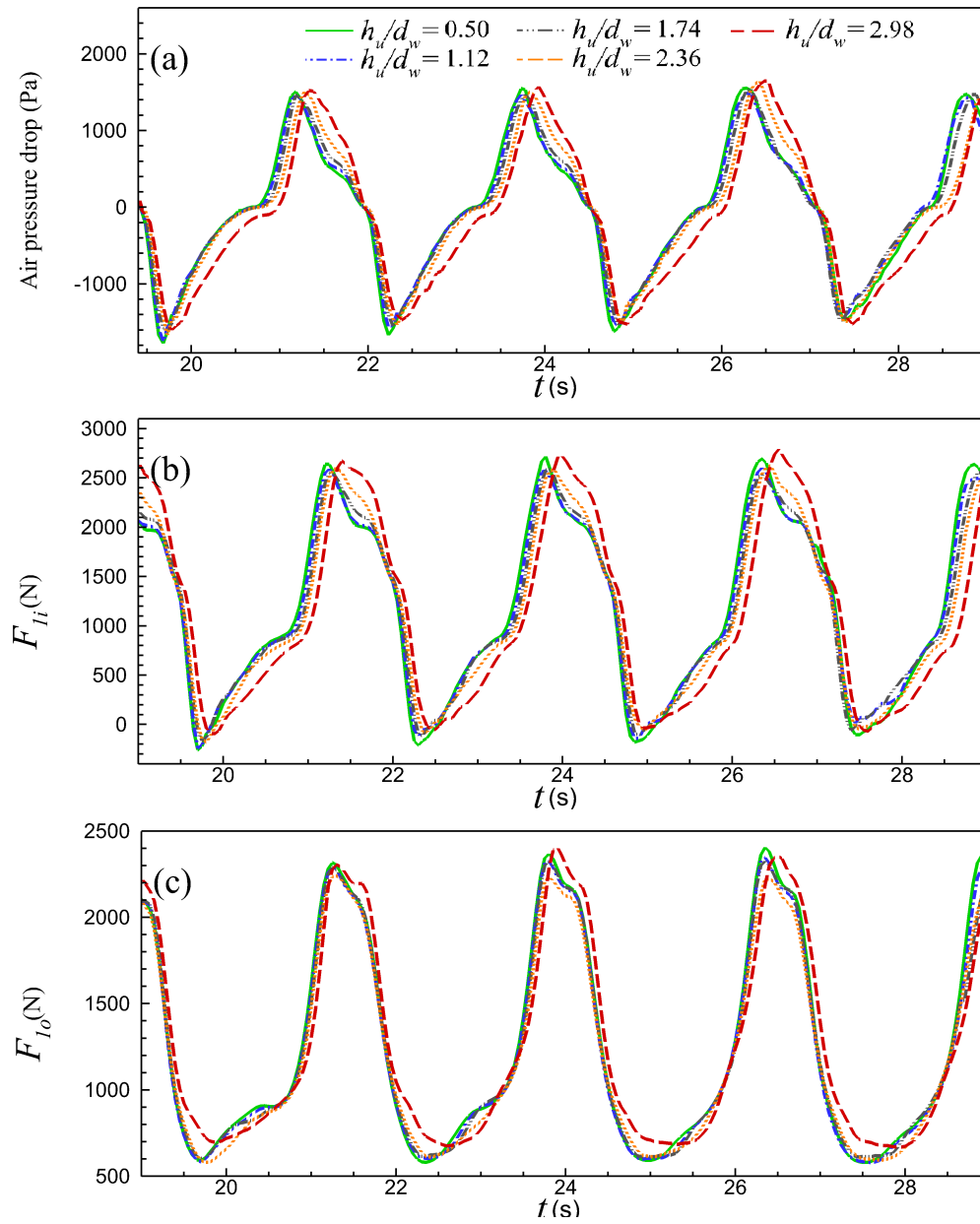
Fig. 7.25 The comparison of air pressure drop (a) inside the chamber, wave forces on the inner F_{1o} (b) and outer F_{1i} (c) side for different vertical duct widths for $Kh = 0.422$.

are discussed. Wave force and moments increase with increasing wave height. Three local horizontal force peaks ($FP1$, $FP2$, and $FP3$) and two local moment peaks ($MP1$ and $MP2$) on the lip wall are observed. Changes in wave period lead to changes in the phase difference of force evolution between the inside and outside of the lip wall. As the period changes, the maximum wave load (torque) occurs at one of $FP1$, $FP2$ and $FP3$ ($MP1$ and $MP2$). As a result, the maximum loads show different patterns at different incident wave periods. Finally, the following conclusions can be drawn:

1. When the dimensionless wavelength of incident wave Kh is less than 0.54 (The dimensionless wavelength corresponding to the natural frequency), the vertical height h_u/d_w setting of 2.12 gives a relatively small horizontal wave force and moment for wall 1. When the dimensionless wavelength of incident wave is greater than the dimensionless wavelength corresponding to the natural frequency, maximum horizontal force decreases with increasing h_u/d_w, and maximum moments increases with increasing h_u/d_w.

2. When the dimensionless wavelength of incident wave is less than the dimensionless wavelength corresponding to the natural frequency, h_u/d_w has a greater effect on maximum horizontal wave forces than maximum bending moments.

3. When the dimensionless wavelength of incident wave is less than the dimensionless wavelength corresponding to the natural frequency, the vertical width b/b_1 setting of 0.5 leads to relatively small horizontal wave force and moment for wall 1.

4. When the dimensionless wavelength of incident wave is less than the dimensionless wavelength corresponding to the natural frequency, maximum horizontal force increases with increasing b/b_1, and maximum moments decreases with increasing b/b_1.

5. The change in U-shaped geometry leads to a change in air pressure inside the chamber and a change in the phase of the forces on the inner and outer walls of wall 1, which ultimately affect the wave loading of wall 1.

6. The geometrical parameters of the U-shape have a significant effect on the phase of wave forces between the both side of wall 1.

The geometry of the U-OWC affects the wave load on the lip wall. By optimising the U-shaped configuration, the maximum wave force and moment can be reduced by more than 20%. When Kh is larger than 0.542, the maximum horizontal wave forces resulting

from optimisation of the geometry have an opposite trend of change to the maximum wave moment. It is therefore difficult to give an optimum design for all wave conditions. In addition, the maximum capture efficiency design should be investigated in the future to find the optimum design with the consideration of both capture efficiency and structural safety.

Chapter 8

Conclusions and Outlook

8.1   General Conclusions

The Oscillating water column (OWC) is one of the most successful wave energy devices and has been widely researched. Integrating OWC devices with breakwaters can cut construction and maintenance costs. However, there is a risk of damage to these OWC installations in extreme sea conditions. The purpose of the present thesis is to use the Smoothed Particle Hydrodynamics (SPH) method to investigate OWC devices to optimise their structural design. SPH is well suited to complex flows, especially for the problems with large deformations and discontinuities, which are present in many violent flow problems. SPH can capture splashes generated by the slamming of extreme waves on OWC devices. Therefore, the SPH model is used to investigate wave loads on OWC devices under rough wave conditions. However, millions or even tens of millions of particles often need to be considered for the simulation of OWC devices in numerical wave tanks. The notoriously expensive computational cost of SPH makes it difficult to implement. Therefore, how to improve its computational efficiency is a key issue in the application of SPH models to OWC device simulations. In this work, the computational efficiency of the SPH model is improved with the following approaches: 1) Simplify an air-water SPH model to a single-phase (water phase) SPH model. 2) Develop a parallel SPH program. 3) Couple the SPH model with the OceanWave3D model, i.e., using more efficient Oceanwave3D model in the region away from the nonlinear flow and using the high fidelity SPH model in the nonlinear region. Finally, the loads on U-shaped OWC devices are studied by the parallel coupling single-phase SPH model. The entire SPH code was developed completely independently, using the Fortran language, and run on a high performance computer. The following section lists some of the most salient conclusions in detail.

8.2 Detailed Conclusions

SPH with Pneumatic Model

Inside the chamber of OWC devices, air and water are strongly coupled. However, air water two-phase SPH model to simulate OWC devices requires more computation cost than single-phase models. Therefore, a single-phase SPH model with a pneumatic model is proposed to simulate OWC devices with a PTO system. The air pressure inside the chamber is predicted based on the relationship between the air pressure and the air volume flux across the orifice. The air pressure being evaluated is applied to the governing equation to solve it for free-surface particles. In this way, the effect of air pressure on water is taken into account without the simulation of air phase.

The free-surface elevations of the present single-phase model agree well with the theoretical results for the communicating vessel situations in chapter 4. It indicates that the single-phase SPH model accurately captures the effect of air pressure on the water phase. The expression between the free-surface velocity and air pressure is very important for the accurate prediction of results. The quadratic relationship is found to work better than the linear one in predicting the response of the OWC device. The free-surface level, air pressure, and hydrodynamics efficiency predicted by the present SPH model are in good agreement with experimental data of different OWC devices. Therefore, the single-phase SPH model in this thesis can be used as a useful tool for studying OWC devices.

Regional Ghost Particle Approach

The front wall of OWC devices has a significant impact on the hydrodynamic performance. In this thesis, a fixed ghost particle boundary is used to model wall conditions. In general, a solid boundary should be represented by many layers of ghost particles with the consideration of the size of support domain. Therefore, the thickness of the front wall influences the choice of particle spacing.

To replicate the thin front wall, the flow field near the front wall is separated into three distinct subdomains, each with its corresponding set of fluid particles and ghost particles. The main idea of the regional ghost particles approach is to decompose the domain near the thin wall and assign the corresponding ghost particles as boundaries. Therefore many layers of particle simulation front walls are not necessarily needed for the purpose of avoiding the interaction of fluid particles on both sides of the thin wall. Particle resolution can be independent of wall thickness. Results show that this approach provides a significant deal of flexibility in terms of initial particle spacing, allowing simulations to be run with fewer

particles than with multi-node ghost particles, but with comparable accuracy according to the numerical validations.

Parallelization SPH Framework

To deal with large scale problems, a novel parallel SPH framework is developed, and scalable on a High Performance Computer (HPC). The new SPH parallel framework uses a background Cartesian grid to decompose the domain, and a grid list to map the entire domain. Meanwhile, within each sub-domain there exists local mesh lists for the purpose of neighbouring particle search. The local mesh lists also facilitate the search for interactive particles, i.e. those particles that need to pass information among processors. In the dynamic load balance strategy, both of two evaluation criteria: computation particle numbers and running time are considered. Load balancing is achieved by updating the sub-domain boundaries according to the local computation load distribution from the previous time step. Also, the initial load balance strategy is developed to maintain the initial homogeneous load balance.

The results show that overall time cost, the load balancing strategy based on running time achieves better parallel efficiency than the one based on computation particle numbers. The wave-structure case demonstrates the ability of the present SPH model to simulate the numerical wave tank with millions of particles over a period of tens of seconds. Some good parallel efficiencies can be found in both strong and weak scaling measurements. However, it still shows a decrease in efficiency in the case of 1920 cores. The reason for this may be the extra expense caused by expensive blocking communication.

Coupling SPH with OceanWave3D

To further increase the speed of the calculation, this thesis proposes a two-way coupled model to hybridize SPH with OceanWave3D. The expensive SPH model is used to simulate the nonlinear region, while the more efficient OceanWave3D is used to simulate the computational domain away from the nonlinear region. SPH and OceanWave3D are overlapping in the coupling region. The entire coupled model is constructed in a parallel framework, where OceanWave3D is allocated only one processor to compute, whereas in the SPH model the MPI parallel model is computed using multiple processors.

According to the results, it was found that OceanWave3D could achieve convergent and accurate results with a larger resolution. The Coupled model shows faster computational efficiency and better results than the SPH-only model. The main reason for this is the reduced numerical dissipation due to the shortened SPH flume length. The calculation speed of

OceanWave3D is much faster than that of the SPH model. However, OceanWave3D cannot simulate breaking waves. This is because the nodes in OceanWave3D only take into account the vertical displacement and therefore cannot be used to simulate breaking waves. The coupled model retains the ability of SPH to simulate nonlinear problems while being more efficient than the SPH-only model.

Application of SPH Model to U-OWC

Finally, the single-phase parallel coupled SPH model is applied to study the U-OWC device. Numerical results of free surface evolution inside the chamber and the pressure measurement points agree well with experimental data. The results demonstrate the present model can capture load on the lip wall well. After that, the horizontal wave forces and bending moments caused by the waves on the lip wall are then addressed.

As wave height rises, horizontal wave load and moments on the lip wall (Wall 1) also rise. It is found that there are three local horizontal force peaks and two local moment peaks on the lip wall. For various wave periods, the phase difference between wave loads on the outside and inside of the lip wall can affect the total horizontal wave forces and wave moments.

When the dimensionless wavelength of incident wave Kh is less than 0.54 (The dimensionless wavelength corresponding to the natural frequency), the vertical height h_u/d_w setting of 2.12 gives a relatively small horizontal wave force and moment for wall 1. When the dimensionless wavelength of incident wave is greater than the dimensionless wavelength corresponding to the natural frequency, maximum horizontal force decreases with increasing h_u/d_w, and maximum moments increases with increasing h_u/d_w. When the dimensionless wavelength of incident wave is less than the dimensionless wavelength corresponding to the natural frequency, h_u/d_w has a greater effect on maximum horizontal wave forces than maximum bending moments. When the dimensionless wavelength of incident wave is less than the dimensionless wavelength corresponding to the natural frequency, the vertical width b/b_1 setting of 0.5 leads to relatively small horizontal wave force and moment for wall 1. When the dimensionless wavelength of incident wave is less than the dimensionless wavelength corresponding to the natural frequency, maximum horizontal force increases with increasing b/b_1, and maximum moments decreases with increasing b/b_1. The change in U-shaped geometry leads to a change in air pressure inside the chamber and a change in the phase of the forces on the inner and outer walls of wall 1, which ultimately affect the wave loading of wall 1. The geometrical parameters of the U-shape have a significant effect on the phase of wave forces between the both side of wall 1.

The maximum wave force and moment may be decreased by more than 20% by carefully optimising the width and height of the U-OWC vertical duct. When the wave period is larger

than 2.25 s, the maximum horizontal wave forces resulting from optimisation of geometry have an opposite trend of change to the maximum wave moment. It is therefore difficult to give an optimum design for all wave conditions.

8.3   Major Contribution

Innovation points in the thesis are listed here:

Model Innovation

In this thesis, a SPH solver for OWC devices with power take-off systems is developed. The code for the SPH solver was developed in-house. In the present model, the specific model innovations are as follows:

1. The single-phase SPH with pneumatic model is proposed to simulate OWC devices with power take-off system. The SPH model takes into account the effect of air on water phase inside the chamber when the air phase is not modelled.

2. The regional ghost particle approach is developed to simulate thin walls and to eliminate the influence of the thickness of the thin wall on the choice of particle resolution.

3. A new SPH parallel framework with dynamic loading is proposed to simulate free surface flows. The dynamic loading strategy can be achieved based on SPH computation times.

4. A two-way coupled model between SPH and OceanWave3D is proposed. The coupled model preserves the ability of the SPH model to handle nonlinear surfaces while being faster to compute than a SPH-only model.

Results Innovation

The proposed SPH solver for OWC devices is used to optimize the design of U-OWC devices. To achieve optimum structural reliability, horizontal wave loads and bending moments of U-OWC devices are studied. Finally, the following results are obtained:

1. As the wave height increases, maximum moments and horizontal wave pressures on the lip wall also significantly increase.

2. For various wave periods, the phase difference between wave loads on the outside and inside of the lip wall can affect the total horizontal wave forces and wave moments.

3. The minimum load and maximum capture efficiency designs for U-OWC breakwaters cannot be satisfied geometrically at the same time.

4. The change in U-shaped geometry leads to a change in air pressure inside the chamber and a change in the phase of the forces on the inner and outer walls of wall 1, which ultimately affect the wave loading of wall 1.

5. The geometrical parameters of the U-shape have a significant effect on the phase of wave forces between the both side of wall 1.

8.4   Limitations of the study

The work presented in this thesis has been shown to provide a parallel coupled SPH model in order to simulate OWC devices, facilitating the application of SPH methods in the field of marine renewable energy. However, there are still many limitations of the present study:

1. The present work is limited to 2D problems. It is necessary to extend the present model to three dimensions (3D). The 3D model is closer to the real situation and allows the effect of oblique waves on the structure to be taken into account.

2. Air compressibility is neglected in the present single phase SPH model. Nevertheless, the air compressibility could play an important role in large-scale OWC device, and it may be necessary consider the air compressibility for the simulation of large-scale OWC installations.

3. The reduction in parallel efficiency in the large-scale (large-scale particle numbers/cores) cases suggests that the current parallel model needs further improvement.

4. Although coupling models have been developed, the choice of coupling region location and size has not been discussed quantitatively.

5. The discussion on U-OWC wave loading is limited to regular waves. Studies that consider site-specific sea states are of more practical interest.

8.5   Recommendations for Future Research

As mentioned above, there are some limitations to the current research. Further improvements are needed in the current study to address these issues:

1. An adaptive refinement model could allow for the use of higher resolutions near the fluid-structure/free surface where it is required to capture nonlinear flows, and low resolutions could be used in the main parts of the flow field. Thus, an adaptive refinement model is expected to reduce calculation costs.

2. A large amount of published literature shows that computationally efficient GPU-accelerated based models are tens of times faster than CPU-based parallel models. The present SPH model could be extended to the one with GPU-accelerated codes.

3. Parallel SPH models will necessitate the development of non-blocking communication to reduce parallel communication times. The current MPI-type parallel model can be combined with the GPU-acceleration model. In this way, the multi-GPUSPH model could be developed to meet the requirements of extreme scale applications.

4. The effect of air compressibility is ignored in the current single-phase SPH with pneumatic model. A multi-phase SPH model could be developed with the air compressibility effect taken into account.

In combination with the above model developments, it is hoped that the efficiency of the current model can be further improved for 3D problems. Moreover, the efficient SPH model will be available to study marine engineering problems in the future. With the ability of the SPH model to simulate strongly nonlinear large deformation problems, applications should focus on the survivability of ocean engineering devices.

References

Abbasi, R. and Ketabdari, M. J. (2022). Enhancement of OWC Wells turbine efficiency and performance using riblets covered blades, a numerical study. *Energy Conversion and Management*, 254:115212.

Agency, I. E. (2017). World energy 2017.

Altomare, C., Crespo, A. J., Rogers, B., Dominguez, J., Gironella, X., and Gómez-Gesteira, M. (2014). Numerical modelling of armour block sea breakwater with smoothed particle hydrodynamics. *Computers & Structures*, 130:34–45.

Altomare, C., Domínguez, J. M., Crespo, A. J. C., González-Cao, J., Suzuki, T., Gómez-Gesteira, M., and Troch, P. (2017). Long-crested wave generation and absorption for SPH–based DualSPHysics model. *Coastal Engineering*, 127:37–54.

Altomare, C., Tagliafierro, B., Dominguez, J., Suzuki, T., and Viccione, G. (2018). Improved relaxation zone method in SPH-based model for coastal engineering applications. *Applied Ocean Research*, 81:15–33.

Antonio, F. d. O. (2010). Wave energy utilization: A review of the technologies. *Renewable and Sustainable Energy Reviews*, 14(3):899–918.

Antuono, M., Colagrossi, A., Marrone, S., and Molteni, D. (2010). Free-surface flows solved by means of SPH schemes with numerical diffusive terms. *Computer Physics Communications*, 181(3):532–549.

Arena, F., Daniele, L., Fiamma, V., Fontana, M., Malara, G., Moretti, G., Romolo, A., Rosati Papini, G. P., Scialò, A., and Vertechy, R. (2018). Field experiments on dielectric elastomer generators integrated on a U-OWC wave energy converter. In *International Conference on Offshore Mechanics and Arctic Engineering*, volume 51319, page V010T09A028. American Society of Mechanical Engineers.

Arena, F., Fiamma, V., Laface, V., Malara, G., Romolo, A., Viviano, A., Sannino, G., and Carillo, A. (2013a). Installing U-OWC devices along Italian coasts. In *International Conference on Offshore Mechanics and Arctic Engineering*, volume 55423, page V008T09A061. American Society of Mechanical Engineers.

Arena, F., Romolo, A., Malara, G., and Ascanelli, A. (2013b). On design and building of a U-OWC wave energy converter in the Mediterranean sea: A case study. In *International Conference on Offshore Mechanics and Arctic Engineering*, volume 55423, page V008T09A102. American Society of Mechanical Engineers.

Ashlin, S. J., Sannasiraj, S., and Sundar, V. (2015). Wave forces on an oscillating water column device. *Procedia Engineering*, 116:1019–1026.

Baez Rivero, I. (2018). Investigation of the robustness of an oscillating water column breakwater under extreme wave conditions. Master's thesis, Delft University of Technology.

Beji, S. and Battjes, J. (1993). Experimental investigation of wave propagation over a bar. *Coastal Engineering*, 19(1-2):151–162.

Bhattacharyya, R. and McCormick, M. E. (2003). Wave energy conversion. *Elsevier ocean engineering book series*, 6:477–562.

Bingham, H. B. and Zhang, H. (2007). On the accuracy of finite-difference solutions for nonlinear water waves. *Journal of Engineering Mathematics*, 58(1):211–228.

Boccotti, P. (2003). On a new wave energy absorber. *Ocean Engineering*, 30(9):1191–1200.

Boccotti, P. (2007). Caisson breakwaters embodying an OWC with a small opening—Part I: Theory. *Ocean Engineering*, 34(5-6):806–819.

Boccotti, P. (2012). Design of breakwater for conversion of wave energy into electrical energy. *Ocean Engineering*, 51:106–118.

Boccotti, P., Filianoti, P., Fiamma, V., and Arena, F. (2007). Caisson breakwaters embodying an OWC with a small opening—Part II: A small-scale field experiment. *Ocean Engineering*, 34(5-6):820–841.

Bonet, J. and Kulasegaram, S. (2001). Remarks on tension instability of Eulerian and Lagrangian corrected smooth particle hydrodynamics (CSPH) methods. *International Journal for Numerical Methods in Engineering*, 52(11):1203–1220.

Bouscasse, B., Colagrossi, A., Marrone, S., and Antuono, M. (2013). Nonlinear water wave interaction with floating bodies in SPH. *Journal of Fluids and Structures*, 42:112–129.

Brito, M. (2018). *Numerical modeling and experimental testing of an oscillating wave surge converter*. PhD thesis, Tese de doutoramento em Engenharia Civil, Instituto Superior Técnico (IST . . . .

Cascajo, R., García, E., Quiles, E., Correcher, A., and Morant, F. (2019). Integration of marine wave energy converters into seaports: A case study in the port of Valencia. *Energies*, 12(5):787.

Cercos-Pita, J. (2015). Aquagpusph, a new free 3d sph solver accelerated with opencl. *Computer Physics Communications*, 192:295–312.

Chen, J., Wen, H., Wang, Y., and Wang, G. (2021). A correlation study of optimal chamber width with the relative front wall draught of onshore OWC device. *Energy*, 225:120307.

Cherfils, J.-M., Pinon, G., and Rivoalen, E. (2012). JOSEPHINE: A parallel SPH code for free-surface flows. *Computer Physics Communications*, 183(7):1468–1480.

Chiron, L., Marrone, S., Di Mascio, A., and Le Touzé, D. (2018). Coupled SPH–FV method with net vorticity and mass transfer. *Journal of Computational Physics*, 364:111–136.

Colagrossi, A. (2005). A meshless Lagrangian method for free-surface and interface flows with fragmentation. *These, Universita di Roma*.

Colagrossi, A. and Landrini, M. (2003). Numerical simulation of interfacial flows by smoothed particle hydrodynamics. *Journal of Computational Physics*, 191(2):448–475.

Cossu, R., Heatherington, C., Penesis, I., Beecroft, R., and Hunter, S. (2020). Seafloor site characterization for a remote island OWC device near King Island, Tasmania, Australia. *Journal of Marine Science and Engineering*, 8(3):194.

Crespo, A., Gómez-Gesteira, M., Narayanaswmy, M., and Dalrymple, R. (2008). A hybrid Boussinesq-SPH model for coastal wave propagation. In *Proceedings of the 3rd SPHERIC Workshop, ERCOFTAC. Lausanne, Switzerland*.

Crespo, A. J., Domínguez, J. M., Rogers, B. D., Gómez-Gesteira, M., Longshaw, S., Canelas, R., Vacondio, R., Barreiro, A., and García-Feal, O. (2015). DualSPHysics: Open-source parallel CFD solver based on Smoothed Particle hydrodynamics (SPH). *Computer Physics Communications*, 187:204–216.

Crespo, A. J. C., Altomare, C., Domínguez, J. M., González-Cao, J., and Gómez-Gesteira, M. (2017). Towards simulating floating offshore oscillating water column converters with Smoothed Particle Hydrodynamics. *Coastal Engineering*, 126:11–26.

Cummins, S. J. and Rudman, M. (1999). An SPH projection method. *Journal of Computational Physics*, 152(2):584–607.

Currie, I. G. (2016). *Fundamental mechanics of fluids*. CRC press.

Dalrymple, R. A. and Rogers, B. (2006). Numerical modeling of water waves with the SPH method. *Coastal Engineering*, 53(2-3):141–147.

Dang, B.-L., Nguyen-Xuan, H., and Wahab, M. A. (2021). Numerical study on wave forces and overtopping over various seawall structures using advanced SPH-based method. *Engineering Structures*, 226:111349.

Dehnen, W. and Aly, H. (2012). Improving convergence in smoothed particle hydrodynamics simulations without pairing instability. *Monthly Notices of the Royal Astronomical Society*, 425(2):1068–1082.

Delauré, Y. and Lewis, A. (2003). 3D hydrodynamic modelling of fixed oscillating water column wave power plant by a boundary element methods. *Ocean Engineering*, 30(3):309–330.

Deng, Z., Huang, Z., and Law, A. W. (2013). Wave power extraction by an axisymmetric oscillating-water-column converter supported by a coaxial tube-sector-shaped structure. *Applied Ocean Research*, 42:114–123.

Deng, Z., Wang, C., Wang, P., Higuera, P., and Wang, R. (2019). Hydrodynamic performance of an offshore-stationary OWC device with a horizontal bottom plate: Experimental and numerical study. *Energy*, 187:115941.

Deng, Z., Wang, L., Zhao, X., and Wang, P. (2020). Wave power extraction by a nearshore oscillating water column converter with a surging lip–wall. *Renewable Energy*, 146:662–674.

Didier, E., Neves, D. R. C. B., Teixeira, P. R. F., Dias, J., and Neves, M. G. (2016). Smoothed Particle Hydrodynamics numerical model for modeling an oscillating water chamber. *Ocean Engineering*, 123:397–410.

Dilts, G. A. (1999). Moving-least-squares-particle hydrodynamics—I. Consistency and stability. *International Journal for Numerical Methods in Engineering*, 44(8):1115–1155.

Domínguez, J. M., Crespo, A. J., Hall, M., Altomare, C., Wu, M., Stratigaki, V., Troch, P., Cappietti, L., and Gómez-Gesteira, M. (2019). SPH simulation of floating structures with moorings. *Coastal Engineering*, 153:103560.

Domínguez, J. M., Crespo, A. J., Valdez-Balderas, D., Rogers, B. D., and Gómez-Gesteira, M. (2013). New multi-GPU implementation for smoothed particle hydrodynamics on heterogeneous clusters. *Computer Physics Communications*, 184(8):1848–1860.

Egorova, M. S., Dyachkov, S. A., Parshikov, A. N., and Zhakhovsky, V. (2019). Parallel SPH modeling using dynamic domain decomposition and load balancing displacement of Voronoi subdomains. *Computer Physics Communications*, 234:112–125.

El Marjani, A., Ruiz, F. C., Rodriguez, M., and Santos, M. P. (2008). Numerical modelling in wave energy conversion systems. *Energy*, 33(8):1246–1253.

Elhanafi, A. (2016). Prediction of regular wave loads on a fixed offshore oscillating water column-wave energy converter using CFD. *Journal of Ocean Engineering and Science*, 1(4):268–283.

Elhanafi, A., Fleming, A., Macfarlane, G., and Leong, Z. (2016). Numerical energy balance analysis for an onshore oscillating water column–wave energy converter. *Energy*, 116:539–557.

Elhanafi, A. and Kim, C. J. (2018). Experimental and numerical investigation on wave height and power take–off damping effects on the hydrodynamic performance of an offshore–stationary OWC wave energy converter. *Renewable Energy*, 125:518–528.

Elhanafi, A., Macfarlane, G., Fleming, A., and Leong, Z. (2017a). Experimental and numerical measurements of wave forces on a 3D offshore stationary OWC wave energy converter. *Ocean Engineering*, 144:98–117.

Elhanafi, A., Macfarlane, G., Fleming, A., and Leong, Z. (2017b). Scaling and air compressibility effects on a three–dimensional offshore stationary OWC wave energy converter. *Applied Energy*, 189:1–20.

Engsig-Karup, A. P., Bingham, H. B., and Lindberg, O. (2009). An efficient flexible-order model for 3D nonlinear water waves. *Journal of Computational Physics*, 228(6):2100–2118.

Evans, D. (1982). Wave-power absorption by systems of oscillating surface pressure distributions. *Journal of Fluid Mechanics*, 114:481–499.

Evans, D. V. (1978). The oscillating water column wave energy device. *IMA Journal of Applied Mathematics*, 22(4):423–433.

Evans, D. V. and Porter, R. (1995). Hydrodynamic characteristics of an oscillating water column device. *Applied Ocean Research*, 17(3):155–164.

Falcão, A. d. O. (2000). The shoreline OWC wave power plant at the Azores. In *Proceedings of 4th European Wave Energy Conference*, pages 42–47.

Falcão, A. d. O., Sarmento, A., et al. (1980). Wave generation by a periodic surface pressure and its application in wave-energy extraction. In *15th International Congress of Theoritical and Applied Mechanics*.

Falcão, A. F., Henriques, J. C., and Cândido, J. J. (2012). Dynamics and optimization of the OWC spar buoy wave energy converter. *Renewable Energy*, 48:369–381.

Falcão, A. F. d. O. and Henriques, J. C. C. (2016). Oscillating water column wave energy converters and air turbines: A review. *Renewable Energy*, 85:1391–1424.

Ferrand, M., Joly, A., Kassiotis, C., Violeau, D., Leroy, A., Morel, F.-X., and Rogers, B. D. (2017). Unsteady open boundaries for SPH using semi-analytical conditions and Riemann solver in 2D. *Computer Physics Communications*, 210:29–44.

Ferrari, A., Dumbser, M., Toro, E. F., and Armanini, A. (2009). A new 3D parallel SPH scheme for free surface flows. *Computers & Fluids*, 38(6):1203–1217.

Fleissner, F. and Eberhard, P. (2008). Parallel load-balanced simulation for short-range interaction particle methods with hierarchical particle grouping based on orthogonal recursive bisection. *International Journal for Numerical Methods in Engineering*, 74.

Fourtakas, G., Stansby, P. K., Rogers, B. D., Lind, S. J., Yan, S., and Ma, Q. (2018). On the coupling of incompressible SPH with a finite element potential flow solver for nonlinear free-surface flows. *International Journal of Offshore and Polar Engineering*, 28(03):248–254.

Gingold, R. A. and Monaghan, J. J. (1977). Smoothed particle hydrodynamics: theory and application to non-spherical stars. *Monthly Notices of the Royal Astronomical Society*, 181(3):375–389.

Goda, Y. (1924). *Random Seas and Design of Maritime Structures*. University of Tokyo Press.

Gomez-Gesteira, M., Rogers, B. D., Crespo, A. J., Dalrymple, R. A., Narayanaswamy, M., and Dominguez, J. M. (2012). SPHysics–development of a free-surface fluid solver–part 1: Theory and formulations. *Computers & Geosciences*, 48:289–299.

Gubesch, E., Abdussamie, N., Penesis, I., and Chin, C. (2022). Maximising the hydrodynamic performance of offshore oscillating water column wave energy converters. *Applied Energy*, 308:118304.

Gunn, K. and Stock-Williams, C. (2012). Quantifying the global wave power resource. *Renewable Energy*, 44:296–304.

Guo, X., Rogers, B. D., Lind, S., and Stansby, P. K. (2018). New massively parallel scheme for incompressible smoothed particle hydrodynamics (ISPH) for highly nonlinear and distorted flow. *Computer Physics Communications*, 233:16–28.

Hansom, J. D., Switzer, A. D., and Pile, J. (2015). *Chapter 11 - Extreme Waves: Causes, Characteristics, and Impact on Coastal Environments and Society*. Hazards and Disasters Series. Elsevier, Boston.

He, F., Zhang, H., Zhao, J., Zheng, S., and Iglesias, G. (2019a). Hydrodynamic performance of a pile-supported OWC breakwater: An analytical study. *Applied Ocean Research*, 88:326–340.

He, M., Gao, X., Xu, W., Ren, B., and Wang, H. (2019b). Potential application of submerged horizontal plate as a wave energy breakwater: A 2D study using the WCSPH method. *Ocean Engineering*, 185:27–46.

Hérault, A., Bilotta, G., Vicari, A., Rustico, E., and Del Negro, C. (2011). Numerical simulation of lava flow using a GPU SPH model. *Annals of Geophysics*, 54(5).

Hotta, H., Miyazaki, T., Washio, Y., and Ishii, S. (1988). On the performance of the wave power device Kaimei—the results on the open sea tests. In *Proceedings of the Seventh International Conference on Offshore Mechanics and Arctic Engineering*, volume 1, pages 91–6.

Hu, Z. Z., Mai, T., Greaves, D., and Raby, A. (2017). Investigations of offshore breaking wave impacts on a large offshore structure. *Journal of Fluids and Structures*, 75:99–116.

Huang, C., Zhang, D., Si, Y., Shi, Y., and Lin, Y. (2018). Coupled finite particle method for simulations of wave and structure interaction. *Coastal Engineering*, 140:147–160.

Huang, X.-T., Sun, P.-N., Lyu, H.-G., and Zhang, A.-M. (2022). Numerical investigations on bionic propulsion problems using the multi-resolution Delta-plus SPH model. *European Journal of Mechanics-B/Fluids*, 95:106–121.

Huang, Z., Xu, C., and Huang, S. (2019). A CFD simulation of wave loads on a pile-type oscillating-water-column device. *Journal of Hydrodynamics*, 31(1):41–49.

Hughes, T. J. (2012). *The finite element method: Linear static and dynamic finite element analysis*. Courier Corporation.

Husain, S. M., Muhammed, J. R., Karunarathna, H. U., and Reeve, D. E. (2014). Investigation of pressure variations over stepped spillways using smooth particle hydrodynamics. *Advances in Water Resources*, 66:52–69.

Ihmsen, M., Akinci, N., Becker, M., and Teschner, M. (2011). A parallel SPH implementation on multi-core CPUs. In *Computer Graphics Forum*, volume 30, pages 99–112. Wiley Online Library.

Iturrioz, A., Guanche, R., Lara, J., Vidal, C., and Losada, I. (2015). Validation of Open-FOAM® for oscillating water column three-dimensional modeling. *Ocean Engineering*, 107:222–236.

Jacobsen, N. G., Fuhrman, D. R., and Fredsøe, J. (2012). A wave generation toolbox for the open-source CFD library: OpenFoam®. *International Journal for Numerical Methods in Fluids*, 70(9):1073–1088.

Ji, Z., Fu, L., Hu, X. Y., and Adams, N. A. (2019). A new multi-resolution parallel framework for SPH. *Computer Methods in Applied Mechanics and Engineering*, 346:1156–1178.

Kamath, A., Bihs, H., and ∅. A. Arntsen (2015). Numerical investigations of the hydrodynamics of an oscillating water column device. *Ocean Engineering*, 102:40–50.

Khan, M. B. and Behera, H. (2021). Impact of sloping porous seabed on the efficiency of an owc against oblique waves. *Renewable Energy*, 173:1027–1039.

Khayyer, A., Gotoh, H., and Shimizu, Y. (2017). Comparative study on accuracy and conservation properties of two particle regularization schemes and proposal of an optimized particle shifting scheme in ISPH context. *Journal of Computational Physics*, 332:236–256.

Kim, B.-H., Wata, J., Zullah, M. A., Ahmed, M. R., and Lee, Y.-H. (2015). Numerical and experimental studies on the PTO system of a novel floating wave energy converter. *Renewable Energy*, 79:111–121.

Kirby, J., Wei, G., Chen, Q., Kennedy, A. B., and Dalrymple, R. A. (1998). Fully nonlinear Boussinesq wave model documentation and user's manual. *Research Rep. CACR-98-06, Center for Applied Coastal Research, University of Delaware, Newark*.

Konispoliatis, D., Mazarakos, T., and Mavrakos, S. (2016). Hydrodynamic analysis of three–unit arrays of floating annular oscillating–water–column wave energy converters. *Applied Ocean Research*, 61:42–64.

Koo, W. and Kim, M.-H. (2010). Nonlinear time-domain simulation of a land-based oscillating water column. *Journal of Waterway, Port, Coastal, and Ocean Engineering*, 136(5):276–285.

Kuo, Y.-S., Lin, C.-S., Chung, C.-Y., and Wang, Y.-K. (2015). Wave loading distribution of oscillating water column caisson breakwaters under non-breaking wave forces. *Journal of Marine Science and Technology*, 23(1):10.

Kurniawan, A., Greaves, D., and Chaplin, J. (2014). Wave energy devices with compressible volumes. *Proceedings of the Royal Society A: Mathematical, Physical and Engineering Sciences*, 470(2172):20140559.

Lancaster, P. and Salkauskas, K. (1981). Surfaces generated by moving least squares methods. *Mathematics of computation*, 37(155):141–158.

Larsen, J. and Dancy, H. (1983). Open boundaries in short wave simulations—a new approach. *Coastal Engineering*, 7(3):285–297.

Le Méhauté, B. (2013). *An introduction to hydrodynamics and water waves*. Springer Science & Business Media.

Lee, E.-S., Moulinec, C., Xu, R., Violeau, D., Laurence, D., and Stansby, P. (2008). Comparisons of weakly compressible and truly incompressible algorithms for the SPH mesh free particle method. *Journal of Computational Physics*, 227(18):8417–8436.

LeVeque, R. J. et al. (2002). *Finite volume methods for hyperbolic problems*, volume 31. Cambridge university press.

Lin, C., Wang, X., Pastor, M., Zhang, T., Li, T., Lin, C., Su, Y., Li, Y., and Weng, K. (2021). Application of a hybrid SPH-Boussinesq model to predict the lifecycle of landslide-generated waves. *Ocean Engineering*, 223:108658.

Lind, S. J., Xu, R., Stansby, P. K., and Rogers, B. D. (2012). Incompressible smoothed particle hydrodynamics for free-surface flows: A generalised diffusion-based algorithm for stability and validations for impulsive flows and propagating waves. *Journal of Computational Physics*, 231(4):1499–1523.

Liu, M., Xie, W., and Liu, G. (2005). Modeling incompressible flows using a finite particle method. *Applied Mathematical Modelling*, 29(12):1252–1270.

Liu, M. B. and Liu, G. R. (2010). Smoothed particle hydrodynamics (SPH): An overview and recent developments. *Archives of Computational Methods in Engineering*, 17:25–76.

Liu, X., Lin, P., and Shao, S. (2015). ISPH wave simulation by using an internal wave maker. *Coastal Engineering*, 95:160–170.

Liu, Z., Cui, Y., Xu, C., Sun, L., Li, M., and Jin, J. (2019). Experimental and numerical studies on an OWC axial-flow impulse turbine in reciprocating air flows. *Renewable and Sustainable Energy Reviews*, 113:109272.

López, D., Marivela, R., and Garrote, L. (2010). Smoothed particle hydrodynamics model applied to hydraulic structures: A hydraulic jump test case. *Journal of Hydraulic Research*, 48(sup1):142–158.

López, I., Carballo, R., Taveira-Pinto, F., and Iglesias, G. (2020). Sensitivity of OWC performance to air compressibility. *Renewable Energy*, 145:1334–1347.

López, I., Pereiras, B., Castro, F., and Iglesias, G. (2014). Optimisation of turbine-induced damping for an OWC wave energy converter using a RANS–VOF numerical model. *Applied Energy*, 127:105–114.

López, I., Pereiras, B., Castro, F., and Iglesias, G. (2016). Holistic performance analysis and turbine-induced damping for an OWC wave energy converter. *Renewable Energy*, 85:1155–1163.

Lucy, L. B. (1977). A numerical approach to the testing of the fission hypothesis. *The Astronomical Journal*, 82:1013–1024.

Luo, Y., Wang, Z., Peng, G., Xiao, Y., Zhai, L., Liu, X., and Zhang, Q. (2014). Numerical simulation of a heave-only floating OWC (oscillating water column) device. *Energy*, 76:799–806.

Lyu, H.-G. and Sun, P.-N. (2022). Further enhancement of the particle shifting technique: Towards better volume conservation and particle distribution in SPH simulations of violent free-surface flows. *Applied Mathematical Modelling*, 101:214–238.

Mahnamfar, F. and Altunkaynak, A. (2017). Comparison of numerical and experimental analyses for optimizing the geometry of OWC systems. *Ocean Engineering*, 130:10–24.

Mai, T., Hu, Z. Z., Greaves, D., and Raby, A. (2015). Investigation of hydroelasticity: Wave impact on a truncated vertical wall. In *The Twenty-fifth International Ocean and Polar Engineering Conference*. OnePetro.

Malara, G. and Arena, F. (2013). Analytical modelling of an U-oscillating water column and performance in random waves. *Renewable Energy*, 60:116–126.

Malara, G. and Arena, F. (2019). Response of U-oscillating water column arrays: Semi-analytical approach and numerical results. *Renewable Energy*, 138:1152–1165.

Marrone, S., Antuono, M., Colagrossi, A., Colicchio, G., Touzé, D. L., and Graziani, G. (2011). δ–SPH model for simulating violent impact flows. *Computer Methods in Applied Mechanics and Engineering*, 200(13):1526–1542.

Marrone, S., Bouscasse, B., Colagrossi, A., and Antuono, M. (2012). Study of ship wave breaking patterns using 3D parallel SPH simulations. *Computers & Fluids*, 69:54–66.

Marrone, S., Colagrossi, A., Le Touzé, D., and Graziani, G. (2010). Fast free-surface detection and level-set function definition in SPH solvers. *Journal of Computational Physics*, 229(10):3652–3663.

Marrone, S., Di Mascio, A., and Le Touzé, D. (2016). Coupling of smoothed particle hydrodynamics with finite volume method for free-surface flows. *Journal of Computational Physics*, 310:161–180.

Martins-rivas, H. and Mei, C. C. (2009a). Wave power extraction from an oscillating water column along a straight coast. *Ocean Engineering*, 36(6-7):426–433.

Martins-rivas, H. and Mei, C. C. (2009b). Wave power extraction from an oscillating water column at the tip of a breakwater. *Journal of Fluid Mechanics*, 626:395–414.

Maruzewski, P., Touzé, D. L., Oger, G., and Avellan, F. (2010). SPH high-performance computing simulations of rigid solids impacting the free-surface of water. *Journal of Hydraulic Research*, 48:126 – 134.

Masuda, Y. and McCormick, M. E. (1986). Experiences in pneumatic wave energy conversion in Japan. In *Coastal Engineering*, pages 1–33. ASCE.

Mayer, S., Garapon, A., and Sørensen, L. S. (1998). A fractional step method for unsteady free-surface flow with applications to non-linear wave dynamics. *International Journal for Numerical Methods in Fluids*, 28(2):293–315.

Meringolo, D. D., Aristodemo, F., and Veltri, P. (2015). SPH numerical modeling of wave–perforated breakwater interaction. *Coastal Engineering*, 101:48 – 68.

Molteni, D. and Colagrossi, A. (2009). A simple procedure to improve the pressure evaluation in hydrodynamic context using the SPH. *Computer Physics Communications*, 180(6):861–872.

Molteni, D., Grammauta, R., and Vitanza, E. (2013). Simple absorbing layer conditions for shallow wave simulations with smoothed particle hydrodynamics. *Ocean Engineering*, 62:78–90.

Monaghan, J. (1989). On the problem of penetration in particle methods. *Journal of Computational Physics*, 82(1):1–15.

Monaghan, J. J. (1992). Smoothed particle hydrodynamics. *Annual review of astronomy and astrophysics*, 30:543–574.

Monaghan, J. J. (1994). Simulating free surface flows with SPH. *Journal of Computational Physics*, 110(2):399–406.

Monaghan, J. J. and Kos, A. (1999). Solitary waves on a cretan beach. *Journal of Waterway, Port, Coastal, and Ocean Engineering*, 125(3):145–155.

Monk, K., Winands, V., and Lopes, M. (2018). Chamber pressure skewness corrections using a passive relief valve system at the Pico oscillating water column wave energy plant. *Renewable Energy*, 128:230–240.

Morris, J. P. (1996). *Analysis of smoothed particle hydrodynamics with applications*. PhD thesis, Monash University Australia.

Muljadi, E. and Yu, Y.-H. (2015). Review of marine hydrokinetic power generation and power plant. *Electric Power Components and Systems*, 43(12):1422–1433.

Murotani, K., Koshizuka, S., Tamai, T., Shibata, K., Mitsume, N., Yoshimura, S., Tanaka, S., Hasegawa, K., Nagai, E., and Fujisawa, T. (2014). Development of hierarchical domain decomposition explicit MPS method and application to large-scale tsunami analysis with floating objects.

Napoli, E., De Marchis, M., Gianguzzi, C., Milici, B., and Monteleone, A. (2016). A coupled finite volume–smoothed particle hydrodynamics method for incompressible flows. *Computer Methods in Applied Mechanics and Engineering*, 310:674–693.

Narayanaswamy, M., Crespo, A. J. C., Gómez-Gesteira, M., and Dalrymple, R. A. (2010). SPHysics-FUNWAVE hybrid model for coastal wave propagation. *Journal of Hydraulic Research*, 48(sup1):85–93.

Ni, X., Feng, W., Huang, S., Zhang, Y., and Feng, X. (2018). A SPH numerical wave flume with non-reflective open boundary conditions. *Ocean Engineering*, 163:483–501.

Ni, X., Feng, W., Huang, S., Zhao, X., and Li, X. (2020). Hybrid SW-NS SPH models using open boundary conditions for simulation of free-surface flows. *Ocean Engineering*, 196:106845.

Ni, X. Y. and Feng, W. B. (2013). Numerical simulation of wave overtopping based on DualSPHysics. In *Applied Mechanics and Materials*, volume 405, pages 1463–1471. Trans Tech Publ.

Ning, D.-z., Guo, B.-m., Wang, R.-q., Vyzikas, T., and Greaves, D. (2020). Geometrical investigation of a U-shaped oscillating water column wave energy device. *Applied Ocean Research*, 97:102105.

Ning, D.-Z., Shi, J., Zou, Q.-P., and Teng, B. (2015). Investigation of hydrodynamic performance of an OWC (oscillating water column) wave energy device using a fully nonlinear HOBEM (higher-order boundary element method). *Energy*, 83:177–188.

Ning, D.-Z., Wang, R.-Q., Gou, Y., Zhao, M., and Teng, B. (2016). Numerical and experimental investigation of wave dynamics on a land-fixed OWC device. *Energy*, 115:326–337.

Ogata, T., Washio, Y., Osawa, H., Tsuritani, Y., Yamashita, S., and Nagata, Y. (2002). The open sea tests of the offshore floating type wave power device "Mighty Whale": Performance of the prototype. In *International Conference on Offshore Mechanics and Arctic Engineering*, volume 36142, pages 517–524.

Oger, G., Le Touzé, D., Guibert, D., De Leffe, M., Biddiscombe, J., Soumagne, J., and Piccinali, J.-G. (2016). On distributed memory MPI-based parallelization of SPH codes in massive HPC context. *Computer Physics Communications*, 200:1–14.

Ohneda, H., Igarashi, S., Shinbo, O., Sekihara, S., Suzuki, K., Kubota, H., Ogino, H., and Morita, H. (1991). Construction procedure of a wave power extracting caisson breakwater. In *Proceedings of 3rd Symposium on Ocean Energy Utilization*, pages 171–179.

Patterson, C., Dunsire, R., and Hillier, S. (2010). Development of wave energy breakwater at Siadar, Isle of Lewis. In *Coasts, marine structures and breakwaters: Adapting to change: Proceedings of the 9th international conference organised by the Institution of Civil Engineers and held in Edinburgh on 16 to 18 September 2009*, pages 738–749. Thomas Telford Ltd.

Paulsen, B. T., Bredmose, H., and Bingham, H. B. (2014). An efficient domain decomposition strategy for wave loads on surface piercing circular cylinders. *Coastal Engineering*, 86:57–76.

Pawitan, K. A., Dimakopoulos, A. S., Vicinanza, D., Allsop, W., and Bruce, T. (2019). A loading model for an OWC caisson based upon large-scale measurements. *Coastal Engineering*, 145:1–20.

Quartier, N., Crespo, A. J., Domínguez, J. M., Stratigaki, V., and Troch, P. (2021). Efficient response of an onshore oscillating water column wave energy converter using a one-phase SPH model coupled with a multiphysics library. *Applied Ocean Research*, 115:102856.

Ramachandran, P. (2016). PySPH: a reproducible and high-performance framework for smoothed particle hydrodynamics. In *Proceedings of the 15th python in science conference*, pages 127–135.

Ravindran, M. and Koola, P. M. (1991). Energy from sea waves—the Indian wave energy programme. *Current Science*, 60(12):676–680.

Rea, J. A., Kelly, J. F., Alcorn, R., and O'Sullivan, D. (2011). Development and operation of a power take off rig for ocean energy research and testing. In *Proceedings of the Ninth EWTEC 2011, Southampton, UK*.

Rezanejad, K., Bhattacharjee, J., and Soares, C. G. (2015). Analytical and numerical study of dual-chamber oscillating water columns on stepped bottom. *Renewable Energy*, 75:272–282.

Ricci, P. (2012). Modelling, optimisation and control of wave energy point-absorbers. *University of Lisbon Lisbon, Portugal.*

Robinson, M. J. (2009). *Turbulence and viscous mixing using smoothed particle hydrodynamics.* PhD thesis, Monash University.

Rogers, B., Dalrymple, R., Gómez-Gesteira, M., and Crespo, A. (2011). User guide for the parallelsphysics code using mpi v2. 0.

Sampath, R., Montanari, N., Akinci, N., Prescott, S., and Smith, C. (2016). Large-scale solitary wave simulation with implicit incompressible SPH. *Journal of Ocean Engineering and Marine Energy*, 2(3):313–329.

Sarmento, A. J. N. A. and Falcão, A. F. d. O. (1985). Wave generation by an oscillating surface–pressure and its application in wave–energy extraction. *Journal of Fluid Mechanics*, 150:467–485.

Scandura, P., Malara, G., and Arena, F. (2021). The inclusion of non-linearities in a mathematical model for U-Oscillating Water Column wave energy converters. *Energy*, 218:119320.

Schaller, M., Gonnet, P., Draper, P. W., Chalk, A. B., Bower, R. G., Willis, J., and Hausammann, L. (2018). SWIFT: SPH with inter-dependent fine-grained tasking. *Astrophysics Source Code Library*, pages ascl–1805.

Scialò, A., Henriques, J., Malara, G., Falcão, A., Gato, L., and Arena, F. (2021). Power take-off selection for a fixed U-OWC wave power plant in the Mediterranean sea: The case of Roccella Jonica. *Energy*, 215:119085.

Sheng, W., Thiebaut, F., Babuchon, M., Brooks, J., Lewis, A., and Alcorn, R. (2013). Investigation to air compressibility of oscillating water column wave energy converters. In *International Conference on Offshore Mechanics and Arctic Engineering*, volume 55423, page V008T09A005. American Society of Mechanical Engineers.

Simonetti, I., Cappietti, L., Elsafti, H., and Oumeraci, H. (2017). Optimization of the geometry and the turbine induced damping for fixed detached and asymmetric OWC devices: A numerical study. *Energy*, 139:1197–1209.

Simonetti, I., Cappietti, L., Elsafti, H., and Oumeraci, H. (2018). Evaluation of air compressibility effects on the performance of fixed OWC wave energy converters using CFD modelling. *Renewable Energy*, 119:741–753.

Skillen, A., Lind, S., Stansby, P. K., and Rogers, B. D. (2013). Incompressible smoothed particle hydrodynamics (SPH) with reduced temporal noise and generalised Fickian smoothing applied to body–water slam and efficient wave–body interaction. *Computer Methods in Applied Mechanics and Engineering*, 265:163–173.

Smith, G. D., Smith, G. D., and Smith, G. D. S. (1985). *Numerical solution of partial differential equations: Finite difference methods.* Oxford university press.

Souto-Iglesias, A., Delorme, L., Pérez-Rojas, L., and Abril-Pérez, S. (2006). Liquid moment amplitude assessment in sloshing type problems with smooth particle hydrodynamics. *Ocean Engineering*, 33(11-12):1462–1484.

Spanos, P. D., Strati, F. M., Malara, G., and Arena, F. (2018). An approach for non-linear stochastic analysis of U-shaped OWC wave energy converters. *Probabilistic Engineering Mechanics*, 54:44–52.

Strati, F. M., Malara, G., Laface, V., Romolo, A., and Arena, F. (2015). A control strategy for PTO systems in a U-OWC device. In *International Conference on Offshore Mechanics and Arctic Engineering*, volume 56499, page V003T02A066. American Society of Mechanical Engineers.

Sun, P., Colagrossi, A., Marrone, S., and Zhang, A. (2017). The δplus-SPH model: Simple procedures for a further improvement of the SPH scheme. *Computer Methods in Applied Mechanics and Engineering*, 315:25–49.

Sun, P., Zhang, A.-M., Marrone, S., and Ming, F. (2018a). An accurate and efficient SPH modeling of the water entry of circular cylinder. *Applied Ocean Research*, 72:60–75.

Sun, P.-N., Colagrossi, A., and Zhang, A.-M. (2018b). Numerical simulation of the self-propulsive motion of a fishlike swimming foil using the δ+-SPH model. *Theoretical and Applied Mechanics Letters*, 8(2):115–125.

Thakker, A., Dhanasekaran, T., Takao, M., and Setoguchi, T. (2003). Effects of compressibility on the performance of a wave-energy conversion device with an impulse turbine using a numerical simulation technique. *International Journal of Rotating Machinery*, 9(6):443–450.

Torre-Enciso, Y., Ortubia, I., De Aguileta, L. L., and Marqués, J. (2009). Mutriku wave power plant: From the thinking out to the reality. In *Proceedings of the 8th European wave and tidal energy conference, Uppsala, Sweden*, volume 710, pages 319–329.

Verbrugghe, T., Domínguez, J. M., Crespo, A. J., Altomare, C., Stratigaki, V., Troch, P., and Kortenhaus, A. (2018). Coupling methodology for smoothed particle hydrodynamics modelling of non-linear wave-structure interactions. *Coastal Engineering*, 138:184–198.

Verbrugghe, T., Stratigaki, V., Altomare, C., Domínguez, J., Troch, P., and Kortenhaus, A. (2019). Implementation of open boundaries within a two-way coupled SPH model to simulate nonlinear wave–structure interactions. *Energies*, 12(4):697.

Vicinanza, D., Lauro, E. D., Contestabile, P., Gisonni, C., Lara, J. L., and Losada, I. J. (2019). Review of innovative harbor breakwaters for wave-energy conversion. *Journal of Waterway, Port, Coastal, and Ocean Engineering*, 145(4):03119001.

Viviano, A., Musumeci, R. E., Vicinanza, D., and Foti, E. (2019). Pressures induced by regular waves on a large scale OWC. *Coastal Engineering*, 152:103528.

Viviano, A., Naty, S., and Foti, E. (2018). Scale effects in physical modelling of a generalized OWC. *Ocean Engineering*, 162:248–258.

Viviano, A., Naty, S., Foti, E., Bruce, T., Allsop, W., and Vicinanza, D. (2016). Large-scale experiments on the behaviour of a generalised oscillating water column under random waves. *Renewable Energy*, 99:875–887.

Vyzikas, T., Deshoulières, S., Giroux, O., Barton, M., and Greaves, D. (2017). Numerical study of fixed oscillating water column with RANS–type two–phase CFD model. *Renewable Energy*, 102:294–305.

Wang, C. and Zhang, Y. (2021a). Hydrodynamic performance of an offshore oscillating water column device mounted over an immersed horizontal plate: A numerical study. *Energy*, 222:119964.

Wang, C. and Zhang, Y. (2021b). Numerical investigation on the wave power extraction for a 3D dual-chamber oscillating water column system composed of two closely connected circular sub-units. *Applied Energy*, 295:117009.

Wang, C., Zhang, Y., and Deng, Z. (2021). Inclusion of a pitching mid-wall for a dual-chamber oscillating water column wave energy converter device. *Renewable Energy*.

Wang, D., Katory, M., and Li, Y. S. (2002). Analytical and experimental investigation on the hydrodynamic performance of onshore wave-power devices. *Ocean Engineering*, 29(8):871–885.

Wang, R. Q. and Ning, D. Z. (2020). Dynamic analysis of wave action on an OWC wave energy converter under the influence of viscosity. *Renewable Energy*, 150:578–588.

Wang, R.-q., Ning, D.-z., Zhang, C.-w., Zou, Q.-p., and Liu, Z. (2018). Nonlinear and viscous effects on the hydrodynamic performance of a fixed OWC wave energy converter. *Coastal Engineering*, 131:42–50.

Wang, R. Q., Ning, D. Z., and Zou, Q. Q. (2020). Wave loads on a land-based dual-chamber oscillating water column wave energy device. *Coastal Engineering*, 160:103744.

Washio, Y., Osawa, H., Nagata, Y., Fujii, F., Furuyama, H., and Fujita, T. (2000). The offshore floating type wave power device Mighty Whale: Open sea tests. In *The Tenth International Offshore and Polar Engineering Conference*. OnePetro.

Wen, H., Ren, B., and Yu, X. (2018). An improved SPH model for turbulent hydrodynamics of a 2D oscillating water chamber. *Ocean Engineering*, 150:152–166.

Wendland, H. (1995). Piecewise polynomial, positive definite and compactly supported radial functions of minimal degree. *Advances in computational Mathematics*, 4(1):389–396.

Whittaker, T., Beattie, W., Folley, M., Boake, C., Wright, A., Osterried, M., and Heath, T. (2004). The Limpet wave power project—The first years of operation. *Renewable Energy*.

Whittaker, T., McIlwaine, S., and Raghunathan, S. (1993). A review of the Islay shoreline wave power station. In *Proceedings of First European Wave Energy Symposium*, pages 283–6.

Xu, R., Stansby, P., and Laurence, D. (2009). Accuracy and stability in incompressible SPH (ISPH) based on the projection method and a new approach. *Journal of Computational Physics*, 228(18):6703–6725.

Yeylaghi, S. (2016). A parallel explicit incompressible smoothed particle hydrodynamics (ISPH) model for nonlinear hydrodynamic applications.

Zago, V., Schulze, L. J., Bilotta, G., Almashan, N., and Dalrymple, R. (2021). Overcoming excessive numerical dissipation in SPH modeling of water waves. *Coastal Engineering*, 170:104018.

Zhang, A.-m., Sun, P.-n., Ming, F.-r., and Colagrossi, A. (2017). Smoothed particle hydrodynamics and its applications in fluid-structure interactions. *Journal of Hydrodynamics, Ser. B*, 29(2):187–216.

Zhang, D. H., Li, W., and Lin, Y. G. (2009). Wave energy in China: Current status and perspectives. *Renewable Energy*, 34(10):2089–2092.

Zhang, N., Yan, S., Zheng, X., and Ma, Q. (2020). A 3D hybrid model coupling SPH and QALE-FEM for simulating nonlinear wave-structure interaction. *International Journal of Offshore and Polar Engineering*, 30(01):11–19.

Zhang, Y., Zou, Q. P., and Greaves, D. (2012). Air–water two-phase flow modelling of hydrodynamic performance of an oscillating water column device. *Renewable Energy*, 41:159–170.

Zhang, Z., Long, T., Chang, J., and Liu, M. (2019). A smoothed particle element method (SPEM) for modeling fluid–structure interaction problems with large fluid deformations. *Computer Methods in Applied Mechanics and Engineering*, 356:261–293.

Zhao, R., Faltinsen, O., and Aarsnes, J. (1996). Water entry of arbitrary two-dimensional sections with and without flow separation. In *Proceedings of the 21st Symposium on Naval Hydrodynamics*, pages 408–423.

Zheng, S., Antonini, A., Zhang, Y., Greaves, D., Miles, J., and Iglesias, G. (2019a). Wave power extraction from multiple oscillating water columns along a straight coast. *Journal of Fluid Mechanics*, 878:445–480.

Zheng, S., Zhang, Y., and Iglesias, G. (2019b). Coast/breakwater–integrated OWC: A theoretical model. *Marine Structures*, 66:121–135.

Zhou, Y., Ning, D., Chen, L., Zhang, C., Lin, L., and Sulisz, W. (2021). Nonlinear wave loads on a stationary cylindrical-type oscillating water column wave energy converter. *Ocean Engineering*, 236:109481.

Zhu, G., Graham, D., Zheng, S., Hughes, J., and Greaves, D. (2020). Hydrodynamics of onshore oscillating water column devices: A numerical study using smoothed particle hydrodynamics. *Ocean Engineering*, 218:108226.

Zhu, G., Hughes, J., Zheng, S., and Greaves, D. (2021). A SPH model with open relaxation boundary for wave generation and absorption. In *The 31st International Ocean and Polar Engineering Conference*. OnePetro.

Zhu, G. X. and Zou, L. (2020). An integrated smoothed particle hydrodynamics model for complex interfacial flows with large density ratios. *International Journal for Numerical Methods in Fluids*, 92(8):950–975.